Bridging Arcs to Shear : Multiscale Dark Matter Mapping in Galaxy Clusters with Strong and Weak Gravitational Lensing

PATEL, NENCY,RUPESHKUMAR

Bridging Arcs to Shear : Multiscale Dark Matter Mapping in Galaxy Clusters with Strong and Weak Gravitational Lensing

Nency R Patel

A thesis presented for the degree of

Doctor of Philosophy

Centre of Extragalactic Astronomy

Institute of Computational Cosmology

The University of Durham

United Kingdom

August 2025

Dedicated to,

Dada

Bridging Arcs to Shear : Multiscale Dark Matter Mapping in Galaxy Clusters with Strong and Weak Gravitational Lensing

Nency R Patel

Abstract

Matter in the Universe is inferred to be dominated by a collisionless, non-baryonic component, dark matter, which accounts for roughly 80% of the total matter content. Since dark matter emits no electromagnetic radiation, its presence must be probed indirectly via its gravitational interactions with baryonic matter. To date, direct detection experiments have yielded null results, and gravitational lensing, where the light from background sources is deflected and distorted by an intervening mass distribution, is one of the primary tools used to probe dark matter indirectly. Galaxy clusters, as the most massive observable structures, assemble via hierarchical accretion and merger events. Their large dark matter content makes them ideal to map dark matter. In dense cluster cores, strong lensing produces multiple, highly distorted images (or arcs) of background galaxies; at larger radii, weak lensing induces coherent shear patterns in the shapes of distant galaxies. By combining both regimes, clusters' projected mass distribution can be reconstructed from their core and up to several megaparsecs.

In this thesis, two contrasting systems are examined via a combined strong and weak lensing analysis. First, MACS J1423 ($z = 0.545$), a highly relaxed system, its mass distribution has been reconstructed using deep imaging from the *Hubble Space Telescope* (*HST*). No significant substructure is detected in the cluster, consistent with a dynamically mature state. Second, Abell 2744 ($z = 0.308$), a major merger, is analysed with joint *HST* and *James Webb Space Telescope* (*JWST*) observations. The resulting mass distribution yields six massive substructures (including its core). The abundance and spatial distribution of these substructures are sensitive to the properties of dark matter,

providing an observational test of dark matter to possibly distinguish between cold, warm and self-interacting dark matter candidates. The potential of the subhalo mass function to put constraints on these dark matter candidates is discussed, and plans for future comparisons with cosmological simulations are outlined.

Finally, the SLICE (Strong LensIng and Cluster Evolution) survey illustrates the next generation of strong and weak lensing studies. A new mass model for MACS J0027, derived from *JWST* imaging, is presented as a proof of concept, and the challenges of combining ultra-deep, multi-wavelength data with sophisticated lensing algorithms are discussed. These developments marks a new era of precision cosmology and dark matter characterisation.

Supervisors: Prof. Mathilde Jauzac, Dr. Anna Niemiec and Prof. Richard Massey

Acknowledgements

The last four years have been a beautiful gift I never expected, and I can not believe it is coming to an end. This journey would not have been possible or as much fun as it was without all the wonderful people by my side.

To my supervisors, Mathilde and Anna. I have admire you two since our first meeting! No matter what, you both have always been there for me, whenever I needed. Thank you Mathilde, for understanding and letting me work from home when I got home sick. For giving me the opportunity to attend conferences, and for pushing me to be a better researcher. Thank you Anna not just for being a great supervisor but also a friend. Thank you for being such a lovely host whenever I visited you and for helping me survive in France with my terrible French. Thank you to both of you for being my greatest support throughout. No amount of words can describe how blessed I feel to have you two as my supervisors. I will be eternally grateful.

To the Durham BUFFALO group. Thank you David for being there when I needed help for anything, and how patiently you would try to solve the issues with me, from lenstool to MUSE, you name it; you have been a great mentor. With Mathilde and Anna not being in Durham, I knew I could always count on you. Thank you to Guillaume for taking time to have chats, not just work related but also to make sure that I am doing okay. Thank you for always being a huge support and for your guidance. Especially, thank you for the career chat! Thank you to Catherine for being an amazing companion, starting from my very first conference. I have very much enjoyed travelling with you. Thank you to Jess, Stephane and Benjamin, for being so helpful and supportive group.

Thank you Alastair for taking the supervision in absence of Mathilde, for all your guidance and also for the constructive feedback for my paper. Thank you

to Richard, for always being so keen to know how my research is going, and for all your support. Thank you Sownak, for providing valueable feedback during the annual reviews and for helping me with my postdoc applications.

Thank you very much Kathy for your advice, guidance, and support. I would not have got this PhD in the first place if not for you.

Thank you Lourdes and Mike for being such a great Mentor! I always loved seeing you two. I can not thank you enough for always going out of your way to support me.

To my office mates. From the first day of my PhD to the last, Marcus, the office would have been so much less charming without your presence. Thank you for bearing with me for the past four years! Thank you Duncan and Victor, for imparting the wisdom, from whiteboard to the disappearing caterpillars. It has been a pleasure to share an office with you. I wish it was more than just a year. Thank you Emmy, for joining us in Rochester. I will miss our chit-chats.

To the Physics Department. Thank you everyone to make it a better place. The list is a long one, but to name a few, Martina, Scott, Ciera, Alexander, James, Zoe, Sarah and Shufei.

To my flatmates. It has been a pleasure to know you and share the flat with you all, Lucy, Annie, Will, Gabriel, Alex, and Weiyi. I will miss our games night, long kitchen talks, watching films together, and our Duke of Wellington trips!

To my foundation, my family. I would not have been here if not for my parents, this thesis is as much yours as it is mine. Relunctantly, a little thank you to my brother, Vraj, it has been more or less of a pleasure to have you here. Thank you to Mama and Mami, for being such a great support. Thank you to the most amazing people in my life, my friends. From school to "life", I would have smiled less, laughed less, and enjoyed less without your presence in my life. To my girls, Shaileja, Mansi and Anushka, and to Jinil, Rakshit and Apoorva. No matter where I am, all I want is to be able to spend as much time as possible with you. Thank you for merely existing. I would not want a world without you guys!

Finally, thank you God for being with me through every moment. Thank you for giving me the strength to keep going, no matter what. I am eternally grateful for everything.

Contents

Declaration

The work in this thesis is based on research carried out between October 2021 and August 2025 while the author was a research student under the supervision of Prof. Mathilde Jauzac, Dr. Anna Niemiec and Prof. Richard Massey at the Centre of Extragalactic Astronomy (CEA) and Institute of Computational Cosmology (ICC), Department of Physics, University of Durham, England. No part of this thesis has been submitted elsewhere for any other degree or qualification, and it is the sole work of the author unless referenced to the contrary in the text.

Some of the work presented in this thesis has been submitted/published in journals - the relevant publications are listed below.

Publications

- Chapter 5 of this thesis has been published in the form of a paper : Patel et al. (2024).
  N.R. Patel, M. Jauzac, A. Niemiec, D. Lagattuta, G. Mahler, B. Beauchesne, A. Edge, H. Ebeling, and M. Limousin.
  The KALEIDOSCOPE survey: a new strong and weak gravitational lensing view of the massive galaxy cluster MACSJ1423.8+2404.
  MNRAS, 533(4):4500–4514, Oct. 2024.doi:10.1093/mnras/stae2069.

- Parts of Chapter 7 has been submitted as a part of Cerny et al. (2025b).
  C.Cerny, G. Mahler, K. Sharon, M. Jauzac, G. Khullar, B. Beauchesne, J.M. Diego, D.J. Lagattuta, M. Limousin, N.R. Patel, J. Richard, C. Cornil-Baiotto, M.D. Gladders, S. Werner, J.E. Doppel, B. Floyd, A.H. Gonzalez, R.J. Massey, M. Montes, M.B. Bayliss, L.E. Bleem, R.E.A. Canning, A.C. Edge, M. McDonald, P. Natarajan, A.A. Stark, and R. Gassis.

Strong LensIng and Cluster Evolution (SLICE) with JWST: Early Results, Lens Models, and High-Redshift Detections.
arXiv e-prints, arXiv:2503.17498, Mar. 2025.doi:10.48550/arXiv.2503.17498.

List of Figures

List of Tables

Chapter 1

Introduction

"In the beginning, there was nothing, which exploded." - Terry Pratchett

The story of our Universe is one of extraordinary transformation; from an unimaginably hot and dense beginning to the vast cosmic structures we observe today. According to the Big Bang theory, the Universe began approximately 13.8 billion years ago as an almost infinitely small and energetic singularity. In an instant, space itself began to expand, setting the stage for the formation of all matter and energy. In the first moments after the Big Bang, the Universe expanded rapidly in an event called cosmic inflation, stretching tiny fluctuations in matter to larger scales. As the Universe continued to expand and cool, the basic forces of nature, like gravity and electromagnetism, began to act. The early Universe was a hot and dense mix of particles, where light could not travel freely because it was being kept scattered by free electrons. About 380,000 years later, the Universe cooled down enough for atoms to form, allowing light to travel freely for the first time. This light is visible today as the cosmic microwave background (CMB), giving us a glimpse of the young Universe. Over the following few hundred million years, small variations in matter grew under gravity, leading to the formation of the first stars and galaxies. These small structures eventually merged together to form the larger cosmic web, made of galaxies, clusters, and voids that are seen today as illustrated

in Figure 1.1 and 1.2.

Despite remarkable progress in our understanding of the formation and evolution, many fundamental questions remain unanswered. Observations suggest that the majority of the Universe is composed of dark matter and dark energy, yet their true nature remains unknown. Among these, dark matter plays a crucial role in shaping the large-scale structure of the Universe, influencing the formation of galaxies and galaxy clusters. Understanding the properties of dark matter is essential for a deeper understanding of cosmic evolution and the fundamental physics governing our Universe. This PhD work aims to contribute to the ongoing effort of unravelling the mysteries of dark matter and its role in shaping the Universe.

1.1 Cosmology

Cosmology, the study of the origin, evolution and eventual fate of the Universe seeks to understand the fundamental physical laws governing the cosmos. Cosmology combines observations with theoretical models to explain how the Universe has changed over time, from the Big Bang to its present state and beyond. Studying cosmology helps us answer fundamental questions about the Universe and our place in it. The period from the 16th to the 19th century marked a profound shift in our understanding of the Universe, transitioning from philosophical and religious interpretations to a scientific approach grounded in observation and mathematics. This era witnessed the emergence of the heliocentric model, Newtonian physics, and the first realisation that some distant 'nebulae' were actually entire galaxies, vast systems separate from our own Milky Way.

Before this scientific revolution, the dominant model of the cosmos was the geocentric system, formulated by Ptolemy in the 2nd century CE. According to this model, the Earth was at the center of the Universe, and all celestial bodies moved around it in complex orbits involving epicycles. However, discrepancies in planetary motion led to growing scepticism about this system. Nicolaus Copernicus was

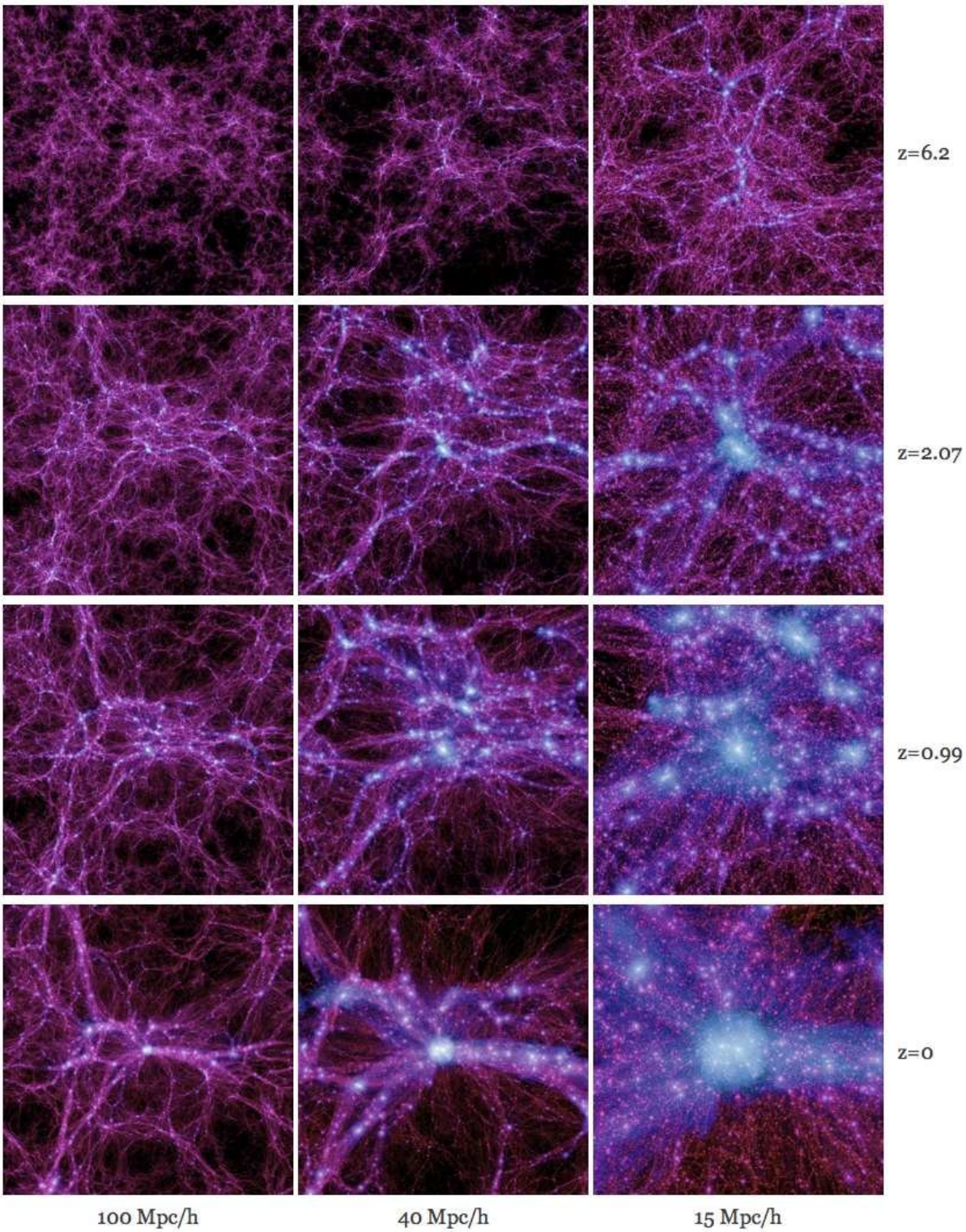

Figure 1.1: Formation and evolution of structures in the Universe as a function of time in the Millenium-II simulations, llustrating the emergence of the cosmic web from high redshift to the present day. Each row corresponds to a different epoch, while each column shows the density projected over a different scales. Credit : Boylan-Kolchin et al. (2009).

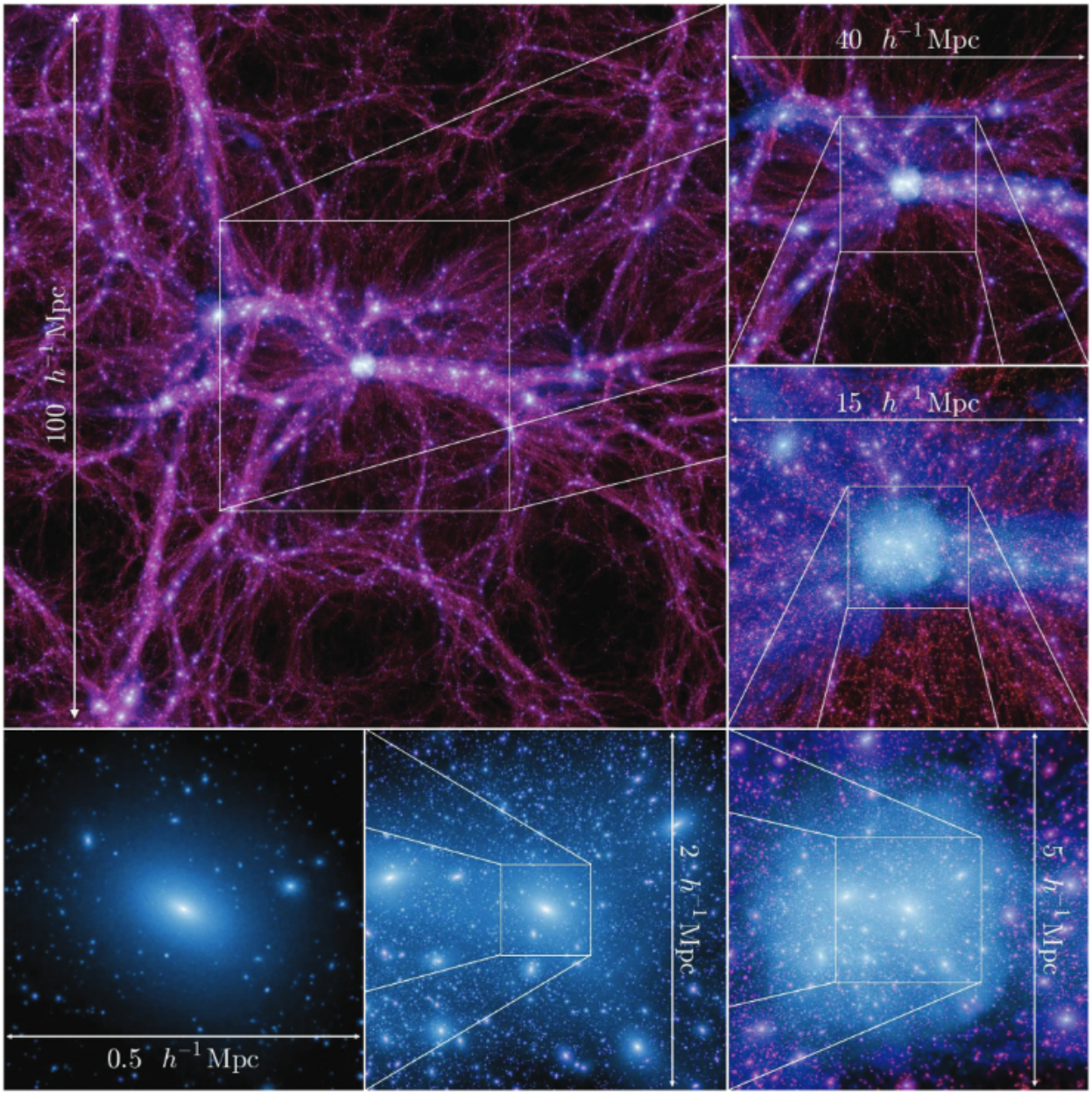

Figure 1.2: Sequential zoom through Millennium-II simulation. It starts at the full scale of the simlation (100 Mpc/h, bottom left in Figure 1.1) and zooms into the largest halo at redshift zero (present day), ending up at a scale of 0.5 Mpc/h. Credit : Boylan-Kolchin et al. (2009).

the first to challenge this long-standing belief with his heliocentric model, published in *De revolutionibus orbium coelestium* (Copernicus, 1543) in 1543. He proposed that the Sun, not the Earth, was at the center of the Universe, and that planets, including Earth, orbited it in perfect circles. This heliocentric model was refined by

Johannes Kepler in the early 17th century. He formulated three laws of planetary motion, showing that planets move in elliptical, not circular, orbits around the Sun. Copernicus and Kepler's work was supported by Galileo Galilei's finding, around the same time, when using his newly invented telescope, he observed four moons orbiting Jupiter and the complete sequence of Venus' phases. These observations offered evidence for the heliocentric theory.

While Kepler and Galileo established that planets orbit the Sun, they did not explain why they followed these motions. Isaac Newton provided the answer with his laws of motion and universal gravitation, published in *Principia Mathematica* (Newton, 1687). Newton's laws describe how objects move and interact with forces, while his law of universal gravitation explaines that every mass attracts every other mass with a force proportional to their masses and inversely proportional to the square of their distance.

As telescopes improved, astronomers began to map the structure of the Milky Way. Charles Messier catalogued over 100 nebulae, some of which were later identified as galaxies. In 1845, Lord Rosse discovered spiral structures in certain nebulae, hinting that they might be separate galaxies rather than clouds of gas within the Milky Way. By the 19th century, advances in thermodynamics and spectroscopy began shaping cosmological ideas. Lord Kelvin's "heat death" concept, proposed in 1852, suggested that a finite Universe would eventually reach a state of maximum entropy, implying it had a beginning (Kelvin, 1852). In spectroscopy, Joseph Fraunhofer discovered absorption lines in sunlight in 1814, and Gustav Kirchhoff and Robert Bunsen showed these lines corresponded to specific elements, particlularly, sodium, calcium, magnesium, iron, hydrogen, nickel and chromium (Kirchhoff and Bunsen, 1860). Additionally, the Doppler effect, proposed in 1842, by Christian Doppler, later became crucial for measuring the expansion of the Universe (Doppler, 1842). The Doppler effect describes the change in the observed wavelength (or frequency) of a wave when the source and observer are in relative motion; shifts light from receding objects toward longer, redder wavelengths (a "redshift"). By measuring

these redshifts in the spectra of distant galaxies, astronomers can calculate their recessional velocities; plotting those velocities against distance provided the key evidence for the expansion of the Universe (see Sect 1.1.2).

By the end of the 19th century, the key foundations of modern cosmology were in place. The heliocentric model had been firmly established, gravity was understood as the governing force of celestial motion, and spectroscopy provided new tools for studying the composition of stars and nebulae. However, the nature of the Universe, whether it was static or dynamic, finite or infinite remained an open question. These mysteries would only be "resolved" in the 20th century with the advent of Einstein's general relativity, the discovery of redshift, and the development of the Big Bang theory.

1.1.1 General Relativity

In 1915, Albert Einstein published his theory of General Relativity (GR Einstein, 1915), fundamentally altering our understanding of gravity. Unlike Newton's law of universal gravitation, which treats gravity as a force between two masses, Einstein's GR describes gravity as the curvature of spacetime caused by the presence of mass and energy. The core idea behind GR is that mass and energy influence the geometry of spacetime, and this curvature dictates how objects move through spacetime. Einstein's theory showed that objects in motion follow paths determined by the curvature of spacetime, which are known as geodesics. The Einstein Field Equations (EFE) are the cornerstone of GR and describe how matter and energy in the Universe influence the curvature of spacetime. The equation is given by:

$$G_{\mu\nu} = \frac{8\pi G}{c^4} T_{\mu\nu}, \tag{1.1}$$

where $G_{\mu\nu}$ is the Einstein tensor, determined by the curvature of spacetime at a specific point in space and time ,and $T_{\mu\nu}$ is the stress-energy tensor, which describes the distribution and flow of energy and momentum in spacetime. G and c are

the gravitational constant and the speed of light, respectively. These equations show that the curvature of spacetime (left-hand side) is directly related to the energy and momentum contained in spacetime (right-hand side). Intially, Einstein believed that the Universe was static and eternal. To maintain this belief of a stationary Universe, he introduced a cosmological constant (Λ) into the equations. to counterbalance the gravitational attraction of matter, preventing the Universe from collapsing. This led to the modified equation:

$$G_{\mu\nu} + \Lambda_{\mu\nu} = \frac{8\pi G}{c^4} T_{\mu\nu}, \tag{1.2}$$

where $g_{\mu\nu}$ is the metric tensor and Λ is the cosmological constant. However, after the discovery of the expansion of the Universe, Einstein referred to the cosmological constant as his "biggest blunder", because he had inserted it just to keep the Universe looking static.

1.1.2 Expansion of the Universe

In 1927, the Big Bang theory was put forward by Georges Lemaitre, suggesting that the Univerwse originated from an extremely dense and hot state, referred to as the "cosmic egg" or primeval atom. Lemaitre's theory implied that the Universe was expanding from a singular starting point. This was confirmed soon when Edwin Hubble made a groundbreaking discovery that would reshape the field of cosmology. Through observations of distant galaxies, Hubble found that galaxies were moving away from us, with their velocities proportional to their distances. This observation led to the formulation of the Hubble's Law (Hubble, 1929), which states that the recessional velocity, v, of a galaxy is proportional to its distance, d :

$$v = H_0 d, \tag{1.3}$$

where H_0 is the Hubble constant, representing the rate of expansion of the Universe. This empirical relationship between redshift and distance provided the first

observational evidence of the expansion of the Universe.

The Big Bang Theory is the leading cosmological model describing the origin and evolution of the Universe. It postulates that the Universe began as a hot, dense singularity approximately 13.8 billion years ago and has been expanding ever since (Peebles, 1993). The early Universe was initially an extremely hot and dense plasma of fundamental particles. As it expanded, it cooled down, allowing matter to form, and, thus, for structure to emerge. The first crucial phase, inflation, occurred within the first 10^{-32} seconds, causing an exponential expansion that smoothed out irregularities and set the stage for cosmic structure formation (Guth, 1981). Following inflation, the Universe transitioned into a radiation-dominated era, during which high-energy photons dominated its energy content.

Approximately 380,000 years after the Big Bang, the Universe had cooled down enough for neutral hydrogen atoms to form, allowing photons to travel freely. This event, known as recombination, led to the release of the Cosmic Microwave Background (CMB) radiation, the oldest light in the Universe, which we observe today as a faint glow permeating the Universe (Penzias and Wilson, 1965; Planck Collaboration, 2020a). Over the next millions of years, gravity amplified small density fluctuations, leading to the formation of the first stars, galaxies, and galaxy clusters (Peebles, 1980). Figure 1.3 shows a sketch of the evolution of the Universe from the Big Bang to the present time.

The evolution of the Universe is described mathematically by the Friedmann equations, derived from GR under the assumption of the Cosmological Principle. The Cosmological Principle is a fundamental assumption that the Universe, on large scales, is both homogenous and isotropic. Homogeneity means that when viewed on sufficiently large scales, the Universe looks the same at every single point. Similarly, isotropy means that the Universe looks the same in all directions for all observers, on large scales. The Cosmological Principle is described by the Friedmann-Lemaitre-Robertson-Walker (FLRW) metric, which is given by:

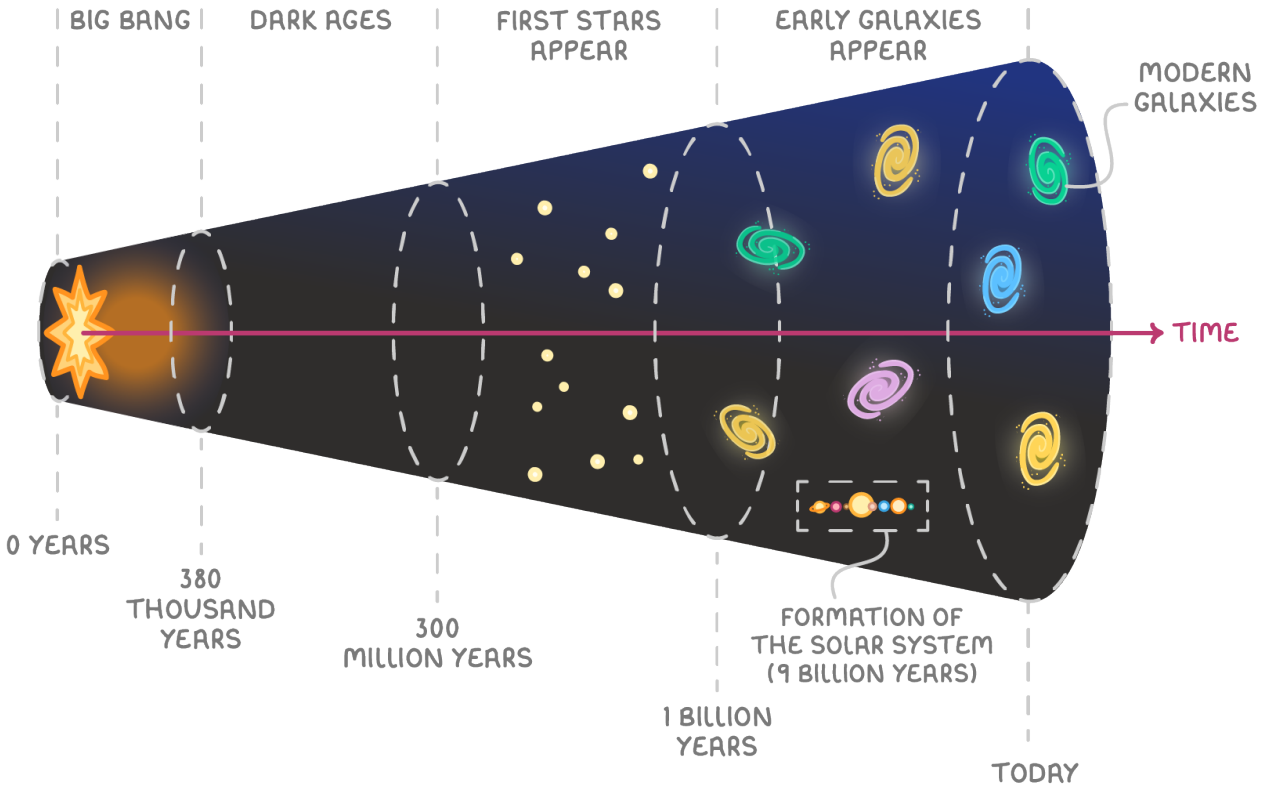

Figure 1.3: The evolution of the Universe from the Big Bang to the present day. From nothing to the formation of the first objects, and to the present day Universe, over the course of 13.8 billion years. Credit : Cognito Edu (2025).

$$ds^2 = -c^2dt^2 + a^2(t)\left[\frac{dr^2}{1-kr} + r^2d\theta^2 + r^2sin^2\theta d\phi^2\right], \tag{1.4}$$

where ds^2 represents the spacetime interval, c is the speed of light, t, the cosmic time, and r, θ, ϕ are the comoving spatial coordinates. The rate of expansion of the Universe is determined by the scale factor, $a(t)$. The overall geometry of the Universe is described by the curvature parameter, k. There are three possible values of k, corresponding to a different spatial curvature : $k = 0$, if the Universe is spatially flat, $k = +1$, if the Universe has a positive curvature with a spherical geometry with a positive curvature, and $k = -1$, if the Universe has a negative curvature with a hyperbolic geometry.

The FLRW metric and Einstein's equations give rise to the Friedmann equations.

The Friedmann's equation describing the expansion of the Universe is given by:

$$H^2 = \left(\frac{\dot{a}}{a}\right)^2 = \frac{8\pi G}{3}\rho - \frac{k}{a^2} + \frac{\Lambda}{3}, \tag{1.5}$$

where $H = (\dot{a}/a)$ is the Hubble parameter, which measures the expansion of the Universe. The energy density of the Universe is represented by ρ, and Λ is the cosmological constant, respresenting the energy density of empty space (dark energy). The Friedmann equation describing the acceleration of the Universe's expansion is given by:

$$H = \frac{\ddot{a}}{a} = -\frac{4\pi G}{3}\left(\rho + \frac{3p}{c^2}\right) + \frac{\Lambda}{3}, \tag{1.6}$$

where p is the pressure of the cosmic fluid.

These equations can be used to determine the overall geometry of the Universe. For a flat, matter dominated Universe, the curvature parameter, k, and the cosmological constant, Λ, is set to zero. The critical density for such a Universe is expressed as:

$$\rho_c = \frac{3H^2}{8\pi G}, \tag{1.7}$$

where $H = (\dot{a}/a)$ is the Hubble parameter. The ratio of the actual energy density of the Universe, (ρ), to the critical density, (ρ_c), gives the density parameter, Ω,

$$\Omega = \frac{\rho}{\rho_c}. \tag{1.8}$$

If $\Omega = 1$, it is a flat Universe, which will continue to expand infinitely but at a decreasing rate. If $\Omega > 1$, it is a closed Universe, in which the expansion will reverse, leading to an eventual collapse known as the Big Crunch. If $\Omega < 1$, the Universe is open, and will expand forever without stopping. The total energy density of the Universe is given by :

$$\Omega_{total} = \Omega_r + \Omega_m + \Omega_\Lambda + \Omega_k, \tag{1.9}$$

where $\Omega_r, \Omega_m, \Omega_\Lambda$ and Ω_k represent the radiation, matter, the cosmological constant and curvature density parameters, respectively. Observations of the CMB indicate

that the total density parameter of the Universe is very close to one, with a measured value of $\Omega_{total} \approx 1.001 \pm 0.002$ (Planck Collaboration, 2020a). This finding suggests that the Universe is almost perfectly flat, consistent with predictions of the standard Λ cold dark matter (ΛCDM) model. However, the total density consists of multiple components that contribute to the energy budget of the cosmos. Current estimates indicate that the matter density parameter, which includes both dark matter and baryonic matter, is approximately $\Omega_m \approx 0.31$. The contribution from radiation, which includes photons and relativistic neutrinos, is significantly smaller, around $\Omega_r \approx 10^{-4}$, reflecting its negligible impact in the current epoch (Ade and et al., 2016). The dominant component in the Universe today is dark energy, which is associated with the cosmological constant, Λ and accounts for $\Omega_\Lambda \approx 0.69$ (Riess, 1998; Perlmutter, 1999). The presence of dark energy is responsible for the observed accelerated expansion of the Universe, a phenomenon that was first confirmed through studies of distant Type Ia supernovae (Schmidt and et al., 1998). That breakthrough earned Saul Perlmutter, Brian P. Schmidt, and Adam G. Riess the 2011 Nobel Prize in Physics "for the discovery of the accelerating expansion of the Universe through observations of distant supernovae." These density measurements, along with the flatness of the Universe, provide strong support for the standard cosmological model in which dark matter and dark energy play a crucial role in shaping the fate of the Universe. This model of the Universe is called ΛCDM (see Sect.1.4 for more details).

1.2 Cosmological distances

In order to study cosmology, observable quantities play an important role. This section presents some of the crucial quantities which are essential for observational cosmology.

In an expanding Universe, as predicted by GR, the light from distant galaxies is stretched as space expands. This stretching of light leads to an increase in

the observed wavelength, a phenomenon known as redshift (z). Mathematically, redshift is given as:

$$1 + z = \frac{\lambda_o}{\lambda_e}, \tag{1.10}$$

where λ_o and λ_e are the emitted and observed wavelength, respectively. The cosmological redshift is linked to the expansion rate of the Universe through the scale factor in the FLRW metric, given by:

$$1 + z = \frac{\lambda_o}{\lambda_e} = \frac{a_0}{a(t)}, \tag{1.11}$$

where a_0 is the scale factor today, and $a(t)$ is the scale factor at the time of emission.

The cosmologocial redshift can be used to measure the comoving distance (D_C) and the angular diameter distance (D_A), two other essential quantity for observational cosomology. Comoving distance represents the present-day separation between two objects, taking into account the expansion of the Universe. It is given by :

$$D_C(z) = c \int_0^z \frac{dz'}{H(z')}, \tag{1.12}$$

where $H(z)$ is the Hubble parameter at redshift z.

Angular diameter distance links the physical size of an object to its observed angular size, and is related to the comoving distance D_C by :

$$D_A = \frac{D_C}{1 + z} = \frac{d}{\theta}, \tag{1.13}$$

where d is the physical size of the object and θ is the angular size.

The comoving and the angular diameter distances can be linked to the luminosity distance (D_L). For an object with intrinsic luminosity, L, and an observed flux, F, its luminosity distance is given as follow :

$$F = \frac{L}{4\pi D_L^2}. \tag{1.14}$$

The three distances are linked as follows :

$$D_C = (1+z)D_A = \frac{D_L}{1+z}. \tag{1.15}$$

1.3 Dark Matter

The concept of dark matter originated from astrophysical observations that suggested the presence of unseen mass influencing cosmic structures. One of the earliest indications came from Lord Kelvin (1904), who estimated the velocity dispersion of stars in the Milky Way and noted discrepancies between the observed motions and the expected values based on visible matter (Kelvin, 1904). Later, in 1922, Jacobus Kapteyn also suggested the presence of dark matter in stellar systems (Kapteyn, 1922).

A major breakthrough occurred in the 1930s when Fritz Zwicky studied the Coma Cluster of galaxies, and applied the Virial theorem to estimate the total mass of the cluster (Zwicky, 1933). He found that the galaxies within the cluster were moving much faster than expected based on the observed luminous matter. To explain this discrepancy, he coined the term "dunkle Materie" (dark matter), suggesting that a large amount of unseen mass was gravitationally bounding the cluster. However, at the time, this idea did not gain widespread acceptance.

Not until late 1970s, that the concept resurfaced when Vera Rubin and Kent Ford measured the rotation curves of spiral galaxies and discovered that the velocity of stars remained nearly constant at large radii, rather than decresing, as expected from Newtonian dynamics (Rubin and Ford, 1970, as shown in Figure 1.4). This provided compelling evidence for an unseen mass component extending beyond the visible disk of galaxies. Subsequent studies confirmed that galaxies are embedded in massive dark matter halos, which dominate their gravitational potential (Rubin et al., 1980).

Interacting only very weakly with gravity and not at all with electromagnetic radi-

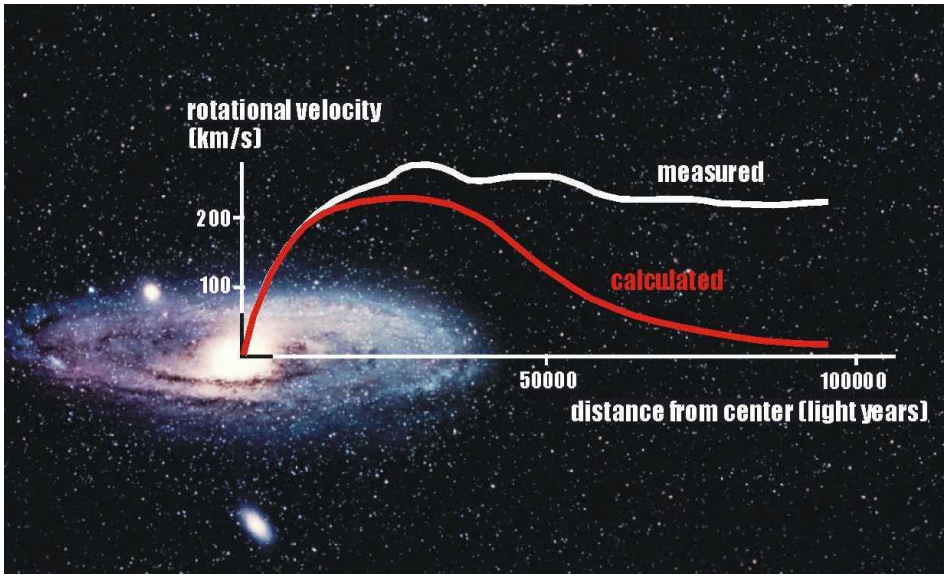

Figure 1.4: The velocity rotation curve of a spiral galaxy as a function of the distance from the center. Unlike the calculated (red line) rotational velocities by Newtonian dynamics, with only baryonic matter in the Universe, the observed (in white) suggest the presence of an additional unseen mass compoenent, dark matter.

ation, the nature of dark matter remains one of the greatest mysteries in modern physics. Despite its elusive nature, dark matter is estimated to make up around 27% of the total mass-energy density, and 80% of the total matter content of the Universe. Since dark matter does not interact electromagnetically, it must be non-baryonic (not made of protons and neutrons). Various theoretical candidates have been proposed, broadly classified into hot, warm, and cold dark matter, depending on their velocity distribution in the early Universe. The velocity of dark matter is related to how far it moved in the early Universe before it slowed down and became gravitationally bound. This is called free-streaming, and plays a key role in determining the smallest structures that can form in the Universe. Dark matter particles with higher velocities can travel farther before being slowed down, erasing the primordial small-scale density fluctuations (Seigar, 2015).

1.3.1 Cold Dark Matter (CDM)

Cold Dark Matter (CDM) is the leading theoretical framework for explaining the large-scale structure formation of the Universe today. It consists of non-relativistic particles that interact primarily through gravity, and do not undergo significant interactions with electromagnetic radiation. The CDM model successfully explains the observed cosmic web, galaxy rotation curves, and gravitational lensing effects (Peebles, 1982; Blumenthal, 1984). In this paradigm, structure formation follows a hierarchical model, where small-scale structures collapse first, and larger structures form through mergers (Navarro, 1996). Free-streaming in CDM predicts the formation of small structures first, which later merge to form larger galaxies and galaxy clusters (Springel, 2005).

One of the key features of CDM is the formation of dark matter halos that serve as the gravitational scaffolding for galaxies. Theory suggests that these halos follow a universal density profile, known as the Navarro-Frenk-White (NFW) profile, given by:

$$\rho(r) = \frac{\rho_s}{(r/r_s)(1 + r/r_s)^2}, \tag{1.16}$$

where ρ_s and r_s are the characteristic density and scale radius of the halo, respectively (Navarro, 1996). This profile predicts a steeply rising density towards the center of halos, leading to what is known as the *core-cusp problem*, where observed galaxy cores appear to have flatter density profiles than predicted by CDM simulations (Bullock and Boylan-Kolchin, 2017).

The ΛCDM model, which combines CDM with a cosmological constant, Λ, is the standard model of cosmology and successfully explains observations such as large-scale structure and galaxy clustering (Planck Collaboration, 2020b). However, certain small-scale challenges, including the missing satellites problem : fewer observed dwarf galaxies than predicted by theory, particularly in the Local Group around the Milky Way and Andromeda, and the *too-big-to-fail* problem : massive dark matter subhalos ($10^9 - 10^{10} M_\odot$) that should form visible galaxies but lack

corresponding stellar populations (Boylan-Kolchin et al., 2011), suggest the need for modifications of the CDM paradigm (Wechsler and Tinker, 2018). Alternative models, such as warm dark matter (WDM) and self-interacting dark matter (SIDM) attempt to address these discrepancies by introducing additional particle interactions or modifying the thermal properties of dark matter.

1.3.2 Warm Dark Matter (WDM)

Warm Dark Matter (WDM) consists of non-relativistic particles that allow small scale structure to form first in a hierarchical manner. However, WDM particles have non-negligible thermal velocities in the early Universe, leading to free-streaming over cosmological distances and suppressing the formation of the smallest structures (Bode et al., 2001). The free-streaming length of WDM depends on its particle mass, with lighter WDM particles (e.g., in the keV mass range) erasing structures below a characteristic scale, thus preventing the overproduction of dwarf galaxies predicted in CDM simulations (Lovell, 2014; Colin et al., 2000). This makes WDM a potential solution to small-scale challenges of CDM, such as the missing satellites problem and the *core-cusp* discrepancy. The leading candidates for WDM include sterile neutrinos, gravitons, and other hypothetical keV-scale particles that decouple while still relativistic, but becoming non-relativistic by the time structures form (Abazajian, 2001). While WDM provides an interesting alternative to CDM, it faces challenges in fully reproducing observed large-scale structure, and additional investigations are needed to determine whether it can serve as the primary dark matter component. A comparision between WDM and CDM is shown in Figure 1.5 for early time and present time Universe. Ongoing and forthcoming data will tighten WDM constraints such as subhalo counts in strong lenses imaged with *JWST* (Gardner et al., 2006) and *Euclid* mission (Laureijs et al., 2011), plus 21 cm power-spectrum measurements from the Square Kilometre Array (SKA; Braun et al. 2019).

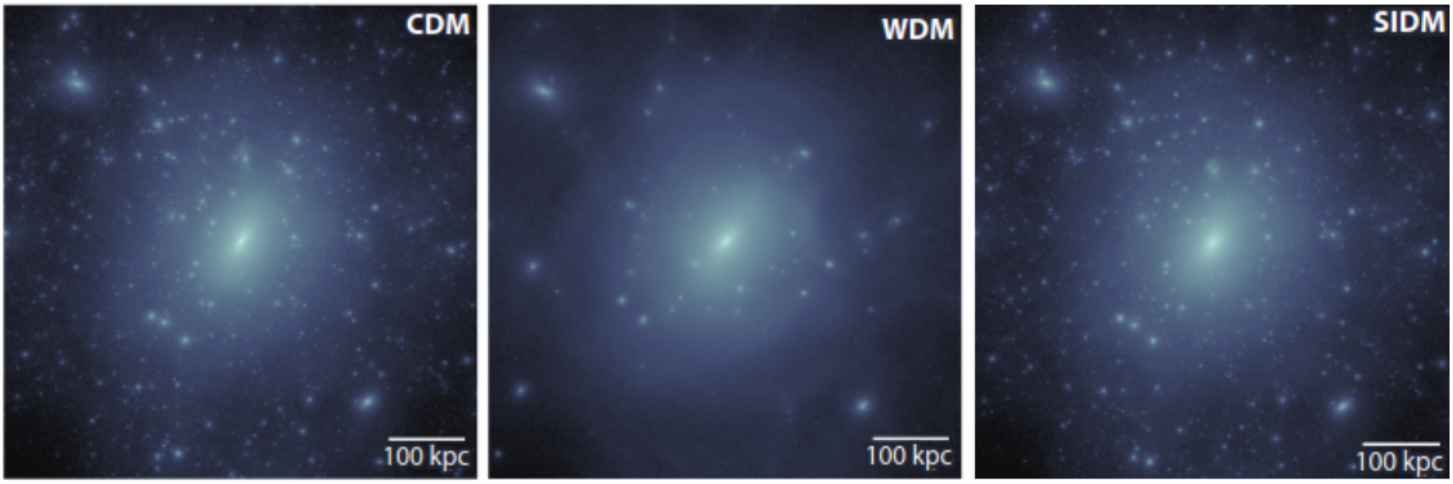

Figure 1.5: Visual comparison of a Milky Way mass dark matter halo formed in three cosmological models : cold dark matter (CDM), self-interacting dark matter (SIDM), and warm dark matter (WDM). The large-scale appearance of the halo is similar in CDM and SIDM, whereas WDM shows a visibly reduced abundance of small-scale substructure. SIDM produces large constant-density cores, while CDM retains a central cusp. Image Credit : Bullock and Boylan-Kolchin (2017).

1.3.3 Self Interacting Dark Matter (SIDM)

If dark matter is made of self-interacting dark matter (SIDM), dark matter particles would experience significant self-interactions beyond gravity. Unlike CDM, where particles interact only through gravitational attraction, SIDM allows for interactions such as elastic scattering, inelastic collisions, and even possible annihilation. SIDM particles maintain typical CDM velocities but undergo velocity-changing collisions through self-interactions, allowing high-velocity particles in dense regions to transfer momentum to slower particles and redistribute kinetic energy, effectively heating the inner regions and reducing central densities. These interactions are typically characterised by a cross-section per unit mass (σ/m) in $\mathrm{cm}^2\mathrm{g}^{-1}$. The motivation for SIDM arises to solve the *core-cusp* problem (de Blok et al., 2001). SIDM models provide a solution by allowing dark matter particles to scatter off each other, redistributing energy and creating a central core instead of a sharp density peak (Spergel and Steinhardt, 2000). Another challenge that SIDM addresses is the *too-big-to-fail problem* (Boylan-Kolchin et al., 2011). SIDM models

can alleviate this discrepancy by making inner halo densities lower due to self-interactions (Vogelsberger et al., 2012). The effectiveness of SIDM depends on the strength of self-interactions, with cross-sections typically constrained to be around $\sigma/m \sim 0.1 - 10 cm^2 g^{-1}$ from astrophysical observations (Rocha et al., 2013; Kaplinghat et al., 2016). While SIDM offers promising solutions to small-scale structure problems, it must also remain consistent with constraints from galaxy clusters, where high-velocity dark matter collisions suggest that the self-interaction cross-section must be small (Randall et al., 2008). Future observations, including strong and weak gravitational lensing in clusters, stellar kinematics in dwarf galaxies, and high-resolution simulations, will help refine the viability of SIDM as a dark matter model.

1.4 The Λ Cold Dark Matter Model (ΛCDM)

The Λ Cold Dark Matter(ΛCDM) model is the standard cosmological model describing the evolution of the Universe, assuming it is primarily composed of CDM and dark energy (Λ). Dark energy, represented by the cosmological constant, drives the accelerated expansion of the Universe. In this model, the Universe is approximately made of 68% dark energy, 27% of dark matter, and 5% of baryons (as shown in Figure 1.6), with a negligible contribution from radiation at the present epoch (Planck Collaboration, 2020a). The ΛCDM model also incorporates inflation, which explains the nearly scale-invariant spectrum of primordial fluctuations seen in the CMB. The predictions of ΛCDM align remarkably well with observational data, including large-scale structure formation and CMB anisotropies, making it the most widely accepted model of the Universe's evolution. However, despite its success, challenges remain, such as discrepancies in the Hubble constant measurements and the nature of dark matter and dark energy, this continues to be a major areas of research.

Cosmological parameters describe the fundamental properties of the Universe and

are constrained by observational data, including CMB, baryon acoustic oscillations (BAO), Type Ia supernovae, and large-scale structure surveys (Planck Collaboration, 2020a; et al., 2021). In the ΛCDM model, the key parameters are as follows:

- **The Hubble Constant (H_0):** The present expansion rate of the Universe, measured in km/s/Mpc. CMB measurements give $H_0 \approx 67.4$ km/s/Mpc (Planck Collaboration, 2020a), whereas local Cepheid-based estimates suggest a higher value of $H_0 \approx 73$ km/s/Mpc (et al., 2021), leading to the Hubble tension.

- **The Matter Density Parameter (Ω_m):** It represents the total matter density (dark + baryonic). Observations suggest $\Omega_m \approx 0.315$ (Planck Collaboration, 2020a).

- **The Dark Energy Density Parameter (Ω_Λ):** It represents the contribution of dark energy, responsible for the accelerated expansion, with $\Omega_\Lambda \approx 0.685$ (Planck Collaboration, 2020a).

- **The Baryon Density Parameter (Ω_b):** It describes the density of baryonic matter, such as protons and neutrons. Measurements indicate $\Omega_b \approx 0.049$, meaning baryonic matter makes up only about 5% of the Universe's total mass-energy density.

- **The Dark Matter Density Parameter (Ω_{DM}):** It accounts for the density of dark matter, which is non-relativistic (cold), and essential to structure formation. The value is typically around $\Omega_{DM} \approx 0.27$.

- **The Scalar Spectral Index (n_s):** It describes the shape of the primordial power spectrum of density fluctuations. Inflationary models predict values close to 1, with Planck observations giving $n_s \approx 0.965$ (Planck Collaboration, 2020a), which means the Universe has slightly fewer small-scale fluctuations than large-scale ones.

- **The Optical Depth (τ):** It measures the reionization history of the Universe, describing how much CMB photons are scattered by free electrons. Current constraints suggests $\tau \approx 0.054$ (Planck Collaboration, 2020a), which means which means only about 5 % of the CMB photons were scattered by free electrons on their way to us.

- **The Matter Power Spectrum Amplitude (σ_8):** It quantifies the amplitude of density fluctuations on an 8 Mpc/h scale, and is crucial for understanding structure formation. The CMB-based value is around $\sigma_8 \approx 0.81$ (Planck Collaboration, 2020a), but there are mild tensions between CMB and large-scale structure measurements. Large-scale structure surveys, particularly weak gravitational lensing, tend to favour lower clustering amplitudes than predicted by ΛCDM with CMB parameters, with the discrepancy being more pronounced at low redshifts (Müller et al., 2024).

- **The Neutrino Mass Sum ($\sum m_\nu$):** Massive neutrinos impact both the CMB and large-scale structure growth. Current limits from cosmology suggest $\sum m_\nu < 0.12$ eV (Planck Collaboration, 2020a), which means that all three known neutrino types together weigh less than about one-tenth of an electron volt, so light they account for under 1 % of the Universe's matter and only mildly slow the growth of cosmic structure.

1.5 Galaxy Clusters

The tendency of nebulae to form clusters was first observed by Charles Messier in 1784 when he noticed remarkable concentration of nebulae in the Virgo constellation. About the same time, William Herschel discovered a similar trend in the Coma constellation. However, it was only in the early 1920s, that clusters of galaxies were recognised, i.e., when Edwin Hubble proved that spiral and elliptical nebulae were actually distant galaxies, and that they cluster to form galaxy

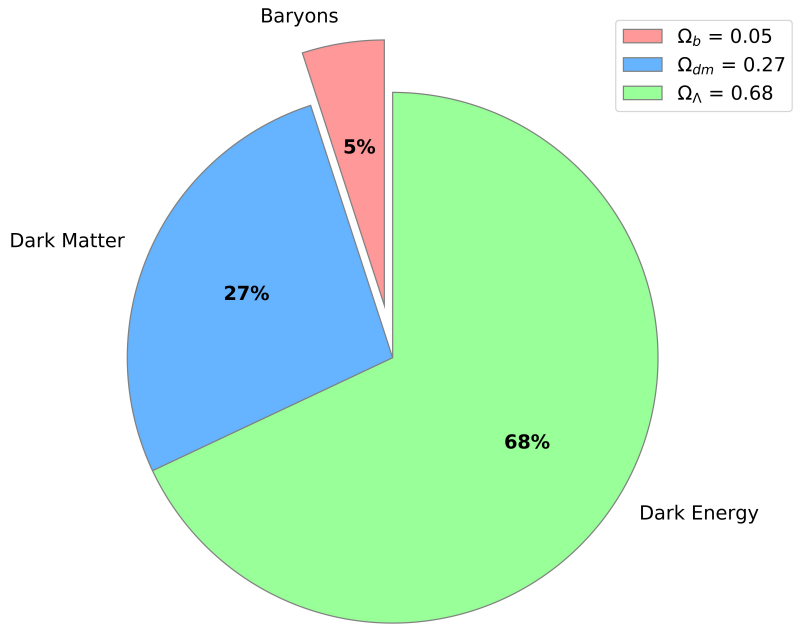

Figure 1.6: The pie chart here represents the main composition of the Universe. As per the ΛCDM model, the Universe is dominated by dark energy (68%), followed by dark matter (27%) and baryons (5%). The contribution of other components such as radiation is very small (0.01%), and negligible as a result.

clusters. In 1933, in an attempt to determine the masses of clusters of galaxies, Fritz Zwicky (Zwicky, 1933) found that the total mass of clusters exceeded the total mass of stars in clusters, indicating some missing mass, commonly known today as dark matter.

An improvement in the detailed and systematic study of galaxy clusters occurred in 1958 when George Abell compiled a catalogue of rich clusters of galaxies (Abell, 1958), called the Abell Catalogue of Clusters of Galaxies. Clusters of galaxies with more than thousand component galaxies are called rich galaxy clusters. Abell compiled the catalogue by visual inspection of wide field plates from the National Geographic Society - Palomar Observatory Sky Survey. The catalogue contained about 2700 galaxy clusters from the Northern Sky, and was limited to only the richest and symmetrical clusters. Later in 1989, an all sky catalogue of over 4000 rich galaxy clusters was compiled by Abell, Ronald Olowin and Harold Corwin (Abell et al., 1989) using data from the UK Schmidt Telescope survey.

In 1996, for the first time, by using rocket based detectors, X-ray emission was detected outside the Milky Way from the M87 galaxy in the Virgo cluster (Byram et al., 1966; Bradt et al., 1967). Then after, X-ray photons were detected from the Perseus cluster (Fritz et al., 1971) and the Coma cluster (Gursky et al., 1971; Meekins et al., 1971). These early detections of X-ray emission were made with rocket-borne detectors; while the significant advance in the study of X-ray astronomy was marked by the launch of Uhuru X-ray satellite in 1970 (Sarazin, 1988). Uhuru enabled a survey of the entire sky for X-ray emission, and confirmed that clusters of galaxies are strong X-ray emission sources (Giacconi et al., 1972).

Clusters of galaxies are the largest known gravitationally bound objects in the Universe. As the name suggest, they contain hundreds to thousands of galaxies, hot X-ray emitting gas (intracluster medium, ICM) and dark matter. Figure 1.7 shows galaxy cluster, Abell 383, in the X-rays, optical and composite (X-rays + optical) respectively. Only 3% and 10% of the total mass of the cluster is composed of stars and gas respectively, with the majority of the mass budget (87%) being made up of dark matter (Gonzalez et al., 2007). Clusters of galaxies are usually extended across a region of roughly 2 to 10 Mpc (10^{23} m) in diameter (Sarazin, 1988) and have masses of about 10^{14} to 10^{15} $M_{\odot}$ ($M_{\odot} = 1.989\times\ 10^{30}$ kg).

1.5.1 Cluster Mass Measurements

Determining the mass of galaxy clusters is crucial for understanding large-scale structure formation, testing cosmological models, and studying dark matter. There are several independent methods to estimate the mass of a cluster, each based on different physical principles. Some of them are discussed briefly in this section.

Figure 1.7: Images of cluster Abell 383 in the X-rays observed by the *Chandra* X-ray teledscope (top), the optical observed by *HST* (middle) and a composite image (bottom). Credit : *Chandra*, NASA.

Gravitational Lensing

One of the predictions of Einstein's theory of GR that light, like massive particles, is deflected in a gravitational field. Gravitational lensing occurs when the light

from a background source is deflected by an intervening mass. As a result they are distorted, magnified and even multiple images can form. Gravitational lensing is largely used to measure total mass of the cluster, taking into account both baryonic and dark matter. This thesis focuses on measuring the mass distribution of galaxy clusters using gravitational lensing. More details on this is given in Chapters 2 and 3.

Hydrostatic Mass

The hydrostatic mass calculation is based on the assumption of hydrostatic equilibrium and spherical symmetry of the hot ionised X-ray emitting gas, making the intracluster medium (ICM). This method uses information on the temperature and density of the ICM, probed via X-ray observations. For the gas to be in hydrostatic equilibrium, the gravitational force on the gas must balance the thermal pressure on it. The mass of the cluster within radius, r, can be thus expressed as,

$$M(r) = -\frac{rk_BT(r)}{G\mu m_p}\left[\frac{\mathrm{dln}\rho_g(r)}{\mathrm{dln}r} + \frac{\mathrm{dln}T(r)}{\mathrm{dln}r}\right], \tag{1.17}$$

where $\rho_g(r)$ is the gas density, G is the gravitational constant, k_B is the Boltzmann constant, T is the temperature of the gas, μ is the mean molecular weight, m_p is the mass of a proton, and n is the number density of the gas.

The cluster mass can be directly measured from the hydrostatic mass analysis. However, due to departures from spherical symmetry and hydrostatic equilibrium, it suffers from biases. Many methods were used to check the validity of the hydrostatic equilibrium. For instance, by comparing the hydrostatic mass with gravitational lensing mass (Mahdavi et al., 2008), it is shown that the hydrostatic mass is approximately 20% smaller than the lensing mass. The lensing mass is used for comparison as it gives a more accurate mass estimate. It traces the total mass distribution of a cluster, and does not depend on gas physics. A ∼30% bias in the hydrostatic mass has been seen using cosmological hydrodynamical simulations

(Suto et al., 2013). A more recent study of 50 galaxy clusters shows that the mean ratio of hydrostatic mass to lensing mass for galaxy clusters is 0.95 ± 0.05 (Smith et al., 2016), meaning that, on, average, the hydrostatic m 'equilibrium estimate of a cluster's mass is about 95% of the "true" mass as measured by lensing. In other words, hydrostatic methods tend to underestimate lensing cluster masses by roughly 5%.

Sunyaev-Zel'dovich (SZ) effect

The scattering of low energy photons to high energies by electrons is called inverse Compton scattering or up-scattering. The up-scattering of CMB photons to higher energies while passing through hot cluster gas energetic electrons is called the Sunyaev-Zel'dovich effect. The SZ effect causes a distortion of the CMB, and the amount of the distortion due to a galaxy cluster depends on the temperature and density of the gas in the cluster (Schneider, 2006).

The thermal SZ signal can be given as

$$Y_{SZ} = \int y \, \mathrm{d}\Omega, \tag{1.18}$$

where y is the Compton parameter, defined as

$$y = \frac{\sigma_T}{m_e c^2} \int n_e \, k_B \, T_e \, \mathrm{d}l, \tag{1.19}$$

where σ_T is the Thomson scattering cross-section, n_e the electron number density, and T_e the electron temperature along the line of sight. Summing y over the cluster's solid angle gives, $Y \propto M_{500}^{5/3}$, where M_{500} is the mass within which the mean density of a cluster is 500 times critical density (Sunyaev and Zeldovich, 1972; Schneider, 2006). Thus, the larger and more massive a cluster is, the more hot gas it contains and the higher its integrated SZ signal Y.

Virial Theorem

Member galaxies of a cluster move under the influence of the gravitational potential. Their velocity dispersion can be used to estimate the total cluster mass via the virial theorem:

$$M_{vir} = \frac{3\sigma_v^2 R}{G} \tag{1.20}$$

where σ_v is the line-of-sight velocity dispersion of galaxies, and R is the characteristic cluster radius. This method assumes that galaxies are in dynamical equilibrium, which may not always be the case due to mergers (Biviano and Salucci, 2006; Saro et al., 2013).

Caustic Mass

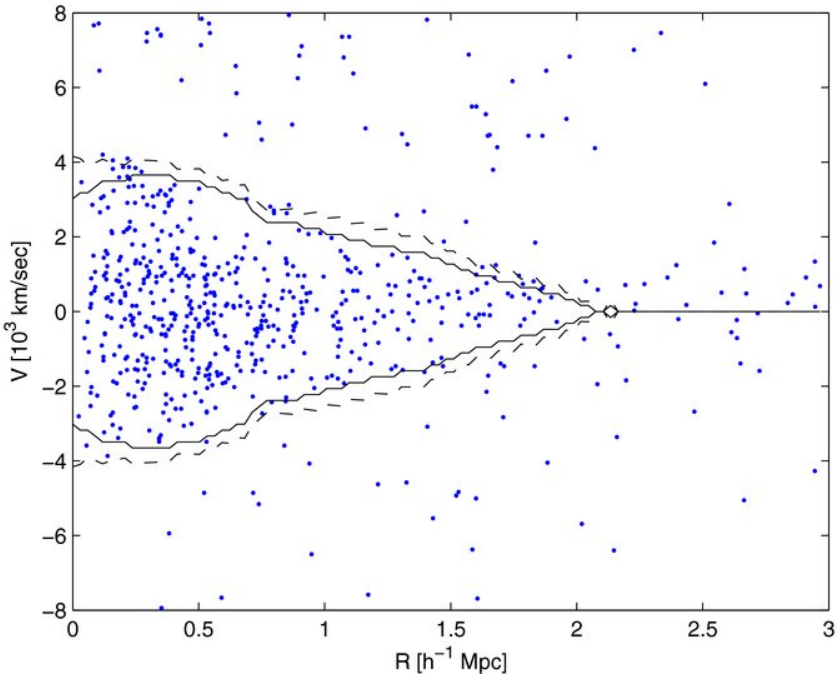

Figure 1.8: Velocity–radius diagram for Abell 1689, showing each galaxy's line-of-sight velocity relative to the cluster mean as a function of projected cluster-centric distance. The overlaid black curve is the caustic envelope, i.e. the fitted escape velocity profile, used to infer the cluster's mass distribution (Lemze et al., 2008).

When clusters are not in equilibrium, the caustic method provides an alternative way to estimate the mass by studying the phase-space distribution (velocity vs.

radius) of galaxies in the cluster. The escape velocity profile is used to determine the mass distribution (Diaferio, 1999). The caustic method uses the trumpet-like pattern (as shown in Figure 1.8) seen when plotting galaxy velocities against their distances from the cluster center. This pattern forms because galaxies are continuously falling into the cluster, creating a boundary that shows the escape velocity at each radius. The method works beyond the main cluster region where other techniques fail because the cluster is still growing. The mass profile is calculated from the caustic amplitude $A(r)$ using $M(r) = (\pi r^2 A(r))/(2G)$, where $A(r)$ is half of the distance between the upper and lower caustic in the velocity-radius plot (Pizzardo et al., 2023).

So far, we have traced the evolution of the Universe from its hot, dense beginnings through the current era of accelerated expansion, introduced the relativistic framework that governs cosmic dynamics, and established the necessity of non-baryonic dark matter to explain structure formation from galactic to cluster-scales. Galaxy clusters, as we have seen, provide ideal laboratories for studying this invisible dark matter component. This work exploits one of the most powerful observational tools for probing the matter distribution in the Universe: gravitational lensing. The following two chapters introduce the fundamentals of gravitational lensing theory (Chapter 2) and the techniques used to model mass distributions in galaxy clusters (Chapter 3).

Chapter 2

Gravitational Lensing

"Space tells matter how to move; matter tells space how to curve." - John Wheeler

Long before Einstein's Theory of General Relativity, the influence of gravity on the behaviour of light rays was mentioned by Newton in his '*Opticks*', published in 1704 (Netwon, 1704). A century later in 1801, gravitational lensing was first proposed by Johann Soldner in his paper (Soldner, 1804) '*Concerning the deflection of a light ray from its straight path due to the attraction of a heavenly body which it passes closely*'. Using Newtonian physics, Soldner predicted that a light ray passing close to the Sun would be deflected by an angle $\alpha = 0.84$ arcsec.

Unaware of Soldner's work, in 1911, Albert Einstein obtained the same value as Soldner for the deflection angle of a ray of light grazing the Sun (Einstein, 1911). Later in 1916, in the General Theory of Relativity (Einstein, 1916), Einstein derived the correct formula for deflection angle α of a light passing at a distance ξ from an object with mass M as

$$\alpha = \frac{4GM}{c^2}\frac{1}{r^2}. \tag{2.1}$$

From his General Theory of Relativity, Einstein obtained a deflection angle of $\alpha = 1.74$ arcsec for the Sun. Three years later, in 1919, gravitational lensing was first observed by Sir Arthur Eddington during a total solar eclipse when the positions of stars in a bright constellation behind the Sun were observed to be moderately shif-

ted from their usual positions (Eddington, 1919). Einstein's value of the deflection angle was confirmed to within 20% by Eddington.

In 1924, Chwolson (Chwolson, 1924) coined the idea of a circular image centred on the foreground star formed as a result of the foreground and background stars being perfectly aligned. More than a decade later in 1936, Einstein mentioned a star to be 'lens-like' and reported the appearance of a 'luminous' circle around the lens (the star in this case) (Einstein, 1936). He found that not only there is a formation of an image but it can also be highly magnified if there is a perfect alignment between the observer, the lens and the source. Einstein ends this idea by saying that "there is no great chance of observing this phenomenon". Only one year later, Fritz Zwicky suggested in his paper (Zwicky, 1937) entitled '*Nebulae as Gravitational Lenses*' that extragalactic nebulae (now known as galaxies) can act as better lenses than stars, and produce well separated images that could be observed.

It was only in 1979 that the first gravitational lensing event was observed when two quasars very close to each other and with similar spectra were discovered (Walsh et al., 1979). It was then confirmed that they were two images of the same object whose light had been deflected by the gravitational field of an intervening galaxy.

The deflection of a light ray due to the distortion of space-time by an intervening mass concentration (called the lens) is called gravitational lensing. The light from the background source is bent and often split by the gravitational potential of the lens, forming multiple, distorted and magnified images of the background source (Kneib and Natarajan, 2011). Figure 2.1 shows an illustration of gravitational lensing where the light from the background galaxy source is deflected by a galaxy cluster (lens) resulting in the formation of two images of the source galaxy.

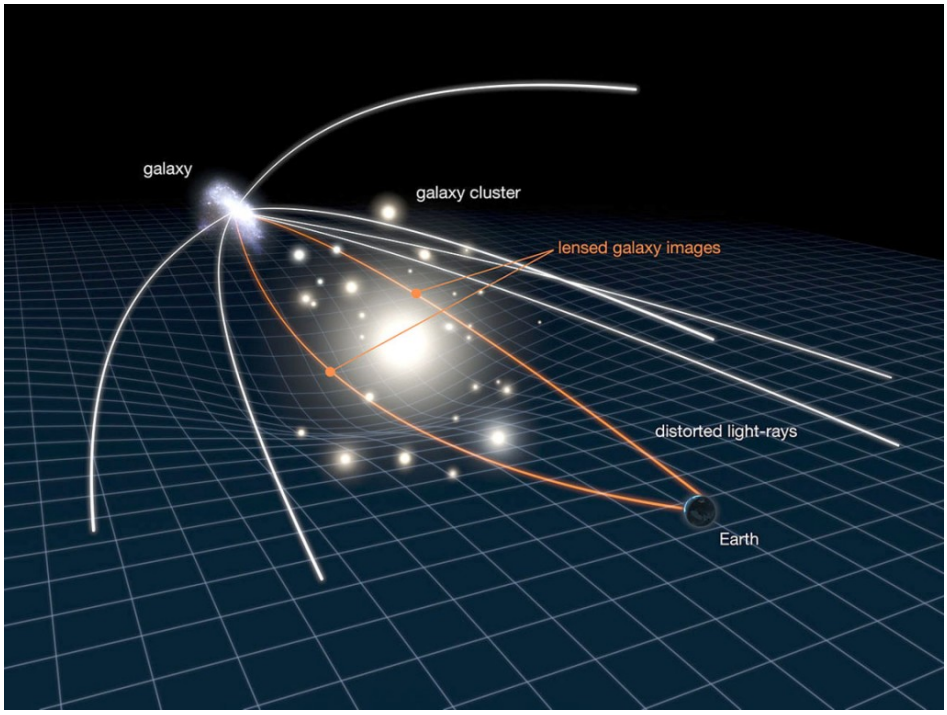

Figure 2.1: Gravitational lensing illustration. The light coming from a background galaxy is deflected by a galaxy cluster, resulting in the formation of two images of the galaxy. Credit : NASA et al. (2011)

2.1 Gravitational Lensing Theory

2.1.1 Lens Equation

A lensed image is seen when the lens equation is satisfied. The lens equation is derived in this section. We are assuming that the Universe is homogeneous and isotropic on large scale (the 'Cosmological Principle'), and we place ourselves in the context of the 'thin lens approximation' where the size of the lens is small compared to the distance between the lens and the source or the observer. The typical size of a cluster is generally of the order of a few Mpc, while the lens-source and lens-observer distances are of the order of a few Gpc.

Let's first consider the situation where the lens is a point mass. Under the small angles assumption and using general relativity, the deflection angle for a light ray passing at impact parameter ξ from a point mass M is given by:

$$\hat{\alpha} = \frac{4GM}{c^2 \xi} \tag{2.2}$$

where G is the gravitational constant and c is the speed of light. This formula shows that more massive lenses and closer approaches result in larger deflections.

Now let's focus on a more complex and realistic lens with a three dimensional mass distribution. Passing from a discrete mass distribution to a continuous one, we can treat the extended lens as having surface mass density $\Sigma(\boldsymbol{\xi})$, where $\boldsymbol{\xi}$ represents coordinates in the plane of the lens. We divide this distribution into infinitesimal mass elements:

$$dm = \Sigma(\boldsymbol{\xi'}) d^2\boldsymbol{\xi'} \tag{2.3}$$

located at position $\boldsymbol{\xi'}$. Each mass element acts like a point mass for deflection purposes, contributing:

$$d\hat{\boldsymbol{\alpha}} = \frac{4G dm}{c^2} \frac{\boldsymbol{\xi} - \boldsymbol{\xi'}}{|\boldsymbol{\xi} - \boldsymbol{\xi'}|^2} = \frac{4G}{c^2} \Sigma(\boldsymbol{\xi'}) \frac{\boldsymbol{\xi} - \boldsymbol{\xi'}}{|\boldsymbol{\xi} - \boldsymbol{\xi'}|^2} d^2\boldsymbol{\xi'} \tag{2.4}$$

The total deflection angle can therefore be expressed as:

$$\hat{\boldsymbol{\alpha}}(\boldsymbol{\xi}) = \frac{4G}{c^2} \int \Sigma(\boldsymbol{\xi'}) \frac{\boldsymbol{\xi} - \boldsymbol{\xi'}}{|\boldsymbol{\xi} - \boldsymbol{\xi'}|^2} d^2\boldsymbol{\xi'} \tag{2.5}$$

where $\Sigma(\boldsymbol{\xi})$ is the projected surface mass density, computed from the 3D mass density $\rho(\boldsymbol{\xi}, l)$ as:

$$\Sigma(\boldsymbol{\xi}) = \int \rho(\boldsymbol{\xi}, l) dl \tag{2.6}$$

where l is the coordinate along the line of sight. This integral formula represents a remarkable result: the deflection at any point depends on the weighted sum of contributions from all mass elements in the lens, with the weighting determined

by both the local surface density and the geometric factor involving the separation vector. The formula applies regardless of the complexity of the mass distribution, from simple spherical halos to irregular galaxy clusters with multiple components.

Now we consider the lensing situation presented in Figure 2.2, where we define a lens located at an angular distance D_L from the observer, and a source located at an angular distance D_S. The angular distance between the lens plane and the source plane is denoted by D_{LS}. The optical axis is defined as the line passing through the observer and perpendicular to the lens and source planes.

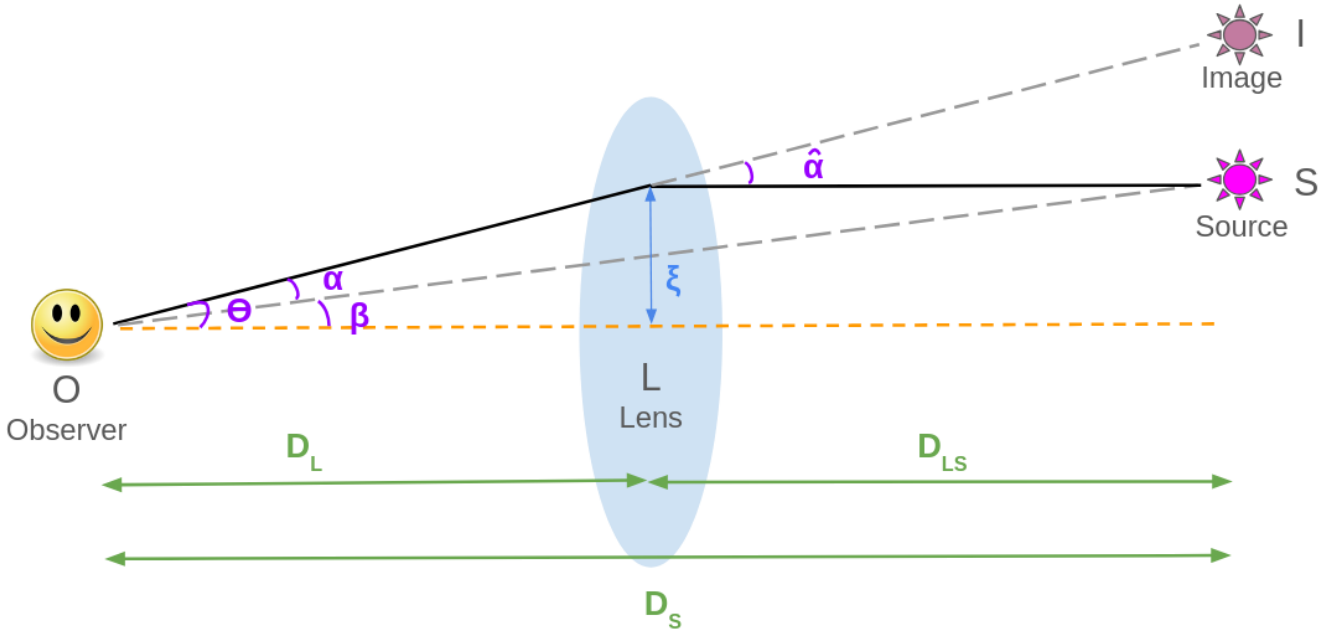

Figure 2.2: Sketch of the gravitational lensing geometry. Light from the distant source, S, leaves at the unlensed angle, $\boldsymbol{\beta}$, relative to the optic axis (dashed orange line), passes the lens, L, at the impact parameter, $\boldsymbol{\xi}$, and is deflected by $\hat{\boldsymbol{\alpha}}$. The observer, O, therefore sees an image, I, at the apparent angle θ. The angular diameter distances are D_L (observer-lens), D_{LS} (lens-source), and D_S (observer-source).

In this geometric setup, a background source emits light that appears at angular position $\boldsymbol{\beta}$ without lensing, but the gravitational field of the lens bends the light ray, causing us to observe the source at apparent position $\boldsymbol{\theta}$. With simple geometric considerations, the following relation can be expressed:

$$\boldsymbol{\theta} D_S = \boldsymbol{\beta} D_S + \hat{\boldsymbol{\alpha}} D_{LS} \tag{2.7}$$

This equation captures how the deflection angle, measured at the lens, translates into the angular shift we observe. The relationship depends on the distances involved in the lensing configuration, showing how the same physical deflection produces different angular effects depending on the cosmological geometry.

If we define the reduced deflection angle as:

$$\boldsymbol{\alpha}(\boldsymbol{\theta}) = \frac{D_{LS}}{D_S} \hat{\boldsymbol{\alpha}}(\boldsymbol{\theta}) \tag{2.8}$$

which incorporates the geometric factors into a single quantity, the lens equation can be simplified as:

$$\boldsymbol{\beta} = \boldsymbol{\theta} - \boldsymbol{\alpha}(\boldsymbol{\theta}) \tag{2.9}$$

This simple equation encodes the entire physics of gravitational lensing, relating the true source position to the observed position through the deflection caused by the intervening mass. The equation relates the true angular position of the source $\boldsymbol{\beta}$ to the apparent position after lensing $\boldsymbol{\theta}$, through the reduced deflection angle $\boldsymbol{\alpha}$.

Moreover for practical applications, we often work with angular coordinates rather than physical distances. Using the relationship $\boldsymbol{\xi} = D_L \boldsymbol{\theta}$ between physical coordinates in the lens plane and angular coordinates as observed, the deflection angle (given in equation2.5) in angular coordinates becomes:

$$\boldsymbol{\alpha}(\boldsymbol{\theta}) = \frac{4G}{c^2} \frac{D_{LS} D_L}{D_S} \int \Sigma(\boldsymbol{\theta}') \frac{\boldsymbol{\theta} - \boldsymbol{\theta}'}{|\boldsymbol{\theta} - \boldsymbol{\theta}'|^2} d^2\boldsymbol{\theta}' \tag{2.10}$$

This formula shows how the observable lensing effect (characterised by the reduced deflection angle $\boldsymbol{\alpha}(\boldsymbol{\theta})$) depends directly on the surface mass density distribution $\Sigma(\boldsymbol{\theta}')$ of the lens.

As seen from the deflection angle formula and the definition of the reduced deflection angle, the deflection depends on both the geometry of the Universe (through the angular distances D_{LS} and D_S) and the matter distribution of the lens (through the projected surface mass density $\Sigma(\xi)$). The effect is determined by how much mass the light ray encounters and how it is distributed spatially, more mass and more centrally concentrated distributions produce stronger deflections.

A particularly important case occurs when the source, lens, and observer are perfectly aligned, corresponding to $\boldsymbol{\beta} = 0$. In this symmetric configuration, the lens equation reduces to:

$$\boldsymbol{\theta}_E = \boldsymbol{\alpha}(\boldsymbol{\theta}_E) \tag{2.11}$$

where $\boldsymbol{\theta}_E$ is called the Einstein radius. The lensing power of a lens is described using its Einstein radius. For a point mass lens, this gives:

$$\boldsymbol{\theta}_E = \sqrt{\frac{4GMD_{LS}}{c^2 D_L D_S}} \tag{2.12}$$

showing that the Einstein radius increases with lens mass and depends on the specific distance configuration. When perfect alignment occurs, the lensed image appears as a ring centered on the lens, known as an Einstein ring (as shown in figure 2.3).

Lenses with larger Einstein radii produce more dramatic lensing effects, including multiple images, significant magnification, and easily detectable distortions. For typical galaxy lenses acting on background quasars, Einstein radii are typically around one arcsecond, while massive galaxy clusters can have Einstein radii of tens of arcseconds when lensing more distant galaxies.

The lens equation framework provides the foundation for extracting physical information from lensing observations. By measuring the positions and properties of lensed images,we can work backwards through the lens equation to infer the mass

Figure 2.3: An Einstein ring in cluster SMACS J0028.2-7537 captured by the *James Webb Space Telescope*. Central to the frame, a massive elliptical galaxy acts as a gravitational lens, appearing as a soft, oval glow around a compact, bright core. Its intense gravity distorts the light from a more distant spiral galaxy directly behind it, stretching that galaxy's spiral arms into an almost complete luminous ring, seen as vivid blue arcs. The ring forms when source, lens, and observer align so precisely that the galaxy's light is curved into a loop by the lens's mass. Credit : ESA/Webb, NASA & CSA, G. Mahler

distribution of the lens. This inverse problem, while mathematically challenging, has enabled remarkable discoveries about dark matter distributions in galaxies and clusters, the nature of dark energy through studies of distant supernovae, and even the detection of planets around other stars through microlensing effects.

2.1.2 Lensing Potential

All of the lensing physics can be encoded in a single scalar function on the sky, the lensing potential, $\psi(\boldsymbol{\theta})$. It is defined by integrating the three dimensional Newtonian potential, Φ, of the deflector along the line of sight, with the appropriate angular diameter distance weights:

$$\psi(\boldsymbol{\theta}) = \frac{2}{c^2}\,\frac{D_L\,D_{LS}}{D_S}\int_{-\infty}^{\infty}\Phi(D_L\,\boldsymbol{\theta},\,z)\,dz. \tag{2.13}$$

By construction, its gradient gives the reduced deflection angle,

$$\boldsymbol{\alpha}(\boldsymbol{\theta}) = \nabla_\theta\,\psi(\boldsymbol{\theta}). \tag{2.14}$$

With this, the lens equation can also be given as

$$\boldsymbol{\beta} = \boldsymbol{\theta} - \nabla_\theta\,\psi(\boldsymbol{\theta}). \tag{2.15}$$

Moreover, ψ satisfies a two-dimensional Poisson equation relating it to the dimensionless surface density (the convergence)

$$\nabla_\theta^2\,\psi(\boldsymbol{\theta}) = 2\,\kappa(\boldsymbol{\theta}), \qquad \kappa(\boldsymbol{\theta}) = \frac{\Sigma(D_L\,\boldsymbol{\theta})}{\Sigma_{crit}}, \tag{2.16}$$

where

$$\Sigma_{\rm crit} = \frac{c^2}{4\pi G}\,\frac{D_S}{D_L\,D_{LS}} \tag{2.17}$$

is the critical surface density of the lens. Thus, the full mapping from source to image deflection, distortion, and magnification can be derived once $\psi(\boldsymbol{\theta})$ (and hence $\kappa(\boldsymbol{\theta})$) is known.

2.1.3 Image Distortion : Convergence & Shear

When a small patch of the source (centered at true position $\boldsymbol{\beta}_0$) is lensed, its image (centerd at $\boldsymbol{\theta_0}$) is distorted. To the first order in the displacement $\delta\boldsymbol{\theta} = \boldsymbol{\theta} - \boldsymbol{\theta_0}$, the change in the apparent position of the source, $\delta\boldsymbol{\beta}$ is

$$\delta\boldsymbol{\beta}_i = A_{ij}\,\delta\boldsymbol{\theta}_j, \tag{2.18}$$

where i and j denote the axes of the angular coordinate on the sky plane $\boldsymbol{\theta} = (\boldsymbol{\theta}_1, \boldsymbol{\theta}_2)$ and the Jacobian matrix A_{ij} is the derivative of the lens mapping,

$$A_{ij} = \frac{\partial\boldsymbol{\beta}_i}{\partial\boldsymbol{\theta}_j} = \delta_{ij} - \frac{\partial^2\psi}{\partial\boldsymbol{\theta}_i\,\partial\boldsymbol{\theta}_j}. \tag{2.19}$$

The Jacobian matrix tells us how an infinitesimal vector in the image plane is stretched, rotated, or sheared when mapped back to the source plane.

If there were no lensing at all, A would be the identity matrix: every small shift in the image would map one-for-one back to the source. Gravitational deflection subtracts off second derivatives of the lensing potential, making A depart from the identity and encoding the distortion. These second derivatives of the lensing potential can be decomposed into two physically distinct parts, the convergence, κ and the shear, $\gamma = (\gamma_1, \gamma_2)$. Defining,

$$\begin{aligned} \kappa &= \tfrac{1}{2}(\psi_{,11} + \psi_{,22}), \\ \gamma &= \gamma_1 + i\gamma_2, \\ \gamma_1 &= \tfrac{1}{2}(\psi_{,11} - \psi_{,22}), \gamma_2 = \psi_{,12}, \end{aligned} \tag{2.20}$$

where, $\psi_{,i,j} = \frac{\partial^2\psi}{\partial\boldsymbol{\theta}_i\,\partial\boldsymbol{\theta}_j}$, and the Jacobian becomes

$$A = \begin{pmatrix} 1-\kappa-\gamma_1 & -\gamma_2 \\ -\gamma_2 & 1-\kappa+\gamma_1 \end{pmatrix}. \tag{2.21}$$

Convergence acts like an isotropic lens, it uniformly magnifies ($\kappa > 0$) or demagnifies ($\kappa < 0$) the image, preserving its shape but changing its size. On the other hand, shear introduces anisotropic distortions, stretching the image along one axis while compressing it along the perpendicular axis. Its magnitude, $|\gamma| = \sqrt{\gamma_1^2 + \gamma_2^2}$, sets the ellipticity, and its phase, $\phi = \frac{1}{2}\arctan(\gamma_2/\gamma_1)$, gives the orientation of the ellipse's major axis (the direction of maximum stretch). If we feed a tiny circular source patch through the matrix given in 2.21, the output is an ellipse whose size has changed by a factor $1-\kappa$ and whose axes have been scaled differently according to γ. Since the matrix A is symmetric, it has two real eigenvalues, which are called the radial and tangential stretch components,

$$\begin{aligned} \lambda_r &= 1 - \kappa + |\gamma| \\ \lambda_t &= 1 - \kappa - |\gamma|. \end{aligned} \tag{2.22}$$

The radial component, λ_r, stretches or compresses images along the radial direction (toward or away from the lens center). On the other hand, the tangential component, λ_t, stretches or compresses images along directions tangent to circles around the lens. Thus, together, κ and γ fully describes the first order distortions of any small source patch under gravitational lensing.

2.1.4 Magnification

The determinant of the Jacobian gives the area distortion,

$$det\, A = (1-\kappa)^2 - |\gamma|^2 = \lambda_t \lambda_r. \tag{2.23}$$

Since gravitational lensing merely bends light without creating or destroying photons, surface-brightness is conserved. Any change in observed flux must arise purely from a change in apparent angular size, i.e. the area distortion, which is quantified by the magnification factor. Thus, the magnification, μ, is defined as the ratio of the solid angle between the lensed image and the unlensed source,

$$\mu = \frac{1}{det\, A} = \frac{1}{(1-\kappa)^2 - |\gamma|^2}. \tag{2.24}$$

2.2 Strong Gravitational Lensing

When a lens is massive enough, the lens equation (Equation 2.9) can accept multiple solutions for $\boldsymbol{\theta}$, for the same source position, $\boldsymbol{\beta}$, creating multiple images of the same source. This regime, in which a foreground mass is dense enough (such as the core of a galaxy cluster) that the lens mapping folds the sky onto itself, makes a single object appear more than once, and is called strong lensing. Strong lensing occurs wherever the Jacobian determinant (given in equation 2.23) drops to zero. At those locations, one of the Jacobian's eigenvalues, the tangential factor $\lambda_t = 1-\kappa-|\gamma|$, or the radial factor $\lambda_r = 1-\kappa+|\gamma|$, vanishes, causing the image to be stretched without limit in that direction and forming giant arcs or, under near perfect alignment, an Einstein ring. The sky locus, where $\det A = 0$, is called a *critical curves*, and is represented by two closed non intersecting lines. Mapping the critical lines back into the source plane through the lens equation produces closed curves called *caustic curves*. Any source that lies inside, or crosses, a caustic gains two additional images, so its image multiplicity jumps from one to three, three to five, and so on. Critical curves come in two types, identified by where they lie with respect to the lens centre. The outer one, located further from the centre, stretches images tangentially, and is therefore called the *tangential critical curve*, while the inner one, closer to the centre, distorts images in the radial direction and is known as the *radial critical curve* as illustrated in Figure 2.4.

Positions and brightness ratios of these images depends sensitively on the projected mass inside the critical curve. As a result, strong lensing configurations provide direct mass measurements of the lens (galaxies or galaxy clusters). For a circularly symmetric lens, the critical and caustic curves are themselves circles, and the tangential caustic shrinks to a single point on the optical axis. For an axis-symmetric

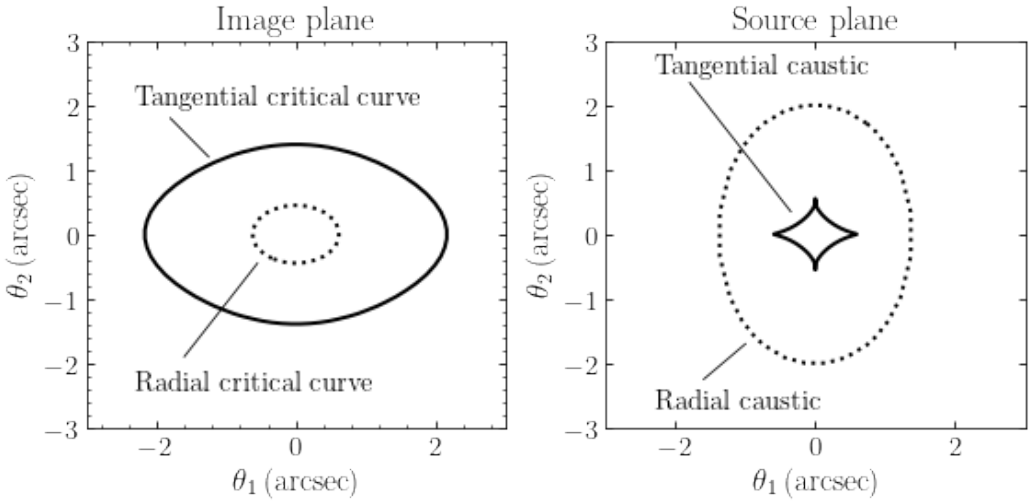

Figure 2.4: Illustration showing the tangential and radial critical curves in the image plane; in the corresponding source plane the tangential and radial caustic lines appear in the opposite order to their critical-curve counterparts. Credit : Bovy (2025).

surface-density, the mass inside radius r satisfies,

$$M(<r) = \frac{c^2\, D_L\, D_S}{4\, G\, D_{LS}}\, r\, \frac{\partial \psi(r)}{\partial r}, \tag{2.25}$$

where $\psi(r)$ is the lensing potential. The *tangential critical curve* occurs where the tangential stretch factor vanishes, i.e.

$$r_t = \frac{\partial \psi(r)}{\partial r}. \tag{2.26}$$

Identifying $r_t = D_L\, \boldsymbol{\theta}_E$ and using $\Sigma_{crit} = \frac{c^2}{4\pi G}\frac{D_S}{D_L D_{LS}}$ (Eq 2.17) yields the familiar Einstein-mass relation,

$$M(<\boldsymbol{\theta}_E) = \pi\, \Sigma_{crit}\, \boldsymbol{\theta}_E^2, \tag{2.27}$$

which allows a nearly model independent measurement of the mass within the Einstein radius $\boldsymbol{\theta}_E$ once the lens and the source redshifts are known.

The *radial critical curve*, on the other hand, is defined by the vanishing of the radial stretch factor, equivalently

$$\frac{\partial^2 \psi(r)}{\partial r^2} = \frac{1}{\pi\, \Sigma_{crit}\, r}\, \frac{\partial M(<r)}{\partial r} = 1. \tag{2.28}$$

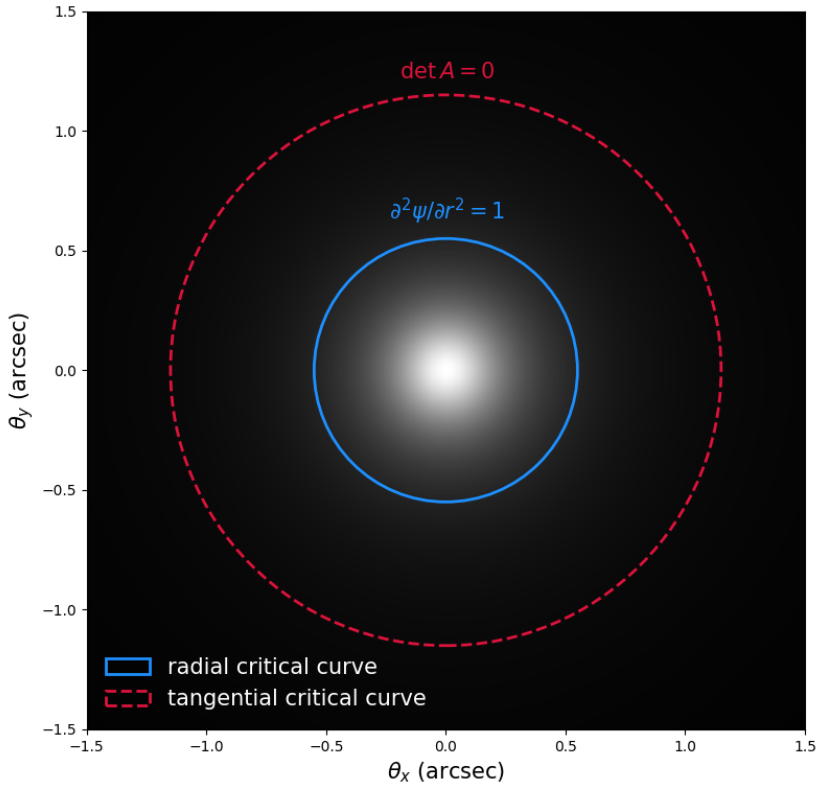

Figure 2.5: Grayscale background shows the absolute magnification $|\mu|$ produced by an axis–symmetric lens; brighter tones correspond to higher magnification. The solid blue circle indicates the radial critical curve, where the radial stretch factor vanishes, whereas the dashed red circle marks the tangential critical curve, where the tangential stretch factor vanishes. Because the radial curve depends on the local surface mass density $\Sigma(r)$ while the tangential curve depends on the mean density inside its radius, the relative spacing of the two curves directly encodes the inner slope of the mass profile: steepening the profile pulls the radial curve inward, whereas flattening it pushes the curve outward.

Because $\partial M/\partial r$ is proportional to the local surface mass density, $\Sigma(r)$, locating this curve constrains the inner slope of the mass profile directly. Figure 2.5 illustrates the tangential and critical curves for an axis symmetric lens.

Together, these relations show how the geometric loci of the two critical curves provide both the total mass enclosed and the detailed shape of the density profile in circular lenses.

In reality, astrophysical lenses almost never exhibit perfect circular symmetry. For arbitrarily shaped or multi component mass distributions, critical curves cannot be

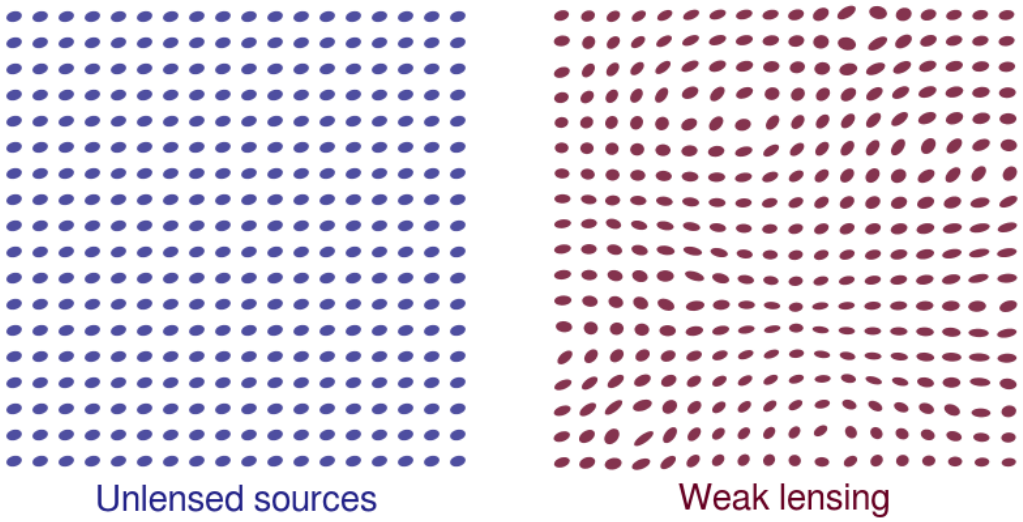

Figure 2.6: Weak lensing illustration. Left panel: Uniformly distributed and identical elliptical objects serving as reference background sources. Right panel: The same objects as observed after weak gravitational lensing effects. This diagram demonstrates how background galaxy shapes become distorted when light passes through the gravitational field of massive foreground structures. The distortion magnitude has been enhanced for clarity compared to actual astronomical observations. Credit : Linc (2016).

located with simple analytic expressions and must instead be found numerically. The exact form of those curves depends on the assumed mass profile and the details of the lens model. The specific techniques for non circular lenses are discussed in Chapter 3.

2.3 Weak Gravitational Lensing

Weak gravitational lensing describes the ubiquitous, subtle bending of light by large scale structure, unlike the rare, high density cores of clusters that produce multiple, highly distorted images, most lines of sight only suffer small deflections. In this regime, individual background galaxies are not split into separate images but instead acquire a tiny, coherent "shear" in their apparent shape; round galaxies become slightly elliptical, elongated preferentially tangentially around mass concentrations as shown in Figure 2.6. Weak lensing operates in the limit where both the convergence and shear are very small, $|\kappa|, |\gamma| \ll 1$. In this regime the lens

mapping remains essentially one-to-one with $\alpha \ll 1$, and simple Taylor expansion of the Jacobian shows

$$detA = (1-\kappa)^2 - |\gamma|^2 \simeq 1 - 2\kappa, \tag{2.29}$$

such hence the flux magnification reduces to

$$\mu \simeq \frac{1}{detA} \simeq 1 + 2\kappa. \tag{2.30}$$

Rather than κ directly, in weak lensing, the reduced shear $\boldsymbol{g}$ is used,

$$\boldsymbol{g}(\boldsymbol{\theta}) = \frac{\gamma(\boldsymbol{\theta})}{1-\kappa(\boldsymbol{\theta})} \tag{2.31}$$

which shows up as a tiny, coherent ellipticity in galaxy images, circles become slight ellipses whose major axes tend to align tangentially around overdensities. The reduced shear g, is the observable quantity in the weak lensing regime, and not the shear, γ. Because each galaxy's intrinsic shape is unknown, one averages the measured shapes (ellipticities) of hundreds to thousands of sources in annuli or grid cells, and obtains an estimate of g at each of these positions. These statistical shear measurements map out the projected mass distribution (both dark and luminous matter) across the sky, allowing us to reconstruct halo density profiles. The quantitative connection between these coherent shape distortions and the underlying mass distribution will be established through the relationship between shear and projected surface density as shown later in this section.

The shear components are related to the second derivatives of the lensing potential ψ:

$$\gamma_1 = \frac{1}{2}\left(\frac{\partial^2\psi}{\partial\boldsymbol{\theta}_1^2} - \frac{\partial^2\psi}{\partial\boldsymbol{\theta}_2^2}\right), \quad \gamma_2 = \frac{\partial^2\psi}{\partial\boldsymbol{\theta}_1\partial\boldsymbol{\theta}_2} \tag{2.32}$$

where the lensing potential is directly related to the projected mass distribution through Poisson's equation in the lens plane.

For weak lensing analyses (in cluster or galaxy scale), the shear field is decomposed into two components defined with respect to the line joining each source galaxy

to the lens center. For a source galaxy with polar angle, ϕ, the observed shear components (γ_1, γ_2) can be rotated into tangential and cross bases through,

$$\begin{aligned} \gamma_t &= -[\gamma_1 \cos 2\phi + \gamma_2 \sin 2\phi] \\ \gamma_\times &= -[-\gamma_1 \sin 2\phi + \gamma_2 \cos 2\phi]. \end{aligned} \tag{2.33}$$

The tangential shear, γ_t, stretches images tangentially around the lens whereas the cross shear, $\gamma_\times$, stretches the images at 45° to the tangential direction. Hence, a circular source lensed purely by tangential shear will appear as a slight ellipse whose major axis is aligned along the circle centered on the lens. A non zero cross shear would twist that ellipse by 45°, which does not arise from a smooth, centro-symmetric mass distribution, making $\gamma_\times$ a useful null test for residual systematics.

In the weak lensing regime where $|\kappa| \ll 1$, the reduced shear approximates the shear itself, $g \simeq \gamma$. Therefore, the tangential shear γ_t directly corresponds to the mean tangential ellipticity observed in background galaxies, and $\gamma_\times$ should vanish in the absence of systematics or non-lensing signals.

Each galaxy has an intrinsic, unknown, ellipticity, ε_S, which weak lensing adds, to produce an observed ellipticity, ε. The observed ellipticity is given as

$$\epsilon = \frac{\epsilon_S + g}{1 + g^* \epsilon_S} \tag{2.34}$$

where g^* is the complex conjugation of g. In the weak limit, $\langle \varepsilon \rangle \approx g$, where the average is taken over many galaxy in a patch of sky. For a galaxy whose light distribution can be approximated by an ellipse with semi-major axis, a , semi-minor axis, b $(a \geq b)$, and position angle, ϕ, the observed ellipticity can be expressed as,

$$\varepsilon = \varepsilon_1 + i\varepsilon_2 = \left(\frac{a^2 - b^2}{a^2 + b^2} \right) e^{2i\phi}. \tag{2.35}$$

The two ellipticity components are given as,

$$\varepsilon_1 = \left(\frac{a^2 - b^2}{a^2 + b^2} \right) \cos 2\phi, \quad \varepsilon_2 = \left(\frac{a^2 - b^2}{a^2 + b^2} \right) \sin 2\phi, \tag{2.36}$$

where ε_1 measures elongation along the x or y axes, and ε_2 measures elongation along the diagonal direction.

Shear components can thus be expressed in terms of ellipticity components as

$$\gamma_t = -(\varepsilon_1 \cos 2\phi + \varepsilon_2 \sin 2\phi), \quad \gamma_\times = -(-\varepsilon_1 \sin 2\phi + \varepsilon_2 \cos 2\phi). \tag{2.37}$$

In practice, a weak–lensing analysis begins with individual source galaxies for which we know (i) the projected separation, R, from a chosen lens galaxy or cluster center and (ii) the observed ellipticity, $\boldsymbol{\varepsilon} = (\varepsilon_1, \varepsilon_2)$. To see how much the cluster's gravity has tangentially stretched each galaxy, we rotate its measured ellipticity so that "around the circle" becomes our reference direction. That rotated value is the galaxy's tangential shear γ_t, which tells us how strongly the image has been pulled in the direction that wraps around the cluster rather than radially in or out. It is given as,

$$\gamma_{t,i}(R_i) \simeq -\big[\varepsilon_{1,i} \cos 2\phi_i + \varepsilon_{2,i} \sin 2\phi_i\big], \tag{2.38}$$

where ϕ_i is the polar angle of the i^{th} source about the lens. Because intrinsic galaxy shapes dominate the noise budget, we stack many of such measurements in narrow radial annuli, forming the mean

$$\langle \gamma_t(R) \rangle = \frac{1}{N} \sum_{i \in \text{bin}} \gamma_{t,i}. \tag{2.39}$$

Stacking suppresses random shape noise and isolates the coherent shear generated by the lens mass. In practice, however, the situation is more complex: the observed ellipticity is not only the sum of the intrinsic shape and the shear distortion but is also convolved with the instrument's point spread function (PSF). Thus what is actually measured is

$$\epsilon_{\text{obs}} = (\epsilon_S + \gamma) \times \text{PSF}, \tag{2.40}$$

and accurate shear estimation requires careful modelling and correction of the PSF convolution.

In the weak-lensing limit this averaged tangential shear is directly proportional to the lens' surface-mass density excess, i.e., the difference between the mean surface density inside radius R and the local value at R:

$$\Delta\Sigma(R) \equiv \overline{\Sigma}(< R) - \Sigma(R) \tag{2.41}$$

where $\Sigma(R)$ is the projected surface density at radius R, and $\overline{\Sigma}(< R)$ its mean interior value as :

$$\Delta\Sigma(R) = \Sigma_{crit} \langle \gamma_t(R) \rangle \tag{2.42}$$

with geometry-only factor, $\Sigma_{\rm crit}$, which depends solely on the angular-diameter distances to the lens D_L, to the source D_S, and between the lens and the source D_{LS} (Eq. 2.17). Hence, once the redshifts are known, the conversion from γ_t to $\Delta\Sigma$ is geometric and model independent. This single equation closes the loop between theory and observation: it links convergence and shear, defined earlier through second derivatives of the lensing potential, to a quantity, $\Delta\Sigma(R)$, that is an immediate, observable probe of the lens' projected mass profile.

2.4 Cluster Lenses

Galaxy clusters are the most massive gravitationally bound systems in the Universe and act as powerful gravitational lenses. Their large masses, predominantly in the form of dark matter, create significant spacetime curvature, bending light from background galaxies and producing a range of observable lensing phenomena, including arcs, multiple images, and shape distortions. These effects enable clusters to serve as both direct probes of their internal mass distributions and as magnifiers of the distant Universe, earning them the titles of "Cosmic Telescopes" or "Natural Telescopes" (Kneib and Natarajan, 2011).

The lensing potential of clusters was recognized relatively early in the development of gravitational lensing theory. Although Einstein himself predicted lensing effects in 1936, the first observational evidence of gravitational lensing by a galaxy cluster came in 1987, when Lynds and Petrosian (1987) and Soucail (1987) independently identified a giant luminous arc in the cluster Abell 370. This arc was interpreted as a strongly lensed background galaxy, marking the beginning of cluster lensing as an observational field. One of the earliest comprehensive explorations of cluster lensing was conducted by Narayan et al. (1984), who explained the multiple imaging

of a quasar as a combination of lensing by individual galaxies and magnification by the cluster's gravitational field. Subsequent work expanded on this framework, establishing cluster as a robust method for mapping mass distributions.

Since then, both observational techniques and theoretical modelling have advanced considerably. Strong lensing is now routinely used to constrain the mass distribution in the dense cluster cores, while weak lensing extends this to the outskirts through the coherent distortion patterns in the shapes of distant galaxies. Together, these regimes allow clusters to be modelled from core to periphery.

In recent years, a series of major observational programs have dramatically advanced cluster lensing science. These efforts have unfolded across successive generations of imaging surveys, each building upon the accomplishments of its predecessors. The Cluster Lensing And Supernova survey with *Hubble* (CLASH, see section 4.3.2 Postman et al., 2012) marked an early milestone in systematic cluster lensing studies, demonstrating the power of multi wavelength observations across 25 massive clusters, enabling detailed strong and weak lensing mass reconstructions (Zitrin et al., 2015; Merten et al., 2015; Umetsu et al., 2016). The CLASH program established the foundation for using photometric redshifts in lensing studies and showed how comprehensive imaging could reveal the complex mass distributions within clusters.

The transformative moment came with the *Hubble* Frontier Fields program (HFF, see section 4.3.3 Lotz et al., 2017), which revolutionised cluster lensing by achieving unprecedented depths of ∼29 AB magnitude across six carefully selected massive clusters. HFF's deep, multi band observations enabled the detection of hundreds of multiply imaged systems, providing the crucial constraints needed for precise strong lensing mass modelling (see section 3.2, and Diego et al., 2016; Jauzac et al., 2015a; Mahler et al., 2018). HFF also revealed thousands of faint high redshift galaxies that had been previously undetectable, opening new windows into cosmic reionisation and early galaxy evolution.

Building upon HFF's success, the Beyond Ultra-deep Frontier Field And Legacy Observation survey (BUFFALO, see section 4.3.4 Steinhardt et al., 2020) extended cluster lensing capabilities by expanding the observational footprint around the same six clusters. This expansion was crucial for cluster lensing analysis because it enabled the combination of strong lensing constraints from cluster cores with weak lensing measurements from the outer regions (Gonzalez et al., 2020; Lagattuta et al., 2023; Niemiec et al., 2023). This dual approach dramatically improved both the precision and accuracy of cluster mass models, providing a more complete picture of dark matter distribution from cluster centers to their outskirts.

A parallel revolution has occurred through the integration of ground based spectroscopic observations, particularly from the Multi Unit Spectroscopic Explorer (MUSE) on the Very Large Telescope (VLT, see section 4.2.4). MUSE's integral field spectroscopy capabilities have transformed cluster lensing analysis by providing spectroscopic redshifts for extremely faint multiply imaged systems that would be impossible to confirm through photometry alone. This spectroscopic validation has dramatically increased the number of reliable multiple image systems available for strong lensing mass modelling, leading to more robust and precise cluster mass reconstructions (Mahler et al., 2018; Jauzac et al., 2019; Lagattuta et al., 2023).

The advent of *JWST* marked another revolutionary leap in cluster lensing capabilities, which unprecedented infrared sensitivity and angular resolution have dramatically improved our vision of cluster lensing. The Strong Lensing and Cluster Evolution (SLICE, see section 4.3.7 Cerny et al., 2025b) survey represents the maturation of cluster lensing into a comprehensive cosmological probe. By systematically surveying 124 clusters selected to trace the same evolutionary track across cosmic time, SLICE enables studies of how cluster properties evolve rather than merely cataloguing them at different epochs. The survey's focus on precisely mapping both dark and luminous matter distributions across this evolutionary sequence provides unprecedented insights into cluster formation processes and the relationship between dark matter halos and their embedded galaxy populations. *JWST*

routinely identifies new multiply imaged systems that were undetectable in *HST* imaging, including faint galaxies at $z > 10$ and dust obscured systems magnified by cluster lenses (e.g. Atek et al., 2023; Meena et al., 2023; Bradač et al., 2024; Rivera-Thorsen et al., 2024). These observations provide detailed morphological and spectral measurements of early galaxies, revealing star forming clumps on tens of parsecs scales and enabling the study of galaxy formation in the first few hundred million years after the Big Bang. *JWST* has also revealed numerous lensed transients and candidate pair instability supernovae behind massive clusters, highlighting the potential of gravitational lensing for time domain astrophysics. Moreover, the increased number of multiple images detected by *JWST* provides powerful new constraints for cluster mass modelling, allowing mass reconstructions with spatial resolution far superior to previous *HST* based models.

Looking at the near future, the ESA *Euclid* mission promises to redefine the landscape of cluster lensing by delivering homogeneous imaging and slitless spectroscopy across roughly one-third of the sky. Early releases have already revealed dozens of new strong lensing clusters, demonstrating the mission's unprecedented efficiency for lens discovery. *Euclid*'s wide field weak lensing measurements will enable statistical galaxy-cluster mass calibration at the percent level, while the discovery of several thousand cluster-scale strong lenses will provide a foundation for precision cosmology, dark-matter tests, and studies of structure growth across cosmic time. The synergy between *Euclid*'s statistical power and *JWST*'s depth is expected to produce the first comprehensive, multi wavelength cluster-lensing framework capable of connecting small scale dark matter physics, cluster astrophysics, and early Universe galaxy evolution within a single coherent observational programme.

Cluster lenses are not only used to study lensing phenomena or lensed galaxies, they are powerful cosmological tools. The positions of multiple images depend on the angular diameter distance ratios between the source, lens, and observer. This geometric dependence allows lensing to probe cosmological parameters (Paczynski and Gorski, 1981; Golse et al., 2002; Meneghetti et al., 2005; Jullo et al., 2010;

Acebron et al., 2017; Grillo et al., 2018; Acebron et al., 2023; Bergamini et al., 2024; Grillo et al., 2024). Observations of multiple arcs at different redshifts have been suggested as sensitive diagnostics of dark energy (Golse et al., 2002; Sereno, 2002; Acebrón et al., 2022; Acebron et al., 2023; Bergamini et al., 2024). Additionally, since clusters form from high density peaks in the primordial density field, their abundance and redshift evolution constrain the matter content of the Universe. Their baryon content also reflects the universal baryon budget, offering insight into big bang nucleosynthesis and the chemical evolution of the cosmos (Bahcall and Fan, 1998; LaRoque et al., 2003; Jullo et al., 2010; Planelles et al., 2013; Allen et al., 2011; Mantz et al., 2014).

Alongside these observational advances, the field of cluster lensing is increasingly being transformed by the adoption of machine learning and artificial intelligence techniques. The unprecedented data volumes expected from surveys such as *Euclid* and *JWST* have motivated the development of automated approaches for strong lens detection, classification, and modelling, which would be infeasible to perform manually at scale. Convolutional neural networks and deep learning architectures have been successfully applied to identify strong lensing features in imaging data, enabling rapid and highly efficient discovery of new cluster lenses in wide-field surveys (Jacobs et al., 2019; Petrillo et al., 2019; Metcalf et al., 2019). Early *Euclid* focused studies demonstrate that such methods can recover cluster-scale lenses with high completeness and purity, even in the presence of complex morphologies and noise (Lanusse et al., 2018; He et al., 2023).

From their first discovery in Abell 370 to their present role in cutting edge space surveys, cluster lenses have become indispensable astrophysical laboratories and cosmological tools, allowing us to peer both into the structure of dark matter halos and deep into the high redshift Universe.

We have now developed the mathematical machinery of gravitational lensing: from the lens equation and lensing potential, through the Jacobian formalism that yields

convergence and shear, to the distinction between the highly non-linear, image multiplying regime of strong lensing and the subtle, statistical distortions of weak lensing. These tools provide the raw observables : multiple image positions and distorted galaxy shapes, but do not by themselves specify how to reconstruct a physically plausible mass distribution. In the next chapter, we will review the principles of strong and weak lensing mass modelling techniques in galaxy clusters.

Chapter 3

Cluster Mass Modelling

"Models are approximations of reality, but they are indispensable to our understanding." - Richard Hamming

As the most massive gravitationally bound structures in the Universe, mapping the mass distribution in galaxy clusters is essential for both cosmology and galaxy evolution. As seen in the previous chapter, cluster lenses are widely used to determine their mass distribution through strong and weak lensing. The multiple images of background sources are used to constrain the strong lensing regions while the distortions in the shapes of the weakly lensed background galaxies are used to constrain the weak lensing regions. Nonetheless, the underlying mass distribution still needs to be reconstructed from these lensing observables. The first employs parametric mass models, in which the cluster's overall mass distribution is represented as a combination of a finite number of analytic components. These components fall into two categories: (i) the large-scale halos, which account for the cluster's dark matter structure and the intracluster medium, and (ii) the galaxy-scale halos, which capture the mass associated to individual (cluster) galaxies. Examples of widely adopted parametric modelling codes are Lenstool (Jullo et al., 2007), Glafic (Oguri, 2010), and the Light-Traces-Mass (LTM) framework Zitrin et al., 2012, 2013. The second class comprises free-form (non-parametric) methods, which discretise the

cluster's projected mass distribution into a grid of "pixels", allowing each pixel's mass to vary freely. These methods optimise the pixel amplitudes to best reproduce the observed lensing image constraints. Notable free-form algorithms include SWUnited (Bradač et al., 2005, 2009), WSLAP+ (Diego et al., 2007; Sendra et al., 2014; Diego et al., 2016), Grale (Liesenborgs et al., 2006, 2009), LensPerfect (Coe et al., 2008, 2010), as well as weak lensing extensions of Lenstool (Jauzac et al., 2012, 2015a; Jullo et al., 2014; Niemiec et al., 2020) and SaWLens (Merten et al., 2009, 2011).

This chapter describes the mass modelling techniques used in this thesis, starting with the observational constraints. It then gives a detailed view of parametric and non-parametric modelling in galaxy clusters, followed by the optimising engine. This work makes use of the LENSTOOL algorithm.

3.1 Observational Constraints

3.1.1 Strong lensing constraints

As seen in section 2.2, critical curves are not directly observable, they are mathematical loci where the Jacobian determinant of the lens mapping goes to zero. However, their presence can be inferred through the formation and configuration of multiple lensed images (or arcs). High-resolution space-based observations from *JWST* and *HST* make these lensing features observable because their exceptional angular resolution can spatially resolve structures on sub-arcsecond scales. This capability is crucial for separating the highly magnified, background source images from the smooth light profile of the foreground lens, which would otherwise be blended together in lower-resolution ground-based observations. Tangentially stretched arcs typically lie near the tangential critical cuve, while radially distorted images appear closer to the centre near the radial critical curve. These characteristic configurations are often referred to as "tangential pairs" or "radial pairs", and

are among the most easily recognisable lensing features (Miralda-Escudé and Fort, 1993).

The number of multiple images produced by a lens corresponds to the number of solutions to the lens equation (Eq.2.9), and depends on the complexity of the underlying mass distribution. One may observe triplets, quadruplets, quintuplets, or even higher-order image multiplicities in particularly complex systems. Catastrophe theory provides a mathematical framework to describe this behaviour: each time a source crosses a caustic in the source plane, two additional images are formed (Thom, 1989; Zeeman, 1977; Erdl and Schneider, 1993). For a non-singular, smoothly varying mass distribution, the total number of images is always expected to be odd (Burke, 1981).

In practice, however, not all of these images are detectable. Some in particular, may be highly demagnified and fall below detection thresholds. These are usually central images in the very inner core of the clusters. In the case of galaxy clusters, the presence of a bright central galaxy often obscures these faint inner images, complicating the task of identifying the full image set and accurately modelling the lens. Nonetheless, the observed image multiplicities and morphologies offer powerful constraints to the projected mass distribution and the lensing potential.

The position, shape and geometry of multiple images of background galaxies will depend on the mass distribution in the galaxy cluster lens, the distance of the source galaxies, together with the alignment between the observer, the cluster and the lensed sources. Consequently, to constrain the mass distribution of a cluster, we employ the observed positions of identified multiple image systems as constraints for our strong lensing mass model within the cluster core, typically covering the central $\sim 100 - 200\,\mathrm{kpc}$ region where the gravitational field is sufficiently strong to produce multiple imaging.

Sources exhibiting similar colour and morphology are first identified by visual inspection and designated as candidate multiple images, or arcs. Whenever possible,

these candidates are then confirmed by matching spectroscopic redshifts; multiple images corresponding to the same background source should have same redshift. In cases where the features are too faint for reliable visual detection, spectroscopic observations, such as those obtained with MUSE, are used to reveal and validate the multiple image systems.

3.1.2 Weak lensing constraints

In the weak lensing regime, the shapes of lensed background sources carry the lensing signal, and, as a result, are used to constrain the mass distribution. Such signal is weak and thus difficult to measure for a single background source. Therefore, a statistical analysis is necessary. The construction of the weak lensing background galaxy catalogue is presented in this section.

3.1.2.1 Shape Measurements

Shape measurements of galaxies, in the context of weak lensing, is a multistage process requiring high-precision image analysis, calibration, and classification. The pyRRG pipeline, based on Rhodes et al. (2000) and presented in Harvey et al. (2019) is used to measure the shapes of background galaxies. It consists of six critical steps: source detection, moment measurements, star-galaxy classification, point spread function (PSF) modelling and correction, shear estimation, and catalogue cleaning and masking.

1) Source Detection The process begins with source detection, which is essential to identify all potential galaxies within the astronomical image. The first step consists in using the 'hot-cold' method as in Leauthaud et al. (2007) to optimally extract sources from the image using the Source-Extractor software (SExtractor, Bertin and Arnouts, 1996). Here, two SExtractor scans of the image are performed: (i) the 'hot' run, objects are detected using a low pixel

threshold, making it sensitive to smaller and fainter sources, including noise; (ii) the 'cold' pass uses a higher pixel threshold and is more effective in identifying extended, brighter objects such as cluster galaxies. The outputs from these two detection passes are merged to form a consolidated and comprehensive object catalogue.

2) Moment Measurement Once the sources have been detected, the second step involves the measurement of the moments, which quantify the shape and size of each galaxy. This process is crucial for understanding how galaxies appear distorted by gravitational lensing effects. The measurement of galaxy shapes is achieved through the calculation of weighted image moments. Image moments are mathematical quantities that describe the spatial distribution of light in a galaxy image. These quantities provide a systematic way to characterize how the galaxy's brightness is distributed across the sky, capturing fundamental morphological properties such as the galaxy's size, ellipticity, and orientation on the celestial sphere.

The moment-based approach is particularly well suited for weak lensing studies because gravitational lensing primarily affects the second-order (quadrupole) moments of the light distribution. When light from a distant galaxy passes through the gravitational field of intervening matter, it undergoes a coherent shear transformation that preserves the galaxy's total brightness while modifying its apparent shape. This transformation can be precisely quantified through changes in the quadrupole moments, making them sensitive probes of the matter distribution along the line of sight.

The intensity distribution, $i(\theta)$, represents the observed brightness of the galaxy as a function of angular position, θ, on the sky. Here, θ denotes the two-dimensional angular coordinate vector, (θ_1, θ_2), which specifies the position of each pixel in the galaxy image relative to some reference point. The intensity distribution effectively maps how the galaxy's light is distributed across different angular positions, creating a brightness profile that contains the galaxy's morphological information.

Using a Gaussian weighting function to suppress noise in the outer regions of the galaxy image, pyRRG computes the second-order moments of the intensity distribution. The weighting function, $w(\theta)$, emphasises the high signal-to-noise regions of the galaxy while suppressing contributions from the noisy outer regions where the galaxy signal becomes comparable to the background noise.

These are defined as:

$$I = \int d^2\theta \, w(\theta) \, i(\theta) \tag{3.1}$$

The quadrupole moment tensor is then given by:

$$J_{ij} = \frac{1}{I} \int d^2\theta \, \theta_i \theta_j \, w(\theta) \, i(\theta) \tag{3.2}$$

where $i(\theta)$ is the observed intensity at angular position θ, and $w(\theta)$ is a Gaussian weight function. In this expression, the indices i and j each run over the two spatial coordinates (1 and 2), so that θ_i and θ_j represent the individual components of the angular position vector.

The ellipticity, ϵ, is defined as :

$$\epsilon = \sqrt{\epsilon_1^2 + \epsilon_2^2} \tag{3.3}$$

with,

$$\epsilon_1 = \frac{J_{11} - J_{22}}{J_{11} + J_{22}}, \qquad \epsilon_2 = \frac{2J_{12}}{J_{11} + J_{22}} \tag{3.4}$$

Here, ϵ_1 quantifies the elongation along the principal axis, while ϵ_2 quantifies the elongation at 45° relative to the coordinate axis.

The effective size of the object is defined as:

$$d = \sqrt{\frac{1}{2}(J_{11} + J_{22})} \tag{3.5}$$

These measurements form the basis to compute gravitational shear, which quantifies the distortion of galaxy shapes due to mass distribution along the line of sight, such as galaxy clusters.

The ellipticity can be related to the semi-major axis, a, and semi-minor, axis, b, of an ellipse by,

$$\epsilon = \frac{a^2 - b^2}{a^2 + b^2}. \tag{3.6}$$

3) Star-Galaxy Classification The third step is star-galaxy classification, a necessary to distinguish galaxies from stars, noise, or saturated artifacts. pyRRG employs a supervised machine learning approach using a Random Forest classifier. Based on the distribution of sources in the magnitude (MAG_AUTO) vs peak surface brightness (MU_MAX) plane, sources are classified as stars, galaxies and fake detections (Leauthaud et al., 2007; Jauzac et al., 2012, 2015a). Fake detections are then removed from our catalogue, and the sequence of stars is kept for the modelling of the point spread function (PSF), mandatory step in the measurement of shapes.

4) Point Spread Function Modelling and Correction This step addresses the instrumental and observational distortions inherent to *HST* imaging. The PSF describes the response of the telescope to a point source of light such as a distant star, and effectively represents the blurring introduced by the optics and the detector. Rather than appearing as infinitesimally small points, stars and galaxies are observed as smeared-out profiles due to diffraction, aberrations, pixel sampling, and time dependent effects like thermal breathing. PSF estimation is crucial in weak lensing studies because these shape distortions, if not properly accounted for, can mimic or dilute the subtle gravitational lensing signal being measured. Accurate PSF modeling allows for the deconvolution of these instrumental effects from the observed galaxy images, restoring a reliable estimate of galaxies' intrinsic shapes

and orientations.

Hubble Space Telescope (HST)

For *HST* observations, pyRRG models the PSF of individual exposures and corrects all galaxy shapes accordingly. It measures the PSF from stars in each exposure, comparing their second- and fourth-order moments to various Tiny Tim models (Krist et al., 2011). Tiny Tim is a standard *HST* PSF modeling software that uses detailed telescope and instrument specifications to accurately reproduce the PSF of different cameras under various observational conditions. pyRRG combines the best-fit PSFs from all individual exposures to obtain a final model matching the combined image. Each exposure's PSF is rotated into the reference frame of the final combined image, ensuring all models share a common north–east orientation. The rotated PSFs are evaluated at each galaxy's detector position, and their flux-normalised moment tensors are summed, optionally weighted by exposure time, to produce a composite PSF whose size, ellipticity, and orientation replicate the instrumental blur in the drizzled (final combined) image.

James Webb Space Telescope (JWST)

JWST PSF modeling can be approached through two complementary methods: empirical measurement from field stars and theoretical modeling using `WebbPSF`. The empirical approach measures PSF moments directly from bright stars distributed throughout the field, then uses mathematical interpolation to estimate the PSF properties at galaxy positions. However, at high galactic latitudes, JWST images may contain insufficient bright stars for reliable empirical PSF modeling, necessitating the use of theoretical models (Harvey and Massey, 2024). `WebbPSF` provides a robust alternative by generating artificial PSF models at any position within the mosaic. The software creates dense grids of synthetic stars throughout each band, accounting for the spatial variations of the PSF across the field of view. For stacked images composed of multiple exposures, the PSF moments are calculated for each exposure at every galaxy position, properly rotated to account for

different orientation angles, and then combined across all exposures to produce a final PSF model that accurately represents the instrumental blur in the drizzled image.

5) Shear Measurement Estimation The corrected galaxy ellipticities, obtained after PSF deconvolution, are translated into a measurement of gravitational shear. In the weak lensing regime, the gravitational shear, γ, quantifies the subtle, coherent distortions in galaxy shapes induced by foreground mass concentrations, such as galaxy clusters, massive elliptical galaxies, and galaxy groups. These distortions are small, and it requires ensemble averaging over hundreds to thousands of background galaxies to extract a signal.

In PYRRG, the shear is derived from observed ellipticities using the relation

$$\gamma_i = \frac{\langle \epsilon_i \rangle}{G}, \tag{3.7}$$

where γ_i denotes the i-th component of the shear ($i = 1, 2$), $\langle \epsilon_i \rangle$ is the average corrected ellipticity component across the sample, and G is a calibration factor called the shear responsivity. G accounts for the non-linear response of the ellipticity to the shear, and corrects for higher-order distortions and measurement noise.

The factor G is computed as

$$G = 2 - \langle \epsilon^2 \rangle - \frac{1}{2}\langle \lambda \rangle - \frac{1}{2}\langle \boldsymbol{\epsilon} \cdot \boldsymbol{\mu} \rangle, \tag{3.8}$$

where $\epsilon^2 = (\epsilon_1^2 + \epsilon_2^2)$ is the squared magnitude of the ellipticity, and $\boldsymbol{\epsilon} \cdot \boldsymbol{\mu} = (\epsilon_1 \mu_1 + \epsilon_2 \mu_2)$ is the inner product of the ellipticity with a correction spinor, $\boldsymbol{\mu}$, derived from the fourth order moments. These correction terms are defined as follows. The two components of the correction spinor $\boldsymbol{\mu}$ are given by

$$\mu_1 = \frac{-J_{1111} + J_{2222}}{2d^2 w^2}, \qquad \mu_2 = \frac{-2(J_{1112} + J_{1222})}{2d^2 w^2}. \tag{3.9}$$

The term λ is computed from the weighted fourth-order image moments as

$$\lambda = \frac{J_{1111} + 2J_{1122} + J_{2222}}{2d^2w^2}. \tag{3.10}$$

Here, J_{ijkl} denote the fourth order weighted moments of the galaxy image, d is the galaxy's size derived from the quadrupole moments, and w is the scale of the Gaussian weighting function used during moment calculation. These corrections ensure that the final shear estimate is unbiased and accurately reflects the true lensing induced distortion.

6) Catalogue cleaning & **masking** This final step is a quality control process to refine the sample of galaxy. Objects located near saturated stars or diffraction spikes are automatically masked using polygonal regions. Duplicate detections are removed by excluding sources found within the isophotal boundary of a larger object. Crucially, foreground contamination is minimised by cross-matching with photometric redshift catalogues from the CLASH (Cluster Lensing And Supernova, Prog.ID: 12790, PI: M. Postman; Postman et al., 2012) survey and excluding galaxies with redshifts below 1.1 times that of the studied cluster. Additionally, galaxies too close to the strong lensing region are excluded to prevent bias from arcs or flexion features. An arc is a background galaxy that the cluster's gravity has stretched into a long, curved streak. Flexion is a twisting effect that bends a galaxy image into a subtle, banana-like shape. Both distortions are far stronger than the gentle stretching (weak shear) we wish to measure. If they were kept and analysed as ordinary weak-shear galaxies, their extreme shapes would give too much weight to those regions and make the mass map appear artificially heavy or clumpy. By excluding them, we ensure that every galaxy in the catalogue sits safely in the weak-lensing regime. The resulting catalogue is then formatted for use with LENSTOOL, the mass modelling code we used that integrates shear data as constraints to reconstruct the underlying mass distribution of the cluster.

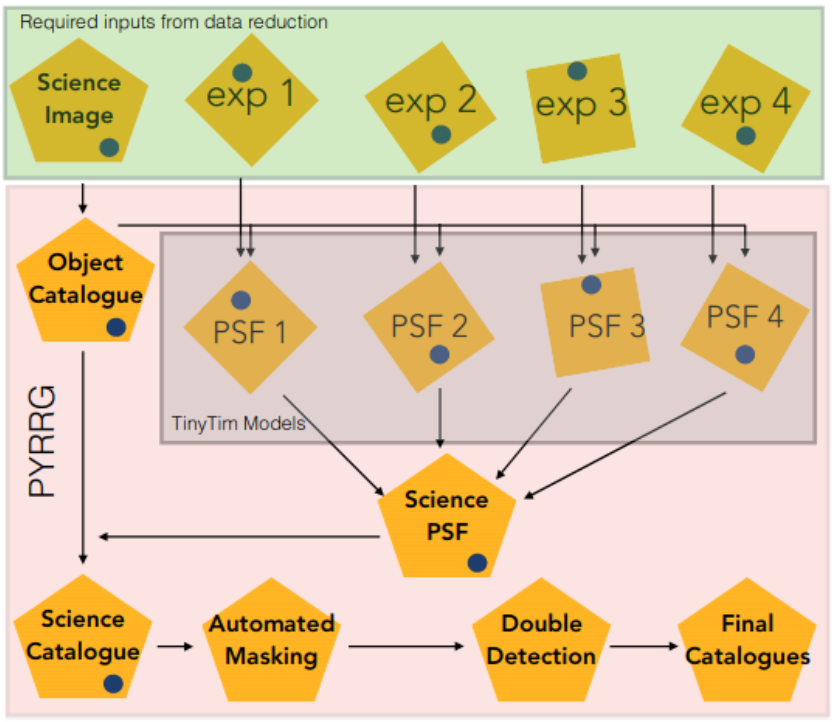

Figure 3.1: An overview of the PYRRG algorithm. It requires theinput science image and associated weight file from the data reduction pipeline, plus all the associated exposures. From this it chooses the 'best' PSF from the TinyTim models and combines them to produce a PSF at the position of each galaxy in the catalogue. It then corrects the galaxies, calculate the shears and outputs a science catalogue. It then carries out post-processing procedures to create a final 'clean' catalogue (Harvey et al., 2019).

3.1.2.2 Background Galaxy Selection

We now have a weak lensing catalogue with all shapes of galaxies measured thanks to PYRRG. However, this catalogue is still contaminated by foreground cluster galaxies. The weak lensing signal is carried by background galaxies, but is diluted by the presence of these contaminants. The confirmed cluster member galaxies from the red sequence (see section 5.2.2) selection are removed to get a cleaner catalogue. Despite removing these cluster member galaxies, the catalogue remains contaminated by faint, small and bluer cluster galaxies (mimicking the colour of background objects), and foreground objects for which redshifts measurements are not available. We thus use a colour-colour selection for galaxies without photometric and/or spectroscopic redshifts (Jauzac et al., 2012, 2015a, 2016; Niemiec et al.,

2023). Galaxies with photometric or spectroscopic redshifts are used to calibrate the regions dominated by the unlensed population (cluster and foreground galaxies). Weakly lensed galaxies are then separated from the unlensed population by a defined polynomial region in the colour-colour space.

The resultant catalogue is further cleaned by removing galaxies whose shape parameters are ill-determined, creating noise in shear measurements larger than the shear signal itself. The following cuts are applied :

- Signal-to-noise ratio cut:

$$\frac{S}{N} = \frac{FLUX\_AUTO}{FLUX\,ERROR\_AUTO} > 4.5$$

- Total ellipticity cut :

$$e = \sqrt{e_1^2 + e_2^2} < 1$$

- Size (defined by PYRRG parameter, d) cut:

$$3.6 < d < 30\,\text{pixels}$$

  This eliminates sources smaller than the PSF and large galaxies (a size similar to cluster members).

- Exposure cut : Sources close to the edges of the images are removed based on the number of exposures for each detection.

- Magnitude cut : Very bright sources are removed to eliminate saturated objects and bright cluster members.

3.2 Parametric Modelling

In the central regions of galaxy clusters, where the strong lensing dominates, the configuration of multiple images systems, along with the spatial distribution of cluster galaxies provide information for priors of the underlying matter distribution.

To fully exploit this information, it is more appropriate to adopt "parametric mass modelling", assuming mass traces light. In parametric mass models, the total mass distribution is divided into different mass components, each represented by a halo which is described by an analytical density profile. The most commonly used profiles includes the Singular Isothermal Sphere potentials (SIS, Binney and Tremaine, 1987), the Navarro-Frenk-White potentials (NFW, Navarro, 1996), and the Pseudo Isothermal Elliptical Mass Distribution potentials (PIEMD, Elíasdóttir, 2007). The parameters of these halos are then optimised to build a model that best reproduces the observed lensing constraints.

Galaxy clusters are decomposed into two main types of mass components: (i) *cluster-scale halos*, which include both dark matter and baryonic intracluster gas, and (ii) *galaxy-scale halos*, which are associated with individual member galaxies and include both stellar and dark matter content. Both observational studies and numerical N-body simulations show that subhalos within a cluster follow a mass distribution well approximated by a Schechter function (e.g. Shaw et al., 2006). Based on this, the total gravitational potential of the cluster can be decomposed as:

$$\phi_{tot} = \sum_i \phi_{c_i} + \sum_j \phi_{p_j}, \tag{3.11}$$

where ϕ_{c_i} denotes the smooth, large-scale potentials of the main cluster halo(s), and ϕ_{p_j} represents the localized potentials of galaxy-scale subhalo(s). This approach, first proposed by Natarajan and Kneib (1997), assumes that each subhalo hosts a visible galaxy, i.e., dark galaxies are not included in the model. Such a decomposition has proven effective in reproducing observed multiple-image configurations and in constraining the sizes and masses of subhalos in clusters (e.g. Smith et al., 2005; Natarajan et al., 2006; Limousin et al., 2010; Jauzac et al., 2015a, 2016; Lagattuta et al., 2023; Limousin et al., 2025).

3.2.1 Modelling cluster mass components

As mentioned before, in the cluster core, where we assume light traces mass, i.e. that dark matter halos (at both cluster and galaxy-scales) follow the light distribution, we use a parametric mass model. The total mass distribution in this region is decomposed into large and small scale components to model cluster and galaxy-scale matter distributions respectively. Each component is modelled assuming a dual Pseudo Isothermal Elliptical density profile (dPIE, Elíasdóttir, 2007), also known as PIEMD profile. This profile is chosen for two key reasons: (i) unlike the NFW profile, the dPIE has a finite total mass and central density; (ii) in dPIE, the mass distribution is partitioned into two segments, the core and the outskirts, allowing greater flexibility in modelling the inner structure of the halo. These regions are characterized by a core radius, $r_{\rm core}$, and a cut radius, $r_{\rm cut}$. The 3D density profile is given by:

$$\rho_{\rm dPIE}(r) = \frac{\rho_0}{(1 + r^2/r_{\rm core}^2)(1 + r^2/r_{\rm cut}^2)}, \quad \text{where } r_{\rm cut} > r_{\rm core}. \tag{3.12}$$

Here, ρ_0 is the central density. The profile is spherical and not strictly isothermal in the core. In the region $r_{\rm core} < r < r_{\rm cut}$, the density follows $\rho \propto r^{-2}$, while in the outer region ($r \gg r_{\rm cut}$), it steepens to $\rho \propto r^{-4}$. Importantly, $r_{\rm cut}$ acts as a scale radius, not a hard truncation point (Limousin et al., 2022).

Gravitational lensing is fundamentally a projected phenomenon that depends on the total mass integrated along the line of sight rather than the specific three-dimensional distribution of matter. The deflection of light rays by gravitational fields is governed by the thin lens approximation, where all deflecting mass is effectively treated as residing in a single plane perpendicular to the observer's line of sight. Consequently, the key quantity governing lensing effects is the surface mass density, $\Sigma(\xi) = \int \rho(\xi, l)$ (as given in Eq. 2.6) which represents the integral of the three-dimensional mass density $\rho(\xi, l)$ along the light path, l. All observable lensing quantities, including shear, convergence, and deflection angles, are directly

related to derivatives of the two-dimensional gravitational potential, which itself depends on the surface mass density through the two-dimensional Poisson equation (as shown in Eq. 2.16). Thus, for lensing, the projected (2D) surface mass density is more useful than the 3D form. It is given by:

$$\Sigma_{\rm dPIE}(R) = \Sigma_0 \frac{r_{\rm cut}\, r_{\rm core}}{r_{\rm cut} - r_{\rm core}} \left(\frac{1}{\sqrt{r_{\rm core}^2 + R^2}} - \frac{1}{\sqrt{r_{\rm cut}^2 + R^2}} \right), \tag{3.13}$$

where R is the projected radial distance, and the central surface density, Σ_0, is defined as:

$$\Sigma_0 = \pi \rho_0 \frac{r_{\rm cut}\, r_{\rm core}}{r_{\rm cut} + r_{\rm core}}. \tag{3.14}$$

Alternatively, the profile can be expressed in terms of the central velocity dispersion σ_0, which is more easily constrained observationally (Limousin et al., 2005):

$$\Sigma_{\rm dPIE}(R) = \frac{\sigma_0^2\, r_{\rm cut}}{2G(r_{\rm cut} - r_{\rm core})} \left(\frac{1}{\sqrt{r_{\rm core}^2 + R^2}} - \frac{1}{\sqrt{r_{\rm cut}^2 + R^2}} \right), \tag{3.15}$$

with the relationship between ρ_0 and σ_0 given by:

$$\rho_0 = \frac{\sigma_0^2}{2\pi G} \left(\frac{r_{\rm cut} + r_{\rm core}}{2 r_{\rm cut}\, r_{\rm core}} \right). \tag{3.16}$$

The enclosed projected mass within radius R is:

$$M_{\rm 2D}(R) = 2\pi\Sigma_0 \frac{r_{\rm cut}\, r_{\rm core}}{r_{\rm cut} - r_{\rm core}} \left(\sqrt{r_{\rm core}^2 + R^2} - r_{\rm core} - \sqrt{r_{\rm cut}^2 + R^2} + r_{\rm cut} \right), \tag{3.17}$$

and the total finite mass is:

$$M_{\rm tot} = 2\pi\Sigma_0 \frac{r_{\rm cut}\, r_{\rm core}}{r_{\rm cut} + r_{\rm core}}. \tag{3.18}$$

In the limit where $r_{\rm core} \to 0$, the cut radius, $r_{\rm cut}$, becomes the half-mass radius, and the effective radius, R_e, defined such that $M_{\rm 2D}(R_e) = M_{\rm tot}/2$ approaches $R_e \approx (3/4)r_{\rm cut}$.

The elliptical versions of these profiles are implemented in LENSTOOL (here treated as spherically symmetric), introducing ellipticity and orientation as additional parameters. Each dPIE halo is therefore characterised by eight parameters: (i) the redshift z; (ii) central position (α, δ); (iii) ellipticity, e, (iv) the orientation angle, θ; (v) the core radius, $r_{\rm core}$; (vi) cut radius, $r_{\rm cut}$; (vii) the central velocity dispersion, σ_0. In the models presented in this thesis, we use dPIE profiles to model cluster-scale dark matter halos and galaxy-scale halos associated with cluster members.

3.2.2 Cluster Members

Cluster Galaxies Identification The parametric mass modelling technique adopted in this study explicitly accounts for the contribution of individual cluster member galaxies to the total gravitational potential. Therefore, constructing a well-defined and reliable catalogue of cluster members is essential. Galaxy clusters are known to have a well defined and very regular population of early type elliptical and lenticular galaxies, called the red sequence (Gladders and Yee, 2000). These red sequence galaxies show a tight relation between their colour and magnitude (Baum, 1959; Visvanathan and Sandage, 1977). We use SEXTRACTOR to detect the objects. To keep the number of objects and their IDs consistent across filters, we run SEXTRACTOR in dual-image mode: one filter is set as the detection (reference) image, and the same apertures are then applied to all other filters. This procedure ensures uniform, matched photometry for all the sources in the SEXTRACTOR output photometry catalogue. Sources considered as bad detections (with a quoted magnitude of 99 from SEXTRACTOR) are removed along with sources at the edges of the instrument's field of view. This catalogue is still contaminated by stars, foreground and background galaxies, which is needed to be removed. Point sources such as foreground stars form a narrow, tilted sequence, the stellar locus, in the

'brightness *vs* magnitude' space. Since all the stars share the PSF size, so as a star brightens its brightest pixel scales almost linearly with its total magnitude. Therefore, sequence of stars is identified using the surface brightness and magnitude of the detected sources (the MAG_AUTO vs MU_MAX diagram, as shown in Figure 5.2), and then removed from the catalogue. Then to identify the red sequence , a colour-magnitude diagram is created (as shown in Figure 5.3). This diagram is produced by plotting the colour, defined as the difference between a galaxy's apparent magnitudes in two photometric bands, against its magnitude. A σ clipping fit is used to fit the red sequence, and a visual inspection is performed to remove any remaining contamination such as foreground or background galaxies that overlap in projection and can look like merging objects even though they are not cluster members. Finally, we remove obvious image artefacts, such as diffraction spikes from bright stars and sources near the detector edges, from the catalogue. If available, photometric and/or spectroscopic redshifts are used to identify cluster members and, also to calibrate the red sequence selection.

Modelling Cluster member galaxies are parameterised in LENSTOOL as small-scale mass clumps. To reduce computational complexity and improve model convergence, all cluster members are assumed to follow common scaling relations. Following the standard assumption that luminosity traces mass, each member galaxy is modelled using a galaxy-scale dPIE halo. To reduce the number of free parameters in the lens model, position, ellipticity and position angle of galaxy-scale components are fixed to follow their light distribution. The remaining halo parameters, central velocity dispersion, σ_0, core radius, $r_{\rm core}$, and cut radius, $r_{\rm cut}$, are scaled relative to a reference galaxy with luminosity $L^\star$ using the Faber–Jackson relation (Faber and Jackson, 1976):

$$\begin{aligned} \sigma_0 &= \sigma_0^\star \left(\frac{L}{L_\star}\right)^{1/4}, \\ r_{\rm core} &= r_{\rm core}^\star \left(\frac{L}{L^\star}\right)^{1/2}, \\ r_{\rm cut} &= r_{\rm cut}^\star \left(\frac{L}{L^\star}\right)^{\alpha} \end{aligned} \tag{3.19}$$

where $\sigma_0^\star$, $r_{\rm core}^\star$, and $r_{\rm cut}^\star$ denote the reference values for the velocity dispersion, core radius, and cut radius, respectively. α is the slope, and is fixed to 1/2, following the work by Jullo and Kneib (2009); Niemiec et al. (2020).

The mass of each galaxy halo is then given by:

$$M = \pi \frac{\sigma_0^2}{G} r_{\rm core} \left(\frac{L}{L^\star}\right), \tag{3.20}$$

Previous studies have shown that $r_{\rm core}$ has minimal influence on galaxy-scale mass models, and can be fixed to a small value without loss of accuracy (e.g. Covone et al., 2006; Limousin et al., 2007; Elíasdóttir, 2007). In our models, we fix $r_{\rm core}^\star = 0.15\,$kpc following Limousin et al. (2007). The remaining parameters, $\sigma_0^\star$ and $r_{\rm cut}^\star$, are optimized during the lens model fitting for a reference galaxy of luminosity $L^\star$. We evaluate different models using both χ^2 statistics and the root mean square (rms, which tells us how closely a lens model reproduces the astrometric positions of the multiple images) offset between observed and predicted image positions, with lower rms values indicating a better fit.

The halo parameters introduced before are sampled with the MCMC scheme presented in Section 3.5. The best-fit model is selected by the minimum $\chi^2_{\rm SL}$ and the corresponding rms image-plane offset as described in Section 3.5.

3.3 Non-parametric Modelling

In contrast to the parametric strong lensing analysis of the core of clusters, we use a non-parametric mass modelling technique to map the mass distribution in

the outskirts, i.e. where weak lensing signal dominates (Jauzac et al., 2012, 2015a, 2016; Gonzalez et al., 2020; Niemiec et al., 2020, 2023).

For weak lensing analyses, a multi-scale grid of potentials is used to decompose the matter distribution. The multi-scale grid method (Jullo and Kneib, 2009; Jauzac et al., 2012) uses an irregular grid composed of Radial Basis Functions (RBFs) to add flexibility to the lensing mass reconstruction. RBFs are real value functions with radial symmetry fixed at all the nodes of the grid. The multi-scale grid is created from a smoothed lightmap of the cluster, and is recursively refined in the densest regions. The distribution of cluster members is used to create a light-map. We use SExtractor segmantation map to extract the light corresponding to these galaxies from the *HST* image and smooth it with a gaussian kernel to get a smoothed lightmap. On this smoothed lightmap, an hexagonal geometry of grid centred on the cluster core is adopted which recursively split into six equi-lateral triangles, as shown in Figure 5.5. Each RBF is modelled with a truncated isothermal mass distribution (TIMD profile, i.e., a circular version of dPIE). This profile consists of a two components pseudo-isothermal mass distribution with a core radius, s, defined as the distance between an RBF and its closest neighbour, and a cut radius, t (Jullo and Kneib, 2009). The true convergence field, $\kappa(\theta)$, is given by:

$$\kappa(\theta) = \frac{1}{\Sigma_{\rm crit}} \Sigma_i v_i^2 f\left(||\theta_i - \theta||, s_i, t_i\right), \tag{3.21}$$

where the RBF at the grid node, θ_i, is defined as :

$$f(R, s, t) = \frac{1}{2G} \frac{t}{t-s} \left(\frac{1}{\sqrt{s^2 + R^2}} - \frac{1}{\sqrt{t^2 + R^2}} \right). \tag{3.22}$$

In a TIMD profile, the scaling factor, v_i^2, is the velocity dispersion at the centre of the gravitational potential, i. Cut radii of all grid potentials are fixed to $s = 3\,t$ (Jullo and Kneib, 2009).

Following this, the shear field is written as

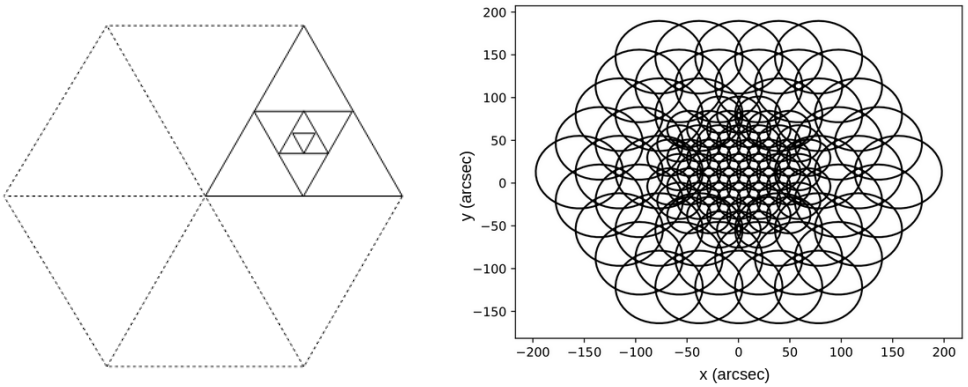

Figure 3.2: Left panel : Adopted hexagonal geometry for the multi-scale grid and recursive splitting into equilateral triangles. The hexagon centered on the cluster center is splitted into 6 equilateral triangles, which are further divided into four sub-triangles based on the input threshold value of the lightmap. This subdivision repeats up to the user-selected level n, yielding a finer mesh in high-density regions and a coarser mesh elsewhere. Credit : (Jullo and Kneib, 2009) Right panel : Image showing an example of a multi-scale irregular grid, constructed using the hexagonal geometry shown in the left panel.

$$\gamma_1(\theta) \;=\; \Sigma_i v_i^2 \Gamma_1^i \left(||\theta_i - \theta_j||,\, s_i,\, t_i\right), \tag{3.23}$$

$$\gamma_2(\theta) \;=\; \Sigma_i v_i^2 \,\Gamma_2^i \left(||\theta_i - \theta_j||,\, s_i,\, t_i\right), \tag{3.24}$$

where Γ_1 and Γ_2 are given in equation A8 in Elíasdóttir (2007).

The ellipticity measurements in the weak lensing regime can be approximately given as a linear relation,

$$\boldsymbol{e} = M_{\gamma v}\boldsymbol{v} + \boldsymbol{n}, \tag{3.25}$$

where $\boldsymbol{v}$ contains the amplitude of the RBFs, and $\boldsymbol{n}$ gives the intrinsic ellipticity and the noise in the shape measurements. The shear components of the matrix $\boldsymbol{M_{\gamma v}}$ containing the cross-contribution of each individual RBF to each individual weak lensing source are scaled by a ratio of angular diameter distances. The elements of this matrix for the two shear components are given by :

$$\Delta_1^{(j,i)} \;=\; \frac{D_{LS,i}}{D_{OS,i}}\,\Gamma_1^i \left(||\theta_i - \theta_j||,\, s_i,\, t_i\right), \tag{3.26}$$

$$\Delta_2^{(j,i)} = \frac{D_{LS,i}}{D_{OS,i}} \Gamma_2^i \left(||\theta_i - \theta_j||, s_i, t_i \right), \tag{3.27}$$

where the elements corresponds to the contribution from each unweighted RBFs j to the shear of image i, and Γ_1 and Γ_2 are given in equation A8 in Elíasdóttir (2007).

3.4 Combining Parametric and Non-parametric models

In order to obtain a full mass reconstruction of a galaxy cluster, we need to combine our parametric strong-lensing mass model with the non-parametric weak-lensing one. For that, we follow the sequential method described initially in Jauzac et al. (2015a) and then developed further in Niemiec et al. (2020) and Niemiec et al. (2023). First, the core is modelled using the strong lensing constraints as described in Sect. 3.2. To the best-fit parametric model of the core, the multi-scale grid of potentials described in Sect. 3.3 is added in the outskirts of the cluster. The observed ellipticity from the sum of the two components of our model can be written as

$$\boldsymbol{e_m} = M_{\gamma v} \boldsymbol{v} + \boldsymbol{e}_{\text{param}} + \boldsymbol{n}, \tag{3.28}$$

where $\mathbf{v}$ contains the amplitude of the RBFs of the multi-scale grid, $\mathbf{e_m} = \mathbf{(e_1, e_2)}$ corresponds to the individual shape measurements of the weak lensing sources, and e_{param} is the fixed ellipticity from the best fit strong lensing model. $\mathbf{n}$ represents the galaxy shape noise component, and $\mathrm{M}_{\gamma v}$ is the matrix which contains the contribution of individual RBFs. This matrix is presented in Sect. 3.3.

As said before, we proceed to a sequential fit. The parametric model presented in Sect. 3.2 is fixed at its best-fit values. The RBF amplitudes are then estimated from the weak lensing constraints. This also ensures that strong lensing constraints are not taken into account twice. Already optimised cluster-scale dark matter halo and cluster member galaxies are combined with RBF grid potentials. As explained

in Sect. 3.3, grid potentials are removed from the cluster core due to the absence of weak lensing constraints in this region.

3.5 Lenstool

LENSTOOL includes a Bayesian Markov Chain Monte Carlo (MCMC) engine, called bayesSys (and its extension MassInf for non-parametric modelling) that converts observables, summarised in Section 3.1, into posterior distributions of mass-model parameters. It supports both analytic halo profiles and multi-scale radial-basis grids. The standard notation, $\beta = \theta - \alpha(\theta)$ (Eq. 2.9), for the source-plane coordinate is adopted, where α is the deflection angle derived from the projected potential, ϕ.

The MCMC algorithm samples the posterior probability distribution of the model parameters, which is defined in terms of the likelihood function.

3.5.1 Strong Lensing Likelihood

In the strong lensing regime, the positions of multiple images are used as constraints to the lens model. The likelihood function assumes that positional measurement errors of images are independent and Gaussian distributed. Following Jullo et al. (2007), the strong lensing likelihood is given by:

$$\mathcal{L}_{SL} = \prod_{i=1}^{M_{SL}} \left[\frac{1}{\prod_j \sqrt{2\pi}\,\sigma_{ij}} \right] \exp\left(-\frac{\chi_i^2}{2} \right), \tag{3.29}$$

where M_{SL} is the number of multiple image systems, σ_{ij} is the positional uncertainty for image j of source i, and χ_i^2 is:

$$\chi_i^2 = \sum_{j=1}^{n_i} \frac{\left\| \mathbf{x}_j^{obs} - \mathbf{x}_j(\boldsymbol{\Theta}, \mathbf{w}) \right\|^2}{\sigma_{ij}^2}, \tag{3.30}$$

with $\mathbf{x}_j^{obs}$, the observed position, and $\mathbf{x}_j(\boldsymbol{\Theta}, \mathbf{w})$, the predicted position from the lens model composed of parametric parameters, $\boldsymbol{\Theta}$, and grid-based weights, $\mathbf{w}$.

The best-fit model is the one that minimizes the total chi-square, and, thereby, maximises the likelihood.

To quantify how well the model reproduces the observed image configuration, we compute the root-mean-square (rms) separation between the predicted and observed image positions:

$$\mathrm{rms} = \sqrt{\frac{1}{N_{tot}} \sum_{i=1}^{N_{tot}} |\mathbf{x}_j^{obs} - \mathbf{x}_j|^2}, \tag{3.31}$$

where N_{tot} is the total number of multiple images. In an ideal world and with a perfect model, rms would be zero. A smaller rms value indicates a better match between the model and the observations. Once the optimal model is found, best-fit parameters for each halo component are extracted and interpreted within the context of the cluster's mass distribution.

3.5.2 Weak Lensing Likelihood

In the linear weak-lensing approximation adopted by LENSTOOL, the observed complex ellipticity of each background galaxy is written as

$$\mathbf{e} = 2\gamma + 2\gamma' + \mathbf{n}, \tag{3.32}$$

where γ is the reduced shear from the free-form (RBF) component, γ' is the shear from the parametric mass model with parameters Θ, and $\mathbf{n}$ represents the intrinsic (zero-mean) galaxy shapes. The factor of two arises from Lenstool's ellipticity convention $|e| = (1-r^2)/(1+r^2)$, with r the axis ratio (Bartelmann and Schneider, 2001).

In the weak lensing regime, background galaxy shapes are only mildly distorted, and their intrinsic ellipticity distribution can be approximated as Gaussian. Following Niemiec et al. (2020), the weak lensing likelihood is thus expressed as:

$$\mathcal{L}_L = \frac{1}{Z_L} \exp\left(-\frac{1}{2}\chi^2_{WL}\right), \tag{3.33}$$

where Z_L is the normalization factor, given as $Z_L = \sqrt{(2\pi)^{2\lambda} \det N_{ee}}$ with a set of λ background galaxies. Since Z_L depends only on the fixed noise properties of the data, it is constant across models and can be omitted when comparing relative likelihoods.

The chi-squared statistic is given by:

$$\chi^2_{WL} = \left(\boldsymbol{e} - 2\boldsymbol{\gamma} - 2\boldsymbol{\gamma}'(\boldsymbol{\Theta})\right)^\top \mathbf{N}_{ee}^{-1} \left(\boldsymbol{e} - 2\boldsymbol{\gamma} - 2\boldsymbol{\gamma}'(\boldsymbol{\Theta})\right). \tag{3.34}$$

Here, $\boldsymbol{e}$ is the vector of observed ellipticities of background galaxies, $\boldsymbol{\gamma}$ is the shear field predicted by the free-form (RBF) model, $\boldsymbol{\gamma}'(\boldsymbol{\Theta})$ is the shear contribution from the parametric model with parameters $\boldsymbol{\Theta}$, and $\mathbf{N}_{ee}$ is the covariance matrix of ellipticity errors, assumed diagonal with elements:

$$N_{ee}^{(i,i)} = \sigma_{\mathrm{m}}^2 + \sigma_{\mathrm{int}}^2, \tag{3.35}$$

where σ_{m} is the measurement error, and σ_{int} is the intrinsic shape noise of galaxies.

This formulation captures the statistical mismatch between the observed ellipticities and the predicted shear from both mass model components. The weak lensing likelihood complements the strong lensing likelihood by constraining the mass distribution in the outer regions of the cluster, where multiple images are not typically observed. Together, these two likelihoods form the total lensing likelihood function used by Lenstool to infer the best-fit model parameters through MCMC sampling.

3.5.3 Combined Likelihood

The mass distribution within the cluster is constrained using two complementary observational datasets: the positions of multiply imaged sources in the strong

lensing core, and the distorted shapes of background galaxies in the weak lensing outskirts. This combined approach facilitates a coherent and wide-field reconstruction of the cluster's projected mass distribution. The total likelihood is the product of the individual likelihoods presented in Sect 3.5.1 and 3.5.2 (Niemiec et al., 2020):

$$\mathcal{L}_{total}(\mathbf{\Theta}, \mathbf{w}) = \mathcal{L}_{SL}(\mathbf{\Theta}, \mathbf{w}) \times \mathcal{L}_{WL}(\mathbf{\Theta}, \mathbf{w}). \tag{3.36}$$

v

With the 'Sequential-fit' approach, used in this work, we first optimise the parametric mass model in the cluster core using strong-lensing constraints. This is done in the image plane, and corresponds to maximizing the likelihood $\mathcal{L}_{\rm SL}(\mathbf{\Theta} \mid \boldsymbol{\theta}_{\rm I})$, where $\boldsymbol{\theta}_{\rm I}$ are the observed multiple image positions. Once the best-fit parameters $\mathbf{\Theta}_{\rm best}$ are obtained, this component is fixed. As a second step, we optimise the grid based model in the outskirts of the cluster using weak lensing constraints, while keeping the parametric model of the core fixed. The corresponding likelihood is $\mathcal{L}_{\rm WL}(\mathbf{w} \mid \mathbf{e}^{\rm obs}, \mathbf{\Theta}_{\rm best})$, where $\mathbf{e}^{\rm obs}$ are the observed galaxy ellipticities, and $\mathbf{w}$ are the weights of the RBFs in the grid model.

This sequential procedure allows for independent treatment of strong and weak lensing regimes, simplifying the modelling process, but at the cost of self-consistency across the entire field. The main limitation of this approach is that the parametric model optimised using strong lensing constraints cannot adjust to better accommodate the weak lensing data in the transition region between the core and outskirts. This can lead to systematic biases in the mass reconstruction, particularly in the intermediate radial range where both strong and weak lensing effects are present but neither dominates.

To address these limitations, Niemiec et al. (2020) introduced the *hybrid*-LENSTOOL. The hybrid method combines the strengths of both parametric and non-parametric mass modelling by allowing simultaneous optimisation of both components. In this framework, the parametric mass model and the grid-based correction are jointly

optimized using the full likelihood (as presented in Eq.3.36). The *hybrid*-LENSTOOL implementation uses a multi-scale approach where the parametric model provides the large-scale mass distribution and the grid-based component adds local corrections. The optimisation is performed using a Bayesian framework with MCMC sampling, allowing for proper uncertainty quantification and exploration of parameter degeneracies. This hybrid approach ensures self-consistency across the entire field, providing a more robust and comprehensive mass reconstruction.

This chapter walked us through the observational constraints for strong and weak lensing, two mass modelling techniques : parametric (in the core) and non-parametric (in the outskirts), eventually combining to get a full mass distribution in the cluster from the core to outskirts. We have seen how strong lensing multiple image configurations in the core and weak lensing shear measurements in the outskirts jointly constrain a cluster's total mass. These data feed into two complementary modelling frameworks: parametric reconstructions for the inner regions, and non-parametric, grid-based technique for the outer regions, which together delivers the total mass distribution in the cluster, from the core to the outskirts. To put these methods into practice, we now assemble the key datasets that will drive our analysis: deep, multi-band *HST* and *JWST* imaging to map both strong and weak lensing signatures; high-resolution Chandra X-ray exposures to trace the intracluster gas; and extensive ground-based photometric catalogues for precise redshift estimates and cluster member identification.

Chapter 4

Observations

"What we observe is not nature itself, but nature exposed to our method of questioning." - Werner Heisenberg

This chapter presents a comprehensive overview of the observational infrastructure that underpins modern gravitational lensing studies of galaxy clusters used in this thesis. The field has evolved dramatically over the past three decades, transitioning from ground-based photographic surveys to sophisticated multi-wavelength campaigns combining space and ground-based facilities. Each telescope and instrument discussed here contributes unique capabilities that, when combined, provide the observational foundation necessary for precise mass modelling and cosmological applications of cluster lensing.

4.1 Space-based Telescopes

4.1.1 *Hubble Space Telescope*

The *Hubble Space Telescope* (*HST*, left panel of Figure 4.1) is a 2.4 meter space-based optical and near-infrared observatory launched in 1990. *HST* has been central to the study of galaxy clusters through gravitational lensing, owing to its exceptional spatial resolution ($\sim 0.05''$) and stable space-based platform. Its cameras,

particularly the Advanced Camera for Surveys (ACS) and Wide Field Camera 3 (WFC3), have delivered deep optical and near-infrared imaging that enables the detection of faint, high-redshift lensed galaxies. These images are essential for strong lensing studies, as they allow accurate identification and localisation of multiple image systems with minimal contamination or distortion from Earth's atmosphere.

HST has been instrumental in surveys such as CLASH (Cluster Lensing And Supernova survey with *Hubble*), HFF (*Hubble* Frontier Fields), and more recently BUFFALO (Beyond the Ultra-deep Frontier Fields and Legacy Observations), which expanded the spatial coverage around the original HFF clusters (See section 4.3). These surveys have provided uniform, and multi-band observations, used for photometric redshift estimation, weak lensing shape measurements, and precise lens modelling.

4.1.2 *James Webb Space Telescope*

Building upon *HST*'s legacy, the *James Webb Space Telescope* (*JWST*, right panel of Figure 4.1) represents the next generation of space-based cluster lensing observations. Launched in December 2021, this 6.5 meter space-based infrared observatory provides unprecedented infrared imaging and spectroscopic capabilities, offering a transformative view of gravitational lensing systems. Its four main scientific instruments work together to observe the Universe in the infrared part of the electromagnetic spectrum: the Near Infrared Camera (NIRCam) serves as the primary imager for capturing the earliest stars and galaxies, the Near Infrared Spectrograph (NIRSpec) determines chemical composition and properties of distant objects through spectral analysis, the Near Infrared Imager and Slitless Spectrograph (NIRISS) provides complementary imaging and multi-object spectroscopy capabilities, and the Mid-Infrared Instrument (MIRI) penetrates dust clouds to observe star and planet formation regions. Together, these instruments enable the detection of extremely faint, high redshift lensed galaxies that were inaccessible with previous

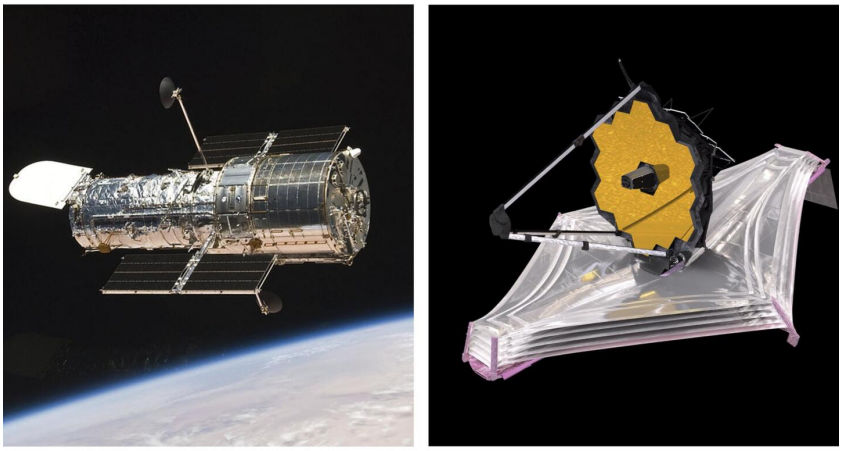

Figure 4.1: Models of the *Hubble Space Telescope* (left) and *James Webb Space Telescope (right).*

instruments. *JWST*'s high sensitivity and resolution at longer wavelengths allow the identification of sources deep in the reionisation epoch.

Cluster surveys using *JWST* are emerging rapidly, with some of the earliest examples including the UNCOVER (Ultradeep NIRSpec and NIRCam Observations before the Epoch of Reionization) survey and the SLICE (Strong LensIng and Cluster Evolution) program. These surveys build upon previous HST legacy fields and extend observations into redshift regimes previously unexplored, reaching $z \sim 10 - 15$ (Naidu et al., 2022; Robertson et al., 2023).

4.1.3 *Chandra* X-ray Observatory

Complementing the optical and infrared capabilities of *HST* and *JWST*, the *Chandra* X-ray Observatory provides crucial information about the hot gas component of galaxy clusters. Launched in 1999, this space-based X-ray telescope provides deep, high-resolution X-ray imaging that is crucial for understanding the hot intracluster medium (ICM) and baryonic mass distribution in galaxy clusters. The telescope's primary imaging instrument, the Advanced CCD Imaging Spectrometer (ACIS), enables spatially-resolved X-ray spectroscopy and imaging over a field of view of $\sim 16' \times 16'$. *Chandra*'s angular resolution of $\sim 0.5''$ and its sensitivity in the 0.5–10

keV energy band make it ideal for mapping the thermal structure, pressure, and temperature gradients in the ICM.

In gravitational lensing studies, *Chandra* observations are complementary to optical/infrared data by revealing the gas morphology and confirming the dynamical state of clusters. This is especially important for interpreting mass reconstructions, identifying merging systems, and distinguishing between dark matter and baryonic mass components. The combination of X-ray gas distributions with lensing mass maps provides powerful constraints on cluster physics and the nature of dark matter (Bradač et al., 2005; Clowe, 2006; Owers et al., 2011; Eckert et al., 2015). *Chandra* observations have also played a key role in identifying offsets between dark matter and baryonic components in merging clusters such as the Bullet Cluster, providing direct empirical evidence for the existence of dark matter as illustrated in Figure 4.2.

4.2 Ground-based Telescopes

4.2.1 W.M. Keck Observatory

The W. M. Keck Observatory, located atop Maunakea in Hawaii, hosts two 10 meter telescopes equipped with advanced optical and near-infrared instruments. They began operations in 1993 and 1996, respectively. As a key facility for spectroscopic follow-up, Keck has been a cornerstone in strong lensing studies, providing high signal-to-noise spectra for background sources and cluster members using instruments such as the Low Resolution Imager and Spectrograph (LRIS), Deep Imaging Multi-Object Spectrograph (DEIMOS), and Multi-Object Spectrometer For Infra-Red Exploration (MOSFIRE).

Keck spectroscopy is critical for refining lens models, as it enables precise redshift measurements of multiple image systems and cluster galaxies. These redshifts reduce degeneracies in mass modelling and help calibrate photometric estimates.

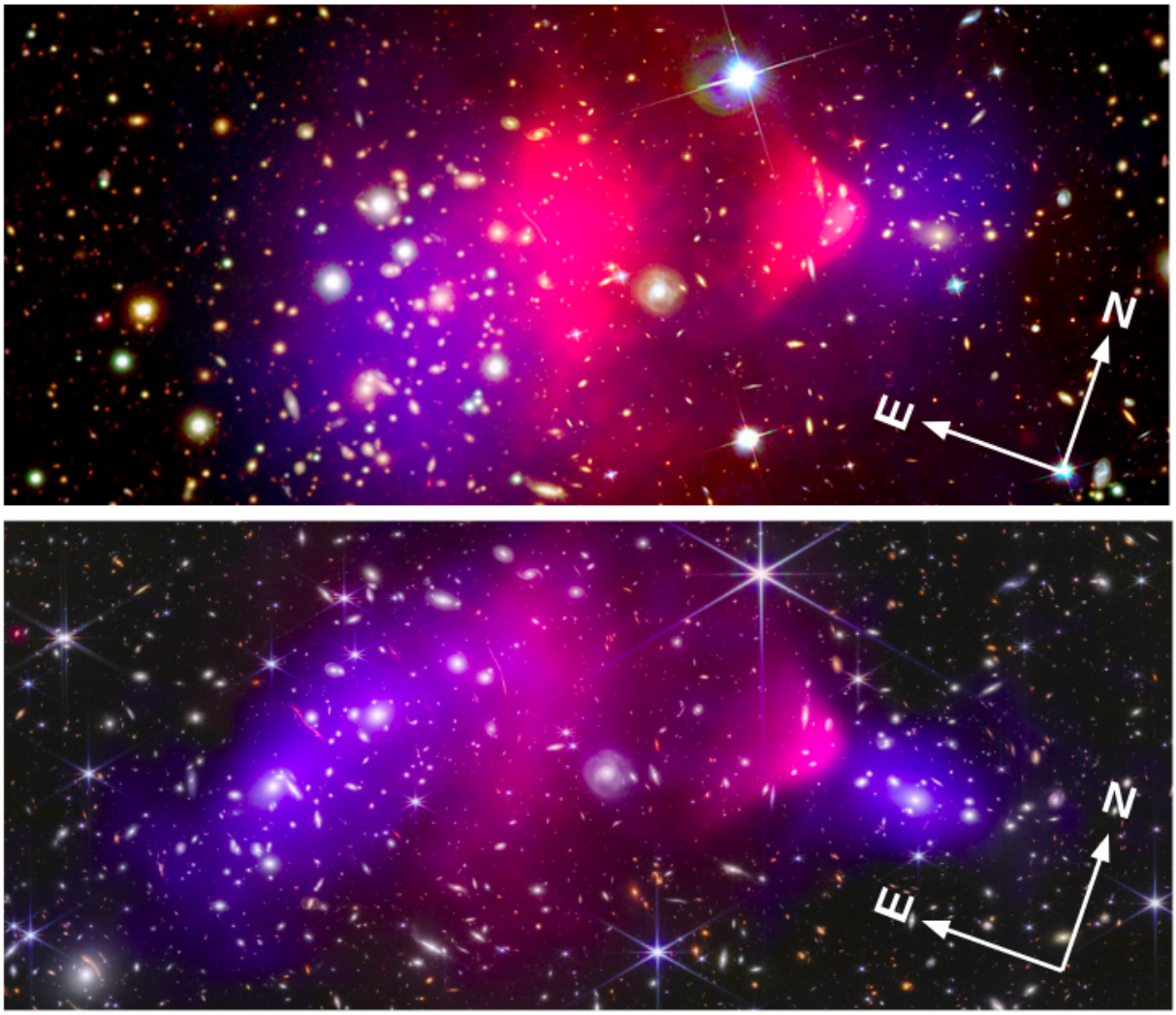

Figure 4.2: Comparison of the Bullet Cluster as seen by *HST* (top) and *JWST* (bottom). The Bullet Cluster is a well-known merging system formed by the collision of two galaxy clusters. The gas component, traced by *Chandra* X-ray observations (shown in pink), is concentrated in distinct regions separate from the main mass peaks. The dark matter distribution, inferred from lensing (shown in purple), is aligned with the locations of the galaxies rather than the X-ray gas. This spatial offset between the baryonic and total mass components provides strong observational support for the existence of dark matter. The comparison between *HST* and *JWST* images reveals additional background sources and finer lensing features, enabling more detailed mass reconstructions and insights into the cluster's merger dynamics. Credit : NASA/ESA/CSA/STScI/Clowe (2006)/Cha et al. (2025).

Keck spectroscopy has also been used to determine the velocity dispersion in BCGs (Sand et al., 2008b; Newman et al., 2013b,a) to further refine the mass model. Combined with space-based imaging, Keck's spectroscopic depth enhances the accuracy and robustness of lens reconstructions (Lubin et al., 2000; Richard et al., 2009; Limousin et al., 2010).

4.2.2 Subaru Telescope

Also located on Maunakea in Hawaii, the Subaru Telescope is a 8.2 meter optical and infrared observatory that began operations in 1999. Initially, the Suprime-Cam wide-field optical imager was deployed on Subaru, enabling early weak-lensing measurements of cluster mass distributions over a $34' \times 27'$ field. It's successor, the Hyper Suprime-Cam (HSC), enables high-precision shape measurements of background galaxies across large areas, crucial for constraining the outer mass profiles of clusters. Its deep, wide-field data has been extensively used in combination with space-based observations for lens modelling and substructure detection (Miyazaki et al., 2018; Oguri et al., 2018). The wide-field capabilities of Subaru complement the high-resolution observations from space-based telescopes, providing the large-scale context necessary for comprehensive cluster mass modelling (Umetsu et al., 2012, 2020; Jauzac et al., 2012, 2016; Niemiec et al., 2023).

4.2.3 Canada France Hawaii Telescope (CFHT)

The Canada France Hawaii Telescope (CFHT) is a 3.6 meter optical and infrared telescope located atop Maunakea in Hawaii, which began operations in 1979. CFHT holds historical significance in cluster lensing studies, as it was used by astronomers from Toulouse Observatory to discover the first gravitational arc in the galaxy cluster Abell 370 in the 1980s. The giant luminous arc became the first spectroscopically confirmed giant-arc lens system (Soucail, 1987; Soucail et al., 1988), marking a pivotal moment in the field's development. Beyond this foundational

contribution, CFHT has played a significant role in wide-field cluster lensing surveys, particularly through its MegaPrime camera, which provides a 1 deg^2 field of view. This wide-field capability makes CFHT particularly valuable for weak lensing studies, as it can efficiently survey large areas around clusters to map their extended mass distributions. CFHT has been instrumental in several major weak lensing surveys, including the Canada France Hawaii Telescope Lensing Survey (Heymans et al., 2012; Erben et al., 2013, CFHTLens), which has contributed to our understanding of cluster mass profiles and the statistical properties of cluster populations. The telescope's stable observing conditions and well-characterized instrumentation make it ideal for precise photometry and shape measurements required for weak lensing analyses.

4.2.4 The Very Large Telescope

Representing the pinnacle of ground-based optical astronomy, the Very Large Telescope (VLT) consists of four 8.2 meter optical and infrared telescopes located at Paranal Observatory in Chile, which began operations in 1998-2000. Operated by the European Southern Observatory (ESO), the VLT plays a critical role in spectroscopic follow-up observations for gravitational lensing studies. One of its most powerful instruments is the Multi Unit Spectroscopic Explorer (MUSE, shown in figure 4.3), an optical integral field spectrograph mounted on VLT Unit Telescope 4.

MUSE provides simultaneous spatial and spectral information across a $1' \times 1'$ field of view, allowing the acquisition of thousands of spectra in a single pointing without pre-selection. This makes it exceptionally well-suited for lensing analyses, as it can efficiently identify multiple-image systems and determine their spectroscopic redshifts with high accuracy. MUSE has been instrumental in improving the precision of strong lensing mass models by providing secure redshifts for both background lensed sources and cluster member galaxies (Caminha et al., 2017; Jauzac et al., 2019; Richard et al., 2021; Lagattuta et al., 2023).

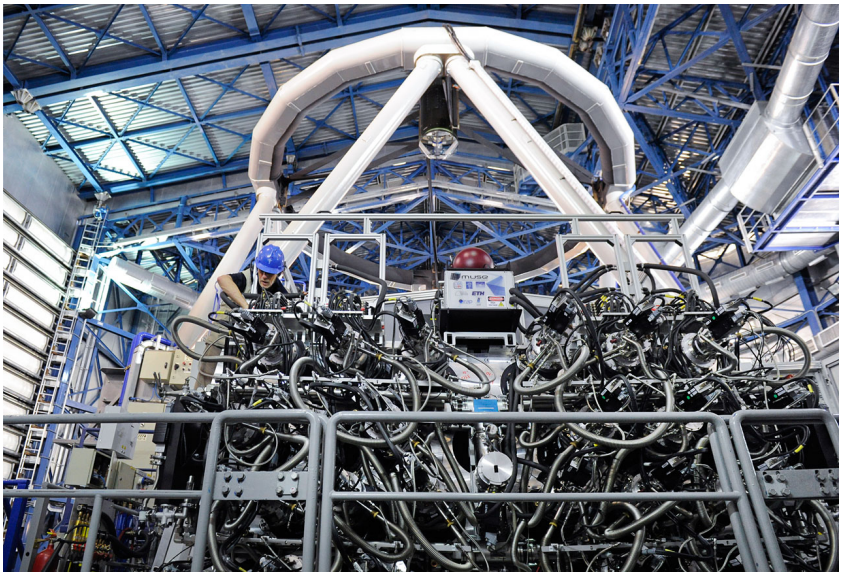

Figure 4.3: The Multi Unit Spectroscopic Explorer (MUSE), mounted on the Very Large Telescope (VLT).

4.3 Survey Programmes

The observational infrastructure described in the previous section has enabled a series of increasingly sophisticated survey programmes that have systematically advanced our understanding of galaxy clusters through gravitational lensing. These surveys have evolved from early X-ray selected cluster catalogues to targeted deep imaging campaigns, and most recently to comprehensive multi-wavelength programs combining space-based and ground-based observations. This section presents the key survey programmes used in this work, which shaped modern cluster lensing studies, organized roughly chronologically to illustrate the field's progression from discovery to precision science.

4.3.1 MAssive Cluster Survey (MACS)

Representing one of the foundational efforts to systematic identification of massive clusters, the MAssive Cluster Survey (MACS, Ebeling et al., 2001) is an X-ray cluster survey that compiled a complete sample of massive and very X-ray luminous ($L_X > 10^{44}$ erg s^{-1}) galaxy clusters at redshifts $z > 0.3$. Cluster candidates were

selected from the ROSAT Bright Source Catalogue (Voges et al., 1999) based on their X-ray flux, and X-ray hardness ratio cuts. More than two-thirds of the MACS cluster sample are new discoveries, with 124 spectroscopically confirmed at $0.3 < z < 0.7$. The University of Hawaii's 2.2 m and the Keck 10 m telescopes were used for spectroscopy. Initially aimed at increasing the number of X-ray luminous clusters at $z > 0.3$, one of the extended goals of the survey was to enable weak lensing measurements of clusters. MACS has provided the foundation for many subsequent lensing studies, with its clusters serving as primary targets for later deep imaging campaigns.

4.3.2 Cluster Lensing And Supernova survey with *Hubble* (CLASH)

Cluster Lensing And Supernova survey with *Hubble* (Postman et al., 2012, CLASH;) marked a transformative milestone in establishing cluster lensing as a precision cosmological tool. CLASH targeted 25 massive galaxy clusters in the redshift range $0.2 < z < 0.9$, combining both X-ray-selected relaxed clusters and high-magnification systems. Its primary objectives were to (i) map the dark matter distribution in clusters using strong and weak lensing, (ii) discover high-redshift galaxies magnified by gravitational lensing, and (iii) detect distant Type Ia supernovae to constrain dark energy.

CLASH employed 16-band *HST* imaging (using ACS and WFC3) to deliver high-precision photometric redshifts and morphological information over a wide wavelength range (200–1700 nm). This multi-filter strategy enabled robust identification of multiple-image systems and background galaxy redshifts, which are critical for accurate lens model constraints. The combination of strong lensing (in the core) and weak lensing (in the outer regions) allowed CLASH to reconstruct full mass profiles of clusters, spanning from the inner few tens of kiloparsecs to megaparsec scales (Zitrin et al., 2015; Merten et al., 2015; Umetsu et al., 2016). CLASH produced public lens models that have since been widely used in extragalactic and high-

redshift galaxy studies and served as a foundation for subsequent major lensing surveys.

4.3.3 *Hubble* Frontier Fields (HFF)

Advancing beyond the broad survey approach of CLASH, the *Hubble* Frontier Fields (HFF, GO: # 11507, PI: Noll, Lotz et al. 2017) program was conducted from 2013 to 2017 using the *HST*. The primary goal of HFF was to push the observational frontier of the distant Universe by leveraging the gravitational lensing power of massive galaxy clusters to magnify background galaxies at high redshift. Six massive lensing clusters - Abell 2744, MACS J0416.1–2403, MACS J0717.5+3745, MACS J1149.5+2223, Abell S1063, and Abell 370 - were selected for deep imaging. Each cluster field was observed in parallel with an adjacent blank field to provide control field data for statistical studies. A total of 140 orbits per cluster (840 orbits in all) was allocated to imaging, split between the Advanced Camera for Surveys (ACS/WFC) and the Wide Field Camera 3 infrared channel (WFC3/IR). Observations were carried out in seven bandpasses spanning the optical to near-infrared: ACS/WFC F435W, F606W and F814W, and WFC3/IR F105W, F125W, F140W and F160W. These filters provide contiguous coverage from 0.4 μm through 1.6 μm, reaching 5σ point-source depths of $\approx$29 AB mag in both cluster and parallel fields (Lotz et al., 2017). These deep, multi-band observations enabled the detection of hundreds of multiply imaged systems, crucial for strong lensing mass modelling (Jauzac et al., 2014, 2015a,b; Wang, 2015; Jauzac et al., 2016; Limousin et al., 2016; Diego et al., 2016; Mahler et al., 2018), and revealed thousands of faint high-redshift galaxies, significantly contributing to studies of cosmic reionization and galaxy evolution (Zitrin, 2014; Atek, 2015; Zheng et al., 2014). The exceptional depth of HFF observations set new standards for cluster lensing studies and provided the foundation for subsequent surveys to build upon.

The extreme depth of these observations revealed thousands of faint high redshift galaxies ($z \gtrsim$ 6–10), transforming the HFF clusters into the most effective cosmic

telescopes prior to the advent of *JWST*. These data enabled some of the earliest constraints on the UV luminosity function during the epoch of reionization (Atek, 2015; Zitrin, 2014), including the identification of remarkably bright $z \sim 10$ galaxy candidates which magnified fluxes would have been inaccessible in blank fields. The increased number of multiply imaged systems (with $\gtrsim 150$ secure images for some clusters) also allowed direct tests of lens model systematics, showing that with deep multi band *HST* data, cluster mass profiles could be recovered at the percent level within the strong lensing regime (Jauzac et al., 2015a).

The HFF data also revealed new astrophysical phenomena, including stellar explosions in multiply imaged galaxies. A notable example is the first multiply imaged supernova, SN Refsdal, discovered in MACS J1149.5+2223 (Kelly et al., 2015). Its time delays and reappearance predictions served as one of the strongest empirical tests of lens model accuracy to date. Additionally, the HFF clusters provided unique laboratories for studying cluster assembly, including the detection of complex substructures in merging systems such as Abell 2744 and MACS J0717 (Jauzac et al., 2012, 2015b, 2016). These analyses helped establish the presence of multi component merger geometries and substantial offsets between dark matter, gas, and galaxies (Jauzac et al., 2016; Wang, 2015).

Taken together, the HFF program provided a major leap in the precision and astrophysical breadth of cluster lensing studies. These data remain benchmarks for exploring lens model degeneracies, testing dark matter predictions, and preparing for the forthcoming high redshift samples from Euclid and *JWST* .

4.3.4 Beyond the Ultra-deep Frontier Fields and Legacy Observations (BUFFALO)

Recognising the need for wider field coverage around the HFF clusters, the BUFFALO (Beyond the Ultra-deep Frontier Fields and Legacy Observations, Steinhardt et al., 2020, GO: #15117, PIs: Steinhardt & Jauzac) survey is built upon

the HFF by extending the area observed by the *HST* for the six HFF clusters as shown in Figure 4.4. The survey expanded the HFF footprint by approximately a factor of four, adding flanking fields around each cluster to reach a total area of $\sim$16 arcmin^2 per cluster (Steinhardt et al., 2020). The coverage was expanded with both ACS in the F606W and F814W pass-bands, and the WFC3 in the F105W, F125W, and F160W pass-bands, achieving depths comparable to the original HFF observations. The main goals of the survey are (1) to use gravitational lensing in massive clusters to study dark matter by combining deep strong lensing and high resolution weak lensing observations to improve the precision and accuracy of the clusters' mass models (Gonzalez et al., 2020; Niemiec et al., 2023; Lagattuta et al., 2023; Perera et al., 2025), and (2) to study the distant Universe using these strong lenses as cosmic telescopes (Diego et al., 2024; Pagul et al., 2024). By providing the wider field coverage that was missing from the original HFF observations, BUFFALO enabled more comprehensive weak lensing analyses and better constraints on cluster mass distributions.

BUFFALO has increased the effective lensing volume available for studies of the high redshift Universe by sampling lower magnification regions surrounding cluster cores. This has enabled a more complete census of lensed galaxies and reduced magnification biases inherent to core only surveys (Diego et al., 2024; Pagul et al., 2024). The survey has also enabled time domain lensing studies, including constraints on the abundance of highly magnified supergiant stars at intermediate redshift through the detection and modelling of transient caustic crossing events, such as those observed in the Spock galaxy at redshift 1 (Diego et al., 2023). Finally, the homogeneous multi band dataset has served as a key legacy resource for follow up with *JWST* and *Euclid*, improving lensing predictions, target selection, and survey optimisation.

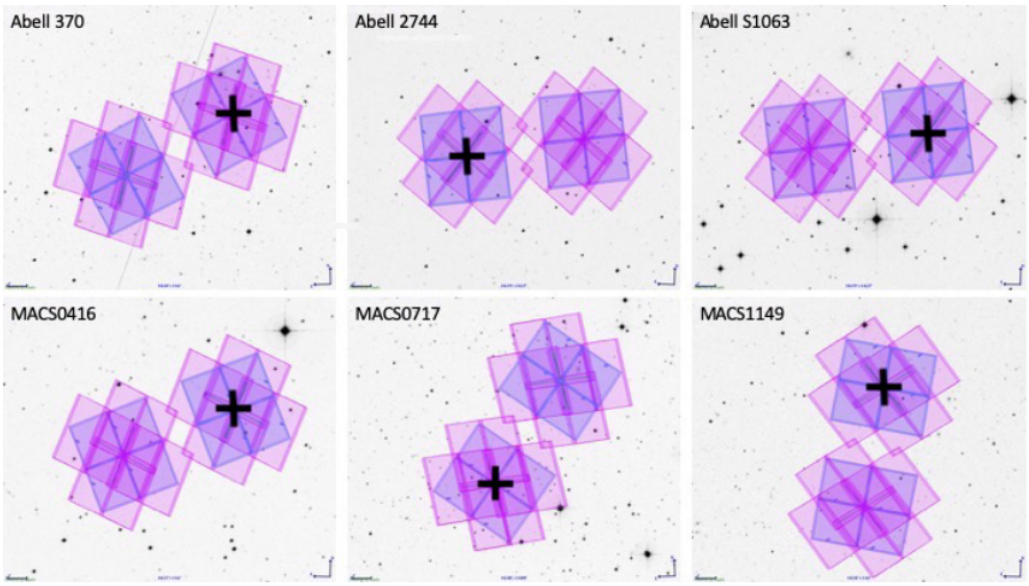

Figure 4.4: The six BUFFALO clusters showing the existing HFF pointings and the extended area from BUFFALO. In each cluster's central region (marked by a black "+"), WFC3 IR observations were executed at two-thirds orbit depth in F105W, F125W, and F160W (blue shading), while parallel ACS exposures covered the same area (and extend beyond it, thanks to ACS's larger field of view) at two-thirds–orbit depth in F606W and four-thirds–orbit depth in F814W (pink shading). The resulting mosaic tiles uniformly sample both the core and flanking regions, seamlessly integrating BUFFALO's new pointings with the pre-existing *HST* data. Image Credit : BUFFALO team (California Institute of Technology, 2015)

4.3.5 The Kaleidoscope Survey

Complementing the deep imaging approach of CLASH, the Kaleidoscope survey (Prog.ID: 0102.A-0718(A), P.I: A. Edge) represents the largest snapshot survey of massive clusters, with 211 cluster cores observed so far, taken with the MUSE spectrograph mounted on the VLT. The target list is comprised of X-ray selected clusters at $z > 0.15$ from the ROSAT All Sky Survey (RASS), with the primary sample being the MACS sample. Clusters are selected on the basis of their X-ray luminosities, $L_X > 3 \times 10^{44}\,\mathrm{erg\,s^{-1}}$ (0.1-2.4 keV). The field of view of MUSE (1'×1') covers the strong lensing region, i.e. inner core, of most galaxy clusters (typically 15-30″), and thus provides spectroscopic observations for most galaxies (foreground, cluster or background objects) in the field. Kaleidoscope observations have already proved extremely successful, and have been used for detailed cluster

analyses (e.g., Jauzac et al., 2019; Mahler et al., 2019; Lagattuta et al., 2023; Cerny et al., 2025b,a), including SMACS J0723.3-7327, the first cluster observed by *JWST* (Caminha et al., 2022; Pascale et al., 2022; Mahler et al., 2023; Diego et al., 2023).

4.3.6 Ultradeep NIRSpec and NIRCam Observations before the Epoch of Reionization (UNCOVER)

Marking the beginning of the *JWST* era in cluster lensing, the *JWST* UNCOVER Treasury Survey (Ultradeep NIRSpec and NIRCam Observations before the Epoch of Reionization; PIs Labbe & Bezanson) is a Cycle 1 program (GO#2561) aimed at probing the early Universe by targeting the powerful gravitational lensing galaxy cluster Abell 2744 at redshift $z = 0.308$ (Furtak et al., 2023a,b). The observation strategy of UNCOVER is shown in Figure 4.5.

Utilising the superior sensitivity of *JWST*, the survey combines ultradeep imaging and spectroscopy to detect and characterize galaxies formed before and during the Epoch of Reionization. Imaging observations were carried out in November 2022 using NIRCam and NIRISS, covering 28.8 arcmin^2 in seven NIRCam filters (F115W to F444W) and 16.8 arcmin^2 in five NIRISS filters, achieving depths of ∼29.5–30 AB magnitudes. The imaging mosaic was deliberately aligned with the $\mu = 2$ gravitational magnification contour to optimize the detection of intrinsically faint galaxies at $z > 10$. UNCOVER demonstrated the transformative potential of *JWST* for cluster lensing studies, revealing previously invisible high redshift galaxy populations and setting the stage for systematic surveys with the new observatory.

Beyond its primary goal of detecting galaxies in the reionization era, the UNCOVER survey has already delivered several major advances in observational cosmology and cluster lensing science. The combination of ultra deep *JWST* imaging with NIRCam and NIRISS, and extensive NIRSpec spectroscopy has enabled robust spectroscopic confirmation of galaxies at redshifts previously accessible only through photometric inference, significantly reducing uncertainties in the high red-

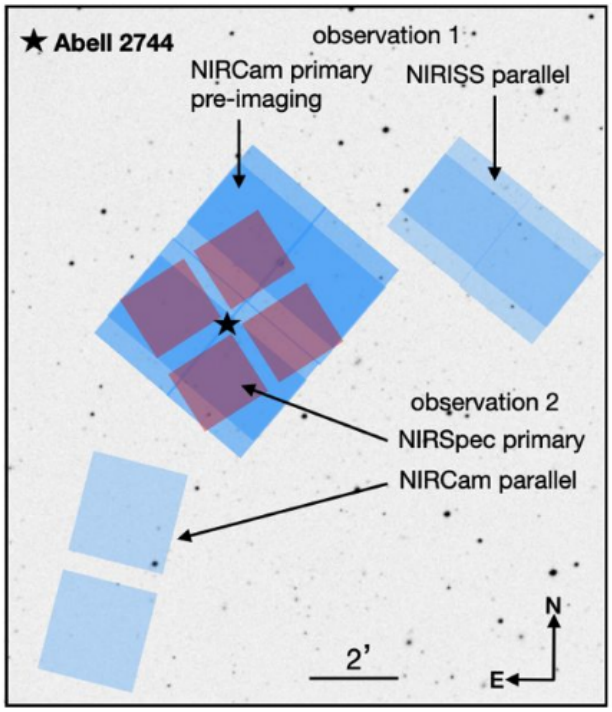

Figure 4.5: UNCOVER observing strategy. The two UNCOVER visits are depicted: Observation 1 comprises NIRCam primary pre-imaging of the cluster core with simultaneous NIRISS parallel pointings; Observation 2 comprises NIRSpec primary spectroscopy with NIRCam in parallel. Blue shading indicates UNCOVER NIRCam footprints, and the central star marks the cluster centre. Image Credit : UNCOVER team (Bezanson et al., 2022).

shift luminosity function and stellar population properties (Furtak et al., 2023a,b). The wide wavelength coverage has further allowed improved constraints on stellar masses, ages, star formation rates, and dust content of early galaxies, providing new insights into the assembly of the first generations of galaxies (Labbe et al., 2024; Bezanson et al., 2022).

4.3.7 Strong LensIng and Cluster Evolution (SLICE)

Representing the current frontier of systematic cluster lensing surveys, the Strong LensIng and Cluster Evolution (SLICE, GO:#5594, PI: G. Mahler) is the first *JWST* cluster survey programme, based on a sample of 182 (142 observed to date) selected clusters within the redshift range $0.2 < z < 1.9$ (Cerny et al., 2025b; Alling-

ham et al., 2025). The survey aims to study the mass distribution and evolution of galaxy clusters through strong gravitational lensing. The survey concentrates on cluster evolution by studying infalling material, specifically cluster galaxies, by precisely mapping the dark and luminous matter distributions within clusters. SLICE represents a new paradigm in cluster lensing studies, combining the unprecedented infrared capabilities of *JWST* and *HST* with a systematic approach to understanding cluster formation and evolution across cosmic time.

The evolution of these survey programmes illustrates the remarkable progress in cluster lensing studies over the past two decades. From the initial identification of suitable cluster samples through X-ray surveys like MACS, to the precision multi-wavelength campaigns of CLASH and HFF, and now to the systematic evolutionary studies enabled by *JWST* through programs like SLICE, each survey has built upon the achievements of its predecessors while pushing the boundaries of what is observationally possible.

With these observations in hand and our theoretical and modelling tools in place, we are now prepared to carry out the strong and weak lensing reconstructions in galaxy clusters. We begin by applying this methodology to the relaxed system MACS J1423 (Chapter 5), then turn to the complex merging cluster Abell 2744 (Chapter 6). Finally, we explore one of the most recent SLICE targets, MACS J0027 (Chapter 7), highlighting the new challenges and opportunities that high-resolution infrared imaging brings to cluster mass modelling.

Chapter 5

MACS J1423

"Balance is not something you find, it's something you create." - Jana Kingsford

This chapter is adapted from the paper : "The Kaleidoscope Survey : A strong and weak gravitational lensing view of the massive galaxy cluster MACS J1423.8+2404" (Patel et al., 2024, MNRAS).

Galaxy clusters can be observed at almost all evolution times. The observer can thus witness different dynamical processes and evolutionary states. This analysis concentrated on dynamically relaxed clusters, i.e. galaxy clusters which tend to show a relatively cool-core, with uniform properties such as temperature and density profiles (Mantz et al., 2016; Vikhlinin et al., 2006). These systems are characterized by symmetric X-ray morphologies with minimal substructure, peaked surface brightness profiles, regular nearly circular outer boundaries, and central dominant galaxies aligned with the cluster X-ray centroid, reflecting their equilibrium state and minimal offset between X-ray, optical, and weak lensing mass centroids. This cluster population provides insights into the physics of the intracluster medium (ICM) and its interactions with cluster galaxies (Mantz et al., 2016), while following well-defined scaling relations more tightly than disturbed systems, making them ideal laboratories for precision cosmology with reduced scatter in their mass-

temperature, mass-luminosity, and mass-gas fraction relations. The restriction to clusters with the highest possible degree of dynamical relaxation (for which the assumption of hydrostatic equilibrium should be most valid) allows for the most precise test of the CDM model predictions (Sanderson et al., 2007), as their formation requires sufficient time for violent relaxation processes to establish equilibrium configurations without major merger disruptions for extended periods. Studying massive relaxed clusters at high redshift ($z > 0.5$) are key to understand structure formation and evolution over cosmological timescales as they trace back to around redshift $z = 0.5$, i.e. 7 billion years after the Big Bang, providing unique insights into cool core physics where radiative cooling times are shorter than the Hubble time and the delicate balance between cooling, star formation, and AGN feedback processes. One way to do so is to use all-sky surveys to detect all clusters, providing us with the capacity to lead statistical analyses and leverage these systems as precise cosmological probes through their abundance as a function of mass and redshift, gas fraction constraints on baryon density, and X-ray luminosity and temperature evolution. While the recent years has been enriched by the successful launch of the *JWST* (December 25 2021) and the *Euclid Space Telescope* (July 1 2023), by the first light commissioning of the Vera Rubin Observatory in October 2019, and by anticipated mid-2027 launch of the *Nancy Grace Roman Space Telescope*, this work concentrates on observations taken with the largest X-ray survey dedicated to galaxy clusters, the MAssive Cluster Survey (MACS Ebeling et al., 2001, see section 4.3.1).

In this chapter, we concentrate on one of the MACS clusters, MACS J1423.8+2404 (MACS J1423 hereafter). MACS J1423 is a massive cluster with a virial mass of $M_{vir} = 4.52^{+0.79}_{-0.64} \times 10^{14}\,\mathrm{M}_{\odot}$ (Sanderson et al., 2007) at redshift, $z = 0.545$, with an X-ray luminosity $L_{\mathrm{X},bol} = 3.7 \times 10^{45}\,\mathrm{erg.s}^{-1}$ (Ebeling et al., 2007). MACS J1423 is part of the 'high-redshift' MACS subsample composed of 12 galaxy clusters at $z > 0.5$, and has been the subject of several analyses since its discovery.

LaRoque et al. (2003) examined its system's Sunyaev-Zel'dovich (SZ) morpho-

logy and galaxy distribution which revealed a cool-core, relaxed cluster. The first gravitational-lensing analysis of MACS J1423 was published in Limousin et al. (2010), followed up by Zitrin et al. (2011); Zitrin et al. (2015), and Merten et al. (2015). All of which confirmed the conclusion of the SZ analysis, MACS J1423 is a dynamically relaxed cluster. As noted by Limousin et al. (2010, hereafter L10), MACS J1423 is a nearly virialised cluster with very little substructure. The system is part of the sample targeted by the Cluster Lensing And Supernova survey with *Hubble* (CLASH, Prog.ID: 12790, PI: M. Postman; Postman et al., 2012) and has been used in several statistical studies, where its relaxed dynamical state has been particularly important for cosmological work using the baryon fraction (LaRoque et al., 2003; Allen et al., 2004; Schmidt and Allen, 2007). MACS J1423 has also been used to study the triaxiality of galaxy clusters (Limousin et al., 2013) and was included in several statistical cluster lensing analyses (Zitrin et al., 2011; Limousin et al., 2013; Applegate et al., 2014; Zitrin et al., 2015; Merten et al., 2015).

5.1 Observations

5.1.1 *Hubble Space Telescope*

MACS J1423 was first observed on 2004 June 16 with the *HST/ACS* for 4.5 ks and 4.6 ks with the F555W and F814W pass-bands respectively (GO: 9722, PI: Ebeling). In 2006, MACS J1423 was then imaged again with *ACS* in the F814W pass-band (Prog.ID: 10493, PI : Gal-Yam). Finally, MACS J1423 is part of CLASH and was thus observed again with *ACS* and the *WFC3* in the F225W, F275W, F390W, F435W, F475W, F606W, F775W, F850LP, F105W, F110W, F125W, F140W and F160W pass-bands. A list of all available observations of MACS J1423 with *HST* is given in Table 5.1.

For the analysis presented in this chapter, we use the CLASH data products in the

F606W, F814W and F160W pass-bands*. For a galaxy cluster at redshift $z = 0.545$, it is important to use filters that capture the rest-frame optical light, particularly the 4000 $\AA$ break to identify the old and red galaxies in the cluster. Given the cluster redshift, the combination of F606W and F814W is best for getting this old population. Additionally, F160W, in combination with F606W and F814W, is well-suited for identifying background galaxies in the cluster.

5.1.2 *Chandra* X-ray Observatory

MACS J1423 was first observed in the X-rays on 2001 June 1 with the *Advanced CCD Imaging Spectrometer (ACIS)* onboard the *Chandra X-ray Observatory* for 18.53 ks (Obs.ID: 1657, P.I : Vanspey-broeck). The cluster was observed again on 2003 August 18 for 115.57 ks (Obs.ID: 4195, P.I: Allen). We reduce the data as in Beauchesne et al. (2024) with the *Chandra* pipeline CIAO† 4.15 (Fruscione et al., 2006) and CALDB 4.10.7 and produce a counts map in the broad energy band (i.e. [0.5,7] keV).

5.1.3 Ground-based Spectroscopy and Photometry

5.1.3.1 Subaru & Canada France Hawaii Telescope (CFHT)

MACS J1423 was observed in the B, V, R_c, I_c and z' bands with the SuprimeCam wide-field imager on the Subaru telescope (Miyazaki et al., 2002), and in the u* and K bands with MegaCam and Wide-field Infrared Camera (WIRCam) on the Canada France Hawaii Telescope (CFHT). The resulting imaging data are used to compute photometric redshifts for all galaxies in a 0.5×0.5 deg^2 field following the methodology described in Ma et al. (2008). To estimate the spectral energy distribution (SED) for all objects within the field of view and to ensure that the images for all bands have the same effective spatial resolution of $1''$, the imaging

*https://archive.stsci.edu/missions/hlsp/clash/macs1423/data/hst/scale_30mas/
†https://cxc.cfa.harvard.edu/ciao/

Table 5.1: List of *HST* observations of MACS J1423 available. In this work, we use the CLASH observations in the F606W, F814W, and F160W pass-bands. Columns 1 and 2 give the right ascension and declination of the observed field in degrees. Column 3 lists the instruments and filters. Column 4 and 5 give the exposure time in seconds and the observation date, respectively. Finally, columns 6 and 7 provide the programme ID and the PI respectively.

R.A. (J2000)	Dec. (J2000)	Instrument/Filter	Exp. Time (s)	Obs. Date	Prog. ID	PI
215.9524858	24.0803087	ACS/F555W	4500.000	2004-06-16	9722	Ebeling
215.9524858	24.0803087	ACS/F814W	4590.000	2004-06-16	9722	Ebeling
215.9525000	24.0803056	ACS/F814W	2184.000	2006-03-24	10493	Gal-Yam
215.9495000	24.0784722	WFC3/F225W	3592.000	2013-02-22	12790	Postman
215.9494593	24.0784797	WFC3/F275W	3680.000	2013-01-13	12790	Postman
215.9495000	24.0784722	WFC3/F390W	1152.000	2013-01-13	12790	Postman
215.9494604	24.0784607		1237.000	2013-02-22	12790	Postman
215.9495000	24.0784722	ACS/F435W	1032.000	2012-12-31	12790	Postman
215.9496433	24.0787853		1066.000	2013-03-05	12790	Postman
215.9497915	24.0786826	ACS/F475W	1092.000	2013-02-03	12790	Postman
215.9496433	24.0787853		1092.000	2013-03-12	12790	Postman
215.9497915	24.0786826	ACS/F606W	1088.000	2013-01-13	12790	Postman
215.9495000	24.0784722		1032.000	2013-02-05	12790	Postman
215.9495000	24.0784722	ACS/F775W	1032.000	2013-01-13	12790	Postman
215.9495000	24.0784722		1032.000	2013-01-19	12790	Postman
215.9494984	24.0785257	ACS/F850LP	1065.000	2012-12-31	12790	Postman
215.9494702	24.0785183		1103.000	2013-01-19	12790	Postman
215.9495000	24.0784722		1032.000	2013-02-03	12790	Postman
215.9495000	24.0784722		1032.000	2013-03-12	12790	Postman
215.9497638	24.0784634	WFC3/F105W	1305.869	2013-01-22	12790	Postman
215.9495000	24.0784722		1508.802	2013-02-05	12790	Postman
215.9495000	24.0784722	WFC3/F110W	1005.802	2013-01-19	12790	Postman
215.9494572	24.0783802		1005.868	2013-03-12	12790	Postman
215.9494138	24.0784107	WFC3/F125W	1005.868	2012-12-31	12790	Postman
215.9495000	24.0784722		1508.802	2013-01-01	12790	Postman
215.9495000	24.0784722	WFC3/F140W	1305.869	2013-01-22	12790	Postman
215.9494572	24.0783802		1005.868	2013-02-05	12790	Postman
215.9495377	24.0786077	WFC3/F160W	1005.868	2012-12-31	12790	Postman
215.9497638	24.0784634		1005.868	2013-01-19	12790	Postman
215.9495000	24.0784722		1508.802	2013-02-03	12790	Postman
215.9495000	24.0784722		1508.802	2013-03-12	12790	Postman

data in various pass-bands are seeing-matched using the technique described in Kartaltepe et al. (2008). SExtractor was used in dual image mode to create the object catalogue with R-band image as the reference detection image. An adaptive SED fitting code Le Phare (Arnouts et al., 1999; Ilbert et al., 2006, 2009) was used to determine the photometric redshifts for galaxies with $m_{\mathrm{R_c}} < 24.0$. To reduce the fraction of catastrophic errors and to mitigate the systematic trends in the difference between spectroscopic and photometric redshifts, Le Phare adjusts the photometric zero points by using galaxies with spectroscopic redshifts as training points. More details are given in Ma et al. (2008).

5.1.3.2 W.M. Keck Observatory

L10 observations were taken with the LRIS (Oke et al., 1995, Prog.ID: H26aL, PI:Henry) and the DEIMOS (Cowley et al., 1997) on the 10 m Keck Telescope on Mauna Kea. LRIS observations provided spectroscopic redshifts for 3 multiple image systems in the cluster. The reduction of these data is described in detail in Kelson et al. (2002). Redshifts of the galaxies in the cluster field were obtained from LRIS and DEIMOS and published by L10. Cluster members were defined as galaxies with redshifts within ± 0.05 of the cluster redshift, $z_{cluster} = 0.545$.

5.1.3.3 The Very Large Telescope

Panoramic, integral-field spectroscopic coverage of MACS J1423 was obtained with MUSE (Bacon et al., 2010) at the VLT, as part of the Kaleidoscope survey. Observations were taken on 2019 March 17 during grey time, under clear sky conditions, with an average seeing of 0.57″and three 970 s exposures, spanning the wavelength range 4800-9300$\mathring{A}$. To reduce systematic effects of bad pixels and variable detector sensitivity, a small dither (0.5″) was applied between exposure. Each exposure was also rotated by 90 degrees from the previous one. However, to maximize integrated depth, the centres of each exposure were coincident - save for the small dither off-

set. Thus, the total exposure time over most of the field of view ($1\times1'^2$) is 2910 s. Specific details of these observations are given in Table 5.2.

The data reduction and spectroscopic extraction were performed by our team following the method presented in Lagattuta et al. (2022), which is briefly summarise here. The reduction occurs in two part. First, we follow the procedure described in the public MUSE Data Reduction Pipeline User Manual*. Namely, we apply bias and flat-field correction, wavelength calibration, line-spread function (LSF) modelling, and sky-subtraction to 2-dimensional "pixel table" configurations of each exposure, using nightly calibration files that accompany the raw science frames. During this step, we also calibrate the flux levels of the data and correct for telluric absorption using a standard star observed immediately after the science frames. Following these corrections, we interpolate the pixels of each exposure onto a regular grid, combine all exposures together, and restructure the data into a cube. After the initial reduction phase, we apply two additional reduction calibrations to the combined cube directly. We model and correct low-level flat-field residuals caused by intra-cluster light (known as "auto-calibration", see e.g. section 2.5 in Richard et al. 2021). Additionally, we apply the Zurich Atmospheric Purge algorithm (ZAP; Soto et al. 2016) to remove any significant sky-line residuals that remain following sky subtraction.

After reducing the cube, we select targets for spectroscopic extraction using two distinct but complementary techniques. In the first method we identify objects in the *HST* images that fall in the MUSE Field of View (FoV). We measure the position and shape of these objects using SExtractor, then convolve the shapes with the MUSE PSF to better match their size in the data cube. The second method also relies on SExtractor, but this time it is run on the cube directly, to identify prominent emission-line objects that may not have significant stellar continuum. The two samples are cross-matched to remove any duplicate detections and extract a spectrum for all remaining targets using the optimally-weighted Horne (1986)

*https://www.eso.org/sci/software/pipelines/muse/

Table 5.2: Summary of the VLT/MUSE observations of MACS J1423 taken as part of the Kaleidoscope Survey. Columns 1 and 2 give the right ascension and declination of the observed field in degrees (J2000). Column 3 gives the redshift of the cluster. Column 4 lists the ESO Programme ID. Column 5 and 6 list the exposure time in seconds and observing date respectively. Column 6 gives the average seeing at the time of observation. The programme ID and PI name are given in column 7 and 8 respectively.

RA (J2000)	DEC (J2000)	z	Exp. Time (s)	Obs. Date	Seeing(")	ESO Programme	PI
215.949458	24.078472	0.5432	2910	2019-03-18	0.57	0102.A-0718(A)	Edge

procedure. Following extraction we run each spectrum through the redshift-fitting software MARZ (Hinton et al., 2016), which provides an initial redshift guess for each object. We then visually inspect the results, accepting or modifying the best-fit MARZ redshift as needed.

The final redshift catalogue for MACS J1423 contains 66 entries, consisting of two stars, three foreground galaxies ($z < z_{\rm cluster}$), 39 cluster members and 16 background galaxies ($z > z_{\rm cluster}$). A list of cluster member galaxies is given in Table 5.3, while multiple-image systems are summarised in Table 5.4. We note that these results highlight MUSE's remarkable efficiency as a spectroscopic detector in crowded (i.e., cluster-core) fields, allowing us to cleanly measure the redshifts of not only multiply-imaged galaxies, but also intervening objects along the line-of-sight.

5.2 Strong Lensing Analysis

5.2.1 Multiple image systems

5.2.1.1 Previous Work

Prior to this analysis, three multiple image systems were reported in L10, and another one in Zitrin et al. (2015, hereafter, Z15). These systems are listed in Table 5.4 as Systems 1- 4. For L10, systems 1 and 2 belong to a single background galaxy, resolved in two components with multiple images organised in an Einstein-cross configuration. A central fifth image is also predicted at the position of the

Table 5.3: Cluster members spectroscopically confirmed by VLT/MUSE observations in MACS J1423. Columns 1 and 2 give the right ascension and declination in degrees (J2000). Column 3 gives their respective measured spectroscopic redshift with VLT/MUSE.

RA (J2000)	DEC (J2000)	z
215.9494838	24.0784459	0.545 (BCG)
215.9523294	24.0707291	0.539
215.9427198	24.0727851	0.537
215.9539395	24.0714300	0.539
215.9586154	24.0710327	0.533
215.9477283	24.0727531	0.546
215.9525992	24.0742691	0.541
215.9517541	24.0741379	0.554
215.9489410	24.0763359	0.537
215.9462858	24.0754164	0.562
215.9474872	24.0761680	0.547
215.9493174	24.0769683	0.555
215.9493511	24.0767400	0.560
215.9448420	24.0770788	0.545
215.9497831	24.0779724	0.523
215.9496876	24.0773563	0.548
215.9484518	24.0770044	0.517
215.9453596	24.0784154	0.546
215.9565067	24.0779951	0.530
215.9516898	24.0782917	0.537
215.9581679	24.0787077	0.552
215.9584832	24.0793582	0.535
215.9448590	24.0785557	0.533
215.9462005	24.0795718	0.531
215.9433649	24.0802384	0.543
215.9510899	24.0808902	0.532
215.9582277	24.0812035	0.552
215.9507082	24.0813282	0.551
215.9403157	24.0823716	0.560
215.9502609	24.0842187	0.550
215.9462506	24.0848389	0.546
215.9472276	24.0841258	0.549
215.9537427	24.0845512	0.554
215.9494303	24.0852384	0.552
215.9451689	24.0847458	0.545
215.9474839	24.0856535	0.546
215.9499363	24.0865008	0.542
215.9488118	24.0860833	0.563
215.9532771	24.0868116	0.540

Table 5.4: Multiple image systems used as constraints in our strong lensing analysis of MACS J1423. Column 1 lists the ID of the multiple images. Columns 2 and 3 give the right ascension and declination in degrees (J2000). Column 4 gives the redshift of each system. Redshifts without error bars correspond to spectroscopic measurements while the presence of error bars highlight the redshifts optimised by our mass model. While spectroscopic redshifts were already measured with LRIS and DEIMOS by L10, the systems with confirmed spectroscopic redshifts with MUSE are highlighted with an $*$. Column 5 gives the magnification estimated from our strong lensing mass model for each multiple images.

ID	RA (deg)	DEC (deg)	z	μ
1.1	215.9577155	24.0746537	2.84	3.49 ± 0.52
1.2	215.9494609	24.0818270	2.84	7.08 ± 1.45
1.3	215.9444674	24.0806542	2.84	9.25 ± 2.04
1.4	215.9459355	24.0763898	2.84	10.89 ± 1.79
1.5	215.9497029	24.0791219	2.84	0.99 ± 0.36
2.1	215.9576456	24.0745519	2.84	3.50 ± 0.52
2.2	215.9495433	24.0817288	2.84	7.15 ± 1.49
2.3	215.9443426	24.0803974	2.84	10.97 ± 2.39
2.4	215.9458112	24.0763495	2.84	11.87 ± 1.96
3.1*	215.9465404	24.0836281	1.779	8.82 ± 1.53
3.2*	215.9523020	24.0831945	1.779	16.74 ± 3.82
3.3*	215.9551508	24.0811756	1.779	13.71 ± 2.45
4.1	215.9481287	24.0771353	1.797 ± 0.062	5.07 ± 1.09
4.2	215.9558429	24.0771761	1.797 ± 0.062	4.15 ± 0.52
4.3	215.9502463	24.0821356	1.797 ± 0.062	11.79 ± 3.18
4.4	215.9459358	24.0817256	1.797 ± 0.062	5.57 ± 0.73
4.5	215.9490200	24.0780830	1.797 ± 0.062	1.48 ± 0.38

brightest cluster galaxy (BCG) located at the very centre of MACS J1423. Due to its large halo of stars, and the fact that central images are usually de-magnified, multiple images located in this region are generally very difficult, if not impossible, to detect. On the other hand, system 3 is seen in a naked-cusp configuration, with three images on the same side of the cluster. Another multiple image system, found by Z15, is composed of five images, and includes a radial arc. System 1 and 2 in L10 are taken as a single system in Z15 without the central radial arc (image 1.5 in L10). All systems can be seen in Fig. 5.1.

5.2.1.2 This work

The four systems discussed in the previous subsection are used. Identifications from the two analyses of L10 and Z15 are combined (see Table 5.4 and Fig. 5.1), and thus use the 4 systems discussed in Sect. 5.2.1.1.

In contrast to L10, the fourth system of Z15 is added, system 4 in Table 5.4, while systems 1, 2 and 3 are considered in the same manner in L10. Adding to that, systems 1 and 2 correspond to the same multiply imaged galaxy, but for which L10 identified 2 components, thus it is split it in two sets of constraints. Then the central radial arc of system 1 is used as done by L10.

To summarise, four multiple image systems are used: system 1 with five multiple images, including the central radial arc (image 1.5), system 2 with four multiple images, system 3 with three multiple images, and system 4 with 5 multiple images, including another central radial arc. System 1, 2 and 3 are all spectroscopically confirmed. However, the MUSE observations are not of enough quality for us to measure a spectroscopic redshift with high confidence for system 4. A low confidence measurement of $z = 1.878$ is obtained which is discussed in more detail in Sect. 5.2.3, however the redshift of this system is let free to vary in our mass model.

5.2.2 Cluster Members

5.2.2.1 Previous Work

L10 obtained spectroscopic redshift measurements with LRIS and DEIMOS as described in Sect. 5.1. These observations provided spectroscopic confirmation of multiple image systems, together with spectroscopy of cluster galaxies within the field of MACS J1423, and allowed them to build a cluster member catalogue. Galaxies with redshifts within $\pm\,0.05$ of the cluster redshift, $z_{cluster} = 0.545$, were considered

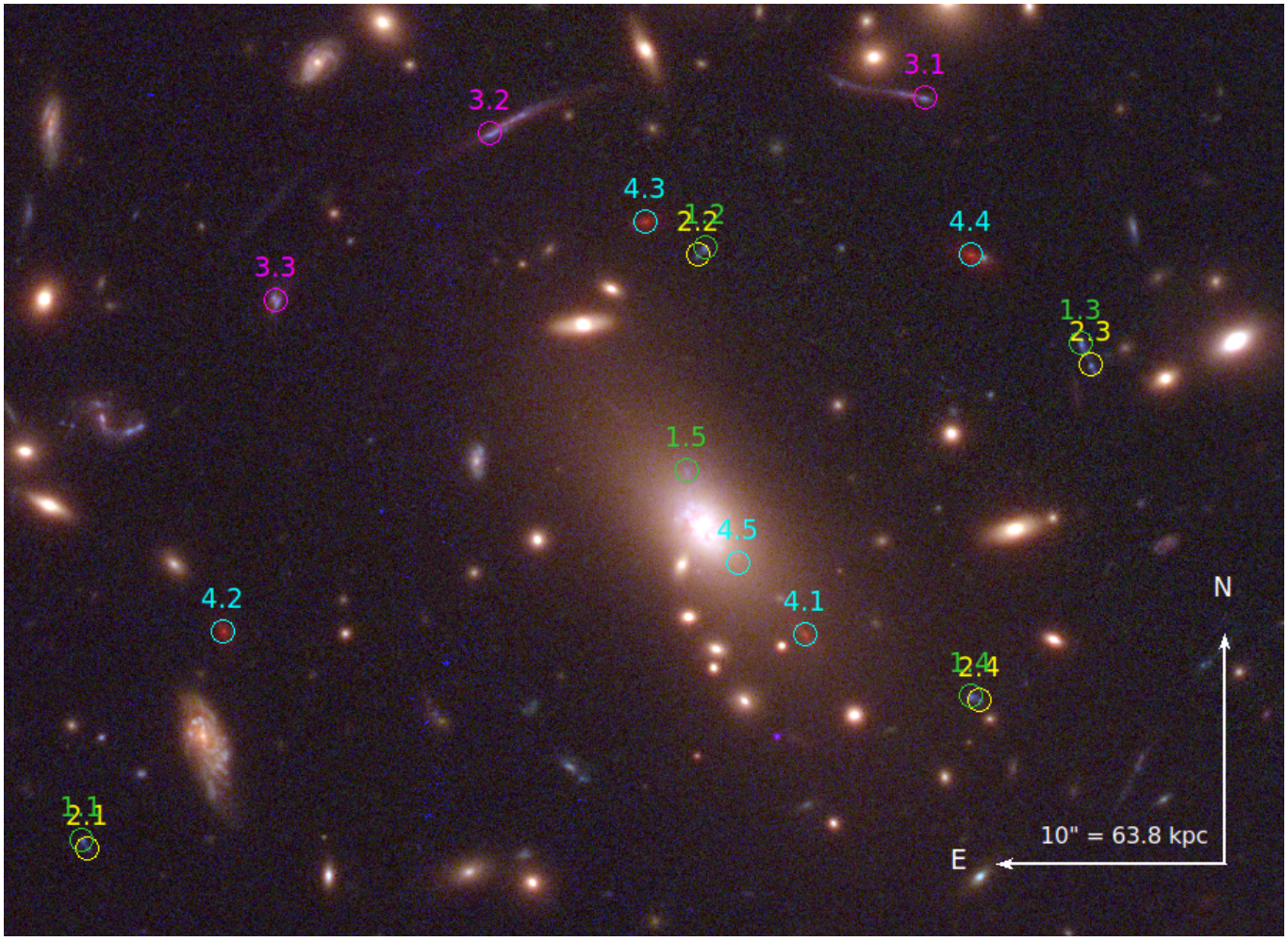

Figure 5.1: *HST* colour composite image of the central region of MACS J1423 created using the F606W for blue, F814W for green and F160W for red colours. Multiple image systems are highlighted with coloured circles and ID following the list given in Table 5.4. The five multiple images of system 1 are shown in green, the four multiple images of system 2 in yellow, the three multiple images of system 3 in magenta, and the five multiple images of system 4 in cyan.

cluster members. The final cluster member catalogue was composed of 30 galaxies, including the BCG.

5.2.2.2 This work

SExtractor is used in dual mode to extract the F606W and F814W photometry for cluster galaxies. The sequence of stars is identified using the surface brightness and magnitude of the detected sources (the MAG_AUTO vs MU_MAX diagram) as shown in Fig. 5.2, and then removed from the catalogue. A colour-magnitude diagram is then created to identify the red sequence itself as shown in Fig. 5.3. Sources considered as bad detections (with a quoted magnitude of 99 from SExtractor) are removed along with sources at the edges of the *HST*/ACS field of view. A 2σ clipping fit is used to fit the red sequence. Cluster members in the inner region of the cluster (R<260 kpc) are confirmed using spectroscopic redshifts measured with our VLT/MUSE observations (see Sect. 5.1.3.3). Our final cluster member catalogue contains 66 galaxies, out of which 39 are spectroscopically confirmed, including the Brightest Cluster Galaxy (BCG).

5.2.3 Parametric mass modelling

In the core of the cluster, dominated by strong lensing, parametric mass modelling is used for the mass reconstruction with Lenstool . There is one cluster-scale halo in our model, for which all parameters are let free to vary except for the cut radius, which generally lies outside the strong lensing region making it difficult to be constrained by our model and is thus fixed to $r_{\rm cut} = 1000$ kpc. For the small-scale halos, there are 65 cluster members, modelled using scaling relations with $mag_0 = 20.05$ at the MACS 1423 cluster redshift in the ACS/F814W passband. Their positions are fixed to that of cluster galaxies, along with their position angle and ellipticity. However, core radii are fixed to a very small value of $r^{\star}_{core} = 0.15$ kpc, while cut radii and velocity dispersions are let free to vary with $5 < r^{\star}_{\rm cut} < 50$ kpc and $100 <$

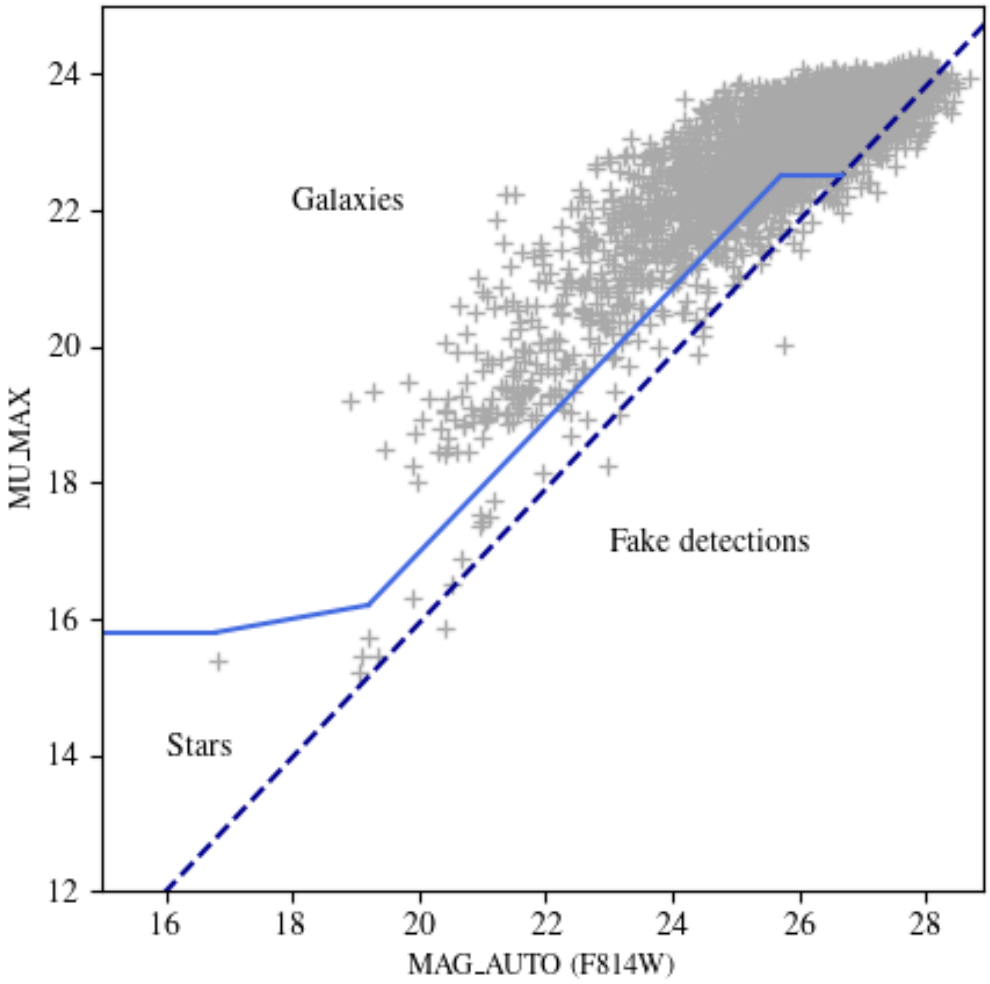

Figure 5.2: Magnitude (MAG_AUTO) vs surface brightness (MU_MAX) diagram for MACS J1423 in the F814W pass-band. Such a diagram allows us to disentangle stars and fake detections from galaxies. The blue polygon highlights the sequence of stars and the limit for fake detections. The grey markers within the polygon are the star sequence and the ones outside are objects identified as galaxies in the cluster.

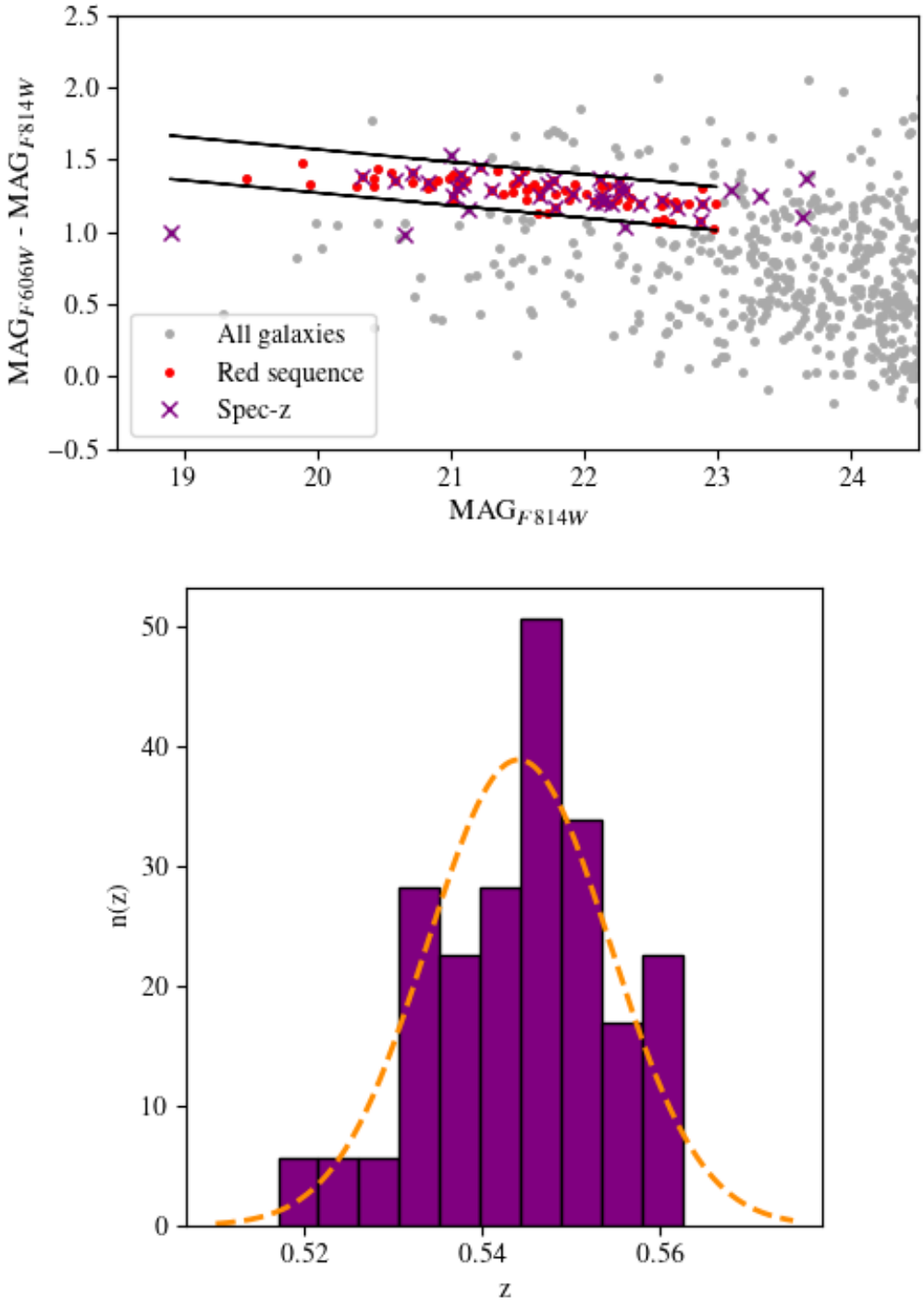

Figure 5.3: Top: Colour (mag_{F606W} - mag_{F814W}) vs magnitude (m_{F814W}) diagram for MACS J1423. All sources from the source extraction done in this work are shown in grey, and the red sequence galaxies are highlighted in red marked within the black lines. The cluster members with spectroscopic redshifts are marked by purple cross. All galaxies within the $2\,\sigma$ of the linear fit are considered as cluster members. Bottom : Histogram of the redshift of spectroscopically confirmed cluster members within MUSE data. The best Gaussian fit is overlaid in orange dashed line.

Table 5.5: Best fit parameters for our strong lensing mass model of the core of MACS J1423. Values given in brackets are fixed in our model, while the ones quoted with error bars are being optimised. The coordinates of the cluster and BCG halos are given in arcseconds relative to the cluster center (R.A., Dec)=(215.94944 24.078499). The log-likelihood ($\ln(\mathcal{L})$), χ^2, χ^2_ν and rms are given in the bottom of the table.

Components	ΔR.A.($''$)	ΔDec ($''$)	e	θ(deg)	$r_{\rm core}$ (kpc)	$r_{\rm cut}$ (kpc)	σ_0 (km s^{-1})
Cluster Halo	-1.2 $\pm$ 0.6	-0.5 $\pm$ 1.1	0.4 $\pm$ 0.04	117 $\pm$ 1	137 $\pm$ 23	[1000]	1186 $\pm$ 57
BCG	[-0.07]	[-0.22]	[0.62]	[310]	[0.15]	49 $\pm$ 40	442 $\pm$ 30
L* Galaxy	-	-	-	-	[0.15]	22 $\pm$ 11	211 $\pm$ 30
$\ln(\mathcal{L})$ = -36.17	χ^2 = 17.03	χ^2_ν = 1.13	rms = 0.90$''$				

$\sigma_0^\star < 250$ km s^{-1} respectively. The BCG in the cluster is modelled separately from the rest of cluster members, since extremely luminous central cluster galaxies often not follow the scaling relations given in equation 3.19 (Newman et al., 2013b,a).

The free parameters of the different potentials are optimised, using the positions of strongly lensed multiple images as constraints. The goodness of our model to meet the observational constraints is measured with rms and χ^2. For the model described, consisting of one large scale halo and 66 small-scale halos, constrained by the 17 multiple images discussed in Sect. 5.2.1, for the best-fit mass model, an rms of 0.90$''$is obtained, and a reduced χ^2_ν of 1.13. The model predicts a redshift of $z = (1.79 \pm 0.06)$ for system 4, which agrees well with the tentative spectroscopic redshift derived from the VLT/MUSE observations ($z = 1.878$, see Sect. 5.1.3.3). The best-fit parameters of our strong lensing mass model are listed in Table 5.5. The mass contours for this strong-lensing only model is shown in yellow in Figure 5.4. The corresponding surface mass density of MACS J1423 as a function of distance from the cluster center is shown in Fig. 5.7 in magenta. A projected mass enclosed in the strong lensing region of $M(R < 200\,\mathrm{kpc}) = (1.83 \pm 0.04) \times 10^{14}\,\mathrm{M}_\odot$ is measured.

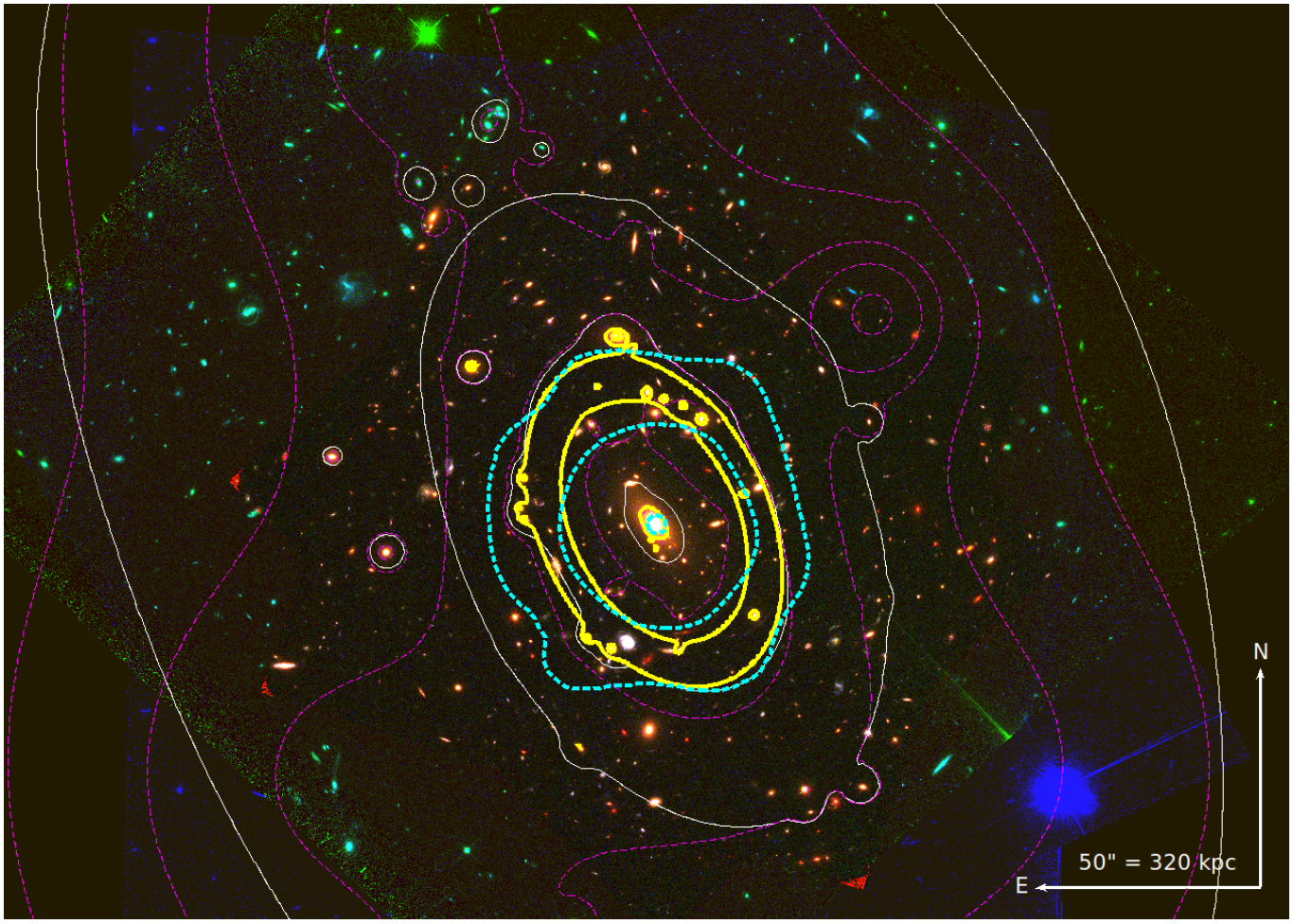

Figure 5.4: *HST* colour composite image of the central region of MACS J1423 created using the F606W for blue, F814W for green and F160W for red colours. The thick solid yellow and thin dashed magenta contours show the mass distribution obtained with our strong-lensing and weak-lensing mass reconstruction as described in Sect. 5.2.3 and Sect. 5.3.2 respectively. The mass contours obtained with our combined mass model, as presented in Sect. 5.4, are shown with thin solid white contours. The thick dashed cyan contours represent the X-ray surface brightness from the *Chandra* observations.

5.3 Weak Lensing Analysis

5.3.1 Weak lensing catalogue

The source detection, photometry and shape measurements are performed with the stacked images in the F606W, F814W, and F160W pass-bands to get the weak lensing catalogue for MACS J1423. The process described in Section 3.1.2 is followed. First, to detect sources and measure their shapes, PYRRG is used with the *HST*/ACS F814W filter (Harvey et al., 2019). The galaxy catalogue from PYRRG is still contaminated by foreground and faint cluster galaxies. A colour-colour selection is performed, place in the ($\mathrm{mag_{F435W}}$ - $\mathrm{mag_{F814W}}$) *vs* ($\mathrm{mag_{F435W}}$ - $\mathrm{mag_{F606W}}$) colour-colour parameter space. As a final step, to remove galaxies with ill-determined shape parameters. The final weak lensing catalogue contains 723 background galaxies, corresponding to a density of ~ 57 galaxies arcmin^{-2}, compared to other massive clusters such as ~ 100 arcmin^{-2} from Jauzac et al. (2015a), ~ 42 arcmin^{-2} from Niemiec et al. (2023) in the deep *Hubble Frontier Fields*, and ~ 13 arcmin^{-2} from Umetsu et al. (2012) in the Subaru sample.

5.3.2 Grid mass modelling

In the outskirts of the cluster, the non-paramteric grid is used to perform weak lensing analysis as described in Section 3.3. The grid is constructed using the smoothed light map of the cluster which is made using publicly available scripts [*]. After testing different grid resolutions, grid composed of 628 RBFs is found to be optimal. Core radii, s, are ranging from 5″ and 40″. The resulting grid is shown in Fig. 5.5 on the smoothed cluster light map. Each circle on the light map represents one RBF potential, and the densest region corresponds to $s = 5''$. Our grid-only model, covering the full ACS field (100″or 640kpc), uses only background galaxies as constraints. The surface mass density for the corresponding

[*] https://github.com/AnnaNiemiec/grid_lenstool

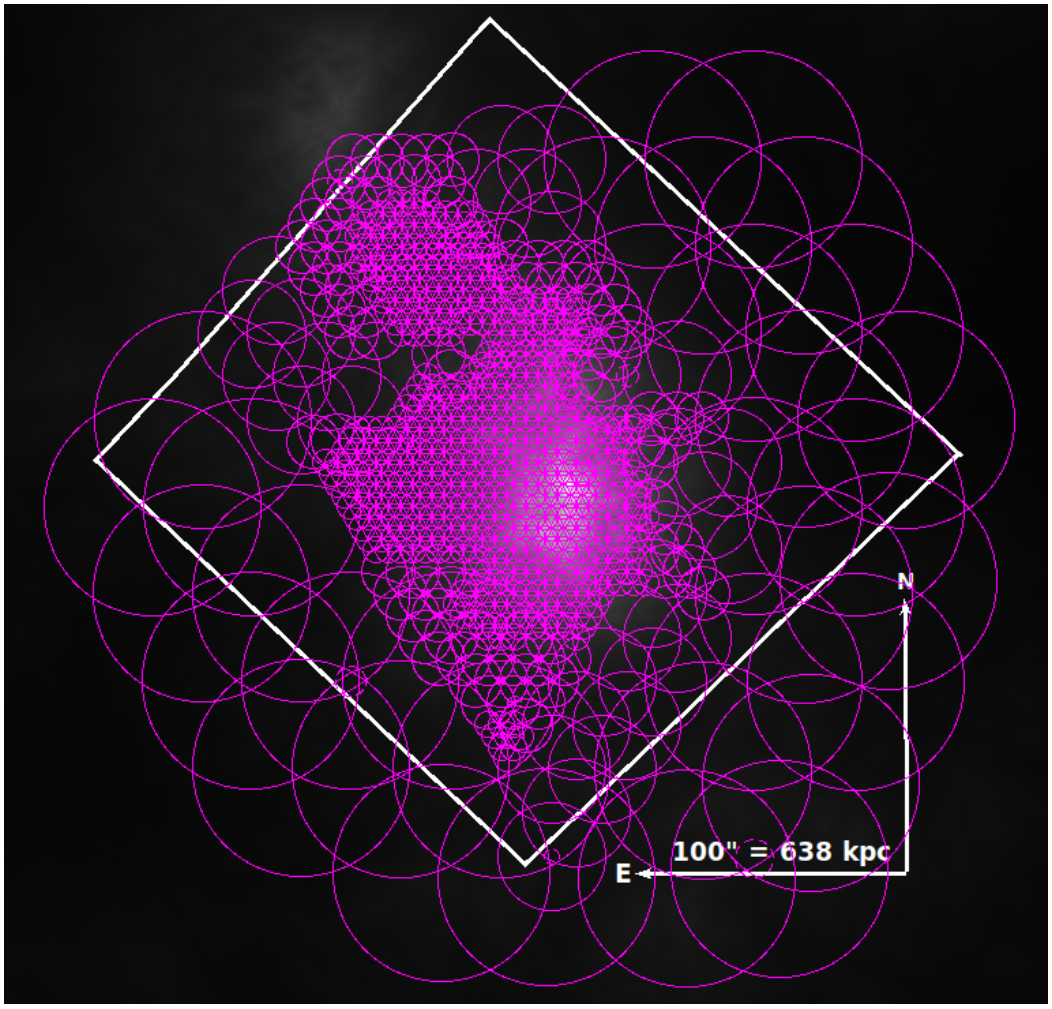

Figure 5.5: Smooth light map of MACS J1423. The non-parametric grid of potentials used for our weak-lensing analysis is highlighted with magenta circles. The grid is multi-scale, i.e. with a finer resolution in the densest regions of the cluster. The grid is composed of 162 RBFs, the densest regions modelled by RBFs with a core radius of 10.6″. The ACS field of view is shown by the white box.

model is shown in Fig. 5.7. The projected surface mass within the full ACS field is $M(R < 640\,\mathrm{kpc}) = (2.1 \pm 0.8) \times 10^{14}\,\mathrm{M}_{\odot}$.

5.4 Combining Strong and Weak Lensing

In order to obtain a full mass reconstruction of MACS J1423, we need to combine our parametric strong-lensing mass model with the non-parametric weak-lensing one. For that, the sequential fit method is followed. First, the core is modelled

using the strong lensing constraints as described in Sect. 5.2. To the best-fit parametric model of the core, the multi-scale grid of potentials described in Sect. 5.3.2 is added in the outskirts of the cluster. The parametric model presented in Sect. 5.2.3 is fixed at its best-fit values. As shown in Fig. 5.7, the error on the parametric model in the cluster core is much smaller than the error on the grid model. Consequently, fixing this component to the best-fit should not have a significant impact on the overall error propagation and model fitting process. The RBF amplitudes are then estimated from the weak lensing constraints. This also ensures that strong lensing constraints are not taken into account twice. Already optimised cluster-scale dark matter halo and cluster member galaxies are combined with the RBF grid potentials. As explained in Sect. 5.3.2, grid potentials are removed from the cluster core due to the absence of weak lensing constraints in this region. A zoom-in combined parametric and non-parametric potentials is shown in Fig. 5.6. The projected surface mass density resulting from our combined strong and weak lensing mass model of MACS J1423 is shown in Fig. 5.7. The contribution of the strong and weak lensing optimisation is decomposed. A (combined strong and weak lensing) projected mass over the full *HST*/ACS field of view ($R < 100''$) of $M(R < 640\,\mathrm{kpc}) = (6.6 \pm 0.6) \times 10^{14}\,\mathrm{M}_{\odot}$ is measured.

5.5 Discussion & Conclusion

5.5.1 Comparison between different models

There are three main models presented in this analysis : the parametric model for the cluster inner core, the non-parametric grid model for the outskirts and the combined model accommodating both strong and weak lensing regions. Mass contours corresponding to all these three models are shown in Fig. 5.4. In addition to these contours, the smoothed X-ray surface brightness contours are also shown. A general trend in the elongation of the system is seen for all models even if some deviations can be seen in mass contours from the grid-only model as compared to

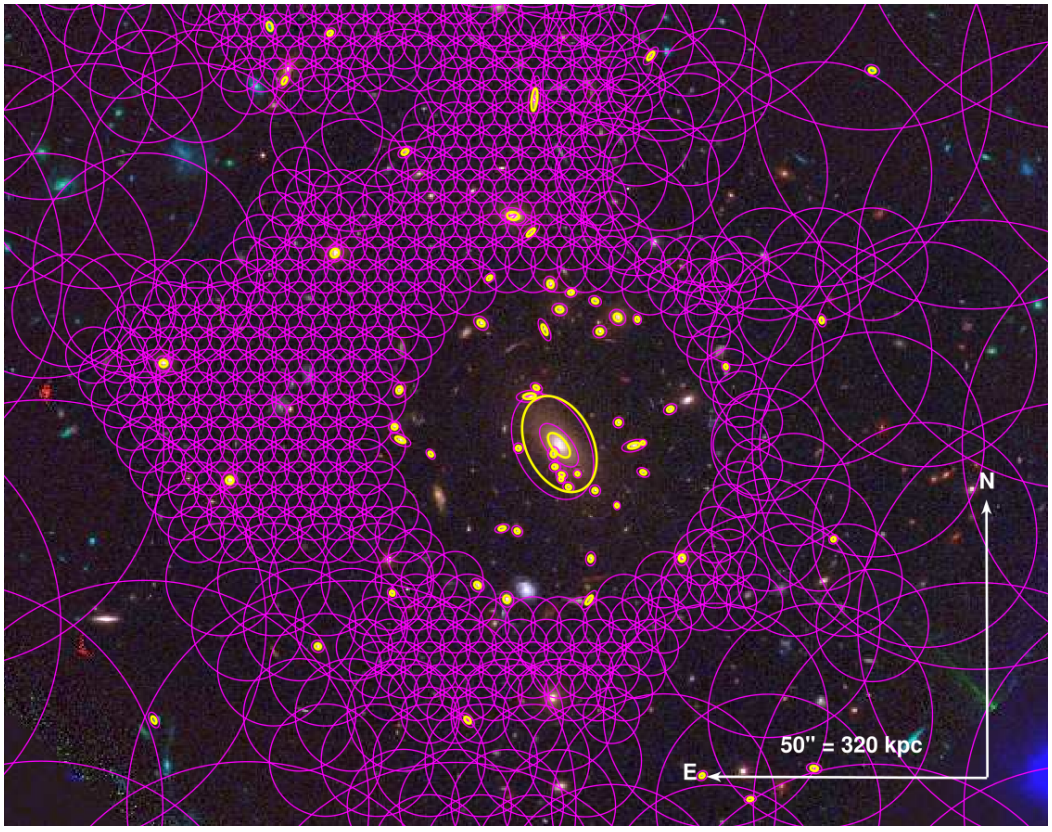

Figure 5.6: A zoom-in colour composite image on the core of MACS J1423 to highlight the combined strong and weak lensing analysis pursued in this work. The strong lensing mass components, fixed to the best fit parametric mass model, are shown in yellow, and the non-parametric grid potentials are shown in magenta.

the parametric and combined models. Figure 5.7 shows the 2-D surface density profile for our three models. As seen in Fig. 5.7, the amplitude of the grid-only model is low compared to the parametric and combined model throughout the cluster region. In the core of the cluster, this is assignable to the absence of strong lensing constraints and the contribution from any cluster-scale halo. However for the outer regions, either the grid-only model is underestimating the mass or there is an overestimation from the parametric model. A plausible explanation to the later can be that outer regions of the cluster are affected by the elongation of the cluster-scale halo (with $r_{\rm cut} = 1000\,{\rm kpc}$). To inspect this, a parametric model was ran including weak lensing constraints in the outskirts along with strong lensing constraints in the core. The presence of constraints (weak lensing) in the outer regions of the cluster can be used to constrain $r_{\rm cut}$ of the cluster-scale halo. The

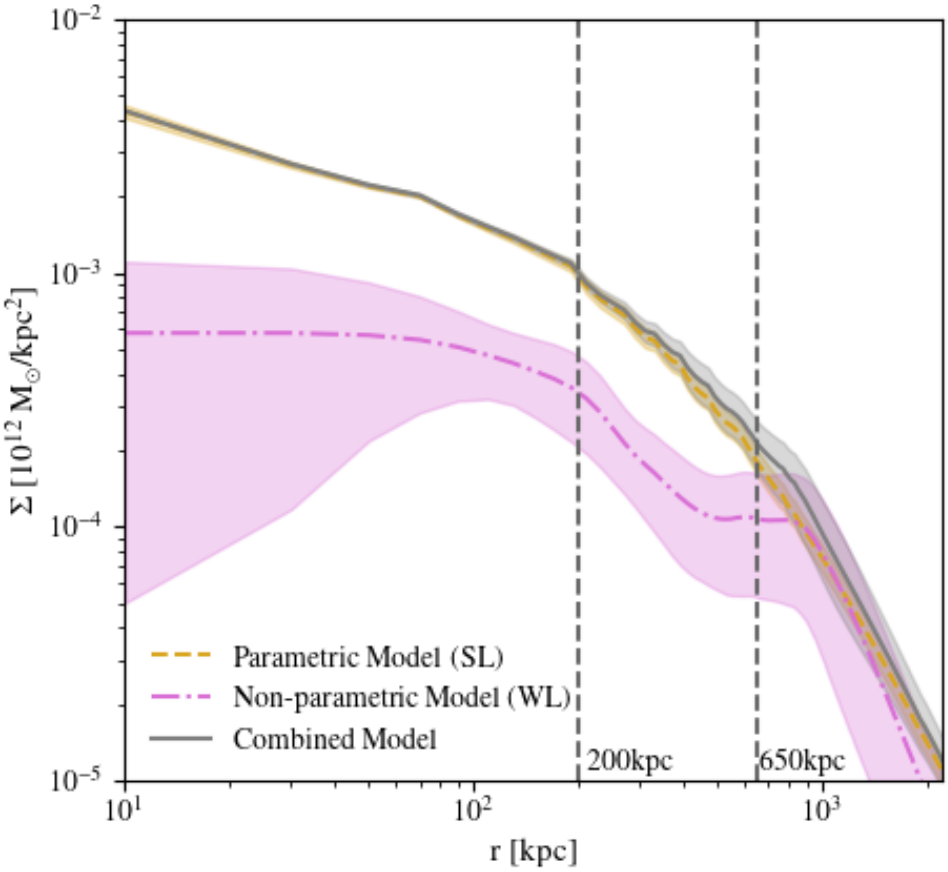

Figure 5.7: The surface mass density profiles of MACS J1423. The only strong lensing (sec 5.2) and weak lensing (sec 5.3) analysis are represented in yellow and magenta colour respectively. The profile in grey colour shows the combined model. The two vertical dark grey dashed lines represents the end of strong lensing and weak lensing regions respectively from left to right.

difference in the surface density was not resolved even after constraining the cluster-scale $r_{\rm cut}$. Similar problems are also seen in Niemiec et al. (2023) with a much more complicated cluster using same techniques as described in this work. The reason for this difference in the amplitude between the grid-only and combined model in the outskirts needs to be investigated.

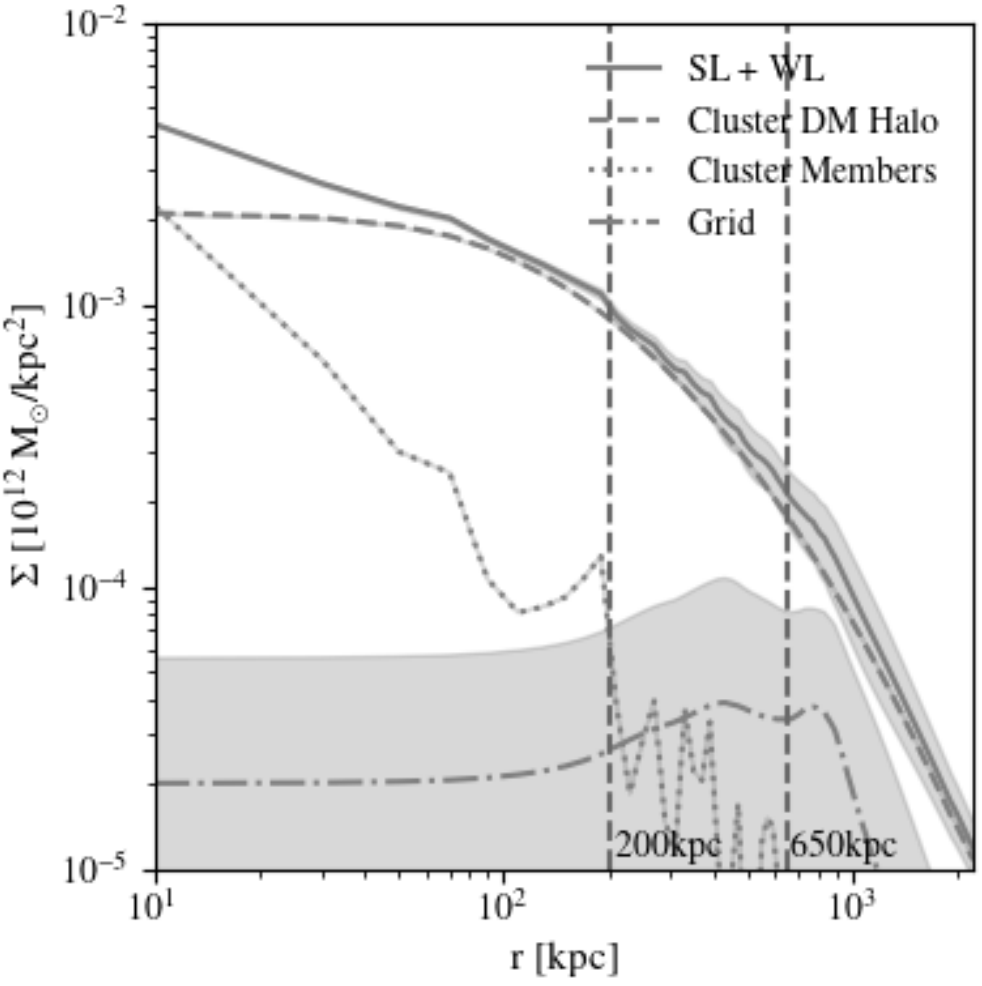

Figure 5.8: The surface mass density profiles of MACS J1423. The full combined strong and weak lensing model is represented by the solid line. The different components of this model i.e. cluster-scale halo, cluster members and the grid potentials are shown with dashed, dotted and dashed-dotted lines respectively. The two vertical dark grey dashed lines represents the end of the strong and weak lensing regions respectively from left to right.

Table 5.6: A summary table to compare the mass of MACS J1423 with previous works. The masses measured within 130 kpc, 200 kpc, 415 kpc and 640 kpc using different methods are quoted in units of $10^{14}\,M_{\odot}$. The other works in the table corresponds to : LaRoque et al. (2003, LR03) and Schmidt and Allen (2007, SA07), Zitrin et al. (2011, Z11), Limousin et al. (2010, L10). The WL only model is not included in the inner regions of the cluster i.e. for $R < 130$ kpc and $R < 200$ kpc due to lack of WL constraints in these regions. Similarly, the SL only model is not included in outer regions of the cluster i.e. for $R < 415$ kpc and $R < 640$ kpc due to lack of SL constraints in these regions.

	Method	LR03	SA07	L10	Z11	This work
$R < 130$ kpc	SL only	-	-	-	1.3 ± 0.4	0.96 ± 0.01
	SL + WL	-	-	..	-	0.97 ± 0.02
$R < 200$ kpc	SL only	-	-	..	-	1.82 ± 0.05
	SL + WL	-	-	..	-	1.85 ± 0.05
$R < 415$ kpc	SZ	$5.0^{+3.1}_{-0.9}$	-	-	-	-
	X-rays	-	$3.1^{+0.9}_{-0.7}$	-	-	-
	WL only	-	-	-	-	1.3 ± 0.4
	SL + WL only	-	-	4.3 ± 0.6	-	4.4 ± 0.3
$R < 640$ kpc	WL only	-	-	-	-	2.1 ± 0.8
	SL + WL only	-	-	...	-	6.6 ± 0.6

5.5.2 Comparison with previous works

In L10, mass modelling is slightly different than in this work, even if both analyses uses LENSTOOL. While the BCG is optimised independently from the other cluster galaxies (which are assume to follow a scaling relation), L10 assumed the BCG follows the scaling relation presented in equation 3.19. They measure a projected mass within 65″(∼415 kpc) of $M_{\rm L10}(R < 415\,{\rm kpc}) = (4.3 \pm 0.6) \times 10^{14}\,M_{\odot}$ which is within the errorbars of our strong + weak lensing analysis, $M(R < 415\,{\rm kpc}) = (4.4 \pm 0.3) \times 10^{14}\,M_{\odot}$.

Z15 uses a different algorithm than in this work, LTM (Light-Traces-Mass), and its dPIE+NFW version of it. Z15 quotes a rms of 1.21″, and 1.47″ for LTM and dPIE+NFW respectively, slightly higher than the rms of 0.9″obtained with our strong-lensing analysis. Zitrin et al. (2011) measure a projected strong lensing mass enclosed within an effective Einstein radius of 20″ (∼130 kpc) of $M_{Z11}(R < 130\,{\rm kpc}) = (1.30\pm0.40)\times10^{14}\,M_{\odot}$. This is in good agreement with what is obtained

for our strong lensing model $M(R < 130\,\mathrm{kpc}) = (0.96 \pm 0.01) \times 10^{14}\,\mathrm{M}_{\odot}$.

The Sunyaev-Zel'dovich (SZ) effect analysis presented in LaRoque et al. (2003) quotes a mass of $M_{\mathrm{LR03}}(R < 415\,\mathrm{kpc}) = 5.0^{+3.1}_{-0.9} \times 10^{14}\,\mathrm{M}_{\odot}$. The *Chandra* X-ray analysis from Schmidt and Allen (2007) quotes a mass of $M_{\mathrm{SA07}}(R < 415\,\mathrm{kpc}) = 3.1^{+0.9}_{-0.7} \times 10^{14}\,\mathrm{M}_{\odot}$. The SZ measurement fall within the error bars of mass estimates obtained with this work. However, the mass estimate obtained from the X-ray analysis is lower than what is measured in this work. L10 discuss this discrepancy and provide a possible explanation to the line-of-sight elongation of MACS J1423. A summary of all masses compared to in this work is given in Table 5.6.

Recently, Mowla et al. (2024) discovered a $z = 8$ galaxy, calling it the Firefly Sparkle arc in MACS J1423 using *JWST* data. They measure magnification between 16-26, with the center of the arc being magnified by a factor of 24 using a strong lensing model. When compared to work presented in this chapter, a magnification of 6 is measured with our strong lensing only model and a magnification of 17 with our strong + weak lensing model. The reason for this difference may be the fact that our models do not include a faint galaxy located near this lensed arc, which may be giving a boost in the magnification locally. Figure 5.10 shows the firefly galaxy in white and this local galaxy in red.

5.5.3 The baryonic mass distribution

5.5.3.1 Gas and Stellar mass distribution

The procedure presented in Beauchesne et al. (2024) is followed to estimate the X-ray gas-density and gas-mass profiles for MACS 1423 using *Chandra* data (see section 4.1.3). The X-ray peak emission in the cluster is also measured using the publicly available code PYPROFFIT (Eckert et al., 2020). It was found that X-rays and lensing distributions are aligned, i.e. the X-rays peak at the center of the cluster i.e. position of the BCG. A gas mass $M_{\mathrm{gas}}(R < 200\,\mathrm{kpc}) = (0.16 \pm 0.0002) \times 10^{14}\,\mathrm{M}_{\odot}$ is measured. The gas mass is converted into gas fraction by taking the ratio

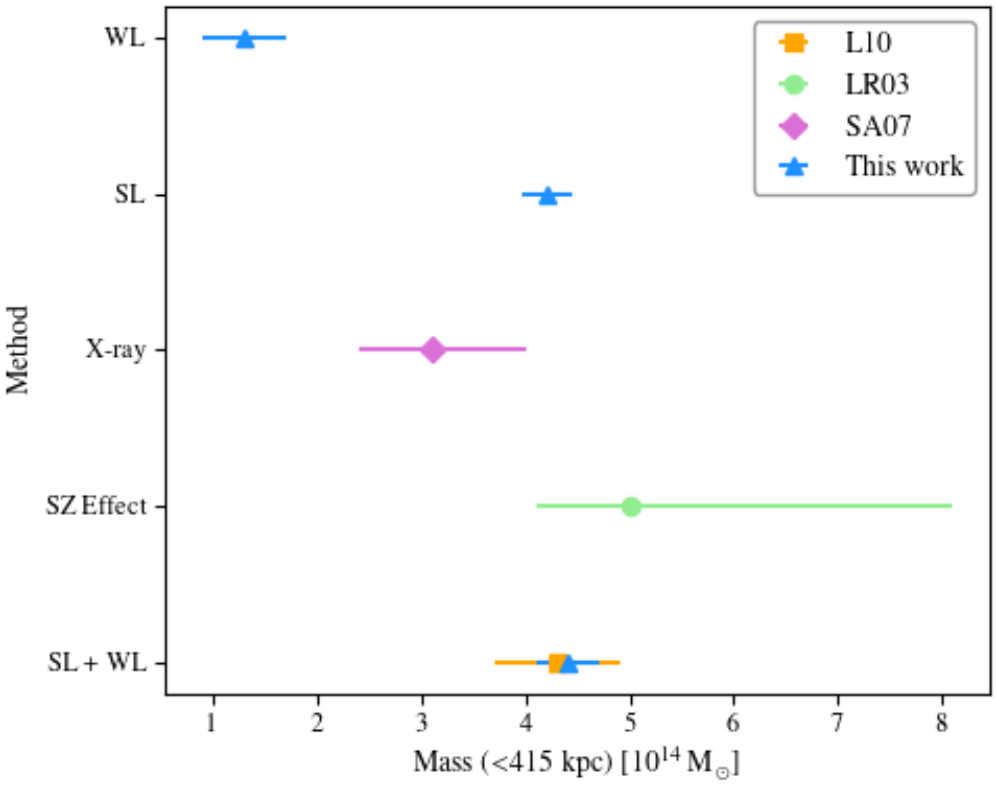

Figure 5.9: A visual representation of the different masses given in table 5.6. The methods used to estimate the enclosed mass within 415 kpc is shown from previous studies : Limousin et al. (2010, L10), LaRoque et al. (2003, LR03) and Schmidt and Allen (2007, SA07).

between the gas mass and the mass of the cluster with 200 kpc. A gas fraction of $f_{\rm gas}(R < 200\,{\rm kpc}) = 0.08 \pm 0.01$ is estimated.

To measure the stellar mass distribution, the procedure described in Jauzac et al. (2015a) was followed. A stellar masses of cluster galaxies using the relation $\log(M_\star/L_{\rm K}) = az + b$ was estimated, where z is the redshift of the cluster, here $z = 0.545$. The relation established by Arnouts et al. (2007) for quiescent (red) galaxies in the VVDS survey (Le Fèvre et al., 2005), adopting a Salpeter initial mass function (IMF), and $L_{\rm K}$ is the luminosity in K-band. The parameters a and b are given by:

$$a = -0.18 \pm 0.03,$$

$$b = -0.05 \pm 0.03.$$

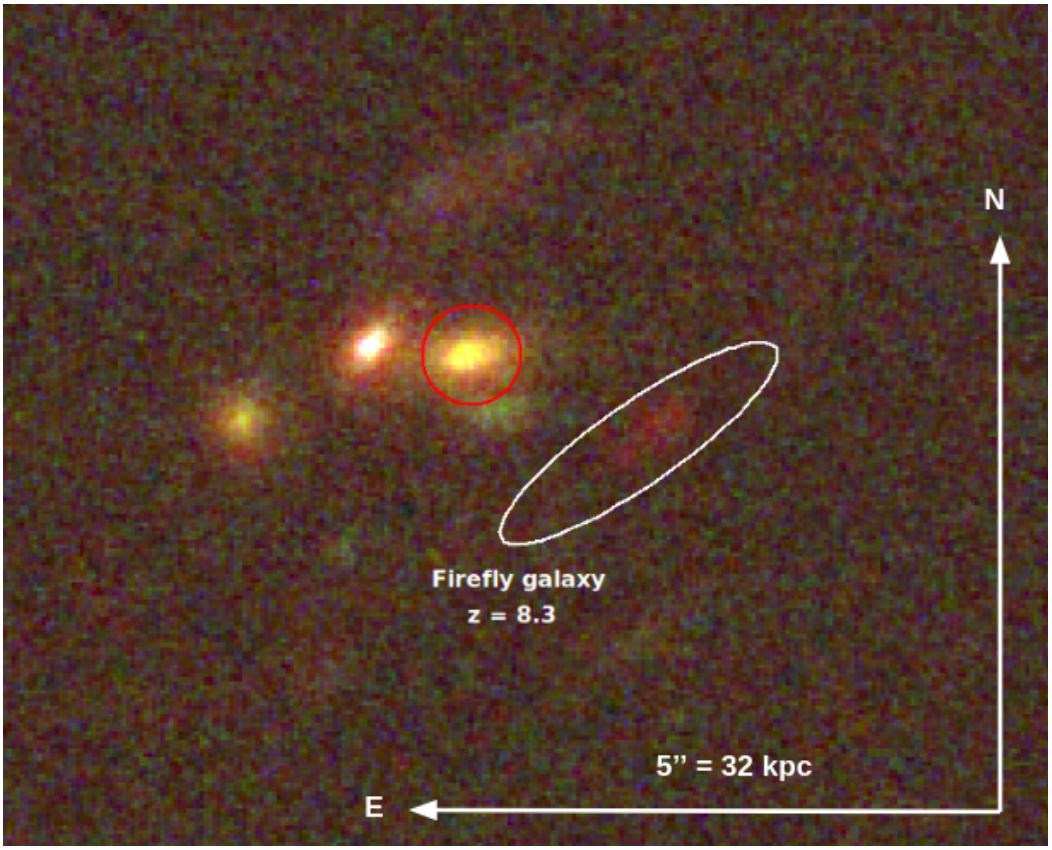

Figure 5.10: The firefly galaxy at $z = 8.3$ found by Mowla et al. (2024) is shown by the white ellipse. The galaxy highlighted in red may be giving a boost in the magnification locally. This *HST* image is created using the F606W for blue, F814W for green and F160W for red colours.

This relation is applied to our 66 cluster member galaxies. First, the K-band luminosity of our galaxies observed in F814W band is estimated using the theoretical models from Bruzual and Charlot (2003). Assuming a range of exponentially decaying star histories within the range τ = 0.1 - 2 Gyr, a typical colour $(m_{\rm F814W} - m_{\rm K}) = 1.5199$ (AB system) is estimated. A total stellar mass within the full ACS field of view, $M_\star(R < 640\,{\rm kpc}) = (5.7 \pm 0.5) \times 10^{12}\,{\rm M}_\odot$ and mass-to-light ratio of $M_\star/L_{\rm K} = 0.7 \pm 0.1\,{\rm M}_\odot/{\rm L}_\odot$ is measured. The fraction of total mass in stars, $f_\star$, is estimated by taking the ratio between the total stellar mass and the total mass of the cluster derived from our combined strong and weak lensing analysis. A stellar fraction of $f_\star = 0.006 \pm 0.001$ is found across the ACS field of view.

5.5.3.2 Baryon fraction

The derived gas and stellar masses are used to estimate the baryon fraction within the cluster. Figure 5.11 shows the mass contribution from the gas and stars in the cluster as well as the baryon fraction. It was seen that the gas fraction increases as a function of radius while the stellar fraction drops as we move away from the center. Within the ACS field of view, 640 kpc from the center core, a gas fraction of 0.09 ± 0.01 and a stellar fraction of 0.006 ± 0.001 is measured. The total baryon fraction within this radius is thus $f_{\rm b} = 0.095 \pm 0.012$. The cosmic baryon fraction measured by Planck Collaboration (2020a), is 0.154 and the baryon fraction in cluster is 0.153 (Krolewski and Percival, 2024). The discrepancy might be due to several factors. Since the selection of cluster members mostly considered red galaxies and the ones spectroscopically confirmed are confined to the MUSE field of view (only $1'$x $1'$), the contribution from less massive star forming galaxies is not accounted for. Moreover, the stellar mass from the intra-cluster light (ICL) is not included which can account for 10-40% of the total stellar mass in the cluster (Gonzalez et al., 2007; Giodini et al., 2009; Laganá et al., 2013).

5.5.4 A possible test bench for dark matter

Estimating the 3-D matter distribution in galaxy clusters plays an important role in testing the ΛCDM. Owing to the fact that lensing is sensitive to the integrated mass along the line-of-sight, the mass of a cluster is often overestimated due to the presence of mass concentrations not physically related to the cluster or to divergences from the spherical symmetry (Gavazzi, 2005). It was common practice to study dark matter distribution in clusters using X-rays and the assumption of spherical symmetry until departures from isothermality and spherical symmetry was found in *XMM-Newton* and *Chandra* observations in the core of several clusters. Moreover, the CDM paradigm predicts highly elongated axis ratios for dark matter halos in clusters (Wang and White, 2009), contradicting the assumption of spherical

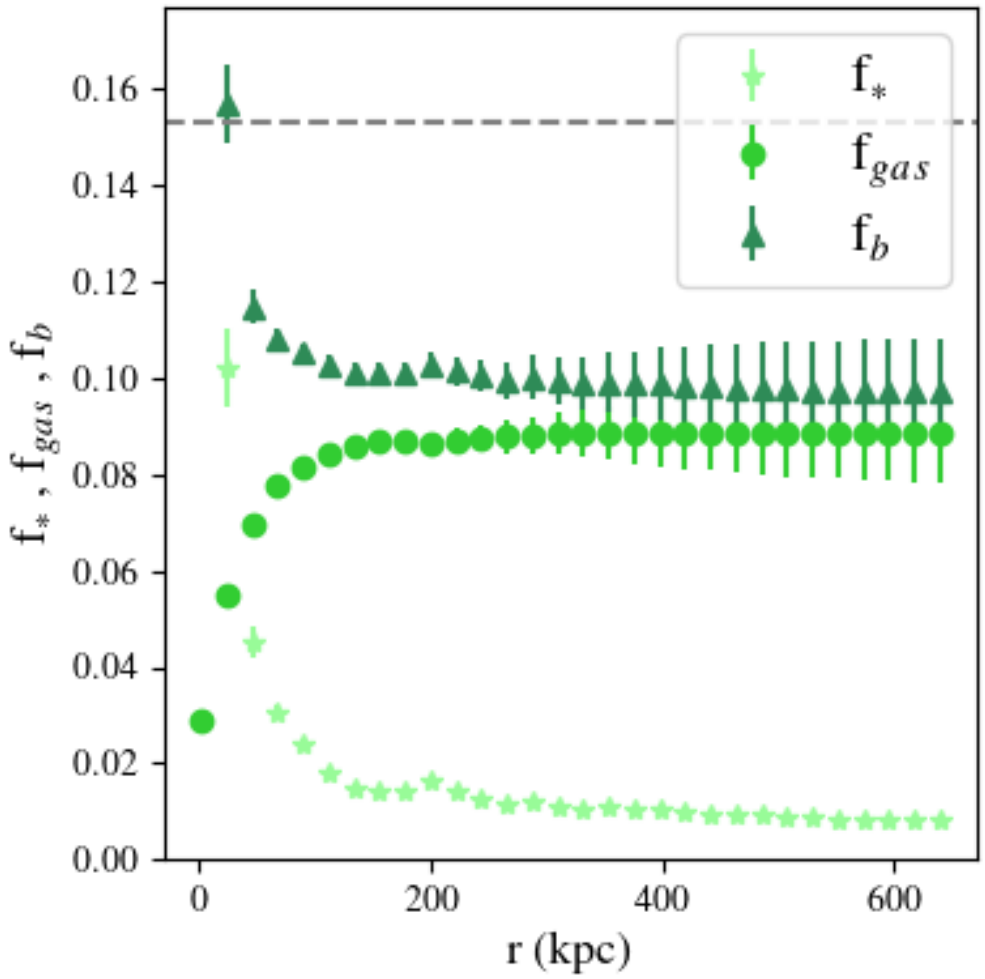

Figure 5.11: Fractions of stars, gas, and baryons within the ACS field of view, 640 kpc from the center core. The grey dashed line represents the baryon fraction in cluster (Krolewski and Percival, 2024).

shape. In a study by Gavazzi (2005), it was found that the discrepancy between the X-ray and gravitational lensing measurements can be explained by a non-spherical shape of clusters. Evidently, several studies suggest that prominent strong lensing observations are often accompanied by preferential elongations along the lines of sight or major axes preferentially oriented towards the lines of sight (Peng et al., 2009; Corless et al., 2009).

The 3-D shape of the MACS J1423 has been investigated in the past by Morandi and Limousin (2012) and Limousin et al. (2013), concluding that the cluster is

rather triaxial in shape and elongated along the line-of-sight. Morandi and Limousin (2012) find that the cluster is triaxial, with a dark matter halo axis ratio of 1.53±0.15 and 1.44±0.07, on the plane of sky and along the line-of-sight respectively. Their study suggested that the mass discrepancy between X-rays and lensing can be solved with such a geometry. As mentioned earlier, the mass estimate from our strong + weak lensing analysis is larger than the X-rays, which might be due to the presence of structure along the line-of-sight as noted by Limousin et al. (2010); Morandi and Limousin (2012) and Limousin et al. (2013).

The ΛCDM model predicts a cuspy central density profile for dark matter halos (Gao et al., 2012; Navarro et al., 1996), while observations indicate a flattened core (Navarro et al., 2010; Sand et al., 2008a). Understanding dark matter distribution is crucial for studying the formation of galaxies and clusters, and understanding the properties of dark matter. Precise mass measurements using gravitational lensing and ground-based spectra can help constrain central density profiles (Newman et al., 2011, 2013b,a). In particular, the presence of radial arcs in the core of clusters are a now well recognised and powerful tool to constrain the very central (R <20 kpc) mass distribution in galaxy clusters (Hattori et al., 1999). As discussed in Sect. 5.2.1, MACS J1423 has two radial arcs (images 1.5 and 4.5), making this cluster an excellent candidate to be used as a dark matter test bench following similar methods as the ones presented in Wyithe et al. (2001) and Newman et al. (2013b). The recent analysis by Cerny et al. (2025a) presents a new way to use radial arcs as dark matter probes, following the work from Newman et al. (2013b). Cerny et al. (2025a) utilize lower-quality *HST* and VLT/MUSE Kaleidoscope data, enabling systematic analysis without extensive high-resolution spectroscopy. Such analysis considering MACS J1423 as part of a cluster sample is being pursued by our team.

5.5.5 Summary & conclusion

This chapter present a combined strong and weak lensing mass model of the massive galaxy cluster, MACS J1423 at $z = 0.545$, one of 12 high-redshift MACS clusters. The cluster is modelled using a sequential fit which is composed of two different steps: *(i)* the modelling of the strong-lensing region using a parametric mass model for which we assume that light traces mass, and *(ii)* the modelling of the weak-lensing region using a multi-scale grid of potentials in order to include more flexibility in the modelling of this region where the lensing signal is much more diffuse than in the core.

Our strong lensing model is optimised using four multiple image systems, of which system 3 is spectroscopically confirmed with MUSE. VLT/MUSE observations of the core of MACS J1423, taken as part of the Kaleidoscope survey, were used to confirm existing spectroscopic measurements of multiple image systems, and new spectroscopic measurements were obtained for 39 cluster galaxies. A cluster galaxy catalogue composed of 66 galaxies is compiled using the red sequence technique and calibrated with our VLT/MUSE spectroscopic redshift measurements. Our best-fit mass model recovers the multiple image positions with a rms of $0.90''$, and yields a projected enclosed mass of $M(R < 200\,\mathrm{kpc}) = (1.82 \pm 0.05) \times 10^{14}\,\mathrm{M}_{\odot}$.

In contrast to the parametric model in the core, since the positions of mass clumps are not known in the outskirts, a more flexible, non-parametric grid of mass potentials is used. The weakly lensed background galaxies, carrying the weak lensing signal, are used as constraints in the outskirts. A total of 723 background galaxies selected within the *HST*/ACS field of view, i.e. a density of $57\,\mathrm{gal.arcmin}^{-2}$ are used. The weak lensing only model yields a projected enclosed mass of $M(R < 640\,\mathrm{kpc}) = (3.8 \pm 0.8) \times 10^{14}\,\mathrm{M}_{\odot}$.

To combine strong and weak lensing analyses, the sequential fit method is used as described in Jauzac et al. (2015a) and Niemiec et al. (2020, 2023). To the parametric best-fit model of the cluster core, a non-parametric grid is added to

model outskirts of clusters. The combined strong and weak lensing analysis of MACS J1423 yields a mass of $M(R < 200\,\mathrm{kpc}) = (1.85 \pm 0.05) \times 10^{14}\,\mathrm{M}_{\odot}$ in the core, and an enclosed mass of $M(R < 640\,\mathrm{kpc}) = (6.6 \pm 0.6) \times 10^{14}\,\mathrm{M}_{\odot}$ within the full *HST*/ACS field of view (R <100″).

The high mass, strong lensing power and relaxed dynamical state of MACS J1423 are powerful criteria to use as a possible dark matter test bench. The mass discrepancy between our lensing analysis and X-rays suggests elongation along the line-of-sight, indicating triaxial geometry of the cluster. This can be used to further investigate and test the ΛCDM paradigm of the Universe. Furthermore, the high redshift of the cluster, helps in understanding of the formation and evolution of structure in the early Universe. This high redshift is also advantageous because it corresponds to an earlier cosmic epoch - when cluster-scale structure was still rapidly assembling and the intracluster medium was in the process of thermalising. Observations of MACS J1423 therefore probe the mass-accretion history, the onset of galaxy quenching in dense environments, and the evolution of scaling relations at a time when the Universe was significantly younger. In this way, empirical measurements of mass, concentration and gas temperature can be directly compared with ΛCDM based simulations at the same epoch, providing stringent tests of the predicted growth rate and internal structure of massive halos.

In this chapter, MACS J1423 was examined as an exemplar of a dynamically settled cluster. In the following chapter, Abell 2744 will be considered; despite its complex structure and multiple mass peaks, a consistent mass reconstruction is nevertheless delivered by our modelling framework.

Chapter 6

Abell 2744

"What seems like chaos is often times a complex system of order." - Steve Maraboli

Galaxy clusters can be observed at almost all evolution times across a cosmic time range of about 3.4 Gyr to 13.8 Gyr. The observers can thus witness different dynamical processes and evolutionary states. While dynamically relaxed clusters provide insights into equilibrium physics and precision cosmology, merging galaxy clusters represent some of the most energetic events in the Universe since the Big Bang, offering unique opportunities to study fundamental physics under extreme conditions. These collisions between massive structures containing trillions of stars, vast quantities of hot gas, and enormous reservoirs of dark matter provide natural laboratories for investigating the behaviour of different matter components and testing our understanding of cosmological structure formation.

The physics of cluster mergers reveals how the two main mass components behave differently during collisions: dark matter is nearly collisionless, responding only to gravity, while gas is subject to pressure forces and dissipation, creating shocks and turbulence during collisions. The differential behaviours create observable signatures that allow us to probe the fundamental properties of dark matter and the physics of the intracluster medium. Matter contained in clusters falls into three main categories: dark matter, gas, and stars, each of which has decidedly

different collisional properties that are revealed by spatial separations between these components after a cluster merger.

During merger events, separate distributions of galaxies, intracluster gas and dark matter may become spatially segregated, permitting separate observations where visually observable galaxies behave as collisionless particles, the baryonic intracluster plasma is fluid-like and experiences ram pressure stripping and shock heating, while dark matter moves relatively unobstructed through the collision. These merger systems provide several key observational windows into fundamental physics, where X-ray observations reveal the hot gas distribution, and gravitational lensing maps the total matter distribution which is dominated by dark matter. The spatial separation between these components during and after mergers has provided some of the strongest evidences for dark matter's existence and properties, with such decoupling of dark and baryonic matter seen most famously in the bullet cluster, where the hot gas is seen clearly lagging behind the dark matter after the two clusters shot through each other (as shown in Figure 4.2, Clowe 2006).

Perhaps most remarkably, extreme mass concentrations in merging clusters create some of the most powerful gravitational lenses in the Universe, where the collision between galaxy clusters creates a ripple of dark matter which leaves distinct footprints in the shapes of background galaxies, allowing us to study not only the merger physics but also to peer into the distant Universe. Complex mass distributions in merging clusters create complex lensing patterns that can reveal fine-scale structure in the dark matter distribution and provide independent measurements of cluster masses. This multi-probe approach, combining lensing with X-ray and optical observations, has made merging clusters among the most valuable targets for understanding both cluster physics and cosmology.

This chapter focuses on one of the most fascinating and complex galaxy cluster in the observable Universe, Abell 2744 (also known as AC 118, MACS J0014.3-3022 and the "Pandora's Cluster"). At a redshift of $z = 0.308$, and a total projected mass of approximately $2.56 \times 10^{15} M_{\odot}$, Abell 2744 ranks among the most massive

galaxy clusters discovered to date. Due to its dynamic state and powerful lensing capabilities, the cluster has been extensively studied by Smail (1997); Allen (1998); Giovannini (1999); Govoni (2001); Girardi and Mezzetti (2001); Kempner and David (2004); Cypriano (2004); Zhang (2004); Boschin (2006); Braglia (2007); Shan (2010); Owers et al. (2011); Merten et al. (2011); Zitrin (2014); Atek (2015); Lam (2014); Wang (2015); Ishigaki (2015); Jauzac et al. (2015b); Eckert et al. (2015); Jauzac et al. (2016); Medezinski et al. (2016); Schwinn et al. (2017, 2018); Jauzac et al. (2018); Mahler et al. (2018); Sebesta et al. (2019); Richard et al. (2021); Bergamini et al. (2023a,b); Furtak et al. (2023b); Harvey and Massey (2024); Chadayammuri et al. (2024); Gallo et al. (2024); Cha et al. (2024).

Abell 2744 is an X-ray luminous cluster ($L_{\rm X} = 3.1 \times 10^{45}$ erg s^{-1} Allen, 1998), and was first identified as a major merger through radio observations of its extended halo (Giovannini, 1999; Govoni, 2001). X-ray studies confirmed this merger scenario and revealed complex substructures (Kempner and David, 2004; Zhang, 2004; Owers et al., 2011), while kinematic analyses detected bimodal velocity dispersion and multiple galaxy groups (Girardi and Mezzetti, 2001; Boschin, 2006; Braglia, 2007).

Gravitational lensing studies began with Smail (1997) who identified strong-lensing features using *HST* data. Allen (1998) found discrepancies between X-ray and lensing masses, supporting the merger interpretation. Merten et al. (2011) conducted the first comprehensive multi-wavelength analysis of the cluster, combining strong-lensing, weak-lensing, and X-ray data. After the HFF observations, high precision strong lensing analyses were performed (Wang, 2015; Jauzac et al., 2015b) and also combined with MUSE spectroscopy (Mahler et al., 2018; Richard et al., 2021; Bergamini et al., 2023a). Medezinski et al. (2016) performed a weak lensing analysis, followed by a combined strong and weak lensing analysis from Jauzac et al. (2016). The latest lensing analysis of Abell 2744 comes from *JWST* , including strong lensing analysis (Furtak et al., 2023b), weak lensing analysis (Harvey and Massey, 2024) and combined strong and weak lensing analysis (Cha et al., 2024).

The work presented in this chapter is built up on previous studies (Jauzac et al., 2015b, 2016; Mahler et al., 2018; Furtak et al., 2023b), with a focus on achieving a more precise and ideally accurate modelling of the North and the North-West components of the cluster. Figure 6.1 shows a colour composite image of Abell 2744 from *HST*/BUFFALO observations in which the core, North and North-West regions are highlighted in cyan. These are two massive substructures were identified in earlier analyses using *HST* observations (Merten et al., 2011; Jauzac et al., 2016), and *JWST* observations revealed several new multiple images (Furtak et al., 2023b), confirming their high density and the necessity to properly include them in the mass model of the overall cluster as independent substructures.

In this work, the mass model of Abell 2744 is constrained by combining *HST*/BUFFALO and *JWST*/UNCOVER observations. The strong lensing analysis is divided into three regions : the core, North and North-West. In the previous studies, due to lack of constraints the North and North-West regions were fixed while optimising the core. However, in this work the new *JWST*/UNCOVER in these regions are used and the mass distribution in the cluster is optimised together for the core, North and North-West to obtain a high-precision strong lensing mass model of Abell 2744. Similarly, for weak lensing analysis, the weak lensing catalogue is made by combining the background galaxies from *HST*/BUFFALO and *JWST*/UNCOVER selection. The final combined strong and weak lensing mass model, reveals six substructures (including the core). The abundance and mass of these substructures can be used to study the nature of dark matter through the subhalo mass function.

6.1 Observations

As one of the most studied galaxy clusters, Abell 2744 has been extensively targeted by numerous imaging and spectroscopic campaigns spanning multiple wavelengths. Deep *HST* imaging was obtained using ACS and WFC3 as part of the HFF (PI:

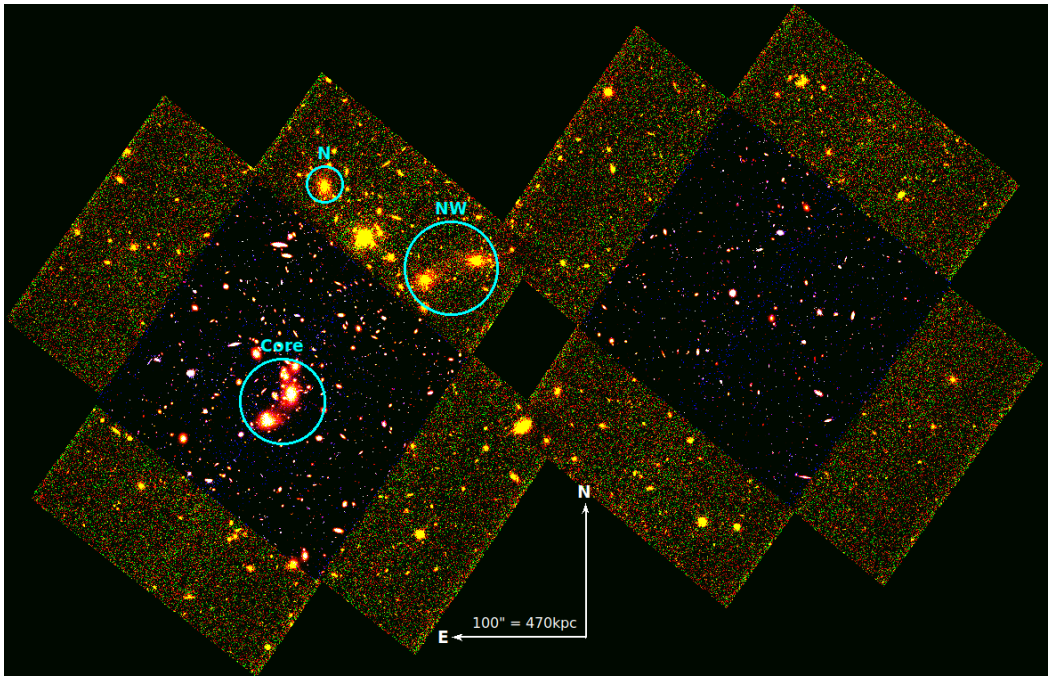

Figure 6.1: *HST* colour composite image of the central region of Abell 2744 created using the F435W for blue, F606W for green and F814W for red colours. The Core, North and North-west substructures are highlighted in cyan circles.

Noll) and BUFFALO (PI: Steinhardt & Jauzac) programmes, providing high-resolution optical and near-infrared coverage. These are complemented by extremely deep *JWST* NIRSpec and NIRCam observations from the UNCOVER (PI: Labbe & Bezanson) programme, enabling detection of faint, high-redshift galaxies. Spectroscopically, Abell 2744 has been studied through the Grism Lens-Amplified Survey from Space (GLASS; Treu et al. 2015), which combines HFF imaging with slitless spectroscopy and follow-up ground-based spectroscopy from Keck and VLT/MUSE. Additionally, the cluster was observed in the submillimeter regime as part of the ALMA (Atacama Large Millimeter/submillimeter Array) Frontier Fields survey (González-López et al., 2017). Recently, the MegaScience (PI: Suess) programme (Suess et al., 2024), a *JWST*/NIRCam medium-band imaging survey, has provided further high-quality photometric data. In the X-ray regime, *Chandra* and *XMM-Newton* observations have revealed complex thermal structures associated with the ongoing merger activity in the intracluster medium (e.g. Owers et al., 2011; Eckert et al., 2015; Chadayammuri et al., 2024). This

section only concentrates on the observations directly used in this work.

6.1.1 *Hubble Space Telescope*

Abell 2744 has been observed by *HST* through two major programs. Initially, it was observed as part of the HFF program between 2013 October 25 and 2014 July 1, using seven filters: three ACS filters (F435W, F606W, and F814W), and four WFC3 filters (F105W, F125W, F140W, and F160W). The ACS images are taken with 24, 14 and 46 orbits respectively, and the WFC3 with 24.5, 12, 10 and 14.5 orbits respectively. For this work, we utilise data from the BUFFALO program, which observed Abell 2744 between 2019 May 15 and 2019 December 7. BUFFALO observations employed five filters: two ACS filters (F606W and F814W) with exposure depths of 1538s and 2934s respectively, and three WFC3 filters (F105W, F125W, and F160W) with exposure depths of 1426s, 1467s, and 1579s respectively.

The individual exposures are used to facilitate PSF modelling for weak-lensing measurements (as described in Sect 3.1.2). All HST imaging data were astrometrically aligned relative to each other and registered to the Gaia absolute astrometric reference frame. The aligned data were then combined into mosaics with pixel scales of 30 mas for ACS and 60 mas for WFC3, following the methodology described in Koekemoer et al. (2011).

6.1.2 *James Webb Space Telescope*

Abell 2744 was observed by *JWST* as a part of the UNCOVER survey (refer to Section 4.3.6 for details). The cluster was observed in six broad-band filters, F115W, F150W, F200W, F277W, F356W and F444W, and in one medium band filter, F410M, for 4-6 hours each. The data were then reduced and drizzled into mosaics with the `grism redshift and line analysis software for space-based spectroscopy` (`grizli`, Brammer, 2023). These mosaics were constructed by com-

bining the *JWST* observations of Abell 2744 from the GLASS-*JWST* survey (Treu et al., 2022), obtained with NIRCam and NIRISS, together with the NIRCam data acquired under the Director's Discretionary Time program (PID 2767; PI Kelly). These publicly available NIRcam mosaic images of Abell 2744 processed by the UNCOVER team are used in this work. With a field of view of ∼45 arcmin^2, the UNCOVER mosaics represents the widest ultra-deep imaging coverage of Abell 2744 to date.

6.1.3 Spectroscopy and Photometry

Spectroscopic Redshifts

Spectroscopic coverage of Abell 2744 is available throughout the *HST*/BUFFALO footprint, drawn from a variety of publicly-available sources. The majority of redshifts come from a deep (19 hour) MUSE mosaic taken as part of the MUSE GTO lensing clusters program (PI J. Richard; Mahler et al. 2018.) This is supplemented by grism spectroscopy taken from the GLASS(PI T. Treu; Schmidt et al. 2014) as well as other archival coverage available in the NASA Extragalactic Database (NED).

To build a "full" redshift catalogue, we combine information from each individual source (RA, Dec, redshift, and confidence value) into a master list. We first visually inspect the positions of each entry by overlaying their coordinates on the BUFFALO images and adjusting the centroid values of each object to match the observed *HST*. Next, we normalize the confidence values of each redshift to a common scale, choosing the 3 (secure redshift) / 2 (highly probable redshift) / 1 (low confidence/guess redshift) convention employed by the MUSE GTO team (e.g., Lagattuta et al., 2019; Richard et al., 2021). Finally, we remove any duplicate entries that appear in multiple catalogues, leaving a single redshift entry for each distinct object. In cases where overlapping entries disagree on the final redshift, we select the entry with the higher confidence value. We obtain a final catalogue

Table 6.1: List of observations of Abell 2744 used in this work. Columns 1 and 2 give the right ascension and declination of the observed field in degrees. Column 3 lists the instruments and filters. Column 4 and 5 give the exposure time in seconds and the observation date, respectively. Finally, columns 6 and 7 provide the programme ID and the PI.

Programme/Survey	Instrument	Date	Exp. Time (s)	Prog. ID	PI
		HST			
HFF	WFC3/F105W	25/10/13-01/07/14	24.5 orbits*	13495	Lotz
	WFC3/F125W		12 orbits		
	WFC3/F140W		10 orbits		
	WFC3/F160W		14.5 orbits		
	ACS/F435W		24 orbits		
	ACS/F606W		14 orbits		
	ACS/F814W		46 orbits		
BUFFALO	ACS/F606W	15/05/19-07/12/19	1538	15117	Steinhardt
	ACS/F814W		2934		
	WFC3/F105W		1426		
	WFC3/F125W		1467		
	WFC3/F160W		1579		
		JWST			
UNCOVER	NIRCam/F115W	2/11/22-15/11/22	21600	2561	Labbe
	NIRCam/F115W		21600		
	NIRCam/F150W		13320		
	NIRCam/F200W		13320		
	NIRCam/F277W		13320		
	NIRCam/F356W		13320		
	NIRCam/F410W		13320		
	NIRCam/F444W		16560		
	NIRISS/F115W		13320		
	NIRISS/F150W		13320		
	NIRISS/F200W		13320		
	NIRISS/F356W		7560		
	NIRISS/F444W		7560		
	NIRCam/F090W	01/07/23-30/08/23	19080		
	NIRCam/F115W		19080		
	NIRCam/F150W		19080		
	NIRCam/F200W		9360		
	NIRCam/F277W		9360		
	NIRCam/F335W		9360		
	NIRCam/F356W		9360		
	NIRCam/F410W		9360		
	NIRCam/F444W		19080		

* Due to the large exposure time of HFF, exposure times are reported in orbits rather than seconds.

of 788 redshifts, which we then use for cluster member identification, foreground contamination removal, and lens modelling.

In addition to this, spectroscopic redshifts from UNCOVER, presented in Price et al. (2025) are used. Spectra were reduced using the `msaexp` pipeline (Brammer, 2022), which performs optimal extraction accounting for spatial PSF variation and includes corrections for path-loss and local background contamination. Redshifts were measured using a two-step process: (i) fitting galaxy templates to estimate the redshift, (ii) refining this estimate by identifying and fitting emission lines in the spectra. When emission lines were clearly detected (with signal-to-noise ratio above 3), these provided the most accurate redshift measurements. For galaxies without clear emission lines, template fitting was used instead. Each spectrum was visually inspected to ensure accurate results, with manual corrections applied when needed.

Photometric Redshifts

In this work, photometric redshifts from the Medium Bands, Mega Science survey (MegaScience, PID : 4111, PI Suess) were used, one of the deepest multi-band photometric datasets currently available for high-redshift galaxy clusters (Suess et al., 2024). MegaScience is a *JWST* Cycle 2 survey executed in November 2023, build upon and extending the UNCOVER Cycle 1 Treasury survey. MegaScience provides a uniquely comprehensive dataset, combining deep (∼28–30 $\mathrm{mag_{AB}}$) NIRCam imaging in eleven medium-band filters (F140M, F162M, F182M, F210M, F250M, F300M, F335M, F360M, F430M, F460M, and F480M) and the two shortest-wavelength broadband filters (F070W and F090W) over a ∼30 arcmin^2 region centered on Abell 2744. These data complement the UNCOVER observations, enabling precise spectral energy distribution (SED) fitting across the full suite of NIRCam filters.

Photometric redshifts were calculated using the `eazy-py` code (Brammer et al.,

2008), following the method described in Weaver et al. (2024). Fits were performed with templates that include redshift-based age limits to avoid unphysical solutions, and AGN models from Killi et al. (2023) were incorporated to account for accretion-driven power-law continua, emission lines and dust-reprocessed infrared light from the active nucleus, thus preventing nuclear emission from biasing both redshift estimates and derived galaxy properties. To estimate physical properties like stellar mass, star formation rate, and dust content, the same photometry was also analysed using the `Prospector` code (Johnson et al., 2021), following the approach presented in Wang et al. (2024). The use of medium-band filters helped improve the accuracy of photometric redshifts and reduced the number of incorrect estimates (catastrophic outliers) by a factor of 2–3, as confirmed by comparison with *JWST* spectroscopic redshifts.

6.2 Strong Lensing Analysis

6.2.1 Multiple Image Systems

Strong lensing features in the central region of Abell 2744 have been the subject of identification efforts spanning multiple observational campaigns. Prior to HFF observations, early lens models by Merten et al. (2011), Richard et al. (2014) and Johnson et al. (2014) constructed a catalogue of 55 multiple systems, including three secure spectroscopic redshifts (Johnson et al., 2014). Subsequent analysis of the HFF data by Lam (2014); Jauzac et al. (2015b); Ishigaki (2015) identified approximately 185 images. This work was complemented by spectroscopic redshifts of 7 lensed sources obtained by the GLASS team (Wang, 2015). The comprehensive HFF imaging, combined with GLASS and MUSE spectroscopic observations, ultimately identified 60 multiply-imaged galaxies within Abell 2744 core, generating 188 individual images throughout the cluster core (Mahler et al., 2018; Richard et al., 2021). To ensure maximum reliability, this catalogue was subsequently refined by Bergamini et al. (2023a) to create a secure, purely spectroscopic sample.

The strong lensing model presented here employs spectroscopically-confirmed images only, which comprises 90 multiple images from 30 distinct background sources, to accurately constrain the mass distribution within the main cluster core.

In addition to multiple images in the core, we use the latest *JWST* multiple images identification in the North (N) and North-West (NW) regions of the cluster (Furtak et al., 2023a; Price et al., 2025) to constrain these outer regions. Pre-*JWST* studies had no spectroscopically confirmed multiple systems in the N region, and only one system (Bergamini et al., 2023a) in the NW region. With *JWST* observations from UNCOVER, one spectroscopically confirmed system is now identified in the N region, comprising three multiple images that are further resolved into two distinct clumps each. In the NW region of the cluster, seven spectroscopically confirmed systems with 22 multiple images have been identified (Furtak et al., 2023a; Price et al., 2025) and are incorporated into the strong lensing analysis in this work. A list of all the multiple images used in the model is given in Table 7.3 (in appendix).

6.2.2 Cluster Members

The spectroscopic redshifts from BUFFALO (Section 6.1.3) are used to compile a list of secure cluster members. Galaxies at the cluster redshift, i.e., $0.29 < z < 0.32$, are considered as cluster members and form the foundation to define the red sequence. A colour-magnitude diagram ($m_{F606W} - m_{F814W}$ vs m_{F814W}) is constructed using spectroscopically identified cluster galaxies within this redshift range. For galaxies without spectroscopic redshifts, SExtractor is used in dual mode to extract *HST*/F606W and *HST*/F814W photometry. These photometrically selected candidates are then located on the same colour-magnitude parameter space to identify red sequence cluster members, as shown in Figure 6.2. The red sequence is then fitted with a linear relationship using an iterative 3σ clipping process. This iterative approach eliminates blue cluster member galaxies and defines spectroscopically confirmed red sequence while its scatter is measured. The red sequence is defined as galaxies falling within a region in colour-magnitude space

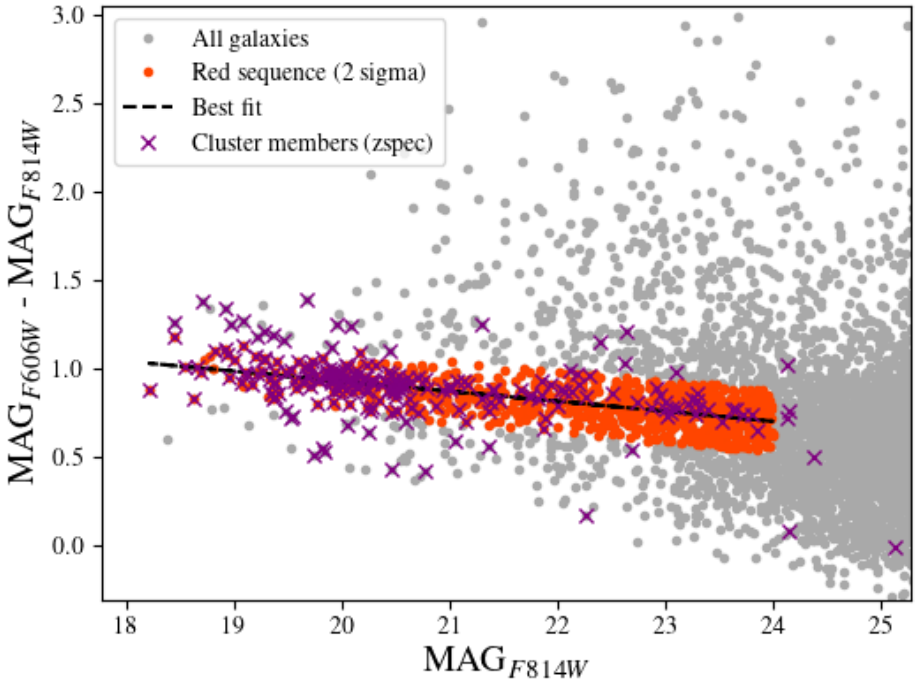

Figure 6.2: Colour (mag_{F606W} - mag_{F814W}) vs magnitude (m_{F814W}) diagram for Abell 2744. All sources from the source extraction done in this work are shown in grey, and the red sequence galaxies are highlighted in red. The cluster members with spectroscopic redshifts are marked by purple cross. We consider all galaxies within the $2\,\sigma$ of the linear fit as cluster members.

bounded by 2σ above and below the linear fit, with the bright limit set by the BCG (Brightest Cluster Galaxy) *HST*/F814W magnitude and the faint limit set to 24 mag. To note, spectroscopically confirmed cluster galaxies fainter than 24 mag, are retained. The final cluster member catalogue contains 945 galaxies, out of which 222 are spectroscopically confirmed, including the five BCGs - two in the core, two in the NW and one in the N structures.

6.2.3 Parametric Mass Modelling

Unlike previous studies where parametric modelling was performed by optimizing the core while keeping the N-NW regions fixed, here, all three regions are optimised simultaneously. However, given the complex structure of Abell 2744, the modelling

procedure is implemented by stages. First, the core is optimized while the N-NW regions are kept fixed; then the N-NW region is optimized while the core is kept fixed to the best-fit parameters obtained from the previous step. Subsequently, these two models are used as priors when all cluster components are optimized simultaneously.

The core contains two cluster-scale halos, while the N and NW regions contain three cluster-scale halos, one in the N and two in NW region. All parameters for these halos are set to vary freely except for the cut radius, which generally lies outside the strong lensing region, making it difficult to be constrained by our model. It is thus fixed to $r_{\rm cut}$=1000 kpc. The cluster contains two BCGs in the core, two in the NW region, and one in the N region. All cluster-scale halos are initially centered on these BCGs in their respective regions, with their positions set to be determined by the model optimisation.

Dual Pseudo-Isothermal Elliptical (dPIE) profiles are assigned to each cluster member, with their velocity dispersions, and cut radii tied to the galaxy luminosity via empirical scaling relations (as explained in Section 3.2). These scaling relations are normalised to a reference magnitude, $\rm mag_0 = 19.44$ (BCG magnitude) at the Abell 2744 redshift in the *HST*/F814W passband. Such scaling relations allow the masses of the hundreds of galaxies to be inferred directly from their light, thus reducing the number of free parameters. Their centers, position angles, and ellipticities are fixed to those of the corresponding galaxies; the core radius is fixed to $r^{\star}_{\rm core} = 0.15$ kpc, while the cut radius, $r^{\star}_{\rm cut}$, and velocity dispersion, $\sigma^{\star}_{0}$, are allowed to vary under Gaussian priors derived from previous models. Since using all 945 cluster galaxies is computationally expensive, preliminary models include only bright galaxies (mag < 21) and those within $10''$ of a multiple image. This is to capture the dominant deflectors (brighter galaxies are more massive) and local perturbations that most strongly influence the lensing, while the number of free parameters is dramatically reduced, making the initial optimization computationally feasible. The final model, however, uses all 945 galaxies. As with MACS J1423,

the two BCGs in the core are modelled separately from the other cluster members.

During the simultaneous optimisation of all components, less time was allocated by the model to MCMC sampling of the N–NW regions than to the core, owing to the larger number of constraints in the core. Consequently, the N–NW components were found to be poorly constrained, as evidenced by their significantly higher rms (root mean square separation between observed and model predicted image positions) values compared to the overall model rms, especially in the northern region, where only one multiple image system (System 78 in Table 7.3) is present. For example, an rms of 3.30″was measured for System 78, compared to the model's overall rms of 1.41″. Since the core had already been tightly constrained by previous studies, the focus of this strong-lensing analysis was placed on improving constraints in the N–NW regions. To ensure thorough sampling of these areas, a combination of Gaussian and uniform priors was tested. By applying Gaussian priors in the core (to restrict sampling) alongside uniform priors in the N–NW regions (to allow broader exploration), an optimal reduction of the overall rms was achieved. The final model, where all cluster components are modelled simultaneously, yields an rms of 0.83″. The parameters of this strong lensing mass model that minimises the χ^2 between the observed and model predicted positions of the multiple image systems, the best-fit parameters, are listed in Table 6.2. The corresponding surface mass density of Abell 2744 as a function of distance from the cluster center is shown in yellow in Fig. 6.6. From the best-fit model, a projected mass of $M(R < 200\text{kpc}) = (1.83 \pm 0.04) \times 10^{14}$,$\text{M}_\odot$ is measured.

6.3 Weak Lensing Analysis

6.3.1 *HST* Weak Lensing Catalogue

Source detection, photometry, and shape measurements are conducted using stacked images from BUFFALO in the F606W, F814W, and F160W passbands to generate

Table 6.2: Best fit parameters for our strong lensing mass model of Abell 2744. Values given in brackets are fixed in our model, while the ones quoted with error bars are being optimised. Coordinates of the cluster and BCG halos are given in arcseconds relative to the cluster center (R.A., Dec)=(3.586259 -30.400174). DM1 and DM2 corresponds to the cluster-scale dark matter haloes used in the core, DM3 and DM4, for NW halos and DM5 for N halo. The two BCGs in the core, optimised separately from the other cluster members are used as BCG1 and BCG2.

Components	ΔR.A.($''$)	ΔDec ($''$)	e	θ(deg)	$r_{\rm core}$ (kpc)	$r_{\rm cut}$ (kpc)	σ_0 (km s^{-1})
DM1	0.32 $\pm$ 0.13	2.13 $\pm$ 0.47	0.85 $\pm$ 0.02	92.65 $\pm$ 0.99	94.16 $\pm$ 3.77	[1000]	566.88 $\pm$ 12.27
DM2	-16.75 $\pm$ 0.09	-15.02 $\pm$ 0.11	0.54 $\pm$ 0.01	50.62 $\pm$ 0.21	53.56 $\pm$ 2.83	[1000]	831.38 $\pm$ 4.36
DM3	109.99 $\pm$ 1.65	90.35 $\pm$ 1.20	0.79 $\pm$ 0.03	30.22 $\pm$ 3.24	46.8 $\pm$ 24.96	[1000]	473.93 $\pm$ 77.27
DM4	140.13 $\pm$ 1.94	101.16 $\pm$ 1.16	0.36 $\pm$ 0.12	8.13 $\pm$ 5.85	77.06 $\pm$ 21.62	[1000]	734.27 $\pm$ 99.34
DM5	[24.25]	[155.82]	0.58 $\pm$ 0.04	31.82 $\pm$ 3.25	10.53 $\pm$ 2.89	[1000]	544.11 $\pm$ 16.54
BCG1	[-17.94]	[-19.96]	[0.37]	[14.80]	[0.15]	44.38 $\pm$ 17.28	314.08 $\pm$ 11.45
BCG2	[0.00]	[0.00]	[0.20]	[-76.0]	[0.15]	30.12 $\pm$ 8.42	413.92 $\pm$ 16.30
L* Galaxy	-	-	-	-	[0.15]	19.4 $\pm$ 5.2	191.5 $\pm$ 8.5

the weak lensing catalogue for Abell 2744, following the methodology outlined in Chapter 3/Section 3.1.2. Galaxy detection and shape measurements are performed using pyRRG (Harvey et al., 2019) with the *HST*/ACS F814W filter as the detection band. The resulting galaxy catalogue from pyRRG contains contamination from foreground stars and faint cluster member galaxies. To address this contamination, colour-colour selection is applied in the (magF435W - magF814W) *vs* (magF435W - magF606W) parameter space to isolate background galaxies suitable for weak lensing analyses. Cluster members and foreground galaxies with spectroscopically confirmed redshifts, as well as red sequence identifications, are used to isolate background galaxies as shown in Figure 6.3.

To further clean the catalogue, additional quality cuts are applied: (i) sources located close to the edges of different exposures are removed by applying a cut on the number of exposures for each detected source as done in Niemiec et al. (2023) (N23, hereafter), (ii) only sources with ellipticity in the range $0 < e < 1$ are retained, (iii) sources with signal-to-noise ratio $S/N < 4.5$ are removed, (iv) only sources with size parameters in the range $3.6 < d < 30$ pixels are kept

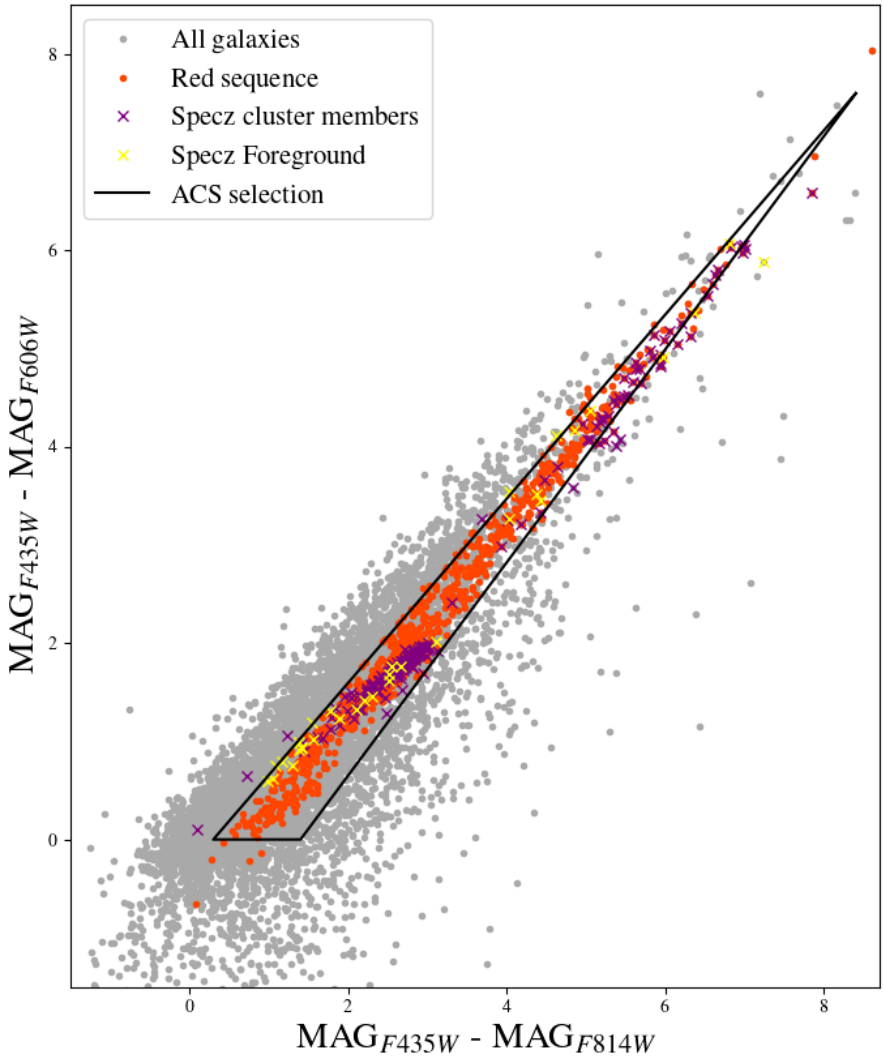

Figure 6.3: A colour-colour diagram showing the selection of background galaxies for Abell 2744. The cluster members from the red sequence detection are shown in red, and spectroscopically confirmed cluster members are shown in purple colour. The foreground galaxies with spectroscopic redshifts are shown in yellow colour. The solid black line denotes the ACS selection to separate the background galaxies.

following Jauzac et al. (2012, 2016); Niemiec et al. (2023) (v) very faint sources are removed with an F814W magnitude cut at 29 in the HFF footprint and 27 elsewhere following N23, and finally (vi) very bright sources with F814W magnitude brighter than 23 are removed across the entire BUFFALO footprint. The final catalogue contains 3308 background galaxies suitable for the weak lensing analysis. This corresponds to a source density of ∼57 galaxies. acrmin^{-2}, compared to other *HST* analyses, such as ∼110 galaxies.acrmin^{-2} from Jauzac et al. (2016), ∼42 galaxies. acrmin^{-2} from N23 in HFF, and ∼13 galaxies. acrmin^{-2} in the Subaru sample.

6.3.2 *JWST* Weak Lensing Catalogue

For the *JWST* weak lensing catalogue, UNCOVER imaging in the F115W, F150W, and F200W filters is used. Following the same approach as for *HST* , PYRRG (Harvey et al., 2019; Harvey and Massey, 2024) is used for source detection, photometry, and galaxy shape measurements as described in Chapter 3/Section 3.1.2.

Spectroscopic redshifts from UNCOVER and photometric redshifts from MegaScience are used to retain only sources with $z > 0.32$, ensuring the selection of background galaxies behind the cluster. Additional quality cuts are applied to remove sources with ill-defined shapes, including signal-to-noise, ellipticity, and size cuts implemented in the same manner as described before for *HST* data. To preserve the quality of the lensing signal, sources with photometric redshift uncertainties exceeding 1σ are removed. Similarly, very bright (mag < 20) and very faint (mag > 27.5) sources are excluded for the same reason, as done in Harvey and Massey (2024). To further refine the catalogue and ensure contamination-free selection, cross-matching is performed with cluster members and foreground galaxies identified from BUFFALO, with any matches subsequently removed. A comparison of shear measurements across the F115W, F150W, and F200W filters revealed that the weak lensing signal is optimal in F150W (Harvey and Massey, 2024). Therefore, this analysis uses weak lensing measurements derived from the F150W filter.

The final *JWST* weak lensing catalogue contains 2353 sources, corresponding to a source density of ∼50 galaxies arcmin^{-2}, compared to ∼150 galaxies arcmin^{-2} from Harvey and Massey (2024) and ∼350 galaxies arcmin^{-2}.

6.3.3 Grid Modelling

To perform the weak lensing analysis, we combine the two catalogues from BUFFALO and UNCOVER. For sources present in both catalogues, those from UNCOVER are retained due to *JWST*'s superior spatial resolution and lower noise characteristics, which provide more accurate shape measurements and improved weak lensing signal quality. The combined catalogue contains 5209 galaxies, corresponding to a source density of ∼66 galaxies per arcmin^2.

A lightmap of Abell 2744 is created using the distribution of cluster galaxies. Using this lightmap, a multiscale grid is built to decompose the mass distribution. After testing different grid resolutions, we converge on an optimal grid composed of 1392 RBFs (Jauzac et al., 2012, 2015a; Niemiec et al., 2023). Core radii, s, are ranging from 14″ and 171″. The resulting grid is shown in Fig. 6.4 on the smoothed cluster light map. The surface mass density for the corresponding model is shown in Fig. 6.6. The projected surface mass within 1000 kpc, $M(R < 1000\,\mathrm{kpc}) = (1.32 \pm 0.11) \times 10^{15}\,\mathrm{M}_\odot$.

6.4 Combining Strong and Weak Lensing

To obtain a full, strong and weak lensing model of the cluster, a sequential fit is performed by combining the parametric and non-parametric models. First, the core is modelled using strong lensing constraints as described in Sect. 6.2. To the best-fit parametric model of the core, the multi-scale grid of potentials described in Sect. 6.3.3 is added to model the outskirts of the cluster. The parametric model presented in Sect. 6.2.3 is fixed to its best-fit values. RBF amplitudes are then

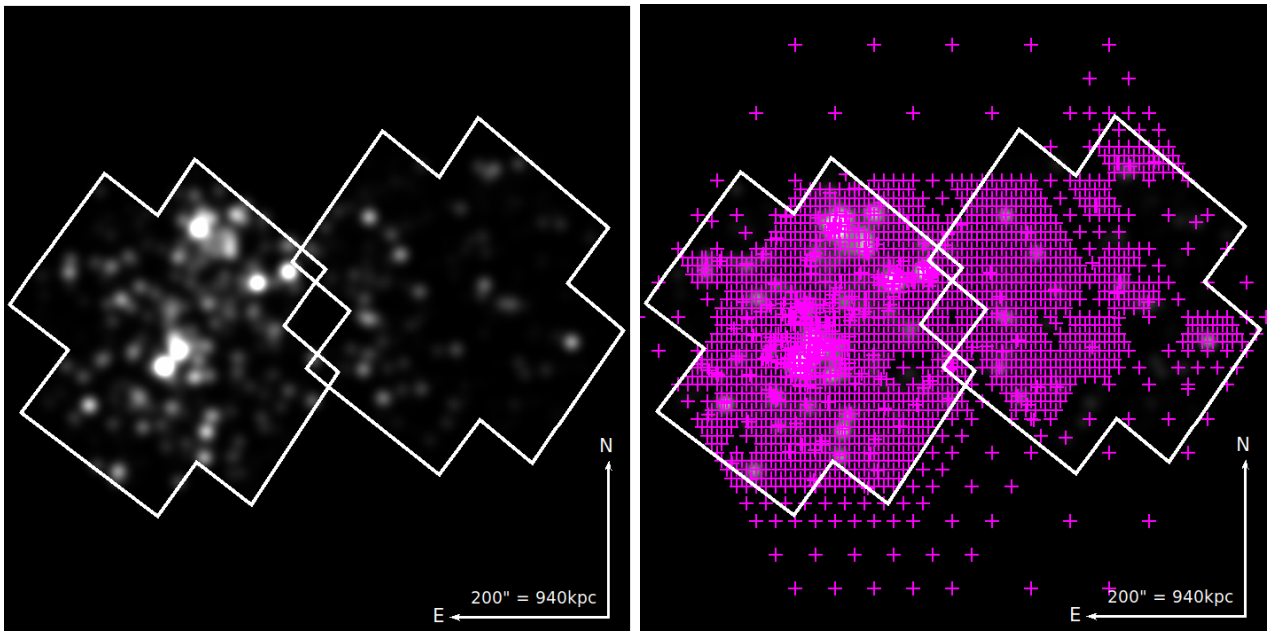

Figure 6.4: Left : Smoothed lightmap of Abell 2744. Right : Non-parametric grid of potentials used for weak lensing only analysis highlighted in magenta crosses. The crosses are positioned at the center of the grid potentials. The grid is composed of 1392 RBFs. The white solid line outlines the BUFFALO field of view.

estimated from the weak lensing constraints. Already optimised cluster-scale dark matter halo and cluster member galaxies are combined with RBF grid potentials. The grid potentials are removed from the cluster core, N and NW substructures due to the absence of weak lensing constraints in this region. The projected surface mass density resulting from the combined strong and weak lensing mass model of Abell 2744 is shown in Fig. 6.6 and Fig. 6.7. A total (combined strong and weak lensing) projected mass of $M(R < 1000\,\mathrm{kpc}) = (2.50 \pm 0.20) \times 10^{14}\,\mathrm{M}_{\odot}$ is measured within 1000 kpc from the combined strong and weak lensing analysis.

6.5 Substructure Detection

The presence of substructures can be inferred from the projected density profiles where the peaks in the profiles are caused by overdensities in the mass maps. However, in order to detect the substructures from the mass map of Abell 2744 in a

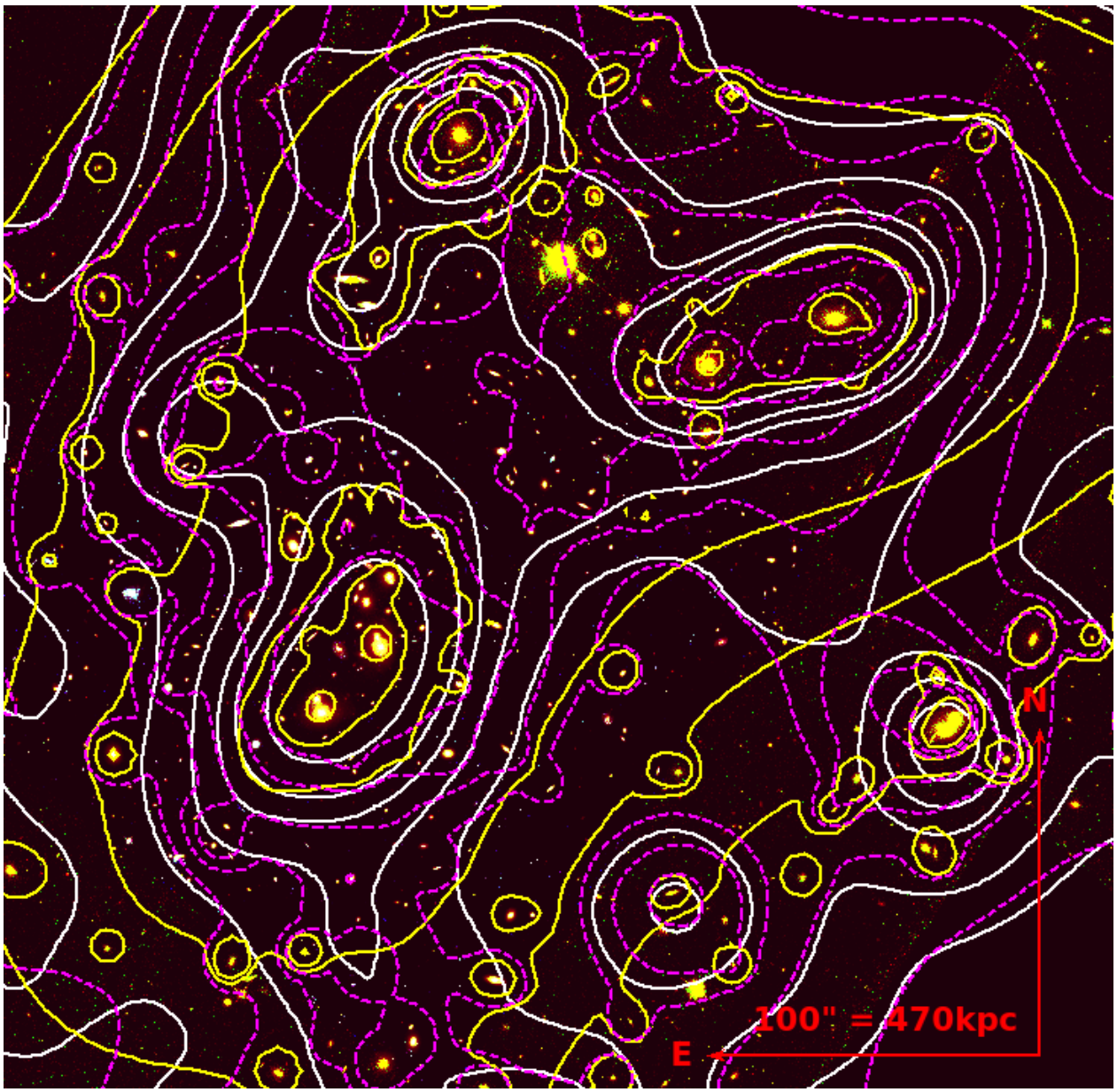

Figure 6.5: *HST* colour composite image of the central region of Abell 2744 created using the F435W for blue, F606W for green and F814W for red colours. The thick solid yellow and thin dashed magenta contours show the mass distribution obtained with our strong-lensing and weak-lensing mass reconstruction as described in Sect. 6.2.3 and Sect. 6.3.3 respectively. The mass contours obtained with our combined mass model, as presented in Sect. 6.4, are shown with thin solid white contours. The the core, N and NW are marked in cyan circles.

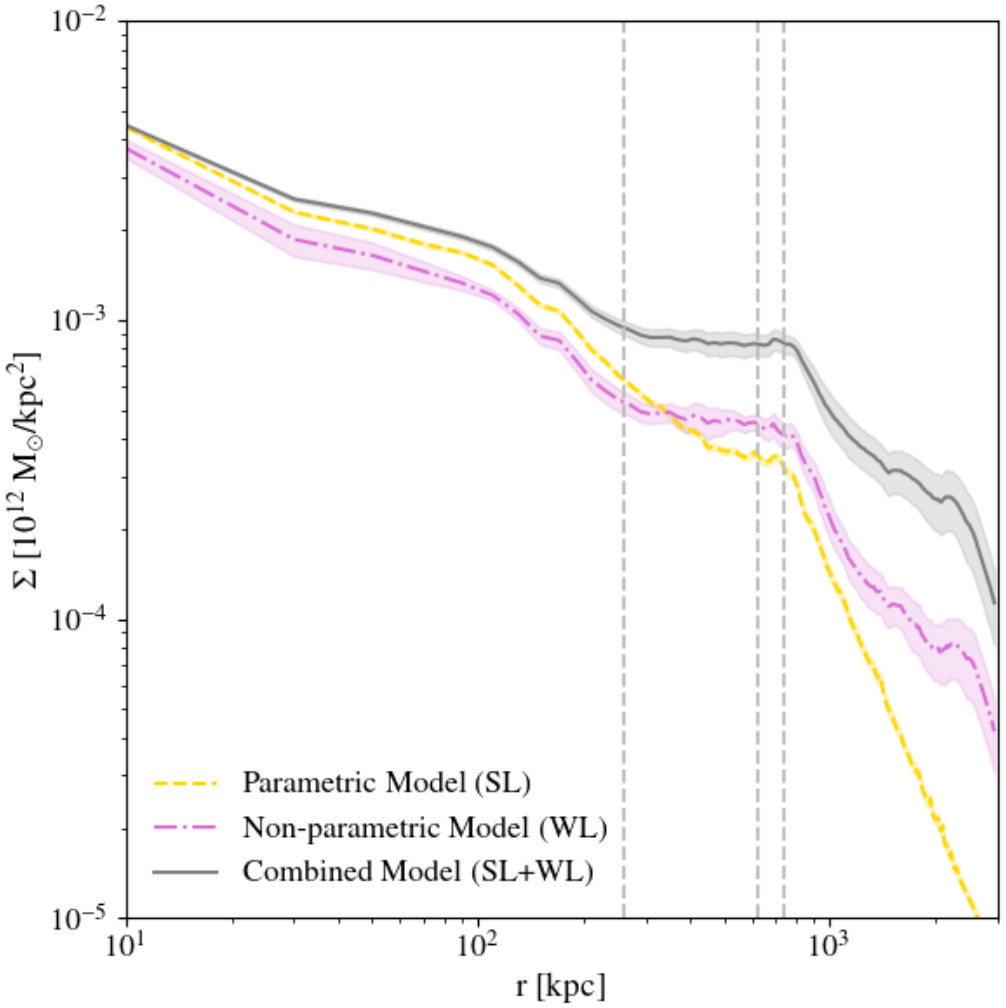

Figure 6.6: The surface mass density profiles of Abell 2744. The parametric model for only strong lensing (Sec. 6.2.3), and non-parametric grid model for weak lensing only (Sec. 6.3.3) is shown in yellow and magenta colour respectively. The profile in grey colour shows the combined strong and weak lensing analysis. The first vertical grey dashed line denotes the limit of the core at 260 kpc, the second and third denotes the NW and N substructures at 620 kpc and 740 kpc respectively.

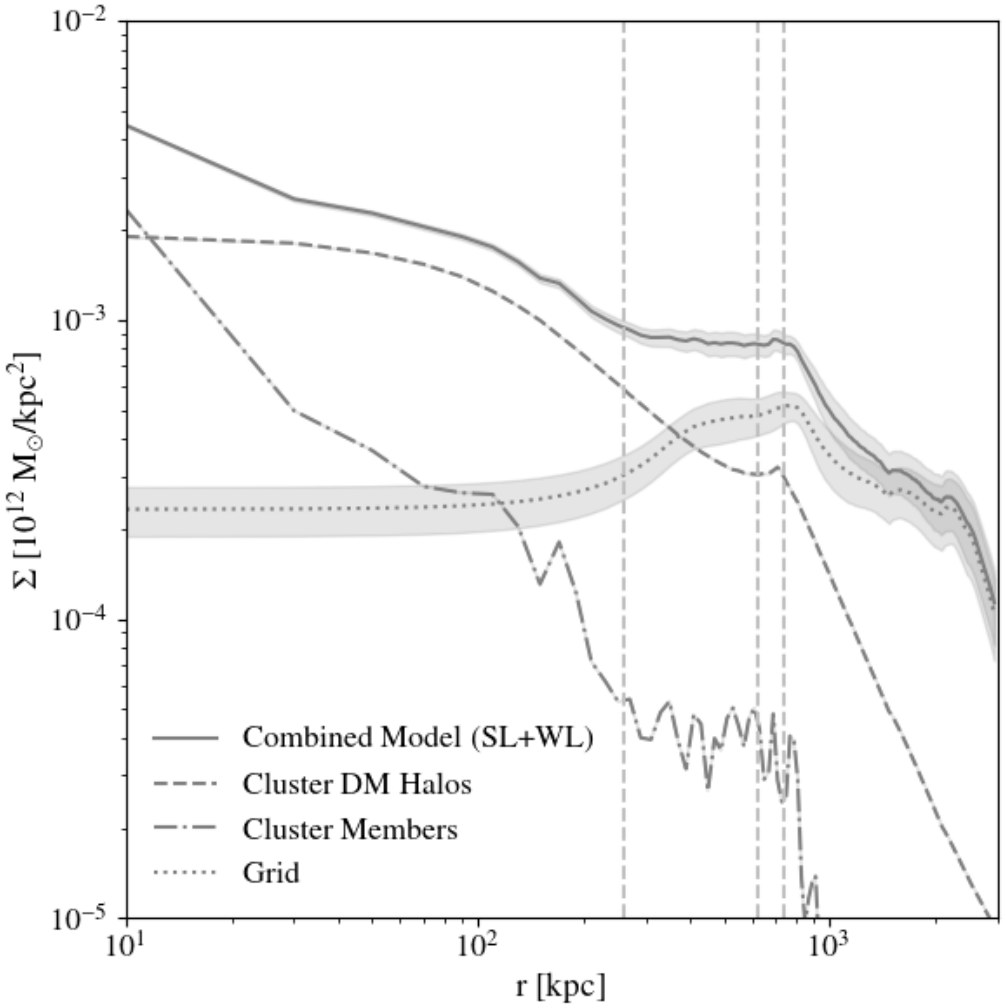

Figure 6.7: The surface mass density profiles of Abell 2744. The full combined strong and weak lensing model is represented by the solid line. The different components of this model i.e. cluster-scale halos (Core, N and NW), cluster members and the grid potentials are shown in dashed, dotted and dashed-dotted lines respectively. The first vertical grey dashed line denotes the limit of the core at 260 kpc, the second and third denotes the NW and N substructures at 620 kpc and 740 kpc respectively.

more systematic manner, a wavelet transform (WT) is used to identify the positions of the peaks on sub-cluster-scales in the mass map as done in Schwinn et al. (2018). The WT has been widely adopted in signal and image processing due to its ability to isolate features at specific scales while retaining spatial information. It is a mathematical tool that allows a signal to be analysed in both position and scale simultaneously. In this framework, the signal is decomposed into a series of components by convolving it with a set of basis functions, called wavelets, that are derived by scaling and translating a common reference known as the mother wavelet. This process enables the detection of localised features at specific spatial scales, in contrast to traditional techniques that separate signals purely by frequency. As a result, structures of different sizes can be isolated while preserving information about their exact locations.

When applied to two-dimensional mass maps of galaxy clusters, the wavelet transform allows the extraction of substructure signals at cluster relevant scales. The transformation produces a set of wavelet coefficients, each of which quantifies the strength of the signal at a given spatial position and scale. A high wavelet coefficient at a particular location implies a strong resemblance between the local mass distribution and the wavelet shape at that scale, indicating the presence of a significant feature, such as a mass peak. Conversely, low coefficients correspond to either noise or smooth background structure.

In this study, the wavelet transform is used to identify significant substructures within the projected mass maps. A set of selection criteria is defined based on both the spatial scale and the amplitude of the wavelet coefficients. Only those peaks that exceed a specified threshold are retained (discussed below), ensuring that the detected substructures are statistically meaningful and comparable in significance to those found in Abell 2744. When comparing with simulations, this allows for a consistent detection of substructures across both observed and simulated data sets, independent of the subhalo identification method originally applied in simulations. Such uniform treatment reduces potential biases and ensures that only

those substructures that contribute significantly at a given scale are considered. The robustness and effectiveness of this technique have been demonstrated in several earlier studies focused on cluster substructure analysis (Flin and Krywult, 2006; Livermore et al., 2017; Schwinn et al., 2018).

The one-dimensional (1D) continuous wavelet transform is performed using the publicly available Python package `pywt`. The Mexican Hat wavelet is chosen as the mother wavelet, as its shape closely resembles the expected density profile of subhaloes and provides the best match compared to alternative wavelet functions. Although the input is a two-dimensional (2D) mass map, the wavelet transform is applied in a separable manner: first along the rows and then along the columns of the map. At each position, the wavelet coefficients quantify the strength of the local signal at a given spatial scale. The final coefficient map is obtained by computing the arithmetic mean of the row-wise and column-wise coefficients, yielding a scale sensitive and spatially resolved representation of potential substructures. To detect significant substructures, a quantitative selection criterion is defined based on two parameters: the scale of the wavelet transform and a threshold on the coefficient amplitude. These parameters are calibrated to maximise recovery of substructures identified in the density profiles from the lensing analyses in this study and by Jauzac et al. (2016, J16, hereafter), resulting in the adoption of a WT scale of 40 pixels (182 kpc) and a coefficient threshold of $W \geq 2.6 \times 10^{10}$ $M_{\odot}$ pc^{-1}.

All pixels with coefficients at least five times greater than the map's average value are initially flagged as potential substructure locations. From this set, 20% of the pixels are randomly sampled to reduce computational overhead and prioritise compact, high-significance regions. Around each of the selected pixels, a circular aperture of radius 100 kpc is drawn. The pixel with the highest wavelet coefficient within each aperture is identified, and the aperture is recentered on that pixel. This process is iterated ten times to ensure robust detection of all statistically significant peaks while enforcing a minimum spacing of 100 kpc between substructures. This distance criterion avoids overlapping apertures, which would hinder independent

mass estimates. Lastly, any substructure with an aperture mass M(<150 kpc)< $3 \times 10^{13} M_{\odot}$, or located farther than 2.5 Mpc from the cluster centre (end of the parallel field), is discarded from the final sample.

This method succesfully detects the core, N and NW structures in the cluster. Apart from this, it also finds comparitvely less massive substructures in the West region of the cluster (W), and one on the East (S1), as shown the Figure 6.8. There is also another detection (S5), in the parallel field of BUFFALO, around 2.1 Mpc away from the cluster center. This detection has a low signal to noise, and as a result is considered as a candidate. This is the first detection of S5, thanks to the wide field of view of BUFFALO. It is associated with a few cluster members (from the red sequence) but spectroscopic redshifts are needed to confirm it.

J16 detected eight substructures : core, N, NW (S3 and S4), West (Wbis), S4 which is located near the NW substructure, and two more S1 and S2 in the East, as shown in Figure 6.8. Table 6.3 shows comparision of masses of the detected substructures with J16. The core component of the cluster has a mass of $M_{\mathrm{SL+WL_{core}}}(R < 150\,\mathrm{kpc}) = (13.14 \pm 0.28) \times 10^{13}$ $\mathrm{M}_{\odot}$, which is in agreement with J16, $M_{\mathrm{J16_{core}}}(R < 150\,\mathrm{kpc}) = (13.55 \pm 0.09) \times 10^{13}$ $\mathrm{M}_{\odot}$. The N and NW peaks are recovered at positions consistent with J16. Although J16 treated NW and S3 as separate substructures, they correspond here to a single NW region in this work, exhibiting two mass peaks associated with the two brightest cluster galaxies. For direct comparison, these peaks are labeled NW1 and NW2 in Table 6.3. However, both N and NW (NW and S3 in J16), are revealed to be more massive in our mass model compared to J16 as shown in Table 6.3. For W, J16 detected a subtructure, W_{bis}, which they concluded to be probably a background structure projected onto the cluster after finding that the galaxies in its vicinity are background galaxies. However, the substructure found in this work, is farther to the West from W_{bis}, and is associated with cluster galaxies. The S1 substructure, located northeast of the core, is detected at a position closely matching that of J16 and aligns with the gas bridge reported by Eckert et al. (2015). The additional components S2 (North of

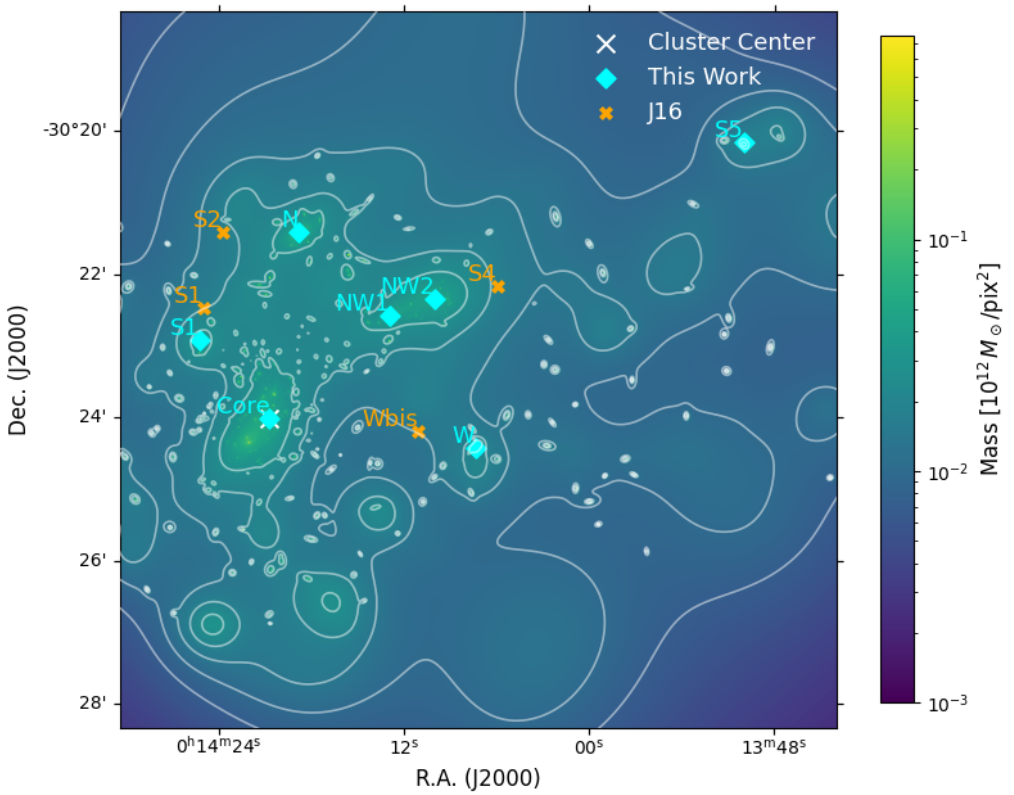

Figure 6.8: Substructures in Abell 2744 identified using the wavelet transform method in the strong+weak lensing mass map. The colour map and the contours show the 2D surface density. Substructures detected in this work are marked in cyan coloured diamonds while the ones from J16 are highlighted with orange cross.

S1 and East of N) and S4 (West of NW), reported by J16, are not recovered in this analysis. This non-detection may be attributable to the cluster-scale halos in the N and NW regions in our model effectively incorporating the mass contribution in those areas. As discussed in Sect. 6.6.2, the strong+weak model in this work yields more mass in the outskirts compared to the previous studies. This effect is also observed on substructures in the outskirts. It is noted that substructures in Table 6.3 corresponding to this work are more massive than in J16. Although, the mass of the core is within errorbars of J16.

Table 6.3: Substructure detections with the WT method. This work detects six substructures, Core, N, NW (NW1 and NW2), W, S1 and S5. First column gives the ID of these subtructures, their R.A. and Dec. (J2000), are given in column 2 and 3 respectively. Column 4 gives the mass enclosed within 150kpc (in $10^{13}M_{\odot}$) and their distance from the cluster center (D_{D-C}) is shown in column 5. Column 6 compares the mass (within 150kpc) to that of J16.

ID	R.A. (deg)	Dec. (deg)	M(r<150 kpc) ($10^{13}M_{\odot}$)	D_{C-S} (kpc)	M_{J16}(r < 150 kpc) ($10^{13}M_{\odot}$)
Core	3.586484	-30.400171	13.14 ± 0.28	-	13.55 ± 0.09
N	3.578403	-30.356798	9.56 ± 0.46	739	6.10 ± 0.50
NW1	3.553918	-30.376269	9.68 ± 0.37	619	7.90 ± 0.60
NW2	3.541670	-30.372377	10.53 ± 0.31	799	6.50 ± 0.60
W	3.530713	-30.407135	5.89 ± 0.46	815	-
S1	3.605168	-30.382088	7.22 ± 0.51	410	5.00 ± 0.40
S5	3.458225	-30.335933	8.42 ± 0.41	2152	-

6.6 Discussion & Conclusion

6.6.1 Comparison between different models

Three main mass models are presented in this analysis: a parametric model for the cluster core, a non-parametric grid-based model for the outskirts, and a combined model that integrates both strong and weak lensing constraints across the entire field. Resulting mass distributions from these models are shown in Figure 6.5. The inner core and prominent substructures to the north and north-west (N and NW) are well traced by the parametric model and are also visible, with less defined contours in the grid-only model.

Figure 6.6 presents the two-dimensional surface density profiles derived from each model. As observed, the amplitude of the grid-only model remains consistently lower than that of the parametric and combined models across all scales in the cluster. This discrepancy arises due to the absence of strong-lensing constraints in the grid-only model and the lack of an explicit large-scale cluster halo component.

In contrast, the combined model exhibits systematically higher amplitudes compared to individual models, particularly in the outer regions of the cluster. Notably,

the total mass inferred from the combined model exceeds the sum of the parametric and grid-only contributions in the outskirts. Ideally, in a sequential-fit approach, the mass distribution derived from the parametric model should be accounted for during the grid optimisation step, allowing for the grid amplitudes to be adjusted accordingly. However, in practice, the combined model appears to overestimate the mass in the outskirts. This effect warrants further investigation, using simulations to better understand the origin of the discrepancy. A similar issue was reported by Niemiec et al. (2023), who also found an overestimation of mass in the outer regions for the combined lensing models from both joint and sequential fit in LENSTOOL .

6.6.2 Comparison with Previous Work

Jauzac et al. (2015b) performed a strong lensing analysis of Abell 2744 with deep HFF observations using LENSTOOL . They found a projected mass within 250 kpc of $M_{\rm J15}(R < 250\,{\rm kpc}) = (2.76 \pm 0.08) \times 10^{14}$ $M_\odot$, which is slightly larger than the strong lensing mass in this work, $M_{\rm SL}(R < 250\,{\rm kpc}) = (2.22 \pm 0.04) \times 10^{14}$ $M_\odot$.

From the strong+weak lensing analysis with HFF in the core with LENSTOOL by J16, they found, a projected mass within 250 kpc of $M_{\rm J16}(R < 250\,{\rm kpc}) = (2.77 \pm 0.01) \times 10^{14}$ $M_\odot$, which is within the errorbars of the strong+weak lensing mass in this work, $M_{\rm SL+WL}(R < 250\,{\rm kpc}) = (2.73 \pm 0.06) \times 10^{14}$ $M_\odot$. J16 presented a projected mass within 1.3 Mpc of $M_{\rm J16}(R < 1.3\,{\rm Mpc}) = (2.3 \pm 0.1) \times 10^{15}$ $M_\odot$, while this work gets a much higher mass, $M_{\rm SL+WL}(R < 1.3\,{\rm Mpc}) = (3.38 \pm 0.34) \times 10^{15}$ $M_\odot$. The mass from this work is much higher that of J16, due to the overestimation of combined mass in this work, as mentioned in the previous section.

From the *JWST*/UNCOVER observations, Furtak et al. (2023a) performed a strong lensing analysis of Abell 2744, yielding a projected mass of $M_{\rm F23}(R < 200\,{\rm kpc}) = (1.60 \pm 0.22) \times 10^{14}$ $M_\odot$, which is within errorbars of strong lensing model in this work, $M_{\rm SL}(R < 200\,{\rm kpc}) = (1.69 \pm 0.03) \times 10^{14}$ $M_\odot$, but lower than the combined model but still within its errorbars, $M_{\rm SL+WL}(R < 200\,{\rm kpc}) =$

$(2.01 \pm 0.06) \times 10^{14}$ $M_{\odot}$.

One of the very first weak lensing only analyses with *JWST* of Abell 2744 was done by Harvey and Massey (2024) using a non-parametric method, with a background source density of ∼150 galaxies arcmin^{-2} compared to ∼60 galaxies arcmin^{-2} from *JWST* in this work. The difference in the source density comes from the method used to obtain the weak lensing catalogue. In this analysis background sources with spectroscopic redshift and secured photometric redshifts are taken into account, while Harvey and Massey (2024) makes the lensing cuts mentioned in Chapter 3/Section 3.1.2, but did not perform a colour-colour selection, necessary to remove contamination from cluster and foreground galaxies. Harvey and Massey (2024) finds a mass of $M_{\rm H24}(R < 250\,{\rm kpc}) = (1.60 \pm 0.06) \times 10^{14}$ $M_{\odot}$, which is within errorbars from the weak lensing mass from this work $M_{\rm WL}(R < 250\,{\rm kpc}) = (1.77 \pm 0.09) \times 10^{14}$ $M_{\odot}$. It should be noted that masses derived from weak-lensing alone and confined to the core region (250 kpc) are systematically lower than those from strong-lensing or combined models, owing to the lack of lensing constraints in the central cluster core.

Another recent, *JWST* strong–weak lensing analysis was performed by Cha et al. (2024). In that study, a free-form maximum entropy reconstruction (MARS) algorithm was employed, in contrast to the combination of parametric and non-parametric methods utilized here. A weak-lensing source density of ∼350 galaxies. arcmin^{-2} was obtained, owing to a background selection based solely on photometric redshifts without further quality cuts. Cha et al. (2024) reported a projected mass of $M_{\rm SL+WL}(R < 1000\,{\rm kpc}) = (1.19) \times 10^{15}$ $M_{\odot}$, which is much lower compared to this work, $M_{\rm SL+WL}(R < 1000\,{\rm kpc}) = (2.50 \pm 0.20) \times 10^{15}$ $M_{\odot}$. However, it is comparable to the strong lensing only and weak lensing only mass from this work, $M_{\rm SL}(R < 1000\,{\rm kpc}) = (1.12 \pm 0.03) \times 10^{15}$ $M_{\odot}$ and $M_{\rm WL}(R < 1000\,{\rm kpc}) = (1.32 \pm 0.11) \times 10^{15}$ $M_{\odot}$ respectively.

Although, both Harvey and Massey (2024) and Cha et al. (2024), recovers the three main structures in the cluster, the core, N and NW, but shows no evidence

Table 6.4: A summary table to compare the mass of Abell 2744 with previous works. Masses measured within 200 kpc, 250 kpc, 1000 kpc and 1300 kpc using different methods are quoted in units of $10^{14}\,M_{\odot}$. Other works are listed : Jauzac et al. (2015b, J15) and Jauzac et al. (2016, J16), Furtak et al. (2023b, F23), and Cha et al. (2024, C24).

	Method	J15	J16	F23	C24	This work
$R < 200$ kpc	SL only	2.16 ± 0.05	-	1.60 ± 0.22	-	1.69 ± 0.03
	SL + WL	-	-	-	1.73	2.01 ± 0.05
$R < 250$ kpc	SL only	2.76 ± 0.08	-	-	-	2.22 ± 0.04
	SL + WL	-	2.77 ± 0.01	-	-	2.73 ± 0.09
$R < 1000$ kpc	WL only	-	-	-	-	13.24 ± 1.07
	SL + WL only	-	18.5 ± 0.7	-	11.9	4.4 ± 0.3
$R < 1300$ kpc	WL only	-	-	-	-	16.71 ± 1.57
	SL + WL only	-	23±1	-	-	33.86 ± 0.34

of any other substructures, in contrast to those identified by J16 and in this work. A summary of comparison with previous studies is presented in Table 6.4.

6.6.3 Subhalo mass function (SHMF)

The range of substructure masses and their spatial distribution in dynamically complex, non-relaxed clusters such as Abell 2744 provides a valuable opportunity to probe the subhalo mass function (SHMF) across diverse environments. The SHMF characterises the number of dark matter subhaloes embedded within the host halo of a galaxy cluster as a function of their mass. It serves not only as a critical diagnostic of hierarchical structure formation but also as a direct observational probe of the underlying nature of dark matter.

Within the standard ΛCDM framework, the SHMF is predicted to follow a steep power-law distribution, indicating a high abundance of low-mass subhaloes. However, various theoretical uncertainties and observational challenges, such as the missing satellites problem and the cusp-core discrepancy, suggest that the ΛCDM prediction may be incomplete. To address these issues, alternative dark matter models such as WDM (Warm Dark Matter) and SIDM (Self-Interacting Dark Matter) have been proposed, each offering distinct predictions for the SHMF. For in-

stance, in WDM scenarios, a sharp suppression of low-mass subhaloes is expected below approximately 10^8–10^9 $M_\odot$ (Lovell, 2014; Kennedy et al., 2014), while SIDM models predict a 30–50% reduction in the abundance of centrally concentrated low-mass subhaloes, potentially mitigating observed tensions more effectively (Vogelsberger et al., 2012; Rocha et al., 2013).

Previous studies have shown that both WDM and SIDM models produce fewer low-mass subhaloes compared to CDM scenarios (Springel et al., 2008; Lovell, 2014). In future work, the observational results obtained from Abell 2744 will be compared with high-resolution hydro-simulations of galaxy clusters, such as those from the BAHAMAS project (Robertson et al., 2019), which include variations from CDM corresponding to WDM, and SIDM cosmologies. Such comparisons will enable the investigation of how subhalo abundance and internal structure vary across different dark matter models, potentially offering new constraints on the fundamental nature of dark matter.

6.6.4 Summary & conclusion

This chapter presents a combined strong and weak lensing mass model of the massive non-relaxed cluster, Abell 2744 at $z = 0.308$, one of the six HFF and BUFFALO clusters. The model is made using the sequential fit (described in Sect. 3.5.2) by combining a parametric model using strong lensing constraints in the core and the non-parametric grid model using weak lensing constraints in the outskirts.

The strong lensing model is optimized using spectroscopically confirmed multiple image systems in the core, N, and NW regions from BUFFALO and UNCOVER observations. All components are optimized simultaneously to obtain a precise mass distribution not only of the core but also of the N and NW regions, which were poorly constrained prior to *JWST* observations due to lack of multiple images from *HST*. The best-fit model achieves an rms of 0.83″ with a projected enclosed

mass of $M_{\rm SL}(R < 200, {\rm kpc}) = (1.69 \pm 0.03) \times 10^{14}$ $\rm M_\odot$ in the core.

In the outskirts, the model is optimised using weakly lensed background galaxies as constraints within a non-parametric grid framework. Combining constraints from *HST*/BUFFALO and *JWST*/UNCOVER provides a total of 5209 background galaxies, yielding a source density of ∼66 galaxies per arcmin^2. This is the first time, a combined *HST* and *JWST* weak lensing is performed. This weak lensing-only model yields a projected mass of $M_{\rm WL}(R < 1000, {\rm kpc}) = (1.32 \pm 0.11) \times 10^{15}$ $\rm M_\odot$.

In the final model, which constitutes strong and weak lensing, the sequential fit is performed. First, the parametric model is fixed to the best-fit parameters, and a non-parametric grid is added to model the outskirts of the cluster. The combined model yields a mass of $M_{\rm SL+WL}(R < 200\,{\rm kpc}) = (2.01 \pm 0.06) \times 10^{14}$ $\rm M_\odot$ in the core, and an enclosed mass of $M_{\rm SL+WL}(R < 1000\,{\rm kpc}) = (2.50 \pm 0.20) \times 10^{15}$ $\rm M_\odot$ within 1000 kpc from the center of the cluster.

Massive galaxy clusters with substantial substructure, such as Abell 2744, are recognised as valuable laboratories for testing the ΛCDM model of cosmology (Jauzac et al., 2016; Schwinn et al., 2017, 2018; Jauzac et al., 2018). Through detailed gravitational lensing analyses, evidence for numerous massive substructures can be revealed. These features trace the hierarchical assembly of clusters and offer observational probes of the dark matter distribution.

By comparing such observations with theoretical predictions from simulations under different dark matter scenarios (e.g., CDM, WDM and SIDM),meaningful constraints on the nature of dark matter can be established. In particular, the mass, distribution, and abundance of substructures are expected to vary between models, and thus the results obtained for Abell 2744 can serve as a basis for future investigations into the subhalo mass function and dark matter physics at cluster-scales. I am currently working on this, and preparing a comparison between the observations and simulations for publication in the near future.

Looking ahead, the *JWST*/SLICE programme is already in progress and is delivering lensing-quality imaging for a larger sample of massive galaxy clusters. In the following and final chapter, a strong lensing model of one SLICE cluster is presented as a case study, laying the groundwork for extending this analysis to the full sample. This expanded approach will pave the way for a statistically robust investigation of cluster substructure and provide new insights into the nature of dark matter.

Chapter 7

A SLICE of Future

"The only impossible journey is the one you never begin." - Tony Robbins

The field of gravitational lensing has entered a new era with the commissioning of *JWST* . Building on the legacy of *HST* and lensing-focused programmes such as CLASH, HFF, and BUFFALO, JWST offers a transformative leap in both depth and resolution, particularly in the near-infrared regime. This has opened a new observational window into the high-redshift Universe, and with it, a shift in the landscape of cluster lensing studies. Thanks to its exceptional infrared sensitivity and spatial resolution, *JWST* enables the detection of intrinsically fainter and more distant lensed galaxies, more detailed reconstructions of mass distributions in clusters, and the study of cluster evolution across a broad redshift baseline. As a result, we are now entering an era in which gravitational lensing science is both richer in signal and more demanding in complexity.

Among the flagship programmes of this new era is the Strong LensIng and Cluster Evolution (SLICE) survey (*JWST* GO: #5594, PI: G. Mahler). As described in Section 4.3.7, SLICE targets a sample of 182 galaxy clusters over the redshift range $0.2 < z < 1.9$, out of which 124 clusters have been observed to date. SLICE is designed to pursue two interconnected science goals. First, the study of the buildup of stellar mass in clusters, focusing on the growth of brightest cluster

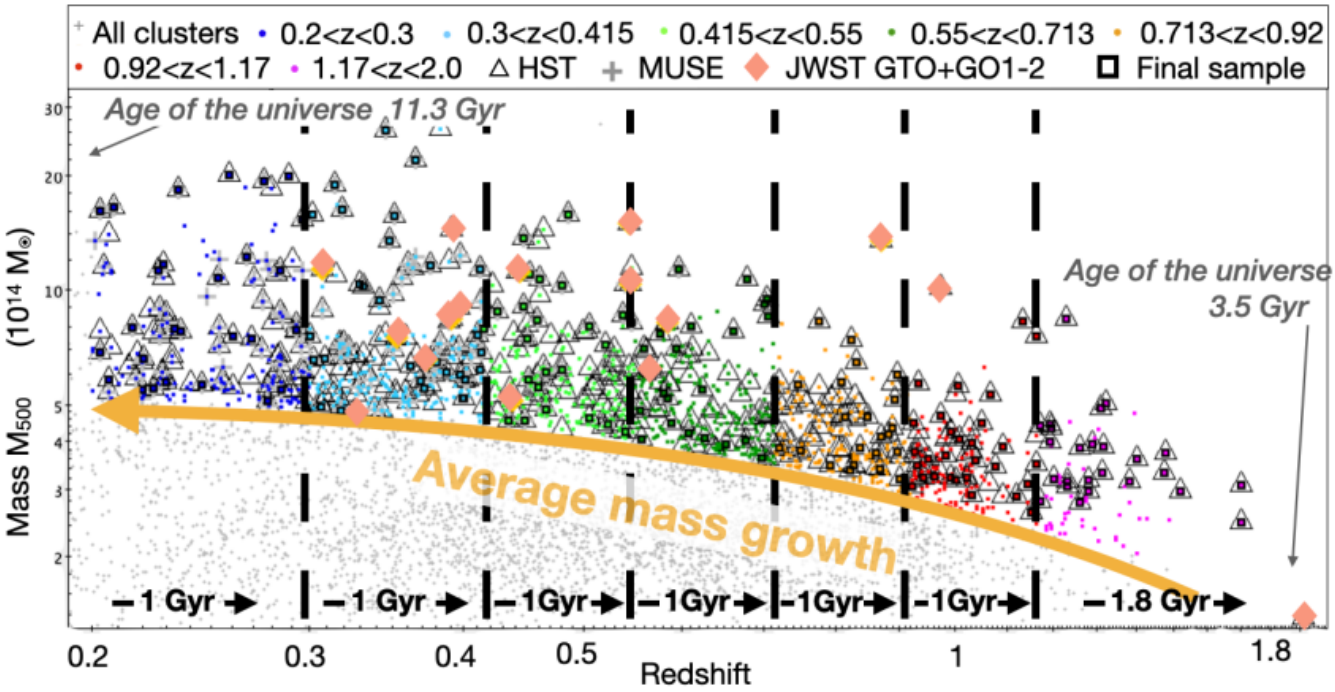

Figure 7.1: Mass-redshift diagram of SZ and X-ray catalogues from surveys including SPT (South Pole Telescope), ACT (Atacama Cosmology Telescope), Planck (Planck Satellite), BCS (ROSAT Brightest Cluster Sample), eBCS (Extended ROSAT Brightest Cluster Sample), REFLEX (ROSAT–ESO Flux-Limited X-ray Galaxy Cluster Survey) and MACS. Clusters highlighted by colours are above the mass growth (Fakhouri and Ma, 2008) of a $M_{500} = 2 \times 10^{14}\,M_{\odot}$ at $z = 1.9$. Our highest redshift clusters are still in a mass range where strong lensing is expected (Sharon et al., 2020). The sample provides evenly spaced look-back time (except the last bin). Dark squares show our final 182 cluster sampling. This sample uniquely traces the formation history of massive clusters and their substructures through time. (Credit : *JWST* #5594 PI: G. Mahler)

galaxies (BCGs) and the surrounding intra-cluster light (ICL), which is traced by old stellar populations and resolved globular cluster systems (e.g. **??**), i.e., the unique infrared sensitivity and the detection of tidal features, diffuse light fronts, and other ICL substructures (Montes and Trujillo, 2022), shedding light on the dynamical history of galaxy clusters. Second, SLICE seeks to map the underlying dark matter distribution, primarily through strong lensing modelling in clusters, but also in non-lensing clusters via the spatial distribution of globular clusters, which serve as reliable tracers of dark matter density (Lee et al., 2010; Ko et al., 2017), thereby offering a coherent view of the co-evolution of luminous and dark

matter in massive halos. One of the strengths of the sample is that it is selected (on average) to sample clusters that are on the same evolutionary track as shown in Figure 7.1. This approach enables studies of evolution with cosmic time of the properties that we aim to measure, and not only measure them in many clusters.

As part of the first public data release of the SLICE programme, strong lensing models for 14 massive galaxy clusters have been constructed and published (Cerny et al., 2025b), establishing a foundational dataset for studies of cluster lensing and structural evolution. MACS J0027.8+2616 (hereafter MACS 0027), at $z = 0.365$, is one of the clusters for which the strong lensing analysis has been conducted in this work. Originally identified by Repp and Ebeling (2018) as part of the MACS survey, MACS 0027 has been observed with both *HST* and *Chandra*. However, no lensing-based mass model was published. This work therefore presents the first strong lensing model of MACS 0027, constructed using high-resolution *JWST* imaging from the SLICE programme.

7.1 Observations

7.1.1 *Hubble Space Telescope*

MACS J0027 was observed by *HST* with ACS/F775W between January 17 2004 and May 29 2004 (PID : #9770, PI : Jorgensen), for 14370 s and then later for the MACS survey with ACS/F606W on October 2, 2010 (PID : #12166, PI : Ebeling) for 1200 s. The images were retrived from MAST and reduced to match the footprint, pixel scale and WCS of the new *JWST* data from SLICE. The final reference image was set to the NIRCam/F150W2 mosaic. When necessary, additional alignment was performed using `tweakreg` and `tweakback` to ensure consistency with the NIRCam WCS solution.

Table 7.1: List of observations of MACS J0027 used in this work. Columns 1 and 2 give the right ascension and declination of the observed field in degrees. Column 3 lists the instruments and filters. Column 4 and 5 give the exposure time in seconds and the observation date, respectively. Finally, columns 6 and 7 provide the programme ID and the PI respectively.

R.A. (J2000)	Dec. (J2000)	Instrument/Filter	Exp. Time (s)	Obs. Date	Prog. ID	PI
6.9662000	26.2742000	ACS/F606W	1200	2010-10-02	12166	Ebeling
6.9662000	26.2742000	ACS/F775W	14370	2004-01-17	9770	Jorgensen
6.9662000	26.2742000	NIRCam/F150W2	1836	024-08-21	5594	Mahler
6.9662000	26.2742000	NIRCam/F322W2	1836	024-08-21	5594	Mahler

7.1.2 *James Webb Space Telescope*

MACS J0027 is one of the very first observed SLICE clusters. It was observed on August 21st 2024, using NIRCam/F150W2 and NIRCam/F322W2 filters for an exposure time of 1836 s in both the filters. The NIRCam data reduction follows the procedure described by Rigby et al. (2025), as used in the *JWST* ERS program TEMPLATES. Level 1b products from MAST were processed using an STScI-adapted Python script and a modified version of the JWST pipeline (v1.15.1) with CRDS pmap 1303; a full description will be provided in Mahler et al. (in prep). The corrected frames were then processed into Level 3 mosaics in the F150W2 and F322W2 filters. The final mosaics are WCS-matched to Gaia, and the *HST* data were aligned to the *JWST* frames within astrometric uncertainties.

7.2 Strong Lensing Analysis

7.2.1 Multiple Images

Four multiple image systems, where 2 systems have spectroscopic redshifts from MUSE, are used in this model. System 1 consists of four multiple images arranged in an Einstein-cross configuration, with a spectroscopic redshift measurement of $z_{spec} = 3.127$. MUSE also reveals a total of five images with a spectroscopic redshift of $z_{spec} = 4.45$. Inspection of the *JWST* imaging shows that three of

these images share the same colour and morphology, and are spatially arranged in a configuration consistent with expectations from lensing. These three images are labelled as System 3. The other two sources at this redshift do not share the morphology or colours of System 3, but according to the best-fit lens model, they may be counter-images of each other. Thus, these two sources are labelled as candidate System 7, though they are not used in the lens model. The five MUSE sources are likely associated with two different galaxies at the same redshift, separated by ~ 30 kpc in the source plane. It is further discussed in Section 7.3.

Systems 1 and 2 have a large amount of substructure that is only visible in the *JWST* imaging, and these substructure components are used as additional constraints in the model.

A radial arc near the BCG is visually identified, but is not associated with any system due to the difficulty in securing a reliable spectroscopic redshift for it. Two other candidate systems are identified, systems 5 and 6. For the final model, only systems 1, 2, 3 and 4 are included, while keeping systems 5, 6 and 7 as candidates. It is noted that apart from these systems, there are several individually-lensed arcs found in *JWST* imaging that have no obvious counter images at the depth of the available data. All the multiple image systems are shown in Figure 7.2 and a list of these is given in appendix in Table 7.4. Figures 7.4, 7.5 and 7.6 (in appendix) shows zoomed in images of all the multiple images (including the candidates) from both *JWST* and *HST* observations.

7.2.2 Cluster Members

SExtractor is used to extract photometric information in dual mode for F606W and F775W. As done in MACS 1423 (Patel et al., 2024) and Abell 2744, the photometric data is used to select red sequence galaxies on a colour-magnitude diagram ($m_{F606W} - m_{F775W}$ *vs* m_{F775W}). The red sequence is fitted with a linear relation using iterative 3σ clipping. All galaxies within 2.5σ above and below this linear fit

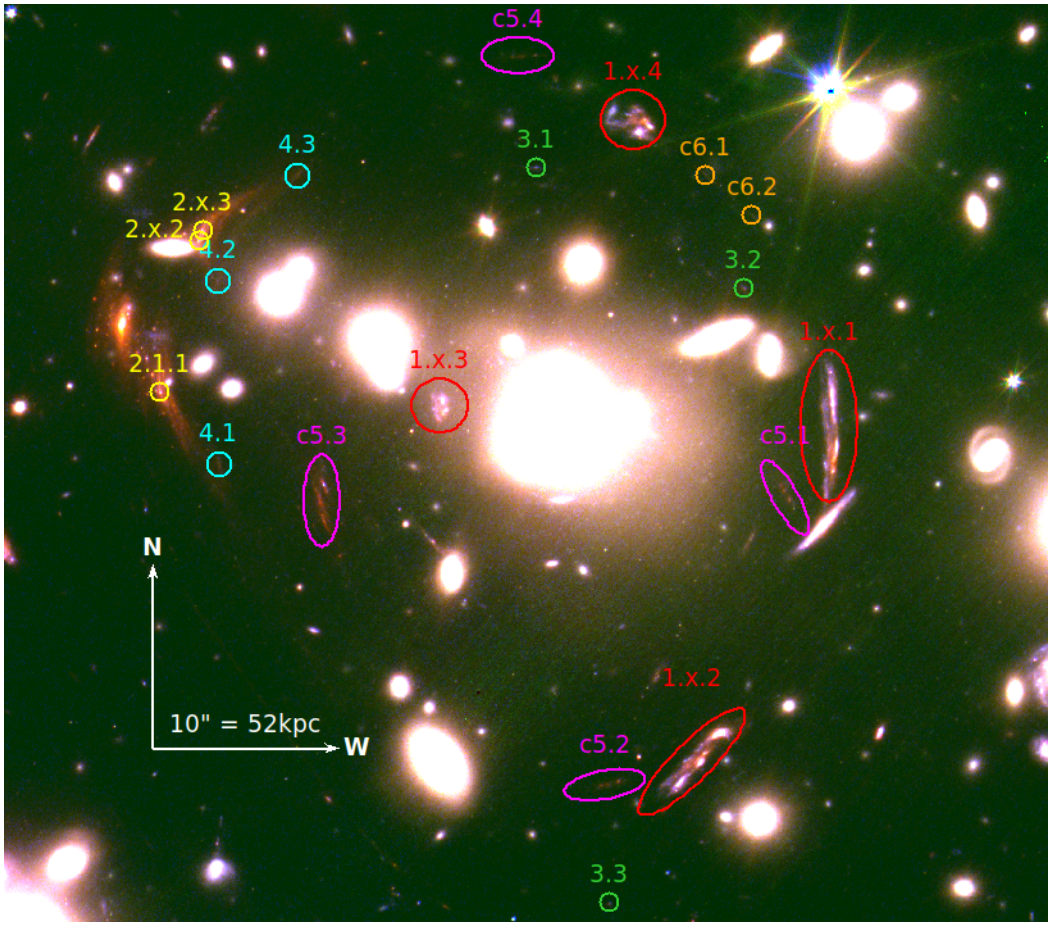

Figure 7.2: A *HST-JWST* colour composite image of MACS J0027 made using the ACS/F775W (blue), NIRCam/F150W2 (green) and NIRCam/F322W2 (red) passbands. Multiple image systems are highlighted with coloured circles and ID following the list given in Table 7.4. Images with ID such as 1.x.1 means that the image is divided into clumps, where 'x' denotes the ID of the clump.

in the colour-magnitude space are defined as red sequence. A bright limit is set to 19.39 mag by the BCG F775W magnitude and the fain limit is set to 23 mag. The final cluster member catalogue contains 172 galaxies, including the BCG.

7.2.3 Parametric Modelling

Parametric modelling is performed in the core of the cluster to map the mass distribution in this region with strong lensing. LENSTOOL is used for mass reconstruction. MACS J0027 is a dynamically relaxed system, similar to MACS J1423, with one BCG, as a result there is only one cluster-scale halo in the model. All

Table 7.2: Best fit parameters for our strong lensing mass model of MACS J0027. Values given in brackets are fixed in our model, while the ones quoted with error bars are being optimised. The coordinates of the cluster and BCG halos are given in arcseconds relative to the cluster center (R.A., Dec)=(6.9407970 26.2740340).

Components	ΔR.A.($''$)	ΔDec ($''$)	e	θ(deg)	$r_{\rm core}$ (kpc)	$r_{\rm cut}$ (kpc)	σ_0 (km s^{-1})
DMH	$3.830^{+0.33}_{-0.59}$	$-2.721^{+0.07}_{-0.41}$	$0.123^{+0.03}_{-0.01}$	$1.456^{+0.28}_{-0.76}$	$24.219^{+1.59}_{-2.70}$	[197.05]	1199^{+33}_{-77}
L$_*$ Gal.	–	–	–	–	[0.03]	3^{+4}_{-1}	258^{+58}_{-62}

parameters for this halo are free to vary except the cut radius, which is fixed to $r_{\rm cut} = 1000\,$kpc. For the small-scale halos, there are 172 cluster members, modelled using scaling relations with $mag_0 = 19.4$ at the MACS J0027 cluster redshift ($z = 0.365$) in the *HST*/F775W passband. Their positions, ellipticity and position angle are fixed to that of cluster galaxies. However, core radii are fixed to $r^\star_{core} = 0.15\,$kpc, while cut radii and velocity dispersions are let free to vary within $5 < r^\star_{\rm cut} < 50\,$kpc and $100 < \sigma^\star_0 < 400$ km s^{-1}, respectively.

MACS J0027 is optimised with a total of 4 multiple-image systems, corresponding to 19 images and 31 lensing constraints (additional constraints from the clumps within multiple images). The best-fit mass model yields an rms of $0.44''$, and a projected mass within 200 kpc of $M(R < 200, {\rm kpc}) = (1.73 \pm 0.07) \times 10^{14}$,M$_\odot$. The model optimises the redshift for system 2 and 4. The best-fit optimisation of the redshift for system 2 varies depending on the substructure clump used to perform the fit. The model predicts a redshift of $z = (5.64 \pm 0.36)$ and $z = (3.57 \pm 0.91)$, for the first (2.1) and second (2.2) clumps, respectively. For system 4, it predicts a redshift $z = (4.41 \pm 0.25)$. The mass contours from this strong lensing mass reconstruction is shown in Figure 7.3 and the best-fit parameters of this mass model are listed in Table 7.2.

7.3 Discussion & Conclusion

In this chapter, a strong lensing model for MACS J0027, one of the 14 galaxy clusters studied as part of the SLICE programme, has been presented. This model,

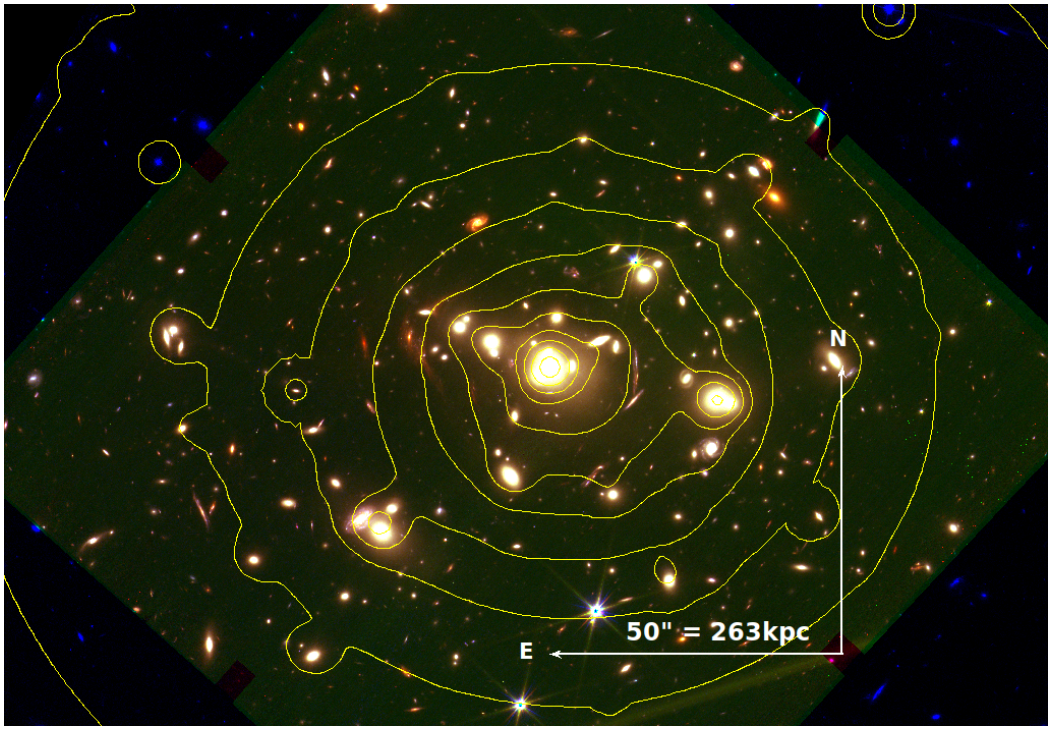

Figure 7.3: *HST*-*JWST* colour composite image of the central region of MACS J0027 created using *HST*/F775W (blue), *JWST*/150W2 (green) and *JWST*/322W2 (red). The yellow contours shows the mass distribution obtained with our strong lensing mass reconstruction as described in Section 7.2.3.

published in Cerny et al. (2025b), constitutes the first detailed lensing analysis of MACS J0027. The model incorporates four securely identified multiple image systems, along with three additional candidates. Of the confirmed systems, two were identifiable in archival *HST* imaging. However, the internal substructures within the multiple images, such as clumps and knots, were not resolved in *HST* and only became apparent in *JWST* imaging due to its superior resolution. In addition, none of the three candidate systems identified with *JWST* were detectable in *HST*. This highlights the critical advantage of *JWST* in unveiling faint and morphologically complex lensing features that were previously inaccessible.

7.3.1 High redshift detection with SLICE

The identification of overdensities of high redshift galaxies in the background of massive clusters is particularly compelling in the context of strong gravitational

lensing. Lensing magnification enhances both the brightness and apparent size of background galaxies, making them more readily detectable. However, such overdensities can result from either actual physical associations such as proto-clusters or from multiple lensed images of the same galaxy. Disentangling these scenarios is crucial and requires robust lens models to correctly identify multiply-imaged systems. Spectroscopic redshifts play a key role in this effort, helping to confirm whether detected sources are physically distinct or multiple images of a single background galaxy (Zheng et al., 2014; Caputi et al., 2021; Laporte et al., 2022; Noirot et al., 2023; Morishita et al., 2023).

In the field of MACS J0027, a galaxy at redshift $z = 4.45$ has been detected in more than five locations within the MUSE datacube. Four of these detections are also visible in the *JWST* imaging. However, their geometric configuration does not resemble that of a typical multiple image system. Consequently, this group of detections was initially considered as a proto-cluster candidate. Nonetheless, the strong lensing model of MACS J0027 predicts that three of these detections correspond to multiple images of the same source (classified as System 3), while the remaining detections show no evidence of multiplicity. At present, it remains unclear whether this is a genuine proto-cluster or a lensed system; further investigation is necessary.

The SLICE dataset, with its large spatial coverage and exceptional depth, is particularly well suited for the identification and morphological analysis of such high redshift groupings. Several other clusters in the SLICE sample exhibit similar overdensities of high-redshift galaxies. However, without complementary observations, such as deep spectroscopy or additional multi-band photometry distinguishing between multiply-imaged systems and physically associated galaxies remains challenging.

7.3.2 Weak Lensing with SLICE

The unprecedented depth of *JWST* has enabled the detection of thousands of background galaxies previously undetectable with *HST* or ground-based instruments, thereby opening new opportunities for weak lensing analyses. However, weak lensing with *JWST* has so far proven to be particularly challenging.

A key difficulty lies in the modelling of the point spread function (PSF), which is critical for accurate shape measurements of background galaxies. Uncertainties in the PSF model directly propagate into shear measurements, thereby impacting the reliability of the derived weak lensing signals. The PSF modelling is complicated by spatial variations across the detector, wavelength-dependent effects, and detector systematics that affect PSF morphology.

For SLICE specifically, observations are carried out using only two extra-wide *JWST*/NIRCam filters: F150W2 and F322W2. These filters span broad wavelength ranges (F150W2: 1.0–2.4 μm; F322W2: 2.4–4.0 μm), which makes PSF modelling across the field even more complex due to wavelength dependent effects and spatial variations. The extreme width of these filters means that galaxies at different redshifts sample different rest-frame wavelengths, leading to colour dependent PSF variations that must be carefully accounted for in the shear measurement pipeline. The SLICE team is actively developing improved techniques to address these challenges and enable robust shear measurements.

An additional complication arises in the selection of background galaxies for the weak lensing catalogue. Typically, such selection is performed using colour–colour diagrams, which require observations in at least three filters to reliably distinguish background sources from cluster members and foreground contaminants. As SLICE provides only two filters, this selection becomes difficult. In particular, the colours of high-redshift background sources can be mimicked by cluster red-sequence galaxies because the old, metal-rich stellar populations that define the red sequence exhibit strong 4000 Å and Balmer breaks; when those features are

redshifted into the broad F150W2 and F322W2 filters, very red observed colours are produced that closely resemble those of genuinely high-redshift galaxies whose ultraviolet breaks have similarly shifted into the same bands, rendering simple two-filter colour–magnitude cuts ineffective. In some cases, *HST* filters may be used to supplement the colour selection, but not all galaxies detected in *JWST* imaging are visible in *HST*. Many faint

textitJWST detected galaxies lack *HST* counterparts. For sources with available spectroscopic or reliable photometric redshifts, background selection can still be performed based on redshift criteria. However, for galaxies lacking redshift estimates, the background selection becomes more uncertain and requires careful treatment to minimise contamination. The SLICE team has extensive experience in weak lensing analysis and is developing solutions to address these challenges.

7.3.3 Summary & conclusion

SLICE is still in its early stages, and the full scientific potential of this programme has yet to be realised. As demonstrated in this chapter, the dataset brings both advantages and challenges. On the one hand, SLICE enables the detection of extremely faint and high redshift sources, and reveals detailed substructures within lensed galaxy features that were previously inaccessible. On the other hand, these same capabilities introduce new layers of complexity. The increased resolution of *JWST* often reveals multiple knots within individual sources, complicating the identification and association of multiply-imaged systems in strong lensing models. Meanwhile, for weak lensing, the difficulty in accurately selecting background galaxies, especially with only two available filters and the challenge of PSF characterisation across broad wavelength bands introduce systematic uncertainties that affect shear measurements. I am leading the SLICE weak-lensing working group and the development of strategies to overcome these challenges is being undertaken collaboratively with the SLICE team.

From a strong lensing perspective, SLICE provides high fidelity models of cluster

cores, yielding improved constraints on the internal mass distributions and enabling detailed studies of lensed high redshift galaxies. These models not only serve as important lensing tools for source reconstruction but also offer insight into the structure and dynamics of massive clusters. As the SLICE programme progresses, complementary spectroscopic follow-up and multi-band photometry will be essential to refine redshift estimates and further constrain the mass models, particularly in regions where candidate systems lack clear multiplicity or redshift information.

Looking ahead, SLICE aims to combine strong and weak lensing analyses, providing complementary constraints across spatial scales. These models will serve as the foundation for future statistical analyses of large samples of clusters, such as the subhalo mass function (SHMF), which in turn will offer crucial tests of dark matter models.

In summary, SLICE represents a transformative advance in gravitational lensing science. The model of MACS J0027 presented here, and in Cerny et al. (2025b), illustrates the foundation role that SLICE will play in shaping the next generation of lens models characterised by improved spatial resolution, extended redshift coverage, and greater modelling precision. While MACS J0027 serves as a representative case study, it is merely one example within the larger SLICE sample of 124 clusters, each offering a promising window into the high redshift Universe and the dark matter structures that shape it.

Summary

This scientific journey begins with cosmology, where the Universe unfolds according to Einstein's General Relativity. Here, space itself expands, carrying galaxies away from each other in a cosmic dance that has continued for nearly 14 billion years. As deeper exploration into this cosmic story is undertaken, one of the greatest mysteries of modern science is encountered: the invisible scaffolding that holds the Universe together, dark matter. This mysterious substance, which makes up about 80% of all matter in the Universe, does not emit light nor interact electromagnetically, yet its gravitational influence shapes the very structure of the cosmos. Different theoretical frameworks for understanding this enigma are explored in this thesis, from CDM that moves slowly through space, to WDM with slightly higher velocities, and even SIDM that can collide with itself. These theories form the foundation of the ΛCDM model, our best current description of the Universe, where Λ represents dark energy and CDM represents cold dark matter.

Galaxy clusters emerge as the primary laboratories, massive gravitational wells containing hundreds or thousands of galaxies, hot gas, and vast amounts of dark matter. These cosmic giants are the largest gravitationally bound structures in the universe, and they offer unique windows into the nature of dark matter because their immense gravity bends spacetime itself. This bending of spacetime creates a phenomenon that becomes the primary investigative tool: gravitational lensing.

Like a cosmic magnifying glass, the gravity of galaxy clusters deflects and distorts the light from more distant galaxies behind them. Strong gravitational lensing occurs close to the cluster center, where gravity is so intense that background galaxies are stretched into dramatic arcs or split into multiple images of the same object. These spectacular distortions provide precise constraints on the mass distribution in the cluster core. Meanwhile, weak gravitational lensing affects galaxies further from the cluster center, creating subtle shape distortions that, while individually barely perceptible, reveal the cluster's mass distribution when analysed statistically across thousands of background galaxies.

To unlock this potential, precise modelling techniques are required. In the cluster core, where strong lensing regime dominates, parametric model are employed assuming that light traces mass, and in the outskirts of the cluster where weak lensing is into effect, a more flexible non-parametric multi-scale grid of potentials is used to model this region where the lensing signal is more diffuse than in the core. The strong lensing regions are optimised using the positions of the multiple image systems while the weak lensing regions are optimised using shapes of the weakly lensed background sources. An MCMC based software, Lenstool is used to perform the mass reconstruction. When combining the model, there are two ways : sequential fit, where the strong lensing parameters are fixed to the best-fit model and the grid in the weak lensing region is optimised as a second step. Second is the joint-fit, where both the strong and weak lensing regions are optimised simultaneously. In this work, however, only sequential-fit is used.

A comprehensive lensing analysis of the high-redshift, dynamically relaxed cluster MACS J1423, combining strong and weak lensing constraints to construct a robust mass model across both the core and outskirts is presented. The sequential fitting approach, with multiple images and a densely sampled weak lensing catalogue, yields precise mass estimates that are consistent with previous lensing studies, though systematically higher than X-ray-derived values, an offset likely attributable to the cluster's triaxial geometry and line-of-sight elongation. The cluster's well-

aligned baryonic and total mass distributions, coupled with its regular morphology and the presence of central radial arcs, reinforce its status as an excellent candidate for probing the nature of dark matter. As a dynamically relaxed system with well-constrained mass structure, MACS J1423 offers a valuable reference point within the thesis.

Then comes Abell 2744, presenting a detailed strong and weak lensing mass model of the dynamically disturbed cluster, constructed using a sequential fitting approach that combines parametric modelling in the core with a non-parametric grid-based method in the outskirts. Leveraging spectroscopically confirmed multiple image systems and a high-density weak lensing catalogue derived from *JWST* and *HST* observations, the resulting model provides a refined reconstruction of the cluster's mass distribution, particularly improving constraints in the previously under-constrained N and NW regions. While the combined model yields a higher total mass compared to earlier studies, this is attributed to a systematic overestimation in the outskirts, an issue also noted in other lensing works and warranting further examination. Crucially, Abell 2744 exhibits a rich substructure population, enabling the construction of the subhalo mass function (SHMF), which offers a promising avenue to test predictions from various dark matter models. The analysis presented here thus not only characterises the mass distribution of a complex, merging cluster, but also establishes a foundation for future comparisons with cosmological simulations, aimed at constraining the fundamental properties of dark matter through observational lensing signatures.

As this thesis approaches its conclusion, it turns toward the future. The SLICE programme is introduced, a new effort to observe a larger sample of massive clusters with lensing-quality imaging from both *JWST* and *HST*. An early result from SLICE published in Cerny et al. (2025b) is presented in the form of a lens model for MACS J0027. With high-resolution *JWST* imaging, previously unresolved substructures and candidate multiple-image systems have been identified, demonstrating the transformative capabilities of *JWST* over archival *HST* data. The results

also underscore key challenges introduced by this leap in observational power: such as the increased complexity in identification of multiple image substructures and the limitations in weak lensing analyses due to PSF modelling uncertainties and insufficient filter coverage for background galaxy selection. Nevertheless, SLICE holds enormous promise. Its depth and resolution allow for the detection of faint, high-redshift galaxies and enable the construction of high-fidelity lens models. As the programme advances, the integration of spectroscopic follow-up and expanded photometry will be essential for robust redshift estimation and improved lensing constraints. Ultimately, SLICE is poised to serve as the foundation for large-scale statistical studies of galaxy clusters and their substructure, paving the way for new constraints on the nature of dark matter and the evolution of cosmic structure.

A key strength of the lens models presented in this thesis lies in their broader applicability beyond the immediate goal of mass reconstruction. Precise lensing mass models are a prerequisite for a wide range of astrophysical and cosmological applications, including accurate magnification estimates for high redshift galaxy studies, time delay predictions, and detailed comparisons with numerical simulations. These applications can only be achieved when the underlying mass distribution is constrained with sufficient accuracy. The strong lensing, weak lensing, and combined strong+weak lensing models developed in this work achieve a high level of precision in reproducing lensing observables, particularly in the cluster core, thereby providing robust mass maps suitable for these diverse scientific uses.

Despite these strengths, several challenges were identified during the modelling process. One of the most significant issues concerns the discrepancy between mass distributions inferred from strong lensing only models and those obtained when strong and weak lensing constraints are combined. In particular, differences were found in the outer regions of the clusters, where strong lensing alone provides limited leverage on the large scale mass profile. This discrepancy can be largely driven by degeneracies in parameters such as the cut radius of cluster scale halos, which are poorly constrained by strong lensing data alone but have a strong impact

on the inferred total mass distribution.

Several possible strategies were identified to address this limitation. One approach is to incorporate weak lensing information into strong lensing only models by using weak lensing constraints in the outskirts to put better constraints on the cut radius of cluster scale halos. This would allow strong lensing models to retain their high central precision while being better anchored to the large scale mass distribution. A complementary strategy involves systematically testing combined and hybrid modelling approaches on simulated clusters, where the true mass distribution is known. Such tests would enable the performance and biases of strong lensing only, weak lensing only, and combined methods to be quantified in a controlled manner, providing guidance for interpreting discrepancies observed in real data.

In the context of constraining dark matter through the subhalo mass function (SHMF), the results presented in this thesis represent a meaningful but necessarily intermediate step. The subhaloes recovered by the lens models typically lie in the mass range of approximately 10^{12}–10^{13} $M_{\odot}$. This regime corresponds to the most massive galaxy scale subhaloes in cluster cores and enables a first-order characterisation of the high mass end of the SHMF. While this provides a useful consistency check with expectations from structure formation models, it does not yet reach sufficiently low masses to place direct constraints on the particle nature of dark matter, where differences between cold, warm, or self-interacting scenarios are expected to become most pronounced.

The statistical power of SHMF-based constraints is further limited by cluster-to-cluster variance. The inferred subhalo population depends on factors such as merger history, dynamical state, projection effects, and baryonic physics, all of which introduce significant scatter. To average over this variance and obtain statistically meaningful constraints on dark matter models, a sample of at least several tens of clusters is likely required, with homogeneous data quality and a consistent modelling framework. Samples of this size are beyond the scope of the present work but are expected to become accessible with ongoing and forthcoming cluster lensing

surveys.

Finally, it was recognised that the SHMF does not exhaust the information content of lensing based mass reconstructions. Other properties of the reconstructed mass distribution may provide complementary constraints on dark matter physics. In particular, the morphology of the mass distribution, including ellipticity, asymmetry, and the presence of central density cores, may be sensitive to non-standard dark matter scenarios. Additionally, spatial offsets between dark matter, galaxies, and intracluster gas in merging systems, as well as variations in mass smoothness and substructure distribution, offer alternative probes that are less dependent on detecting large numbers of low-mass subhaloes. When combined with SHMF measurements, these morphological and structural observables may provide a more complete and robust framework for testing dark matter models.

In future work, the observational results discussed above will be compared with theoretical predictions from the BAHAMAS (BAryons and HAloes of MAssive Systems) suite of cosmological hydrodynamical simulations. The BAHAMAS project is specifically designed to reproduce the global properties of massive haloes, particularly galaxy clusters, by explicitly modelling the coupled evolution of dark matter, gas, stars, and supermassive black holes within a cosmological volume. By calibrating baryonic feedback processes to match key observational constraints, such as the stellar and gas content of groups and clusters, BAHAMAS will provide a physically realistic framework for interpreting lensing derived substructure measurements. The cold dark matter realisations will therefore serve as a robust benchmark for the expected abundance, spatial distribution, and mass spectrum of subhaloes in a standard ΛCDM Universe.

To explore whether departures from collisionless dark matter physics could alter the predicted subhalo population, the self interacting dark matter extensions of the BAHAMAS simulations developed by Robertson et al. (2019) will also be incorporated. These simulations implement isotropic, velocity independent dark matter self scattering with cross-sections of 0.1, 0.3, and 1.0 $\mathrm{cm}^2\ \mathrm{g}^{-1}$, spanning the range

of values commonly considered in the context of small scale structure. In addition, a velocity dependent SIDM model will be examined, in which self interactions are suppressed at the high relative velocities characteristic of galaxy clusters, while remaining effective on galactic scales.

By comparing the lensing inferred subhalo mass function and projected mass distribution of Abell 2744 with predictions from both the CDM and SIDM BAHAMAS cluster cut-outs, it will be possible to assess how different dark matter interaction scenarios impact subhalo survival and radial distributions. This comparison will provide a controlled and physically motivated framework for interpreting the observational results and for evaluating the extent to which current and future lensing data can place meaningful constraints on non-standard dark matter physics.

Thus, the thesis closes not with an ending, but with a beginning, the promise of future discoveries, new constraints, and deeper insights into the dark cosmos that surrounds us.

Appendix

Table 7.3: Multiple image systems used as constraints in strong-lensing analysis of Abell 2744. Column 1 lists the ID of the multiple images. Columns 2 and 3 give the right ascension and declination in degrees (J2000). Column 4 gives the spectroscopic redshift of each system.

ID	R.A.	Decl.	$z_{\rm spec}$
3.1	3.589625	-30.393906	3.9803
3.2	3.588429	-30.393786	3.9803
4.1	3.592114	-30.402634	3.5719
4.2	3.595643	-30.401623	3.5719
4.4	3.593193	-30.404915	3.5719
4.5	3.593593	-30.405106	3.5719
5.2	3.584982	-30.391374	4.0225
5.3	3.579958	-30.394772	4.0225
105.1	3.583430	-30.392070	4.0225
105.2	3.582292	-30.392789	4.0225
9.1	3.594361	-30.401393	1.8550
9.2	3.594298	-30.401769	1.8550
9.3	3.594656	-30.401569	1.8550

Continued on next page

Table 7.3 – continued from previous page

ID	R.A.	Decl.	z_{spec}
10.1	3.585843	-30.393272	2.5761
10.2	3.585251	-30.393944	2.5761
10.3	3.585416	-30.393838	2.5761
10.4	3.585837	-30.393228	2.5761
11.1	3.596646	-30.394541	1.0990
11.2	3.596523	-30.394387	1.0990
11.3	3.596729	-30.394526	1.0990
12.1	3.588947	-30.394219	1.2243
12.2	3.588794	-30.394220	1.2243
12.3	3.588886	-30.394296	1.2243
15.1	3.573677	-30.383882	1.0410
15.2	3.573412	-30.383669	1.0410
15.3	3.573566	-30.383642	1.0410
16.1	3.586430	-30.393944	1.0350
16.2	3.586416	-30.393949	1.0350
16.3	3.586557	-30.393908	1.0350
17.1	3.594527	-30.392163	1.1316
17.2	3.594558	-30.392221	1.1316
17.3	3.594533	-30.392108	1.1316
18.1	3.583863	-30.408006	0.5420
18.2	3.583514	-30.407516	0.5420
18.3	3.583887	-30.407887	0.5420
19.1	3.595361	-30.403189	0.9124
19.2	3.594953	-30.403290	0.9124
19.3	3.595111	-30.403073	0.9124
20.1	3.580074	-30.395418	1.0352

Continued on next page

Table 7.3 – continued from previous page

ID	R.A.	Decl.	z_{spec}
20.2	3.580091	-30.395489	1.0352
20.3	3.579990	-30.395476	1.0352
21.1	3.585154	-30.397028	1.1599
21.2	3.585147	-30.397098	1.1599
21.3	3.585249	-30.397097	1.1599
22.1	3.576365	-30.389354	1.2150
22.2	3.576230	-30.389432	1.2150
22.3	3.576356	-30.389299	1.2150
24.1	3.577732	-30.388734	1.0630
24.2	3.577554	-30.388748	1.0630
24.3	3.577748	-30.388552	1.0630
26.1	3.593701	-30.395055	1.4342
26.2	3.593495	-30.395220	1.4342
26.3	3.593577	-30.395085	1.4342
29.1	3.578061	-30.387575	2.4223
29.2	3.578083	-30.387654	2.4223
29.3	3.578256	-30.387607	2.4223
30.1	3.586966	-30.394351	1.6287
30.2	3.587012	-30.394482	1.6287
30.3	3.586998	-30.394353	1.6287
31.1	3.578437	-30.384641	1.0643
31.2	3.578446	-30.384715	1.0643
31.3	3.578417	-30.384605	1.0643
32.1	3.585302	-30.389714	1.1450
32.2	3.585310	-30.389832	1.1450
32.3	3.585258	-30.389779	1.1450

Continued on next page

Table 7.3 – continued from previous page

ID	R.A.	Decl.	z_{spec}
33.1	3.586483	-30.391773	1.4230
33.2	3.586325	-30.391918	1.4230
33.3	3.586457	-30.391657	1.4230
34.1	3.577514	-30.388714	1.1794
34.2	3.577313	-30.389029	1.1794
34.3	3.577533	-30.388567	1.1794
35.1	3.590066	-30.399158	1.3575
35.2	3.589634	-30.399295	1.3575
35.3	3.589728	-30.399165	1.3575
36.1	3.586714	-30.390273	0.9702
36.2	3.586779	-30.390316	0.9702
36.3	3.586717	-30.390248	0.9702
37.1	3.577367	-30.388643	1.1510
37.2	3.577341	-30.388736	1.1510
37.3	3.577366	-30.388576	1.1510
38.1	3.589164	-30.395882	1.3961
38.2	3.589197	-30.395859	1.3961
38.3	3.588974	-30.395846	1.3961
39.1	3.580801	-30.391286	1.0817
39.2	3.580830	-30.391226	1.0817
39.3	3.580802	-30.391260	1.0817
40.1	3.578430	-30.385300	1.0145
40.2	3.578435	-30.385358	1.0145
40.3	3.578423	-30.385291	1.0145
41.1	3.590015	-30.397977	1.3470
41.2	3.590052	-30.397817	1.3470

Continued on next page

Table 7.3 – continued from previous page

ID	R.A.	Decl.	z_{spec}
41.3	3.589939	-30.398045	1.3470
42.1	3.581421	-30.389530	1.0730
42.2	3.581435	-30.389475	1.0730
42.3	3.581418	-30.389594	1.0730
43.1	3.589624	-30.396153	1.3424
43.2	3.589560	-30.396106	1.3424
43.3	3.589666	-30.396187	1.3424
44.1	3.578215	-30.387551	0.9748
44.2	3.578246	-30.387557	0.9748
44.3	3.578214	-30.387445	0.9748
45.1	3.585887	-30.390446	1.2062
45.2	3.585893	-30.390360	1.2062
45.3	3.585801	-30.390453	1.2062
46.1	3.588102	-30.393315	1.0510
46.2	3.588104	-30.393316	1.0510
46.3	3.588078	-30.393327	1.0510
47.1	3.588950	-30.393730	1.0562
47.2	3.588944	-30.393739	1.0562
47.3	3.588983	-30.393702	1.0562
48.1	3.588197	-30.390789	1.0913
48.2	3.588154	-30.390789	1.0913
48.3	3.588217	-30.390712	1.0913
49.1	3.588703	-30.393008	1.0887
49.2	3.588681	-30.393022	1.0887
49.3	3.588711	-30.393022	1.0887
50.1	3.582546	-30.390576	1.2650

Continued on next page

Table 7.3 – continued from previous page

ID	R.A.	Decl.	z_{spec}
50.2	3.582562	-30.390626	1.2650
50.3	3.582531	-30.390568	1.2650
51.1	3.580123	-30.395931	1.0948
51.2	3.580087	-30.396020	1.0948
51.3	3.580129	-30.395859	1.0948
53.1	3.572331	-30.382855	1.0817
53.2	3.572345	-30.382983	1.0817
53.3	3.572225	-30.382904	1.0817
55.1	3.588912	-30.402554	1.2424
55.2	3.588976	-30.402466	1.2424
55.3	3.588803	-30.402517	1.2424
56.1	3.585476	-30.396705	1.0970
56.2	3.585438	-30.396819	1.0970
56.3	3.585466	-30.396615	1.0970
58.1	3.585049	-30.395272	1.0704
58.2	3.585032	-30.395330	1.0704
58.3	3.585065	-30.395215	1.0704
60.1	3.581987	-30.388887	1.0838
60.2	3.581975	-30.388964	1.0838
60.3	3.581996	-30.388941	1.0838
61.1	3.590944	-30.399834	1.2100
61.2	3.590897	-30.399885	1.2100
61.3	3.590897	-30.399818	1.2100
62.1	3.588123	-30.395547	1.0874
62.2	3.588113	-30.395586	1.0874
62.3	3.588147	-30.395523	1.0874

Continued on next page

Table 7.3 – continued from previous page

ID	R.A.	Decl.	z_{spec}
64.1	3.577903	-30.386469	1.0484
64.2	3.577899	-30.386547	1.0484
64.3	3.577877	-30.386461	1.0484
65.1	3.580651	-30.391946	1.0879
65.2	3.580652	-30.391998	1.0879
65.3	3.580637	-30.391918	1.0879
66.1	3.584302	-30.397156	1.1180
66.2	3.584298	-30.397222	1.1180
66.3	3.584286	-30.397150	1.1180
67.1	3.577714	-30.387162	1.0588
67.2	3.577719	-30.387230	1.0588
67.3	3.577692	-30.387143	1.0588
68.1	3.578953	-30.389676	1.0912
68.2	3.578943	-30.389614	1.0912
68.3	3.578921	-30.389666	1.0912
69.1	3.587677	-30.394712	1.0707
69.2	3.587683	-30.394635	1.0707
69.3	3.587680	-30.394703	1.0707
70.1	3.552409	-30.373992	2.3915
70.2	3.552351	-30.374079	2.3915
72.1	3.549645	-30.378464	3.7468
72.2	3.551115	-30.374758	3.7468
72.3	3.552295	-30.372243	3.7468
74.1	3.545136	-30.374918	2.3743
74.2	3.545250	-30.374700	2.3743
74.3	3.547033	-30.369489	2.3743

Continued on next page

Table 7.3 – continued from previous page

ID	R.A.	Decl.	$z_{\rm spec}$
A78.1	3.579614	-30.357722	2.3151
A78.2	3.579236	-30.357810	2.3151
A78.3	3.574876	-30.356072	2.3151
B78.1	3.579706	-30.357722	2.3151
B78.2	3.579162	-30.357838	2.3151
B78.3	3.574914	-30.356079	2.3151

Table 7.4: Multiple image systems used as constraints in strong-lensing analysis of MACS J0027. Column 1 lists the ID of the multiple images. Columns 2 and 3 give the right ascension and declination in degrees (J2000). Column 4 gives the redshift of each system. Redshifts without error bars correspond to spectroscopic measurements while the presence of error bars highlights the redshifts optimised by the mass model.

ID	RA (deg)	Dec. (deg)	z
1.1.1	6.936236	26.274556	3.1267
1.1.2	6.938848	26.268583	
1.1.3	6.942843	26.274449	
1.1.4	6.939522	26.278502	
1.2.1	6.936217	26.274369	
1.2.2	6.938797	26.268650	
1.2.3	6.942850	26.274421	
1.2.4	6.939509	26.278536	
1.3.1	6.936158	26.273721	
1.3.2	6.938467	26.268934	
1.3.3	6.942782	26.274284	
1.3.4	6.939322	26.278602	

Continued on next page

Table 7.4 – continued from previous page

ID	RA (deg)	Dec. (deg)	z
1.4.1	6.936253	26.274864	
1.4.2	6.938879	26.268495	
1.4.3	6.942814	26.274491	
1.4.4	6.939490	26.278434	
1.5.1	6.936227	26.273358	
1.5.2	6.938406	26.269068	
1.5.3	6.942842	26.274233	
1.5.4	6.939418	26.278711	
2.1.1	6.947640	26.274558	$5.639^{+0.21}_{-0.54}$
2.1.2	6.946998	26.276859	
2.1.3	6.946939	26.277012	
2.2.2	6.946946	26.276888	$3.573^{+1.71}_{-0.33}$
2.2.3	6.946902	26.276983	
3.1.1	6.941260	26.277969	4.45
3.1.2	6.937722	26.276142	
3.1.3	6.940009	26.266777	
4.1.1	6.946621	26.273450	$4.411^{+0.17}_{-0.33}$
4.1.2	6.946658	26.276252	
4.1.3	6.945298	26.277877	
c5.1.1	6.937108	26.273139	–
c5.1.2	6.940155	26.268576	
c5.1.3	6.944855	26.272580	
c5.1.4	6.941673	26.279653	
c5.2.1	6.937048	26.273066	
c5.2.2	6.940033	26.268586	
c5.2.3	6.944899	26.272698	

Continued on next page

Table 7.4 – continued from previous page

ID	RA (deg)	Dec. (deg)	z
c5.2.4	6.941504	26.279663	
c5.3.1	6.936962	26.272928	
c5.3.2	6.939858	26.268637	
c5.3.3	6.944925	26.272887	
c5.3.4	6.941269	26.279685	
c6.1.1	6.938385	26.277879	–
c6.1.2	6.937572	26.277232	

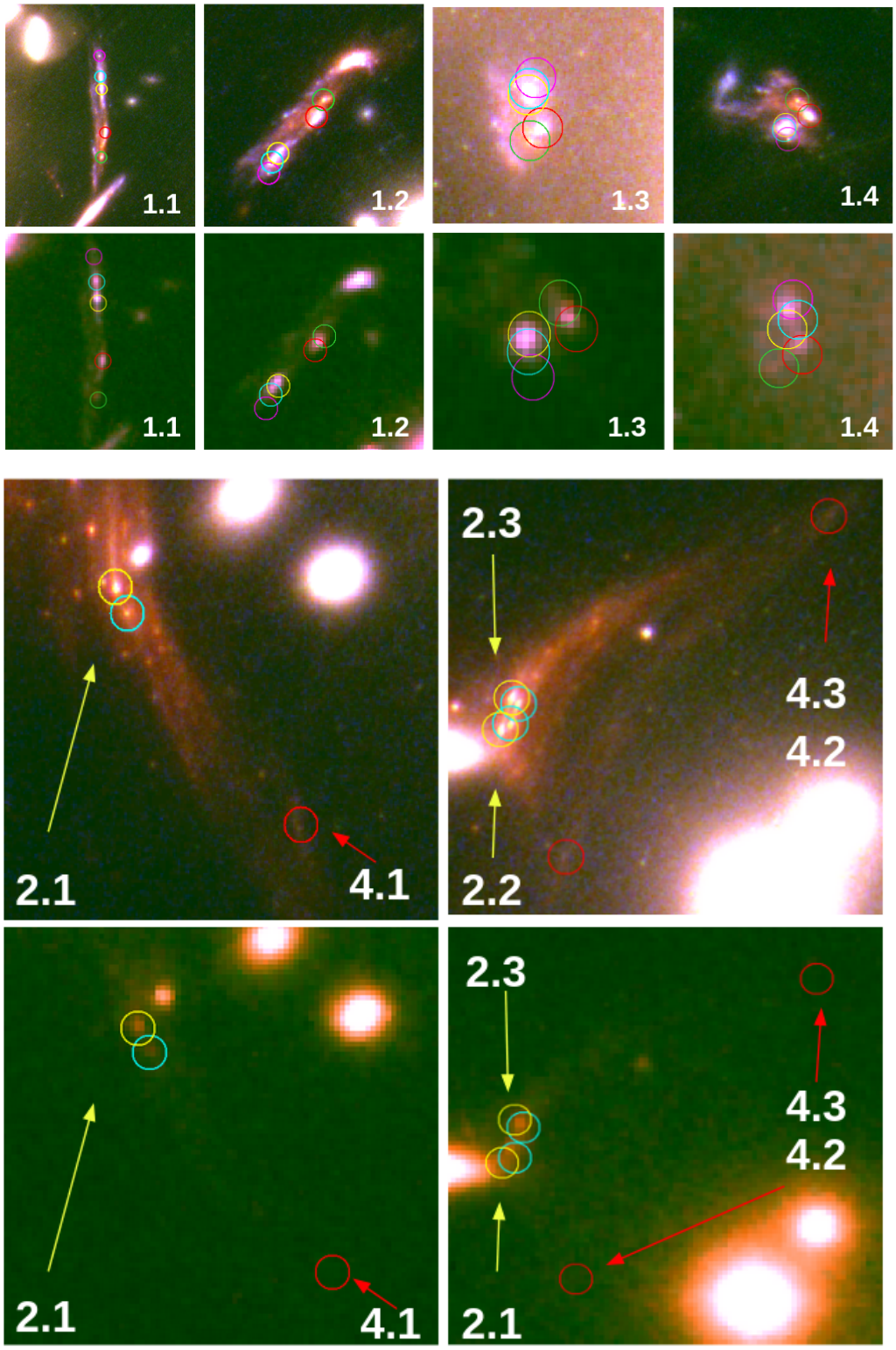

Figure 7.4: Zoomed in images of all the multiple image systems in MACS J0027. Top panel for each system shows the *JWST* images while bottom panel shows *HST* images. The clumps in each image are highlighted in different colours. It can be seen that for many *JWST* images, there is no *HST* counter part. It should be noted that systems 5 and 6 are candidate systems and were not taken into account for the strong lensing analysis.

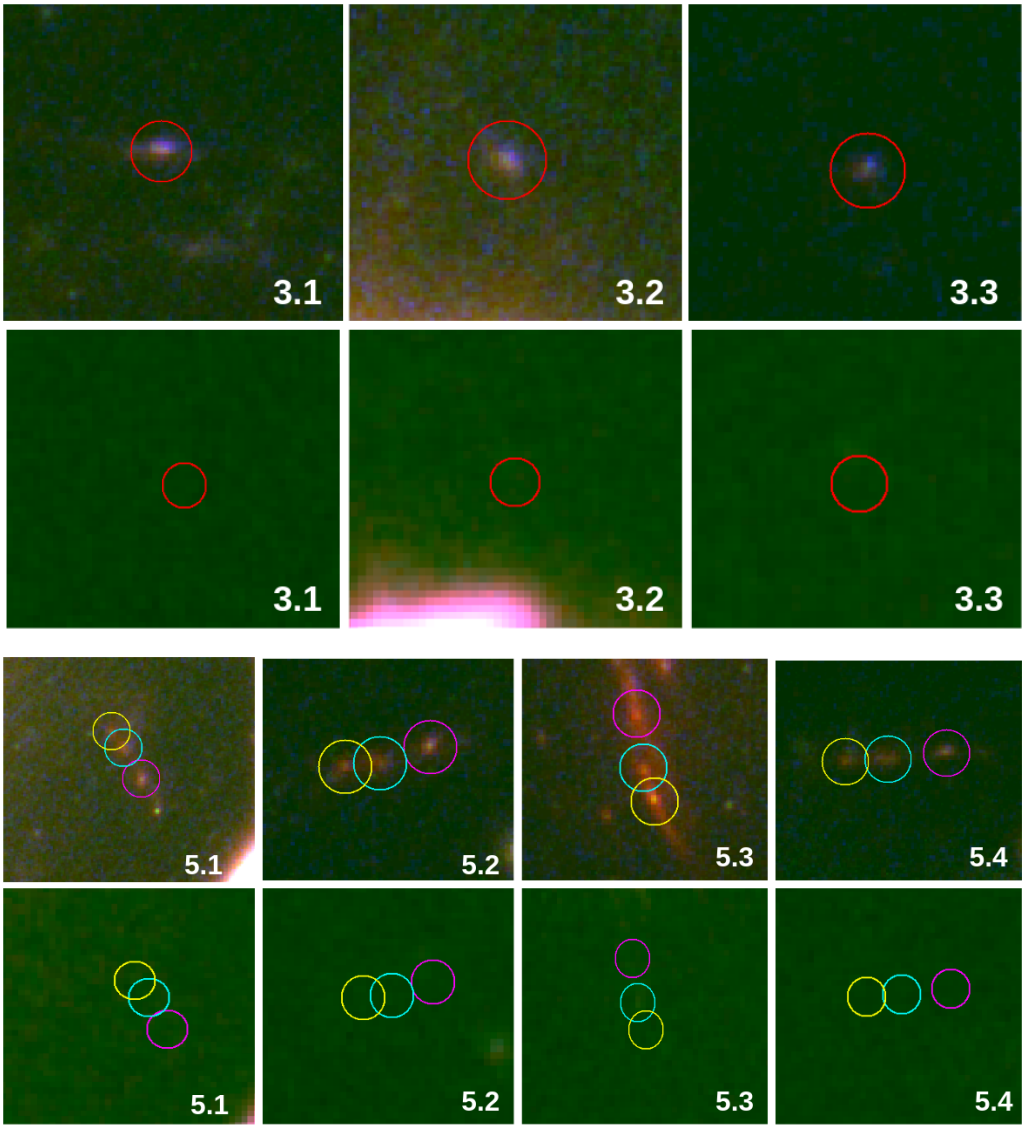

Figure 7.5: Zoomed in images of all the multiple image systems in MACS J0027. Top panel for each system shows the *JWST* images while bottom panel shows *HST* images. The clumps in each image are highlighted in different colours. It can be seen that for many *JWST* images, there is no *HST* counter part. It should be noted that systems 5 and 6 are candidate systems and were not taken into account for the strong lensing analysis.

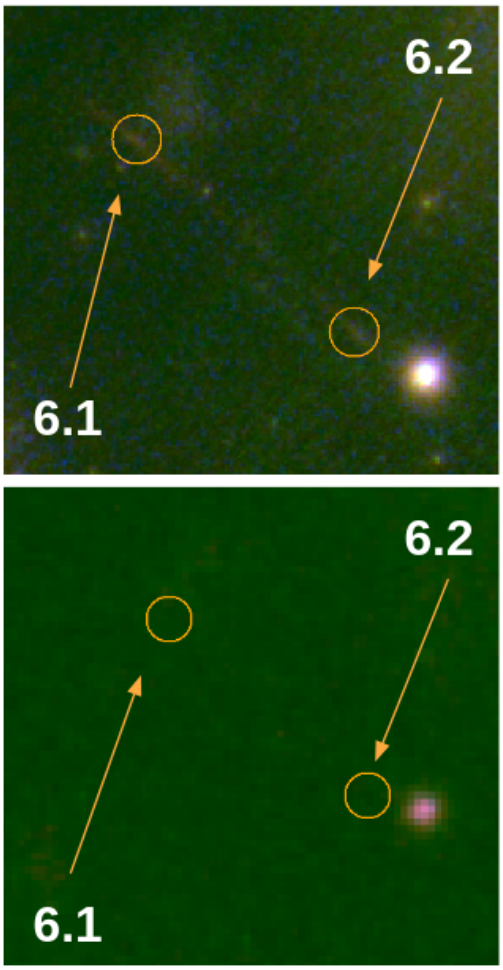

Figure 7.6: Zoomed in images of all the multiple image systems in MACS J0027. Top panel for each system shows the *JWST* images while bottom panel shows *HST* images. The clumps in each image are highlighted in different colours. It can be seen that for many *JWST* images, there is no *HST* counter part. It should be noted that systems 5 and 6 are candidate systems and were not taken into account for the strong lensing analysis.

Bibliography

K. e. a. Abazajian. Production and evolution of sterile neutrino dark matter in the early universe. *Physical Review D*, 64:023501, 2001.

G. O. Abell. The Distribution of Rich Clusters of Galaxies. , 3:211, May 1958. doi: 10.1086/190036.

G. O. Abell, J. Corwin, Harold G., and R. P. Olowin. A Catalog of Rich Clusters of Galaxies. , 70:1, May 1989. doi: 10.1086/191333.

A. Acebron, E. Jullo, M. Limousin, A. Tilquin, C. Giocoli, M. Jauzac, G. Mahler, and J. Richard. Hubble Frontier Fields: systematic errors in strong lensing models of galaxy clusters - implications for cosmography. , 470(2):1809–1825, Sept. 2017. doi: 10.1093/mnras/stx1330.

A. Acebron, S. Schuldt, C. Grillo, P. Bergamini, G. Granata, U. Meštrić, G. B. Caminha, M. Meneghetti, A. Mercurio, P. Rosati, S. H. Suyu, and E. Vanzella. Augmenting the power of time-delay cosmography in lens galaxy clusters by probing their member galaxies. I. Type Ia supernovae. , 680:L9, Dec. 2023. doi: 10.1051/0004-6361/202348090.

A. Acebrón, E. Jullo, M. Limousin, et al. Cosmology with multiple images in the hubble frontier fields clusters. *Astronomy Astrophysics*, 662:A22, 2022. doi: 10.1051/0004-6361/202141858.

P. A. R. Ade and et al. Planck 2015 results. XIII. Cosmological parameters. *Astronomy Astrophysics*, 594, 2016. doi: 10.1051/0004-6361/201525830.

S. W. Allen. The x-ray properties of the most x-ray-luminous clusters of galaxies. i. the data. *Monthly Notices of the Royal Astronomical Society*, 296:392–406, 1998. doi: 10.1046/j.1365-8711.1998.01455.x. URL https://doi.org/10.1046/j.1365-8711.1998.01455.x.

S. W. Allen, R. W. Schmidt, H. Ebeling, A. C. Fabian, and L. van Speybroeck. Constraints on dark energy from Chandra observations of the largest relaxed galaxy clusters. , 353(2):457–467, Sept. 2004. doi: 10.1111/j.1365-2966.2004.08080.x.

S. W. Allen, A. E. Evrard, and A. B. Mantz. Cosmological parameters from observations of galaxy clusters. *Annual Review of Astronomy and Astrophysics*, 49:409–470, 2011. doi: 10.1146/annurev-astro-081710-102514.

J. F. V. Allingham, A. Zitrin, M. Golubchik, L. J. Furtak, M. Bayliss, C. Cerny, J. M. Diego, A. C. Edge, R. Gassis, M. D. Gladders, M. Jauzac, D. J. Lagattuta, M. Limousin, G. Mahler, A. K. Meena, P. Natarajan, and K. Sharon. SLICE: SPT-CL J0546-5345 – A prominent strong-lensing cluster at $z = 1.07$. *arXiv e-prints*, art. arXiv:2507.08949, July 2025.

D. E. Applegate, A. von der Linden, P. L. Kelly, M. T. Allen, S. W. Allen, P. R. Burchat, D. L. Burke, H. Ebeling, A. Mantz, and R. G. Morris. Weighing the Giants - III. Methods and measurements of accurate galaxy cluster weak-lensing masses. , 439(1):48–72, Mar. 2014. doi: 10.1093/mnras/stt2129.

S. Arnouts, S. Cristiani, L. Moscardini, S. Matarrese, F. Lucchin, A. Fontana, and E. Giallongo. Measuring and modelling the redshift evolution of clustering: the Hubble Deep Field North. , 310(2):540–556, Dec. 1999. doi: 10.1046/j.1365-8711.1999.02978.x.

S. Arnouts, C. J. Walcher, O. Le Fèvre, G. Zamorani, O. Ilbert, V. Le Brun, L. Pozzetti, S. Bardelli, L. Tresse, E. Zucca, S. Charlot, F. Lamareille, H. J. McCracken, M. Bolzonella, A. Iovino, C. Lonsdale, M. Polletta, J. Surace, D. Bottini, B. Garilli, D. Maccagni, J. P. Picat, R. Scaramella, M. Scodeggio, G. Vettolani, A. Zanichelli, C. Adami, A. Cappi, P. Ciliegi, T. Contini, S. de la Torre, S. Foucaud, P. Franzetti, I. Gavignaud, L. Guzzo, B. Marano, C. Marinoni, A. Mazure, B. Meneux, R. Merighi, S. Paltani, R. Pellò, A. Pollo, M. Radovich, S. Temporin, and D. Vergani. The SWIRE-VVDS-CFHTLS surveys: stellar mass assembly over the last 10 Gyr. Evidence for a major build up of the red sequence between z = 2 and z = 1. , 476(1):137–150, Dec. 2007. doi: 10.1051/0004-6361:20077632.

H. Atek, J. Richard, J.-P. Kneib, et al. Revealing extremely faint $z > 10$ galaxies behind lensing clusters with jwst. *Astrophysical Journal Letters*, 2023.

H. e. a. Atek. Are ultra-faint galaxies at z 7-8 responsible for cosmic reionization? combined constraints from the hubble frontier fields clusters and parallels. *The Astrophysical Journal*, 800(1):18, 2015. doi: 10.1088/0004-637X/800/1/18. URL https://doi.org/10.1088/0004-637X/800/1/18.

R. Bacon, M. Accardo, L. Adjali, H. Anwand, S. Bauer, I. Biswas, J. Blaizot, D. Boudon, S. Brau-Nogue, J. Brinchmann, P. Caillier, L. Capoani, C. M. Carollo, T. Contini, P. Couderc, E. Daguisé, S. Deiries, B. Delabre, S. Dreizler, J. Dubois, M. Dupieux, C. Dupuy, E. Emsellem, T. Fechner, A. Fleischmann, M. François, G. Gallou, T. Gharsa, A. Glindemann, D. Gojak, B. Guiderdoni, G. Hansali, T. Hahn, A. Jarno, A. Kelz, C. Koehler, J. Kosmalski, F. Laurent, M. Le Floch, S. J. Lilly, J. L. Lizon, M. Loupias, A. Manescau, C. Monstein, H. Nicklas, J. C. Olaya, L. Pares, L. Pasquini, A. Pécontal-Rousset, R. Pelló, C. Petit, E. Popow, R. Reiss, A. Remillieux, E. Renault, M. Roth, G. Rupprecht, D. Serre, J. Schaye, G. Soucail, M. Steinmetz, O. Streicher, R. Stuik, H. Valentin, J. Vernet, P. Weilbacher, L. Wisotzki, and N. Yerle. The MUSE second-

generation VLT instrument. In I. S. McLean, S. K. Ramsay, and H. Takami, editors, *Ground-based and Airborne Instrumentation for Astronomy III*, volume 7735 of *Society of Photo-Optical Instrumentation Engineers (SPIE) Conference Series*, page 773508, July 2010. doi: 10.1117/12.856027.

N. A. Bahcall and X. Fan. The Most Massive Distant Clusters: Determining Ω and σ_8. , 504(1):1–6, Sept. 1998. doi: 10.1086/306088.

M. Bartelmann and P. Schneider. Weak gravitational lensing. *Physics Reports*, 340:291–472, 2001. doi: 10.1016/S0370-1573(00)00082-X.

W. A. Baum. Population Inferences from Star Counts, Surface Brightness and Colors. , 71(419):106–117, Apr. 1959. doi: 10.1086/127346.

B. Beauchesne, B. Clément, P. Hibon, M. Limousin, D. Eckert, J.-P. Kneib, J. Richard, P. Natarajan, M. Jauzac, M. Montes, G. Mahler, A. Claeyssens, A. Jeanneau, A. M. Koekemoer, D. Lagattuta, A. Pagul, and J. Sánchez. A new step forward in realistic cluster lens mass modelling: analysis of Hubble Frontier Field Cluster Abell S1063 from joint lensing, X-ray, and galaxy kinematics data. , 527(2):3246–3275, Jan. 2024. doi: 10.1093/mnras/stad3308.

P. Bergamini, A. Acebron, C. Grillo, P. Rosati, G. B. Caminha, A. Mercurio, E. Vanzella, G. Angora, G. Brammer, M. Meneghetti, and M. Nonino. New high-precision strong lensing modeling of Abell 2744. Preparing for JWST observations. , 670:A60, Feb. 2023a. doi: 10.1051/0004-6361/202244575.

P. Bergamini, A. Acebron, C. Grillo, P. Rosati, G. B. Caminha, A. Mercurio, E. Vanzella, C. Mason, T. Treu, G. Angora, G. B. Brammer, M. Meneghetti, M. Nonino, K. Boyett, M. Bradač, M. Castellano, A. Fontana, T. Morishita, D. Paris, G. Prieto-Lyon, G. Roberts-Borsani, N. Roy, P. Santini, B. Vulcani, X. Wang, and L. Yang. The GLASS-JWST Early Release Science Program. III. Strong-lensing Model of Abell 2744 and Its Infalling Regions. , 952(1):84, July 2023b. doi: 10.3847/1538-4357/acd643.

P. Bergamini, S. Schuldt, A. Acebron, C. Grillo, U. Meštrić, G. Granata, G. B. Caminha, M. Meneghetti, A. Mercurio, P. Rosati, S. H. Suyu, and E. Vanzella. Augmenting the power of time-delay cosmography in lens galaxy clusters by probing their member galaxies. II. Cosmic chronometers. , 682:L2, Feb. 2024. doi: 10.1051/0004-6361/202348267.

E. Bertin and S. Arnouts. SExtractor: Software for source extraction. , 117: 393–404, June 1996. doi: 10.1051/aas:1996164.

R. Bezanson, I. Labbe, K. E. Whitaker, J. Leja, S. H. Price, M. Franx, G. Brammer, D. Marchesini, A. Zitrin, B. Wang, J. R. Weaver, L. J. Furtak, H. Atek, D. Coe, S. E. Cutler, P. Dayal, P. van Dokkum, R. Feldmann, N. F. S. Öehler, S. Fujimoto, M. Geha, K. Glazebrook, A. de Graaff, J. E. Greene, S. Juneau, S. Kassin, M. Kriek, G. Khullar, M. M. Maseda, L. A. Mowla, A. Muzzin, T. Nanayakkara, E. J. Nelson, P. A. Oesch, C. Pacifici, R. Pan, C. Papovich, D. Setton, A. E. Shapley, R. Smit, M. Stefanon, E. N. Taylor, and C. C. Williams. The jwst uncover treasury survey: Ultradeep nirspec and nircam observations before the epoch of reionization. arXiv e-prints, 2022. URL https://arxiv.org/abs/2212.04026.

J. Binney and S. Tremaine. *Galactic Dynamics*. Princeton University Press, Princeton, NJ, 1 edition, 1987. ISBN 9780691084459.

A. Biviano and P. Salucci. The mass profiles of galaxy clusters. *The Astronomy and Astrophysics Review*, 14:1–60, 2006. doi: 10.1007/s00159-006-0003-7.

G. R. e. a. Blumenthal. Formation of galaxies and large-scale structure with cold dark matter. *Nature*, 311:517–525, 1984.

P. Bode, J. P. Ostriker, and N. Turok. Halo formation in warm dark matter models. *Astrophysical Journal*, 556:93–107, 2001.

W. e. a. Boschin. Internal dynamics of the rich abell cluster abcg 209: a young cluster in formation? *Astronomy Astrophysics*, 449:461–471, 2006. doi: 10.1051/0004-6361:20054220. URL https://doi.org/10.1051/0004-6361:20054220.

J. Bovy. *Dynamics and Astrophysics of Galaxies*. Princeton University Press, Princeton, NJ, 2025. URL https://galaxiesbook.org/. In press.

M. Boylan-Kolchin, V. Springel, S. D. M. White, A. Jenkins, and G. Lemson. Resolving cosmic structure formation with the Millennium-II Simulation. , 398 (3):1150–1164, Sept. 2009. doi: 10.1111/j.1365-2966.2009.15191.x.

M. Boylan-Kolchin, J. S. Bullock, and M. Kaplinghat. Too big to fail? the puzzling darkness of massive milky way subhaloes. *Monthly Notices of the Royal Astronomical Society*, 415:L40–L44, 2011. doi: 10.1111/j.1745-3933.2011.01074.x.

M. Bradač, P. Schneider, M. Lombardi, M. Steinmetz, L. King, C. Porciani, and S. Matarrese. Strong and weak lensing united: the combined strong and weak lensing cluster mass reconstruction method. *Astronomy & Astrophysics*, 437: 39–48, 2005. doi: 10.1051/0004-6361:20040444.

M. Bradač, D. Clowe, A. H. Gonzalez, P. Marshall, W. Forman, C. Jones, et al. Combined strong and weak lensing analysis of galaxy clusters. *The Astrophysical Journal*, 705:L184–L188, 2009. doi: 10.1088/0004-637X/705/2/L184.

M. Bradač et al. Cluster-lensed high-redshift galaxies with jwst. *Astrophysical Journal*, 2024.

H. Bradt, W. Mayer, S. Naranan, S. Rappaport, and G. Spada. Evidence for X-Radiation from the Radio Galaxy M87. , 150:L199, Dec 1967. doi: 10.1086/180125.

F. G. e. a. Braglia. Abell 2744: a galaxy cluster caught in the act of merging. *Astronomy Astrophysics*, 470:425–436, 2007. doi: 10.1051/0004-6361:20077283. URL https://doi.org/10.1051/0004-6361:20077283.

G. Brammer. msaexp: NIRSpec analyis tools, Nov. 2022.

G. Brammer. grizli, Sept. 2023.

G. B. Brammer, P. G. van Dokkum, and P. Coppi. EAZY: A Fast, Public Photometric Redshift Code. *The Astrophysical Journal*, 686(2):1503–1513, 2008. doi: 10.1086/591786. URL https://ui.adsabs.harvard.edu/abs/2008ApJ...686.1503B.

R. Braun, A. Bonaldi, T. Bourke, et al. Anticipated Performance of the Square Kilometre Array – Phase 1 (SKA1). *arXiv e-prints*, art. arXiv:1912.12699, 2019.

G. Bruzual and S. Charlot. Stellar population synthesis at the resolution of 2003. , 344(4):1000–1028, Oct. 2003. doi: 10.1046/j.1365-8711.2003.06897.x.

J. S. Bullock and M. Boylan-Kolchin. Small-scale challenges to the λcdm paradigm. *Annual Review of Astronomy and Astrophysics*, 55:343–387, 2017.

W. L. Burke. Multiple gravitational imaging by distributed masses. *The Astrophysical Journal*, 244:L1–L4, 1981.

E. T. Byram, T. A. Chubb, and H. Friedman. Cosmic X-Ray Sources-Galactic and Extragalactic. , 71:379, Aug 1966. doi: 10.1086/109934.

California Institute of Technology. For astronomers. Online: https://buffalo.ipac.caltech.edu/page/astronomers, 2015.

G. B. Caminha, C. Grillo, P. Rosati, I. Balestra, et al. A refined mass model of the hubble frontier fields cluster abell 2744 from a new large set of spectroscopic multiple-image constraints. *Astronomy Astrophysics*, 600:A90, 2017. doi: 10.1051/0004-6361/201629297.

G. B. Caminha, S. H. Suyu, A. Mercurio, G. Brammer, P. Bergamini, A. Acebron, and E. Vanzella. First JWST observations of a gravitational lens. Mass model from new multiple images with near-infrared observations of SMACS J0723.3−7327. , 666:L9, Oct. 2022. doi: 10.1051/0004-6361/202244517.

K. I. Caputi, G. B. Caminha, S. Fujimoto, K. Kohno, F. Sun, E. Egami, S. Deshmukh, F. Tang, Y. Ao, L. Bradley, D. Coe, D. Espada, C. Grillo, B. Hatsukade, K. K. Knudsen, M. M. Lee, G. E. Magdis, K. Morokuma-Matsui, P. Oesch, M. Ouchi, P. Rosati, H. Umehata, F. Valentino, E. Vanzella, W. H. Wang, J. F. Wu, and A. Zitrin. ALMA Lensing Cluster Survey: An ALMA Galaxy Signposting a MUSE Galaxy Group at z = 4.3 Behind "El Gordo". , 908(2):146, Feb. 2021. doi: 10.3847/1538-4357/abd4d0.

C. Cerny, M. Jauzac, D. Lagattuta, A. Niemiec, G. Mahler, A. Edge, R. Massey, and J. Allingham. The Kaleidoscope Survey: Strong Gravitational Lensing in Galaxy Clusters with Radial Arcs. *arXiv e-prints*, art. arXiv:2506.21531, June 2025a. doi: 10.48550/arXiv.2506.21531.

C. Cerny, G. Mahler, K. Sharon, M. Jauzac, G. Khullar, B. Beauchesne, J. M. Diego, D. J. Lagattuta, M. Limousin, N. R. Patel, J. Richard, C. Cornil-Baiotto, M. D. Gladders, S. Werner, J. E. Doppel, B. Floyd, A. H. Gonzalez, R. J. Massey, M. Montes, M. B. Bayliss, L. E. Bleem, R. E. A. Canning, A. C. Edge, M. McDonald, P. Natarjan, A. A. Stark, and R. Gassis. Strong LensIng and Cluster Evolution (SLICE) with JWST: Early Results, Lens Models, and High-Redshift Detections. *arXiv e-prints*, art. arXiv:2503.17498, Mar. 2025b. doi: 10.48550/arXiv.2503.17498.

S. Cha, K. HyeongHan, Z. P. Scofield, H. Joo, and M. J. Jee. Precision MARS Mass Reconstruction of A2744: Synergizing the Largest Strong-lensing and Densest Weak-lensing Data Sets from JWST. , 961(2):186, Feb. 2024. doi: 10.3847/1538-4357/ad0cbf.

S. Cha, B. Y. Cho, H. Joo, W. Lee, K. HyeongHan, Z. P. Scofield, K. Finner, and M. J. Jee. A High-Caliber View of the Bullet Cluster through JWST Strong and Weak Lensing Analyses. , 987(1):L15, July 2025. doi: 10.3847/2041-8213/add2f0.

U. Chadayammuri, Á. Bogdán, G. Schellenberger, and J. ZuHone. Closing Pandora's Box – The deepest X-ray observations of Abell 2744 and a multi-

wavelength merger picture. *arXiv e-prints*, art. arXiv:2407.03142, July 2024. doi: 10.48550/arXiv.2407.03142.

O. Chwolson. Über eine mögliche Form fiktiver Doppelsterne. *Astronomische Nachrichten*, 221:329, June 1924. doi: 10.1002/asna.19242212003.

D. e. a. Clowe. A direct empirical proof of the existence of dark matter. *Astrophysical Journal*, 648, 2006.

D. Coe, N. Benítez, T. Broadhurst, L. A. Moustakas, and H. C. Ford. Lensperfect: Gravitational lens inversion without shape constraints. *The Astrophysical Journal*, 681:814–828, 2008. doi: 10.1086/588740.

D. Coe, L. A. Moustakas, A. Zitrin, et al. Lensperfect ii: Mapping mass distributions in galaxy clusters from observed multiple images. *The Astrophysical Journal*, 723:1678–1696, 2010. doi: 10.1088/0004-637X/723/2/1678.

Cognito Edu. P3: A-Level Physics CIE Subtopic. https://cognitoedu.org/coursesubtopic/p3-alevel-cie_rySBfzCq, 2025. Accessed: 12 July 2025.

P. Colin, V. Avila-Reese, and O. Valenzuela. Substructure and halo density profiles in a warm dark matter cosmology. *Astrophysical Journal*, 539:561–568, 2000.

N. Copernicus. *De Revolutionibus Orbium Coelestium*. Johannes Petreius, 1543.

V. L. Corless, L. J. King, and D. Clowe. A new look at massive clusters: weak lensing constraints on the triaxial dark matter haloes of A1689, A1835 and A2204. , 393(4):1235–1254, Mar. 2009. doi: 10.1111/j.1365-2966.2008.14294.x.

G. Covone, J.-P. Kneib, G. Soucail, J. Richard, and E. Jullo. A strong lensing analysis of the lensing cluster abell 2667 based on acs images. *Astronomy & Astrophysics*, 456(2):409–420, 2006. doi: 10.1051/0004-6361:20065340.

D. J. Cowley, S. Faber, D. F. Hilyard, E. James, and J. Osborne. DEIMOS: a wide-field faint-object spectrograph. In A. L. Ardeberg, editor, *Optical Telescopes of Today and Tomorrow*, volume 2871 of *Society of Photo-Optical Instrumentation*

Engineers (SPIE) Conference Series, pages 1107–1115, Mar. 1997. doi: 10.1117/12.268997.

E. S. e. a. Cypriano. Weak-lensing analysis of the merging cluster abell 2744. *The Astrophysical Journal*, 613:95–105, 2004. doi: 10.1086/422866. URL https://doi.org/10.1086/422866.

W. J. G. de Blok, S. S. McGaugh, A. Bosma, and V. C. Rubin. Mass density profiles of lsb galaxies. *The Astrophysical Journal*, 552:L23, 2001. doi: 10.1086/320262.

A. Diaferio. Mass estimation in the outer regions of galaxy clusters. *Monthly Notices of the Royal Astronomical Society*, 309:610–622, 1999. doi: 10.1046/j.1365-8711.1999.02894.x.

J. M. Diego, M. Tegmark, P. Protopapas, and H. B. Sandvik. Combined reconstruction of weak and strong lensing data with wslap. *Monthly Notices of the Royal Astronomical Society*, 375:958–970, 2007. doi: 10.1111/j.1365-2966.2007.11380.x.

J. M. Diego, I. Sendra, T. Broadhurst, M. Oguri, A. Zitrin, et al. A revised non-parametric mass reconstruction of macsj0416.1–2403 with hubble frontier fields data. *Monthly Notices of the Royal Astronomical Society*, 462:954–970, 2016. doi: 10.1093/mnras/stw1676.

J. M. Diego, M. Pascale, B. Frye, A. Zitrin, T. Broadhurst, G. Mahler, G. B. Caminha, M. Jauzac, M. G. Lee, J. H. Bae, I. S. Jang, and M. Montes. On the correlation between dark matter, intracluster light and globular cluster distribution in SMACS0723. *arXiv e-prints*, art. arXiv:2301.03629, Jan. 2023. doi: 10.48550/arXiv.2301.03629.

J. M. Diego, S. K. Li, A. K. Meena, A. Niemiec, A. Acebron, M. Jauzac, M. F. Struble, A. Amruth, T. J. Broadhurst, C. Cerny, H. Ebeling, A. V. Filippenko, E. Jullo, P. Kelly, A. M. Koekemoer, D. Lagattuta, J. Lim, M. Limousin, G. Mahler, N. Patel, J. Remolina, J. Richard, K. Sharon, C. Steinhardt,

K. Umetsu, L. Williams, A. Zitrin, J. M. Palencia, L. Dai, L. Ji, and M. Pascale. BUFFALO/Flashlights: Constraints on the abundance of lensed supergiant stars in the Spock galaxy at redshift 1. , 681:A124, Jan. 2024. doi: 10.1051/0004-6361/202346761.

C. Doppler. Über das farbige licht der doppelsterne und einiger anderer gestirne des himmels. *Abhandlungen der Königlichen Böhmischen Gesellschaft der Wissenschaften*, 2:465–482, 1842.

H. Ebeling, A. C. Edge, and J. P. Henry. MACS: A Quest for the Most Massive Galaxy Clusters in the Universe. , 553(2):668–676, June 2001. doi: 10.1086/320958.

H. Ebeling, E. Barrett, D. Donovan, C. J. Ma, A. C. Edge, and L. van Speybroeck. A Complete Sample of 12 Very X-Ray Luminous Galaxy Clusters at z $>$ 0.5. , 661(1):L33–L36, May 2007. doi: 10.1086/518603.

D. Eckert, M. Jauzac, H. Shan, et al. Mass and gas in the merging cluster abell 2744. *Nature*, 528:105–107, 2015. doi: 10.1038/nature16058.

D. Eckert, A. Finoguenov, V. Ghirardini, S. Grandis, F. Kaefer, J. Sanders, and M. Ramos-Ceja. Low-scatter galaxy cluster mass proxies for the eROSITA all-sky survey. *The Open Journal of Astrophysics*, 3:12, Sept. 2020. doi: 10.21105/astro.2009.13944.

A. S. Eddington. The Deflection of Light during a Solar Eclipse. , 104(2615):372, Dec. 1919. doi: 10.1038/104372c0.

A. Einstein. Über den Einfluß der Schwerkraft auf die Ausbreitung des Lichtes. *Annalen der Physik*, 340(10):898–908, Jan. 1911. doi: 10.1002/andp.19113401005.

A. Einstein. Die feldgleichungen der gravitation. *Sitzungsberichte der Preussischen Akademie der Wissenschaften*, pages 844–847, 1915.

A. Einstein. Die Grundlage der allgemeinen Relativitätstheorie. *Annalen der Physik*, 354(7):769–822, Jan. 1916. doi: 10.1002/andp.19163540702.

A. Einstein. Lens-Like Action of a Star by the Deviation of Light in the Gravitational Field. *Science*, 84(2188):506–507, Dec. 1936. doi: 10.1126/science.84.2188.506.

Elíasdóttir. *Gravitational Lensing and Galaxy Dynamics in Galaxy Clusters*. PhD thesis, University of Copenhagen, 2007. Available at https://arxiv.org/abs/0710.5636.

T. Erben, H. Hildebrandt, L. Miller, L. van Waerbeke, C. Heymans, H. Hoekstra, T. D. Kitching, Y. Mellier, J. Benjamin, C. Blake, C. Bonnett, O. Cordes, J. Coupon, L. Fu, R. Gavazzi, B. Gillis, E. Grocutt, S. D. J. Gwyn, K. Holhjem, M. J. Hudson, M. Kilbinger, K. Kuijken, M. Milkeraitis, B. T. P. Rowe, T. Schrabback, E. Semboloni, P. Simon, M. Smit, O. Toader, S. Vafaei, E. van Uitert, and M. Velander. CFHTLenS: the Canada-France-Hawaii Telescope Lensing Survey - imaging data and catalogue products. , 433(3):2545–2563, Aug. 2013. doi: 10.1093/mnras/stt928.

H. Erdl and P. Schneider. Classification of critical points for general gravitational lenses. *Astronomy and Astrophysics*, 268:453–471, 1993.

ESA/Webb, NASA & CSA, G. Mahler. Webb spies a spiral through a cosmic lens. URL https://www.esa.int/ESA_Multimedia/Images/2025/03/Webb_spies_a_spiral_through_a_cosmic_lens. Image and description accessed 24 June 2025.

A. G. R. et al. A comprehensive measurement of the local value of the hubble constant with 1 km/s/mpc uncertainty from the hubble space telescope and the sh0es team. *The Astrophysical Journal Letters*, 908(1):L6, 2021. doi: 10.3847/2041-8213/abdbaf.

S. M. Faber and R. E. Jackson. Velocity dispersions and mass-to-light ratios for elliptical galaxies. *The Astrophysical Journal*, 204:668–683, 1976. doi: 10.1086/154215.

O. Fakhouri and C.-P. Ma. The nearly universal merger rate of dark matter haloes in ΛCDM cosmology. , 386(2):577–592, May 2008. doi: 10.1111/j.1365-2966.2008.13075.x.

P. Flin and J. Krywult. Substructures in Abell clusters of galaxies. , 450(1):9–14, Apr. 2006. doi: 10.1051/0004-6361:20041635.

G. Fritz, A. Davidsen, J. F. Meekins, and H. Friedman. Discovery of an X-Ray Source in Perseus. , 164:L81, Mar 1971. doi: 10.1086/180697.

A. Fruscione, J. C. McDowell, G. E. Allen, N. S. Brickhouse, D. J. Burke, J. E. Davis, N. Durham, M. Elvis, E. C. Galle, D. E. Harris, D. P. Huenemoerder, J. C. Houck, B. Ishibashi, M. Karovska, F. Nicastro, M. S. Noble, M. A. Nowak, F. A. Primini, A. Siemiginowska, R. K. Smith, and M. Wise. CIAO: Chandra's data analysis system. In D. R. Silva and R. E. Doxsey, editors, *Society of Photo-Optical Instrumentation Engineers (SPIE) Conference Series*, volume 6270 of *Society of Photo-Optical Instrumentation Engineers (SPIE) Conference Series*, page 62701V, June 2006. doi: 10.1117/12.671760.

L. J. Furtak, A. Zitrin, A. Plat, S. Fujimoto, B. Wang, E. J. Nelson, I. Labbé, R. Bezanson, G. B. Brammer, P. van Dokkum, R. Endsley, K. Glazebrook, J. E. Greene, J. Leja, S. H. Price, R. Smit, D. P. Stark, J. R. Weaver, K. E. Whitaker, H. Atek, J. Chevallard, E. Curtis-Lake, P. Dayal, A. Feltre, M. Franx, Y. Fudamoto, D. Marchesini, L. A. Mowla, R. Pan, K. A. Suess, A. Vidal-García, and C. C. Williams. JWST UNCOVER: Extremely Red and Compact Object at z $_{phot}$ 7.6 Triply Imaged by A2744. , 952(2):142, Aug. 2023a. doi: 10.3847/1538-4357/acdc9d.

L. J. Furtak, A. Zitrin, J. R. Weaver, H. Atek, R. Bezanson, I. Labbé, K. E. Whitaker, J. Leja, S. H. Price, G. B. Brammer, B. Wang, D. Marchesini, R. Pan, P. Dayal, P. van Dokkum, R. Feldmann, S. Fujimoto, M. Franx, G. Khullar, E. J. Nelson, and L. A. Mowla. UNCOVERing the extended strong lensing structures of Abell 2744 with the deepest JWST imaging. , 523(3):4568–4582, Aug. 2023b. doi: 10.1093/mnras/stad1627.

S. Gallo, N. Aghanim, C. Gouin, D. Eckert, M. Douspis, J. Paste, and T. Bonnaire. Tracing gaseous filaments connected to galaxy clusters: The case study of Abell 2744. , 692:A200, Dec. 2024. doi: 10.1051/0004-6361/202451163.

L. Gao, J. F. Navarro, C. S. Frenk, A. Jenkins, V. Springel, and S. D. M. White. The Phoenix Project: the dark side of rich Galaxy clusters. , 425(3):2169–2186, Sept. 2012. doi: 10.1111/j.1365-2966.2012.21564.x.

J. P. Gardner, J. C. Mather, M. Clampin, R. Doyon, M. A. Greenhouse, H. B. Hammel, J. B. Hutchings, P. Jakobsen, S. J. Lilly, K. S. Long, J. I. Lunine, M. J. McCaughrean, M. Mountain, J. Nella, G. H. Rieke, M. J. Rieke, H.-W. Rix, E. P. Smith, G. Sonneborn, M. Stiavelli, H. S. Stockman, R. A. Windhorst, and G. S. Wright. The James Webb Space Telescope. *Space Science Reviews*, 123:485–606, 2006. doi: 10.1007/s11214-006-8315-7.

R. Gavazzi. Projection effects in cluster mass estimates: the case of MS2137-23. , 443(3):793–804, Dec. 2005. doi: 10.1051/0004-6361:20053166.

R. Giacconi, S. Murray, H. Gursky, E. Kellogg, E. Schreier, and H. Tananbaum. The Uhuru catalog of X-ray sources. , 178:281–308, Dec 1972. doi: 10.1086/151790.

S. Giodini, D. Pierini, A. Finoguenov, G. W. Pratt, H. Boehringer, A. Leauthaud, L. Guzzo, H. Aussel, M. Bolzonella, P. Capak, M. Elvis, G. Hasinger, O. Ilbert, J. S. Kartaltepe, A. M. Koekemoer, S. J. Lilly, R. Massey, H. J. McCracken, J. Rhodes, M. Salvato, D. B. Sanders, N. Z. Scoville, S. Sasaki, V. Smolcic,

Y. Taniguchi, D. Thompson, and COSMOS Collaboration. Stellar and Total Baryon Mass Fractions in Groups and Clusters Since Redshift 1. , 703(1):982–993, Sept. 2009. doi: 10.1088/0004-637X/703/1/982.

G. e. a. Giovannini. A new radio halo in abell 2744. *New Astronomy*, 4:141–152, 1999. doi: 10.1016/S1384-1076(99)00008-6. URL https://doi.org/10.1016/S1384-1076(99)00008-6.

M. Girardi and M. Mezzetti. Velocity distribution and substructure in the merging cluster abell 2744. *The Astrophysical Journal*, 548:79–90, 2001. doi: 10.1086/318662. URL https://doi.org/10.1086/318662.

M. D. Gladders and H. K. C. Yee. A New Method For Galaxy Cluster Detection. I. The Algorithm. , 120(4):2148–2162, Oct. 2000. doi: 10.1086/301557.

G. Golse, J. P. Kneib, and G. Soucail. Constraining the cosmological parameters using strong lensing. , 387:788–803, June 2002. doi: 10.1051/0004-6361:20020448.

A. H. Gonzalez, D. Zaritsky, and A. I. Zabludoff. A Census of Baryons in Galaxy Clusters and Groups. , 666(1):147–155, Sept. 2007. doi: 10.1086/519729.

E. J. Gonzalez, M. Chalela, M. Jauzac, D. Eckert, M. Schaller, D. Harvey, A. Niemiec, A. M. Koekemoer, D. Barnes, D. Clowe, T. Connor, J. M. Diego, J. D. Remolina Gonzalez, and C. L. Steinhardt. Setting the scene for BUFFALO: a study of the matter distribution in the HFF galaxy cluster MACS J0416.1-2403 and its parallel field. , 494(1):349–362, May 2020. doi: 10.1093/mnras/staa745.

J. González-López, F. E. Bauer, C. Romero-Cañizales, R. Kneissl, E. Villard, R. Carvajal, S. Kim, N. Laporte, T. Anguita, M. Aravena, R. J. Bouwens, L. Bradley, M. Carrasco, R. Demarco, H. Ford, E. Ibar, L. Infante, H. Messias, A. M. Muñoz Arancibia, N. Nagar, N. Padilla, E. Treister, P. Troncoso, and A. Zitrin. The ALMA Frontier Fields Survey. I. 1.1 mm continuum detections in Abell 2744, MACS J0416.1-2403 and MACS J1149.5+2223. , 597:A41, Jan. 2017. doi: 10.1051/0004-6361/201628806.

F. e. a. Govoni. A study of the large-scale radio emission in the cluster of galaxies abell 2744. *Astronomy Astrophysics*, 376:803–817, 2001. doi: 10.1051/0004-6361:20010979. URL https://doi.org/10.1051/0004-6361:20010979.

C. Grillo, P. Rosati, S. H. Suyu, I. Balestra, G. B. Caminha, A. Halkola, P. L. Kelly, M. Lombardi, A. Mercurio, S. A. Rodney, and T. Treu. Measuring the Value of the Hubble Constant "à la Refsdal". , 860(2):94, June 2018. doi: 10.3847/1538-4357/aac2c9.

C. Grillo, L. Pagano, P. Rosati, and S. H. Suyu. Cosmography with supernova Refsdal through time-delay cluster lensing: Independent measurements of the Hubble constant and geometry of the Universe. , 684:L23, Apr. 2024. doi: 10.1051/0004-6361/202449278.

H. Gursky, E. Kellogg, S. Murray, C. Leong, H. Tananbaum, and R. Giacconi. A Strong X-Ray Source in the Coma Cluster Observed by UHURU. , 167:L81, Aug 1971. doi: 10.1086/180765.

A. H. Guth. Inflationary universe: A possible solution to the horizon and flatness problems. *Physical Review D*, 23:347–356, 1981.

D. Harvey, S.-I. Tam, M. Jauzac, R. Massey, and J. Rhodes. The shape of relaxed galaxy clusters and the public release of a hst shape measurement code, pyrrg. *Monthly Notices of the Royal Astronomical Society*, 000:1–8, 2019.

D. R. Harvey and R. Massey. Weak gravitational lensing measurements of Abell 2744 using JWST and shear measurement algorithm pyRRG-JWST. , 529(2): 802–809, Apr. 2024. doi: 10.1093/mnras/stae370.

M. Hattori, J. Kneib, and N. Makino. Gravitational Lensing in Clusters of Galaxies. *Progress of Theoretical Physics Supplement*, 133:1–51, Jan. 1999. doi: 10.1143/PTPS.133.1.

S. He, R. Li, Z. Cao, N. Li, and R. B. Metcalf. Automated detection of strong gravitational lenses in Euclid-like imaging using deep learning. *Monthly Notices*

of the Royal Astronomical Society, 521(2):2479–2493, 2023. doi: 10.1093/mnras/stad624.

C. Heymans, L. Van Waerbeke, L. Miller, T. Erben, H. Hildebrandt, H. Hoekstra, T. D. Kitching, Y. Mellier, P. Simon, C. Bonnett, J. Coupon, L. Fu, J. Harnois Déraps, M. J. Hudson, M. Kilbinger, K. Kuijken, B. Rowe, T. Schrabback, E. Semboloni, E. van Uitert, S. Vafaei, and M. Velander. CFHTLenS: the Canada-France-Hawaii Telescope Lensing Survey. , 427(1):146–166, Nov. 2012. doi: 10.1111/j.1365-2966.2012.21952.x.

S. R. Hinton, T. M. Davis, C. Lidman, K. Glazebrook, and G. F. Lewis. MARZ: Manual and automatic redshifting software. *Astronomy and Computing*, 15:61–71, Apr. 2016. doi: 10.1016/j.ascom.2016.03.001.

K. Horne. An optimal extraction algorithm for CCD spectroscopy. , 98:609–617, June 1986. doi: 10.1086/131801.

E. Hubble. A relation between distance and radial velocity among extra-galactic nebulae. *Proceedings of the National Academy of Sciences*, 15:168–173, 1929. doi: 10.1073/pnas.15.3.168.

O. Ilbert, S. Arnouts, H. J. McCracken, M. Bolzonella, E. Bertin, O. Le Fèvre, Y. Mellier, G. Zamorani, R. Pellò, A. Iovino, L. Tresse, V. Le Brun, D. Bottini, B. Garilli, D. Maccagni, J. P. Picat, R. Scaramella, M. Scodeggio, G. Vettolani, A. Zanichelli, C. Adami, S. Bardelli, A. Cappi, S. Charlot, P. Ciliegi, T. Contini, O. Cucciati, S. Foucaud, P. Franzetti, I. Gavignaud, L. Guzzo, B. Marano, C. Marinoni, A. Mazure, B. Meneux, R. Merighi, S. Paltani, A. Pollo, L. Pozzetti, M. Radovich, E. Zucca, M. Bondi, A. Bongiorno, G. Busarello, S. de La Torre, L. Gregorini, F. Lamareille, G. Mathez, P. Merluzzi, V. Ripepi, D. Rizzo, and D. Vergani. Accurate photometric redshifts for the CFHT legacy survey calibrated using the VIMOS VLT deep survey. , 457(3):841–856, Oct. 2006. doi: 10.1051/0004-6361:20065138.

O. Ilbert, P. Capak, M. Salvato, H. Aussel, H. J. McCracken, D. B. Sanders, N. Scoville, J. Kartaltepe, S. Arnouts, E. Le Floc'h, B. Mobasher, Y. Taniguchi, F. Lamareille, A. Leauthaud, S. Sasaki, D. Thompson, M. Zamojski, G. Zamorani, S. Bardelli, M. Bolzonella, A. Bongiorno, M. Brusa, K. I. Caputi, C. M. Carollo, T. Contini, R. Cook, G. Coppa, O. Cucciati, S. de la Torre, L. de Ravel, P. Franzetti, B. Garilli, G. Hasinger, A. Iovino, P. Kampczyk, J. P. Kneib, C. Knobel, K. Kovac, J. F. Le Borgne, V. Le Brun, O. Le Fèvre, S. Lilly, D. Looper, C. Maier, V. Mainieri, Y. Mellier, M. Mignoli, T. Murayama, R. Pellò, Y. Peng, E. Pérez-Montero, A. Renzini, E. Ricciardelli, D. Schiminovich, M. Scodeggio, Y. Shioya, J. Silverman, J. Surace, M. Tanaka, L. Tasca, L. Tresse, D. Vergani, and E. Zucca. Cosmos Photometric Redshifts with 30-Bands for 2-deg^2. , 690(2):1236–1249, Jan. 2009. doi: 10.1088/0004-637X/690/2/1236.

M. e. a. Ishigaki. Full-data results of abell 2744 from the hubble frontier fields: Strong lensing mass modeling and high-redshift galaxy candidates. *The Astrophysical Journal*, 799(1):12, 2015. doi: 10.1088/0004-637X/799/1/12. URL https://doi.org/10.1088/0004-637X/799/1/12.

C. Jacobs, T. E. Collett, K. Glazebrook, C. McCarthy, and L. Abramson. Finding strong gravitational lenses in the kilo-degree survey with convolutional neural networks. *Monthly Notices of the Royal Astronomical Society*, 484(4):5330–5349, 2019. doi: 10.1093/mnras/stz272.

M. Jauzac, E. Jullo, J.-P. Kneib, H. Ebeling, A. Leauthaud, C.-J. Ma, M. Limousin, R. Massey, and J. Richard. A weak lensing mass reconstruction of the large-scale filament feeding the massive galaxy cluster MACS J0717.5+3745. , 426(4):3369–3384, Nov. 2012. doi: 10.1111/j.1365-2966.2012.21966.x.

M. Jauzac, B. Clément, M. Limousin, J. Richard, E. Jullo, H. Ebeling, H. Atek, J. P. Kneib, K. Knowles, P. Natarajan, D. Eckert, E. Egami, R. Massey, and M. Rexroth. Hubble Frontier Fields: a high-precision strong-lensing analysis of

galaxy cluster MACSJ0416.1-2403 using ∼200 multiple images. , 443(2):1549–1554, Sept. 2014. doi: 10.1093/mnras/stu1355.

M. Jauzac, E. Jullo, D. Eckert, H. Ebeling, J. Richard, M. Limousin, H. Atek, J.-P. Kneib, B. Clément, E. Egami, D. Harvey, K. Knowles, R. Massey, P. Natarajan, B. Neichel, and M. Rexroth. Hubble Frontier Fields: the geometry and dynamics of the massive galaxy cluster merger MACSJ0416.1-2403. , 446(4):4132–4147, Feb. 2015a. doi: 10.1093/mnras/stu2425.

M. Jauzac, J. Richard, E. Jullo, B. Clément, M. Limousin, J. P. Kneib, H. Ebeling, P. Natarajan, S. Rodney, H. Atek, R. Massey, D. Eckert, E. Egami, and M. Rexroth. Hubble Frontier Fields: a high-precision strong-lensing analysis of the massive galaxy cluster Abell 2744 using ∼180 multiple images. , 452(2):1437–1446, Sept. 2015b. doi: 10.1093/mnras/stv1402.

M. Jauzac, D. Eckert, J. Schwinn, D. Harvey, C. M. Baugh, A. Robertson, S. Bose, R. Massey, M. Owers, H. Ebeling, H. Y. Shan, E. Jullo, J. P. Kneib, J. Richard, H. Atek, B. Clément, E. Egami, H. Israel, K. Knowles, M. Limousin, P. Natarajan, M. Rexroth, P. Taylor, and C. Tchernin. The extraordinary amount of substructure in the Hubble Frontier Fields cluster Abell 2744. , 463(4):3876–3893, Dec. 2016. doi: 10.1093/mnras/stw2251.

M. Jauzac, D. Eckert, M. Schaller, J. Schwinn, R. Massey, Y. Bahé, C. Baugh, D. Barnes, C. Dalla Vecchia, H. Ebeling, D. Harvey, E. Jullo, S. T. Kay, J. P. Kneib, M. Limousin, E. Medezinski, P. Natarajan, M. Nonino, A. Robertson, S. I. Tam, and K. Umetsu. Growing a 'cosmic beast': observations and simulations of MACS J0717.5+3745. , 481(3):2901–2917, Dec. 2018. doi: 10.1093/mnras/sty2366.

M. Jauzac, G. Mahler, A. C. Edge, K. Sharon, S. Gillman, H. Ebeling, D. Harvey, J. Richard, S. L. Hamer, M. Fumagalli, A. Mark Swinbank, J.-P. Kneib, R. Massey, and P. Salomé. The core of the massive cluster merger MACS

J0417.5-1154 as seen by VLT/MUSE. , 483(3):3082–3097, Mar. 2019. doi: 10.1093/mnras/sty3312.

B. D. Johnson, J. Leja, C. Conroy, J. S. Speagle, and Y. Wang. Stellar Population Inference with Prospector. *The Astrophysical Journal Supplement Series*, 254(2): 22, 2021. doi: 10.3847/1538-4365/abef67. URL https://ui.adsabs.harvard.edu/abs/2021ApJS..254...22J.

T. L. Johnson, K. Sharon, M. B. Bayliss, M. D. Gladders, D. Coe, and H. Ebeling. Lens Models and Magnification Maps of the Six Hubble Frontier Fields Clusters. , 797(1):48, Dec. 2014. doi: 10.1088/0004-637X/797/1/48.

E. Jullo and J. P. Kneib. Multiscale cluster lens mass mapping - I. Strong lensing modelling. , 395(3):1319–1332, May 2009. doi: 10.1111/j.1365-2966.2009.14654.x.

E. Jullo, J. P. Kneib, M. Limousin, Á. Elíasdóttir, P. J. Marshall, and T. Verdugo. A Bayesian approach to strong lensing modelling of galaxy clusters. *New Journal of Physics*, 9(12):447, Dec. 2007. doi: 10.1088/1367-2630/9/12/447.

E. Jullo, P. Natarajan, J. P. Kneib, A. D'Aloisio, M. Limousin, J. Richard, and C. Schimd. Cosmological constraints from strong gravitational lensing in clusters of galaxies. *Science*, 329:924–927, Aug. 2010. doi: 10.1126/science.1185759.

E. Jullo, J.-P. Kneib, M. Limousin, Á. Elíasdóttir, G. Bernstein, and P. Natarajan. Lenstool – a bayesian strong and weak lens modeling code. *Monthly Notices of the Royal Astronomical Society*, 437:21–28, 2014. doi: 10.1093/mnras/stt1987.

M. Kaplinghat, S. Tulin, and H. B. Yu. Dark matter halos as particle colliders: Unified solution to small-scale structure puzzles. *Physical Review Letters*, 116: 041302, 2016. doi: 10.1103/PhysRevLett.116.041302.

J. C. Kapteyn. First attempt at a theory of dark matter. *Astrophysical Journal*, 55, 1922.

J. S. Kartaltepe, H. Ebeling, C. J. Ma, and D. Donovan. Probing the large-scale structure around the most distant galaxy clusters from the massive cluster survey. , 389(3):1240–1248, Sept. 2008. doi: 10.1111/j.1365-2966.2008.13620.x.

P. L. Kelly et al. Sn refsdal: The first resolved multiply imaged supernova. *Science*, 347:1123–1126, 2015.

D. D. Kelson, A. I. Zabludoff, K. A. Williams, S. C. Trager, J. S. Mulchaey, and M. Bolte. Determination of the Dark Matter Profile of A2199 from Integrated Starlight. , 576(2):720–737, Sept. 2002. doi: 10.1086/341891.

L. Kelvin. On a universal tendency in nature to the dissipation of mechanical energy. *Philosophical Magazine*, 4(25):304–306, 1852.

L. Kelvin. On the density of dark bodies in space. *Philosophical Transactions of the Royal Society*, 197, 1904.

J. C. Kempner and L. P. David. Chandra observations of the merging cluster abell 2744. *Monthly Notices of the Royal Astronomical Society*, 349:385–396, 2004. doi: 10.1111/j.1365-2966.2004.07490.x. URL https://doi.org/10.1111/j.1365-2966.2004.07490.x.

R. Kennedy, C. Frenk, S. Cole, and A. Benson. Constraining the warm dark matter particle mass with Milky Way satellites. , 442(3):2487–2495, Aug. 2014. doi: 10.1093/mnras/stu719.

M. Killi, D. Watson, S. Fujimoto, H. Akins, K. Knudsen, J. Richard, Y. Harikane, D. Rigopoulou, F. Rizzo, M. Ginolfi, G. Popping, and V. Kokorev. A solar metallicity galaxy at z $>$ 7? Possible detection of the [N II] 122 μm and [O III] 52 μm lines. , 521(2):2526–2534, May 2023. doi: 10.1093/mnras/stad687.

G. Kirchhoff and R. Bunsen. *Chemical Analysis by Observation of Spectra*. Poggendorff's Annalen der Physik und Chemie, 1860.

J.-P. Kneib and P. Natarajan. Gravitational lensing by clusters of galaxies. *The Astronomy and Astrophysics Review*, 19:47, 2011. doi: 10.1007/s00159-011-0047-3.

Y. Ko, H. S. Hwang, M. G. Lee, H. S. Park, S. Lim, J. Sohn, I. S. Jang, N. Hwang, and B.-G. Park. To the Edge of M87 and Beyond: Spectroscopy of Intracluster Globular Clusters and Ultracompact Dwarfs in the Virgo Cluster. , 835(2):212, Feb. 2017. doi: 10.3847/1538-4357/835/2/212.

A. M. Koekemoer, S. M. Faber, H. C. Ferguson, N. A. Grogin, D. D. Kocevski, D. C. Koo, K. Lai, J. M. Lotz, R. A. Lucas, E. J. McGrath, S. Ogaz, A. Rajan, A. G. Riess, S. A. Rodney, L. Strolger, S. Casertano, M. Castellano, T. Dahlen, M. Dickinson, T. Dolch, A. Fontana, M. Giavalisco, A. Grazian, Y. Guo, N. P. Hathi, K.-H. Huang, A. van der Wel, H.-J. Yan, V. Acquaviva, D. M. Alexander, O. Almaini, M. L. N. Ashby, M. Barden, E. F. Bell, F. Bournaud, T. M. Brown, K. I. Caputi, P. Cassata, P. J. Challis, R.-R. Chary, E. Cheung, M. Cirasuolo, C. J. Conselice, A. Roshan Cooray, D. J. Croton, E. Daddi, R. Davé, D. F. de Mello, L. de Ravel, A. Dekel, J. L. Donley, J. S. Dunlop, A. A. Dutton, D. Elbaz, G. G. Fazio, A. V. Filippenko, S. L. Finkelstein, C. Frazer, J. P. Gardner, P. M. Garnavich, E. Gawiser, R. Gruetzbauch, W. G. Hartley, B. Häussler, J. Herrington, P. F. Hopkins, J.-S. Huang, S. W. Jha, A. Johnson, J. S. Kartaltepe, A. A. Khostovan, R. P. Kirshner, C. Lani, K.-S. Lee, W. Li, P. Madau, P. J. McCarthy, D. H. McIntosh, R. J. McLure, C. McPartland, B. Mobasher, H. Moreira, A. Mortlock, L. A. Moustakas, M. Mozena, K. Nandra, J. A. Newman, J. L. Nielsen, S. Niemi, K. G. Noeske, C. J. Papovich, L. Pentericci, A. Pope, J. R. Primack, S. Ravindranath, N. A. Reddy, A. Renzini, H.-W. Rix, A. R. Robaina, D. J. Rosario, P. Rosati, S. Salimbeni, C. Scarlata, B. Siana, L. Simard, J. Smidt, D. Snyder, R. S. Somerville, H. Spinrad, A. N. Straughn, O. Telford, H. I. Teplitz, J. R. Trump, C. Vargas, C. Villforth, C. R. Wagner, P. Wandro, R. H. Wechsler, B. J. Weiner, T. Wiklind, V. Wild, G. Wilson, S. Wuyts, and M. S. Yun. CANDELS: The Cosmic Assembly Near-infrared Deep Extragalactic Leg-

acy Survey—The Hubble Space Telescope Observations, Imaging Data Products, and Mosaics. , 197(2):36, Dec. 2011. doi: 10.1088/0067-0049/197/2/36.

J. E. Krist, R. N. Hook, and F. Stoehr. 20 years of Hubble Space Telescope optical modeling using Tiny Tim. In M. A. Kahan, editor, *Optical Modeling and Performance Predictions V*, volume 8127 of *Society of Photo-Optical Instrumentation Engineers (SPIE) Conference Series*, page 81270J, Oct. 2011. doi: 10.1117/12.892762.

A. Krolewski and W. J. Percival. Measuring the baryon fraction using galaxy clustering. *arXiv e-prints*, art. arXiv:2403.19236, Mar. 2024. doi: 10.48550/arXiv.2403.19236.

I. Labbe, J. E. Greene, J. Matthee, H. Treiber, V. Kokorev, T. B. Miller, I. Kramarenko, D. J. Setton, Y. Ma, A. D. Goulding, R. Bezanson, R. P. Naidu, C. C. Williams, H. Atek, G. Brammer, S. E. Cutler, I. Chemerynska, A. P. Cloonan, P. Dayal, A. de Graaff, Y. Fudamoto, S. Fujimoto, L. J. Furtak, K. Glazebrook, K. E. Heintz, J. Leja, D. Marchesini, T. Nanayakkara, E. J. Nelson, P. A. Oesch, R. Pan, S. H. Price, I. Shivaei, D. Sobral, K. A. Suess, P. van Dokkum, B. Wang, J. R. Weaver, K. E. Whitaker, and A. Zitrin. An unambiguous AGN and a Balmer break in an Ultraluminous Little Red Dot at z=4.47 from Ultradeep UNCOVER and All the Little Things Spectroscopy. *arXiv e-prints*, art. arXiv:2412.04557, Dec. 2024. doi: 10.48550/arXiv.2412.04557.

T. F. Laganá, N. Martinet, F. Durret, G. B. Lima Neto, B. Maughan, and Y. Y. Zhang. A comprehensive picture of baryons in groups and clusters of galaxies. , 555:A66, July 2013. doi: 10.1051/0004-6361/201220423.

D. J. Lagattuta, J. Richard, F. E. Bauer, B. Clément, G. Mahler, G. Soucail, D. Carton, J.-P. Kneib, N. Laporte, J. Martinez, V. Patrício, A. V. Payne, R. Pelló, K. B. Schmidt, and G. de la Vieuville. Probing 3D structure with a large MUSE mosaic: extending the mass model of Frontier Field Abell 370. , 485(3):3738–3760, May 2019. doi: 10.1093/mnras/stz620.

D. J. Lagattuta, J. Richard, F. E. Bauer, C. Cerny, A. Claeyssens, L. Guaita, M. Jauzac, A. Jeanneau, A. M. Koekemoer, G. Mahler, G. Prieto Lyon, A. Acebron, M. Meneghetti, A. Niemiec, A. Zitrin, M. Bianconi, T. Connor, R. Cen, A. Edge, A. L. Faisst, M. Limousin, R. Massey, M. Sereno, K. Sharon, and J. R. Weaver. Pilot-WINGS: An extended MUSE view of the structure of Abell 370. , 514(1):497–517, July 2022. doi: 10.1093/mnras/stac418.

D. J. Lagattuta, J. Richard, H. Ebeling, Q. Basto, C. Cerny, A. Edge, M. Jauzac, G. Mahler, and R. Massey. RXJ0437+00: constraining dark matter with exotic gravitational lenses. , 522(1):1091–1107, June 2023. doi: 10.1093/mnras/stad803.

D. e. a. Lam. A strong lensing analysis of abell 2744. *Monthly Notices of the Royal Astronomical Society*, 437:1698–1709, 2014. doi: 10.1093/mnras/stt2002. URL https://doi.org/10.1093/mnras/stt2002.

F. Lanusse, Q. Ma, N. Li, T. E. Collett, C.-L. Li, S. Ravanbakhsh, R. Mandelbaum, and B. Póczos. Cmu deeplens: Deep learning for automatic detection of strong gravitational lenses. *Monthly Notices of the Royal Astronomical Society*, 473(3): 3895–3906, 2018. doi: 10.1093/mnras/stx1665.

N. Laporte, A. Zitrin, H. Dole, G. Roberts-Borsani, L. J. Furtak, and C. Witten. A lensed protocluster candidate at z = 7.66 identified in JWST observations of the galaxy cluster SMACS0723−7327. , 667:L3, Nov. 2022. doi: 10.1051/0004-6361/202244719.

S. J. LaRoque, M. Joy, J. E. Carlstrom, H. Ebeling, M. Bonamente, K. S. Dawson, A. Edge, W. L. Holzapfel, A. D. Miller, D. Nagai, S. K. Patel, and E. D. Reese. Sunyaev-Zeldovich Effect Imaging of MACS Galaxy Clusters at z>0.5. , 583(2): 559–565, Feb. 2003. doi: 10.1086/345500.

R. Laureijs, J. Amiaux, S. Arduini, et al. Euclid Definition Study Report. Technical Report ESA/SRE(2011)12, European Space Agency, 2011.

O. Le Fèvre, G. Vettolani, B. Garilli, L. Tresse, D. Bottini, V. Le Brun, D. Maccagni, J. P. Picat, R. Scaramella, M. Scodeggio, A. Zanichelli, C. Adami, M. Arnaboldi, S. Arnouts, S. Bardelli, M. Bolzonella, A. Cappi, S. Charlot, P. Ciliegi, T. Contini, S. Foucaud, P. Franzetti, I. Gavignaud, L. Guzzo, O. Ilbert, A. Iovino, H. J. McCracken, B. Marano, C. Marinoni, G. Mathez, A. Mazure, B. Meneux, R. Merighi, S. Paltani, R. Pellò, A. Pollo, L. Pozzetti, M. Radovich, G. Zamorani, E. Zucca, M. Bondi, A. Bongiorno, G. Busarello, F. Lamareille, Y. Mellier, P. Merluzzi, V. Ripepi, and D. Rizzo. The VIMOS VLT deep survey. First epoch VVDS-deep survey: 11 564 spectra with $17.5 \leq$ IAB ≤ 24, and the redshift distribution over $0 \leq z \leq 5$. , 439(3):845–862, Sept. 2005. doi: 10.1051/0004-6361:20041960.

A. Leauthaud, R. Massey, J.-P. Kneib, J. Rhodes, D. E. Johnston, P. Capak, C. Heymans, R. S. Ellis, A. M. Koekemoer, O. Le Fèvre, Y. Mellier, A. Réfrégier, A. C. Robin, N. Scoville, L. Tasca, J. E. Taylor, and L. Van Waerbeke. Weak Gravitational Lensing with COSMOS: Galaxy Selection and Shape Measurements. , 172(1):219–238, Sept. 2007. doi: 10.1086/516598.

M. G. Lee, H. S. Park, and H. S. Hwang. Detection of a Large-Scale Structure of Intracluster Globular Clusters in the Virgo Cluster. *Science*, 328(5976):334, Apr. 2010. doi: 10.1126/science.1186496.

D. Lemze, T. Broadhurst, Y. Rephaeli, R. Barkana, and K. Umetsu. Dynamical study of a1689 from wide-field vlt/vimos spectroscopy: Mass profile, concentration parameter, and velocity anisotropy. *Astrophysical Journal - ASTROPHYS J*, 701, 10 2008. doi: 10.1088/0004-637X/701/2/1336.

J. Liesenborgs, S. de Rijcke, and H. Dejonghe. A genetic algorithm for the non-parametric inversion of strong lensing systems. *Monthly Notices of the Royal Astronomical Society*, 367:1209–1212, 2006. doi: 10.1111/j.1365-2966.2006.10078.x.

J. Liesenborgs, S. de Rijcke, H. Dejonghe, and P. Bekaert. Efficient non-parametric reconstruction of galaxy cluster mass distributions with grale. *Monthly Notices*

of the Royal Astronomical Society, 397:297–306, 2009. doi: 10.1111/j.1365-2966.2009.14948.x.

M. Limousin, J.-P. Kneib, and P. Natarajan. Constraining the mass distribution of galaxies using galaxy-galaxy lensing in clusters and in the field. , 356(1):309–322, Jan. 2005. doi: 10.1111/j.1365-2966.2004.08449.x.

M. Limousin, J. Richard, E. Jullo, J.-P. Kneib, B. Fort, G. Soucail, Elíasdóttir, P. Natarajan, R. S. Ellis, I. Smail, O. Czoske, and G. P. Smith. Combining strong and weak gravitational lensing in abell 1689. *The Astrophysical Journal*, 668(2):643–666, 2007. doi: 10.1086/521237.

M. Limousin, H. Ebeling, C. J. Ma, A. M. Swinbank, G. P. Smith, J. Richard, A. C. Edge, M. Jauzac, J. P. Kneib, P. Marshall, and T. Schrabback. MACS J1423.8+2404: gravitational lensing by a massive, relaxed cluster of galaxies at z = 0.54. , 405(2):777–782, June 2010. doi: 10.1111/j.1365-2966.2010.16518.x.

M. Limousin, A. Morandi, M. Sereno, M. Meneghetti, S. Ettori, M. Bartelmann, and T. Verdugo. The Three-Dimensional Shapes of Galaxy Clusters. , 177(1-4): 155–194, Aug. 2013. doi: 10.1007/s11214-013-9980-y.

M. Limousin, J. Richard, E. Jullo, M. Jauzac, H. Ebeling, M. Bonamigo, A. Alavi, B. Clément, C. Giocoli, J. P. Kneib, T. Verdugo, P. Natarajan, B. Siana, H. Atek, and M. Rexroth. Strong-lensing analysis of MACS J0717.5+3745 from Hubble Frontier Fields observations: How well can the mass distribution be constrained? , 588:A99, Apr. 2016. doi: 10.1051/0004-6361/201527638.

M. Limousin, B. Beauchesne, and E. Jullo. Dark matter in galaxy clusters: Parametric strong-lensing approach. , 664:A90, Aug. 2022. doi: 10.1051/0004-6361/202243278.

M. Limousin, B. Beauchesne, A. Niemiec, J. M. Diego, M. Jauzac, A. Koekemoer, K. Sharon, A. Acebron, D. Lagattuta, G. Mahler, L. L. R. Williams, J. Richard, E. Jullo, L. J. Furtak, A. L. Faisst, B. L. Frye, P. Hibon, P. Natarajan, and

M. Rich. Mass and light in galaxy clusters: The case of Abell 370. , 693:A33, Jan. 2025. doi: 10.1051/0004-6361/202451969.

Linc. Weak lensing illustration. https://commons.wikimedia.org/wiki/File:Weak_lensing_illustration.png, Sept. 2016. Wikimedia Commons image, File: Weak lensing illustration.png. Released under CC0 1.0 on 28 September 2016. Accessed 26 June 2025.

R. C. Livermore, S. L. Finkelstein, and J. M. Lotz. Directly Observing the Galaxies Likely Responsible for Reionization. , 835(2):113, Feb. 2017. doi: 10.3847/1538-4357/835/2/113.

J. M. Lotz et al. The frontier fields: Survey design and initial results. *The Astrophysical Journal*, 837(1):97, 2017.

M. R. e. a. Lovell. Satellite galaxies in semi-analytic models of galaxy formation with warm dark matter. *Monthly Notices of the Royal Astronomical Society*, 439: 300–317, 2014.

L. M. Lubin, C. D. Fassnacht, A. C. S. Readhead, R. D. Blandford, and T. Kundić. A Keck Survey of Gravitational Lens Systems. I. Spectroscopy of SBS 0909+532, HST 1411+5211, and CLASS B2319+051. , 119(2):451–459, Feb. 2000. doi: 10.1086/301229.

R. Lynds and V. Petrosian. Giant luminous arcs in galaxy clusters. *Bulletin of the American Astronomical Society*, 19:833, 1987.

C.-J. Ma, H. Ebeling, D. Donovan, and E. Barrett. The Spatial Distribution of Galaxies of Different Spectral Types in the Massive Intermediate-Redshift Cluster MACS J0717.5+3745. , 684(1):160–176, Sept. 2008. doi: 10.1086/589991.

A. Mahdavi, H. Hoekstra, A. Babul, and J. P. Henry. Evidence for non-hydrostatic gas from the cluster X-ray to lensing mass ratio. , 384(4):1567–1574, Mar. 2008. doi: 10.1111/j.1365-2966.2007.12796.x.

G. Mahler, J. Richard, B. Clément, D. Lagattuta, K. Schmidt, V. Patrício, G. Soucail, R. Bacon, R. Pello, R. Bouwens, M. Maseda, J. Martinez, M. Carollo, H. Inami, F. Leclercq, and L. Wisotzki. Strong-lensing analysis of A2744 with MUSE and Hubble Frontier Fields images. , 473(1):663–692, Jan. 2018. doi: 10.1093/mnras/stx1971.

G. Mahler, K. Sharon, C. Fox, D. Coe, M. Jauzac, V. Strait, A. Edge, A. Acebron, F. Andrade-Santos, R. J. Avila, M. Bradač, L. D. Bradley, D. Carrasco, C. Cerny, N. Cibirka, N. G. Czakon, W. A. Dawson, B. L. Frye, A. T. Hoag, K.-H. Huang, T. L. Johnson, C. Jones, S. Kikuchihara, D. Lam, R. Livermore, L. Lovisari, R. Mainali, S. Ogaz, M. Ouchi, R. Paterno-Mahler, I. U. Roederer, R. E. Ryan, B. Salmon, I. Sendra-Server, D. P. Stark, S. Toft, M. Trenti, K. Umetsu, B. Vulcani, and A. Zitrin. RELICS: Strong Lensing Analysis of MACS J0417.5-1154 and Predictions for Observing the Magnified High-redshift Universe with JWST. , 873(1):96, Mar. 2019. doi: 10.3847/1538-4357/ab042b.

G. Mahler, M. Jauzac, J. Richard, B. Beauchesne, H. Ebeling, D. Lagattuta, P. Natarajan, K. Sharon, H. Atek, A. Claeyssens, B. Clément, D. Eckert, A. Edge, J.-P. Kneib, and A. Niemiec. Precision Modeling of JWST's First Cluster Lens SMACS J0723.3-7327. , 945(1):49, Mar. 2023. doi: 10.3847/1538-4357/acaea9.

A. B. Mantz, S. W. Allen, R. G. Morris, et al. Cosmology and astrophysics from relaxed galaxy clusters – ii. cosmological constraints. *Monthly Notices of the Royal Astronomical Society*, 440:2077–2098, 2014. doi: 10.1093/mnras/stu329.

A. B. Mantz, S. W. Allen, R. G. Morris, D. Rapetti, and H. Ebeling. Cosmology and astrophysics from relaxed galaxy clusters – I. Sample selection. *Monthly Notices of the Royal Astronomical Society*, 462:681–694, 2016. doi: 10.1093/mnras/stw1690.

E. Medezinski, K. Umetsu, N. Okabe, M. Nonino, S. Molnar, R. Massey, R. Dupke, and J. Merten. Frontier Fields: Subaru Weak-Lensing Analysis of the Merging

Galaxy Cluster A2744. , 817(1):24, Jan. 2016. doi: 10.3847/0004-637X/817/1/24.

J. F. Meekins, G. Fritz, T. A. Chubb, and H. Friedman. Physical Sciences: X-rays from the Coma Cluster of Galaxies. , 231(5298):107–108, May 1971. doi: 10.1038/231107a0.

A. K. Meena et al. Jwst detection of faint lensed galaxies behind massive clusters. *Astrophysical Journal*, 2023.

M. Meneghetti, B. Jain, M. Bartelmann, and K. Dolag. Constraints on dark energy models from galaxy clusters with multiple arcs. , 362(4):1301–1310, Oct. 2005. doi: 10.1111/j.1365-2966.2005.09402.x.

J. Merten, M. Cacciato, M. Meneghetti, C. Mignone, M. Bartelmann, K. Dolag, M. Limousin, J.-P. Kneib, F. Frutos-Alfaro, and M. Steinmetz. Combining strong and weak lensing in abell 1689: mass reconstruction with sawlens. *Monthly Notices of the Royal Astronomical Society*, 399:1789–1803, 2009. doi: 10.1111/j.1365-2966.2009.15447.x.

J. Merten, M. Meneghetti, M. Postman, A. Zitrin, K. Umetsu, T. Erben, O. Host, M. Limousin, E. Jullo, and L. Moustakas. Sawlens ii: joint strong and weak lensing analysis of galaxy clusters. *Monthly Notices of the Royal Astronomical Society*, 417:333–347, 2011. doi: 10.1111/j.1365-2966.2011.19190.x.

J. Merten, M. Meneghetti, M. Postman, et al. Clash: The concentration–mass relation of galaxy clusters from strong- and weak-lensing reconstructions. *The Astrophysical Journal*, 806(1):4, 2015. doi: 10.1088/0004-637X/806/1/4.

R. B. Metcalf et al. The strong gravitational lens finding challenge. *Astronomy and Computing*, 28:100307, 2019. doi: 10.1016/j.ascom.2019.100307.

J. Miralda-Escudé and B. Fort. Core images of gravitational lenses. *The Astrophysical Journal*, 417:L5–L8, 1993.

S. Miyazaki, Y. Komiyama, M. Sekiguchi, S. Okamura, M. Doi, H. Furusawa, M. Hamabe, K. Imi, M. Kimura, F. Nakata, N. Okada, M. Ouchi, K. Shimasaku, M. Yagi, and N. Yasuda. Subaru Prime Focus Camera – Suprime-Cam. , 54: 833–853, Dec. 2002. doi: 10.1093/pasj/54.6.833.

S. Miyazaki, M. Oguri, T. Hamana, et al. First-year shear catalog of the subaru hyper suprime-cam subaru strategic program survey. *Publications of the Astronomical Society of Japan*, 70:S27, 2018. doi: 10.1093/pasj/psx063.

M. Montes and I. Trujillo. A New Era of Intracluster Light Studies with JWST. , 940(2):L51, Dec. 2022. doi: 10.3847/2041-8213/ac98c5.

A. Morandi and M. Limousin. Triaxiality, principal axis orientation and non-thermal pressure in Abell 383. , 421(4):3147–3158, Apr. 2012. doi: 10.1111/j.1365-2966.2012.20537.x.

T. Morishita, G. Roberts-Borsani, T. Treu, G. Brammer, C. A. Mason, M. Trenti, B. Vulcani, X. Wang, A. Acebron, Y. Bahé, P. Bergamini, K. Boyett, M. Bradac, A. Calabrò, M. Castellano, W. Chen, G. De Lucia, A. V. Filippenko, A. Fontana, K. Glazebrook, C. Grillo, A. Henry, T. Jones, P. L. Kelly, A. M. Koekemoer, N. Leethochawalit, T.-Y. Lu, D. Marchesini, S. Mascia, A. Mercurio, E. Merlin, B. Metha, T. Nanayakkara, M. Nonino, D. Paris, L. Pentericci, P. Rosati, P. Santini, V. Strait, E. Vanzella, R. A. Windhorst, and L. Xie. Early Results from GLASS-JWST. XIV. A Spectroscopically Confirmed Protocluster 650 Million Years after the Big Bang. , 947(2):L24, Apr. 2023. doi: 10.3847/2041-8213/acb99e.

L. Mowla, K. Iyer, Y. Asada, G. Desprez, V. Y. Y. Tan, N. Martis, G. Sarrouh, V. Strait, R. Abraham, M. Bradač, G. Brammer, A. Muzzin, C. Pacifici, S. Ravindranath, M. Sawicki, C. Willott, V. Estrada-Carpenter, N. Jahan, G. Noirot, J. Matharu, G. Rihtaršič, and J. Zabl. The Firefly Sparkle: The Earliest Stages of the Assembly of A Milky Way-type Galaxy in a 600

Myr Old Universe. *arXiv e-prints*, art. arXiv:2402.08696, Feb. 2024. doi: 10.48550/arXiv.2402.08696.

O. Müller, M. S. Pawlowski, Y. Revaz, A. Venhola, M. Rejkuba, M. Hilker, and K. Lutz. A too-many-dwarf-galaxy-satellites problem in the M 83 group. , 684: L6, Apr. 2024. doi: 10.1051/0004-6361/202348969.

R. P. Naidu, P. A. Oesch, D. J. Setton, J. Matthee, C. Conroy, B. D. Johnson, J. R. Weaver, R. J. Bouwens, G. B. Brammer, P. Dayal, G. D. Illingworth, L. Barrufet, S. Belli, R. Bezanson, S. Bose, K. E. Heintz, J. Leja, E. Leonova, R. Marques-Chaves, M. Stefanon, S. Toft, A. van der Wel, P. van Dokkum, A. Weibel, and K. E. Whitaker. Schrodinger's Galaxy Candidate: Puzzlingly Luminous at $z \approx 17$, or Dusty/Quenched at $z \approx 5$? *arXiv e-prints*, art. arXiv:2208.02794, Aug. 2022. doi: 10.48550/arXiv.2208.02794.

R. Narayan, R. Blandford, and R. Nityananda. Multiple imaging of quasars by galaxies and clusters. , 310(5973):112–115, July 1984. doi: 10.1038/310112a0.

NASA, ESA, and L. Calçada. Gravitational lensing in action. https://esahubble.org/images/heic1106c/, Apr. 2011. ESA/Hubble illustration, Image ID heic1106c, released 12 April 2011. Accessed 26 June 2025.

P. Natarajan and J.-P. Kneib. Lensing by galaxy halos in clusters of galaxies. *Monthly Notices of the Royal Astronomical Society*, 287(3):833–845, 1997. doi: 10.1093/mnras/287.3.833.

P. Natarajan, G. De Lucia, V. Springel, and M. Volonteri. Lensing substructure in cosmological galaxy clusters. *Monthly Notices of the Royal Astronomical Society*, 368(4):2105–2117, 2006. doi: 10.1111/j.1365-2966.2006.10261.x.

F. C. S. W. S. D. M. Navarro, J. F. The structure of cold dark matter halos. *Astrophysical Journal*, 462:563–575, 1996.

J. F. Navarro, V. R. Eke, and C. S. Frenk. The cores of dwarf galaxy haloes. , 283 (3):L72–L78, Dec. 1996. doi: 10.1093/mnras/283.3.L72.

J. F. Navarro, A. Ludlow, V. Springel, J. Wang, M. Vogelsberger, S. D. M. White, A. Jenkins, C. S. Frenk, and A. Helmi. The diversity and similarity of simulated cold dark matter haloes. , 402(1):21–34, Feb. 2010. doi: 10.1111/j.1365-2966.2009.15878.x.

Netwon. *Opticks: or, A treatise of the reflections, refractions, inflexions and colours of light*. Sam. Smith, and Benj. Walford, London, 1704. URL https://doi.org/10.5479/sil.302475.39088000644674.

A. B. Newman, T. Treu, R. S. Ellis, and D. J. Sand. The Dark Matter Distribution in A383: Evidence for a Shallow Density Cusp from Improved Lensing, Stellar Kinematic, and X-ray Data. , 728(2):L39, Feb. 2011. doi: 10.1088/2041-8205/728/2/L39.

A. B. Newman, T. Treu, R. S. Ellis, and D. J. Sand. The Density Profiles of Massive, Relaxed Galaxy Clusters. II. Separating Luminous and Dark Matter in Cluster Cores. , 765(1):25, Mar. 2013a. doi: 10.1088/0004-637X/765/1/25.

A. B. Newman, T. Treu, R. S. Ellis, D. J. Sand, C. Nipoti, J. Richard, and E. Jullo. The Density Profiles of Massive, Relaxed Galaxy Clusters. I. The Total Density Over Three Decades in Radius. , 765(1):24, Mar. 2013b. doi: 10.1088/0004-637X/765/1/24.

I. Newton. *Philosophiæ Naturalis Principia Mathematica*. Royal Society, 1687.

A. Niemiec, M. Jauzac, E. Jullo, M. Limousin, K. Sharon, J.-P. Kneib, P. Natarajan, and J. Richard. hybrid-LENSTOOL: a self-consistent algorithm to model galaxy clusters with strong- and weak-lensing simultaneously. , 493(3):3331–3340, Apr. 2020. doi: 10.1093/mnras/staa473.

A. Niemiec, M. Jauzac, D. Eckert, D. Lagattuta, K. Sharon, A. M. Koekemoer, K. Umetsu, A. Acebron, J. M. Diego, D. Harvey, E. Jullo, V. Kokorev, M. Limousin, G. Mahler, P. Natarajan, M. Nonino, C. Steinhardt, S. I. Tam, and

A. Zitrin. Beyond the ultra-deep frontier fields and legacy observations (BUFFALO): a high-resolution strong+weak-lensing view of Abell 370. , July 2023. doi: 10.1093/mnras/stad1999.

G. Noirot, G. Desprez, Y. Asada, M. Sawicki, V. Estrada-Carpenter, N. Martis, G. Sarrouh, V. Strait, R. Abraham, M. Bradač, G. Brammer, K. Iyer, S. MacFarland, J. Matharu, L. Mowla, A. Muzzin, C. Pacifici, S. Ravindranath, C. J. Willott, L. Albert, R. Doyon, J. B. Hutchings, and N. Rowlands. The first large catalogue of spectroscopic redshifts in webb's first deep field, smacs j0723.37327. *Monthly Notices of the Royal Astronomical Society*, 525(2): 1867–1884, Apr. 2023. ISSN 1365-2966. doi: 10.1093/mnras/stad1019. URL http://dx.doi.org/10.1093/mnras/stad1019.

M. Oguri. GLAFIC: a gravitational lensing analysis code. *Publications of the Astronomical Society of Japan*, 62:1017–1028, 2010. doi: 10.1093/pasj/62.4.1017.

M. Oguri, R. Mandelbaum, E. Medezinski, et al. An accurate mass map of a galaxy cluster with subaru weak lensing. *Monthly Notices of the Royal Astronomical Society*, 478:3653–3671, 2018. doi: 10.1093/mnras/sty1208.

J. B. Oke, J. G. Cohen, M. Carr, J. Cromer, A. Dingizian, F. H. Harris, S. Labrecque, R. Lucinio, W. Schaal, H. Epps, and J. Miller. The Keck Low-Resolution Imaging Spectrometer. , 107:375, Apr. 1995. doi: 10.1086/133562.

M. S. Owers, S. W. Randall, P. E. J. Nulsen, W. J. Couch, et al. Discovery of a merger-driven cold front in abell 2744. *The Astrophysical Journal*, 728(1):27, 2011. doi: 10.1088/0004-637X/728/1/27.

B. Paczynski and K. Gorski. Another possible case of a gravitational lens. , 248: L101–L104, Sept. 1981. doi: 10.1086/183634.

A. Pagul, F. J. Sánchez, I. Davidzon, A. M. Koekemoer, B. Mobasher, M. Jauzac, C. L. Steinhardt, H. Atek, R. Cen, I. Chemerynska, L. J. Furtak, D. J. Lagattuta, G. Mahler, M. Montes, M. Nonino, K. Sharon, and J. R. Weaver. Self-consistent

Combined HST, K-band, and Spitzer Photometric Catalogs of the BUFFALO Survey Fields. , 273(1):10, July 2024. doi: 10.3847/1538-4365/ad40a1.

M. Pascale, B. L. Frye, J. Diego, L. J. Furtak, A. Zitrin, T. Broadhurst, C. J. Conselice, L. Dai, L. Ferreira, N. J. Adams, P. Kamieneski, N. Foo, P. Kelly, W. Chen, J. Lim, A. K. Meena, S. M. Wilkins, R. Bhatawdekar, and R. A. Windhorst. Unscrambling the Lensed Galaxies in JWST Images behind SMACS 0723. , 938(1):L6, Oct. 2022. doi: 10.3847/2041-8213/ac9316.

N. R. Patel, M. Jauzac, A. Niemiec, D. Lagattuta, G. Mahler, B. Beauchesne, A. Edge, H. Ebeling, and M. Limousin. The KALEIDOSCOPE survey: a new strong and weak gravitational lensing view of the massive galaxy cluster MACS J1423.8+2404. , 533(4):4500–4514, Oct. 2024. doi: 10.1093/mnras/stae2069.

P. J. E. Peebles. The large-scale structure of the universe. *Princeton University Press*, 1980.

P. J. E. Peebles. Large-scale background temperature and galaxy formation. *Astrophysical Journal*, 263:L1–L5, 1982.

P. J. E. Peebles. *Principles of Physical Cosmology*. Princeton University Press, 1993.

E. H. Peng, K. Andersson, M. W. Bautz, and G. P. Garmire. Discrepant Mass Estimates in the Cluster of Galaxies Abell 1689. , 701(2):1283–1299, Aug. 2009. doi: 10.1088/0004-637X/701/2/1283.

A. A. Penzias and R. W. Wilson. A measurement of excess antenna temperature at 4080 mc/s. *Astrophysical Journal*, 142:419–421, 1965.

D. Perera, L. L. R. Williams, J. Liesenborgs, P. L. Kelly, S. H. Taft, S. K. Li, M. Jauzac, J. M. Diego, P. Natarajan, C. L. Steinhardt, A. L. Faisst, R. M. Rich, and M. Limousin. BUFFALO wild wings: a high-precision free-form lens model of MACSJ0416 with constraints on dark matter from substructure and highly magnified arcs. , 536(3):2690–2713, Jan. 2025. doi: 10.1093/mnras/stae2753.

S. e. a. Perlmutter. Measurements of omega and lambda from 42 high-redshift supernovae. *Astrophysical Journal*, 517:565–586, 1999.

C. E. Petrillo et al. Finding strong gravitational lenses in the kilo-degree survey using convolutional neural networks. *Monthly Notices of the Royal Astronomical Society*, 484(3):3879–3896, 2019. doi: 10.1093/mnras/stz189.

M. Pizzardo, M. J. Geller, S. J. Kenyon, I. Damjanov, and A. Diaferio. An IllustrisTNG view of the caustic technique for galaxy cluster mass estimation. , 675: A56, July 2023. doi: 10.1051/0004-6361/202346545.

Planck Collaboration. Planck 2018 results: Cosmological parameters. *Astronomy Astrophysics*, 641:A6, 2020a.

Planck Collaboration. Planck 2018 results. vi. cosmological parameters. *Astronomy Astrophysics*, 641:A6, 2020b.

S. Planelles, S. Borgani, D. Fabjan, et al. Baryon census in hydrodynamical simulations of galaxy clusters. *Monthly Notices of the Royal Astronomical Society*, 431:1487–1502, 2013. doi: 10.1093/mnras/stt271.

M. Postman, D. Coe, N. Benítez, L. Bradley, T. Broadhurst, M. Donahue, H. Ford, O. Graur, G. Graves, S. Jouvel, A. Koekemoer, D. Lemze, E. Medezinski, A. Molino, L. Moustakas, S. Ogaz, A. Riess, S. Rodney, P. Rosati, K. Umetsu, W. Zheng, A. Zitrin, M. Bartelmann, R. Bouwens, N. Czakon, S. Golwala, O. Host, L. Infante, S. Jha, Y. Jimenez-Teja, D. Kelson, O. Lahav, R. Lazkoz, D. Maoz, C. McCully, P. Melchior, M. Meneghetti, J. Merten, J. Moustakas, M. Nonino, B. Patel, E. Regös, J. Sayers, S. Seitz, and A. Van der Wel. The Cluster Lensing and Supernova Survey with Hubble: An Overview. , 199(2):25, Apr. 2012. doi: 10.1088/0067-0049/199/2/25.

S. H. Price, R. Bezanson, I. Labbe, L. J. Furtak, A. de Graaff, J. E. Greene, V. Kokorev, D. J. Setton, K. A. Suess, G. Brammer, S. E. Cutler, J. Leja, R. Pan, B. Wang, J. R. Weaver, K. E. Whitaker, H. Atek, A. J. Burgasser,

I. Chemerynska, P. Dayal, R. Feldmann, N. M. Förster Schreiber, Y. Fudamoto, S. Fujimoto, K. Glazebrook, A. D. Goulding, G. Khullar, M. Kriek, D. Marchesini, M. V. Maseda, T. B. Miller, A. Muzzin, T. Nanayakkara, E. Nelson, P. A. Oesch, H. Shipley, R. Smit, E. N. Taylor, P. v. Dokkum, C. C. Williams, and A. Zitrin. The UNCOVER Survey: First Release of Ultradeep JWST/NIRSpec PRISM Spectra for ∼700 Galaxies from z ∼ 0.3–13 in A2744. , 982(1):51, Mar. 2025. doi: 10.3847/1538-4357/adaec1.

S. W. Randall, M. Markevitch, D. Clowe, A. H. Gonzalez, and M. Bradač. Constraints on the self-interaction cross-section of dark matter from numerical simulations of the merging galaxy cluster 1e 0657-56. *The Astrophysical Journal*, 679:1173–1180, 2008. doi: 10.1086/587859.

A. Repp and H. Ebeling. Science from a glimpse: Hubble SNAPshot observations of massive galaxy clusters. , 479(1):844–864, Sept. 2018. doi: 10.1093/mnras/sty1489.

J. Rhodes, A. Refregier, and E. J. Groth. Weak Lensing Measurements: A Revisited Method and Application toHubble Space Telescope Images. , 536(1):79–100, June 2000. doi: 10.1086/308902.

J. Richard, L. Pei, M. Limousin, E. Jullo, and J. P. Kneib. Keck spectroscopic survey of strongly lensed galaxies in Abell 1703: further evidence of a relaxed, unimodal cluster. , 498(1):37–47, Apr. 2009. doi: 10.1051/0004-6361/200811366.

J. Richard, M. Jauzac, M. Limousin, E. Jullo, B. Clément, H. Ebeling, J.-P. Kneib, H. Atek, P. Natarajan, E. Egami, R. Livermore, and R. Bower. Mass and magnification maps for the Hubble Space Telescope Frontier Fields clusters: implications for high-redshift studies. , 444(1):268–289, Oct. 2014. doi: 10.1093/mnras/stu1395.

J. Richard, G. Mahler, D. J. Lagattuta, et al. The muse lensed field survey (mlfs):

strong-lensing constraints from 15 massive galaxy clusters. *Monthly Notices of the Royal Astronomical Society*, 501(1):706–731, 2021. doi: 10.1093/mnras/staa3686.

A. G. e. a. Riess. Observational evidence from supernovae for an accelerating universe and a cosmological constant. *Astronomical Journal*, 116:1009–1038, 1998.

J. R. Rigby, J. D. Vieira, K. A. Phadke, T. A. Hutchison, B. Welch, J. Cathey, J. S. Spilker, A. H. Gonzalez, P. Adhikari, M. Aravena, M. B. Bayliss, J. E. Birkin, E. Bursk, S. C. Chapman, H. Dahle, L. A. Elicker, T. C. Fischer, M. K. Florian, M. D. Gladders, C. C. Hayward, R. Hewald, L. A. Kettler, G. Khullar, S. Kim, D. R. Law, G. Mahler, S. Malhotra, E. J. Murphy, D. Narayanan, G. M. Olivier, J. E. Rhoads, K. Sharon, M. Solimano, A. Thiruvengadam, D. Vizgan, and N. Younker. JWST Early Release Science Program TEMPLATES: Targeting Extremely Magnified Panchromatic Lensed Arcs and Their Extended Star Formation. , 978(1):108, Jan. 2025. doi: 10.3847/1538-4357/ad7501.

T. Rivera-Thorsen et al. Jwst resolves tiny star clusters behind strong-lensing clusters. *Astrophysical Journal*, 2024.

A. Robertson, D. Harvey, R. Massey, V. Eke, I. G. McCarthy, M. Jauzac, B. Li, and J. Schaye. Observable tests of self-interacting dark matter in galaxy clusters: cosmological simulations with SIDM and baryons. , 488(3):3646–3662, Sept. 2019. doi: 10.1093/mnras/stz1815.

B. E. Robertson, S. Tacchella, B. D. Johnson, K. Hainline, L. Whitler, D. J. Eisenstein, R. Endsley, M. Rieke, D. P. Stark, S. Alberts, A. Dressler, E. Egami, R. Hausen, G. Rieke, I. Shivaei, C. C. Williams, C. N. A. Willmer, S. Arribas, N. Bonaventura, A. Bunker, A. J. Cameron, S. Carniani, S. Charlot, J. Chevallard, M. Curti, E. Curtis-Lake, F. D'Eugenio, P. Jakobsen, T. J. Looser, N. Lützgendorf, R. Maiolino, M. V. Maseda, T. Rawle, H. W. Rix, R. Smit, H. Übler, C. Willott, J. Witstok, S. Baum, R. Bhatawdekar, K. Boyett, Z. Chen, A. de

Graaff, M. Florian, J. M. Helton, R. E. Hviding, Z. Ji, N. Kumari, J. Lyu, E. Nelson, L. Sandles, A. Saxena, K. A. Suess, F. Sun, M. Topping, and I. E. B. Wallace. Identification and properties of intense star-forming galaxies at redshifts z > 10. *Nature Astronomy*, 7:611–621, May 2023. doi: 10.1038/s41550-023-01921-1.

M. Rocha, A. H. G. Peter, and J. S. e. a. Bullock. Cosmological simulations with self-interacting dark matter i: Constant density cores and substructure. *Monthly Notices of the Royal Astronomical Society*, 430:81–104, 2013. doi: 10.1093/mnras/sts514.

V. C. Rubin and W. K. Ford. Rotation of the andromeda nebula from a spectroscopic survey of emission regions. *Astrophysical Journal*, 159, 1970.

V. C. Rubin, W. K. Ford, and N. Thonnard. Rotational properties of 21 sc galaxies with a large range of luminosities and radii, from ngc 4605 (r = 4kpc) to ugc 2885 (r = 122kpc). *Astrophysical Journal*, 238:471–487, 1980. doi: 10.1086/158003.

D. J. Sand, T. Treu, R. S. Ellis, G. P. Smith, and J.-P. Kneib. Separating Baryons and Dark Matter in Cluster Cores: A Full Two-dimensional Lensing and Dynamic Analysis of Abell 383 and MS 2137-23. , 674(2):711–727, Feb. 2008a. doi: 10.1086/524652.

D. J. Sand, T. Treu, R. S. Ellis, G. P. Smith, and J.-P. Kneib. Separating Baryons and Dark Matter in Cluster Cores: A Full Two-dimensional Lensing and Dynamic Analysis of Abell 383 and MS 2137-23. , 674(2):711–727, Feb. 2008b. doi: 10.1086/524652.

A. J. R. Sanderson, T. J. Ponman, and E. O'Sullivan. A Chandra X-ray study of galaxy cluster scaling relations. *Monthly Notices of the Royal Astronomical Society*, 379:209–228, 2007. doi: 10.1111/j.1365-2966.2007.11832.x.

C. L. Sarazin. *X-ray emission from clusters of galaxies*. 1988.

A. Saro, J. Mohr, B. Bazin, and M. Dolag. Toward unbiased galaxy cluster masses from line-of-sight velocity dispersions. *The Astrophysical Journal*, 772(1):47,

2013. doi: 10.1088/0004-637X/772/1/47. URL https://doi.org/10.1088/0004-637X/772/1/47.

B. P. Schmidt and et al. The High-Z Supernova Search: Measuring Cosmic Deceleration and Global Curvature of the Universe Using Type Ia Supernovae. *The Astrophysical Journal*, 507, 1998. doi: 10.1086/306308.

K. B. Schmidt, T. Treu, G. B. Brammer, M. Bradač, X. Wang, M. Dijkstra, A. Dressler, A. Fontana, R. Gavazzi, A. L. Henry, A. Hoag, T. A. Jones, P. L. Kelly, M. A. Malkan, C. Mason, L. Pentericci, B. Poggianti, M. Stiavelli, M. Trenti, A. von der Linden, and B. Vulcani. Through the Looking GLASS: HST Spectroscopy of Faint Galaxies Lensed by the Frontier Fields Cluster MACSJ0717.5+3745. , 782(2):L36, Feb. 2014. doi: 10.1088/2041-8205/782/2/L36.

R. W. Schmidt and S. W. Allen. The dark matter haloes of massive, relaxed galaxy clusters observed with Chandra. , 379(1):209–221, July 2007. doi: 10.1111/j.1365-2966.2007.11928.x.

P. Schneider. *Extragalactic Astronomy and Cosmology*. Springer Berlin Heidelberg, Berlin, Heidelberg, 2006. ISBN 978-3-540-33174-2. doi: 10.1007/978-3-540-33175-9. URL http://dx.doi.org/10.1007/978-3-540-33175-9.

J. Schwinn, M. Jauzac, C. M. Baugh, M. Bartelmann, D. Eckert, D. Harvey, P. Natarajan, and R. Massey. Abell 2744: too much substructure for ΛCDM? , 467(3):2913–2923, May 2017. doi: 10.1093/mnras/stx277.

J. Schwinn, C. M. Baugh, M. Jauzac, M. Bartelmann, and D. Eckert. Uncovering substructure with wavelets: proof of concept using Abell 2744. , 481(4):4300–4310, Dec. 2018. doi: 10.1093/mnras/sty2566.

K. Sebesta, L. L. R. Williams, J. Liesenborgs, E. Medezinski, and N. Okabe. Free-form GRALE reconstruction of Abell 2744: robustness of uncertainties against

changes in lensing data. , 488(3):3251–3261, Sept. 2019. doi: 10.1093/mnras/stz1950.

M. S. Seigar. *Dark Matter in the Universe*. 2053-2571. Morgan Claypool Publishers, 2015. ISBN 978-1-6817-4118-5. doi: 10.1088/978-1-6817-4118-5. URL https://dx.doi.org/10.1088/978-1-6817-4118-5.

I. Sendra, J. M. Diego, T. Broadhurst, and R. Lazkoz. Enabling non-parametric strong lensing models to derive reliable cluster mass distributions: Wslap+. *Monthly Notices of the Royal Astronomical Society*, 437:2642–2651, 2014. doi: 10.1093/mnras/stt2122.

M. Sereno. Probing the dark energy with strong lensing by clusters of galaxies. , 393:757–764, Oct. 2002. doi: 10.1051/0004-6361:20021048.

H. e. a. Shan. An analysis of mass distribution in 38 x-ray luminous clusters with strong lensing and x-ray data. *Monthly Notices of the Royal Astronomical Society*, 406:1134–1148, 2010. doi: 10.1111/j.1365-2966.2010.16762.x. URL https://doi.org/10.1111/j.1365-2966.2010.16762.x.

K. Sharon, M. B. Bayliss, H. Dahle, S. J. Dunham, M. K. Florian, M. D. Gladders, T. L. Johnson, G. Mahler, R. Paterno-Mahler, J. R. Rigby, K. E. Whitaker, M. Akhshik, B. P. Koester, K. Murray, J. D. Remolina González, and E. Wuyts. Strong Lens Models for 37 Clusters of Galaxies from the SDSS Giant Arcs Survey. , 247(1):12, Mar. 2020. doi: 10.3847/1538-4365/ab5f13.

L. D. Shaw, J. Weller, J. P. Ostriker, and P. Bode. Statistics of physical properties in simulated galaxy clusters. *The Astrophysical Journal*, 646(2):815–833, 2006. doi: 10.1086/504961.

I. e. a. Smail. The hst medium deep survey - x. morphologies of field galaxies at high redshift. *The Astrophysical Journal Supplement Series*, 110:213–221, 1997. doi: 10.1086/313003. URL https://doi.org/10.1086/313003.

G. P. Smith, J.-P. Kneib, I. Smail, P. Mazzotta, H. Ebeling, and O. Czoske. A hubble space telescope lensing survey of x-ray luminous galaxy clusters – ii. mass structure in a383. *Monthly Notices of the Royal Astronomical Society*, 359 (2):417–446, 2005. doi: 10.1111/j.1365-2966.2005.08914.x.

G. P. Smith, P. Mazzotta, N. Okabe, F. Ziparo, S. L. Mulroy, A. Babul, A. Finoguenov, I. G. McCarthy, M. Lieu, Y. M. Bahé, H. Bourdin, A. E. Evrard, T. Futamase, C. P. Haines, M. Jauzac, D. P. Marrone, R. Martino, P. E. May, J. E. Taylor, and K. Umetsu. LoCuSS: Testing hydrostatic equilibrium in galaxy clusters. , 456(1):L74–L78, Feb. 2016. doi: 10.1093/mnrasl/slv175.

Soldner. Ueber das allgemeine Gesetz für die Expansivkraft des Wasserdampfes durch Wärme, nach Dalton's Versuchen; nebst einer Anwendung dieses Gesetzes auf das Verdunsten der Flüssigkeiten. *Annalen der Physik*, 17(5):44–81, Jan. 1804. doi: 10.1002/andp.18040170505.

K. T. Soto, S. J. Lilly, R. Bacon, J. Richard, and S. Conseil. ZAP - enhanced PCA sky subtraction for integral field spectroscopy. , 458(3):3210–3220, May 2016. doi: 10.1093/mnras/stw474.

G. Soucail, Y. Mellier, B. Fort, F. Hammer, and G. Mathez. Confirmation of the gravitational lens nature of the giant luminous arc in a 370. *Astronomy and Astrophysics*, 191:L19–L21, 1988.

G. e. a. Soucail. The giant arc in abell 370 - a gravitational lensing effect? *Astronomy and Astrophysics*, 172:L14–L16, 1987.

D. N. Spergel and P. J. Steinhardt. Observational evidence for self-interacting cold dark matter. *Physical Review Letters*, 84:3760, 2000. doi: 10.1103/PhysRevLett.84.3760.

V. Springel. The cosmological simulation code gadget-2. *Monthly Notices of the Royal Astronomical Society*, 364(4):1105–1134, 2005. doi: 10.1111/j.1365-2966.2005.09655.x. URL https://doi.org/10.1111/j.1365-2966.2005.09655.x.

V. Springel, J. Wang, M. Vogelsberger, A. Ludlow, A. Jenkins, A. Helmi, J. F. Navarro, C. S. Frenk, and S. D. M. White. The Aquarius Project: the subhaloes of galactic haloes. , 391(4):1685–1711, Dec. 2008. doi: 10.1111/j.1365-2966.2008.14066.x.

C. L. Steinhardt et al. The buffalo survey: A hubble frontier fields legacy program. *The Astrophysical Journal Supplement Series*, 247(2):64, 2020.

K. A. Suess, J. R. Weaver, S. H. Price, R. Pan, B. Wang, R. Bezanson, G. Brammer, S. E. Cutler, I. Labbé, J. Leja, C. C. Williams, K. E. Whitaker, H. Atek, P. Dayal, A. de Graaff, R. Feldmann, M. Franx, Y. Fudamoto, S. Fujimoto, L. J. Furtak, A. D. Goulding, J. E. Greene, G. Khullar, V. Kokorev, M. Kriek, B. Lorenz, D. Marchesini, M. V. Maseda, J. Matthee, T. B. Miller, I. Mitsuhashi, L. A. Mowla, A. Muzzin, R. P. Naidu, T. Nanayakkara, E. J. Nelson, P. A. Oesch, D. J. Setton, H. Shipley, R. Smit, J. S. Spilker, P. van Dokkum, and A. Zitrin. Medium Bands, Mega Science: A JWST/NIRCam Medium-band Imaging Survey of A2744. , 976(1):101, Nov. 2024. doi: 10.3847/1538-4357/ad75fe.

R. A. Sunyaev and Y. B. Zeldovich. The observations of relic radiation as a test of the nature of x-ray radiation from the clusters of galaxies. *Comments on Astrophysics and Space Physics*, 4:173–178, 1972.

D. Suto, H. Kawahara, T. Kitayama, S. Sasaki, Y. Suto, and R. Cen. Validity of Hydrostatic Equilibrium in Galaxy Clusters from Cosmological Hydrodynamical Simulations. , 767(1):79, Apr. 2013. doi: 10.1088/0004-637X/767/1/79.

R. Thom. *Structural Stability and Morphogenesis*. Westview Press, 1989.

T. Treu, G. Brammer, J. M. Diego, et al. Refined mass model of macs j1149.5+2223. *The Astrophysical Journal*, 812(2):114, 2015. doi: 10.1088/0004-637X/812/2/114.

T. Treu, G. Roberts-Borsani, M. Bradac, G. Brammer, A. Fontana, A. Henry, C. Mason, T. Morishita, L. Pentericci, X. Wang, A. Acebron, M. Bagley, P. Ber-

gamini, D. Belfiori, A. Bonchi, K. Boyett, K. Boutsia, A. Calabró, G. B. Caminha, M. Castellano, A. Dressler, K. Glazebrook, C. Grillo, C. Jacobs, T. Jones, P. L. Kelly, N. Leethochawalit, M. A. Malkan, D. Marchesini, S. Mascia, A. Mercurio, E. Merlin, T. Nanayakkara, M. Nonino, D. Paris, B. Poggianti, P. Rosati, P. Santini, C. Scarlata, H. V. Shipley, V. Strait, M. Trenti, C. Tubthong, E. Vanzella, B. Vulcani, and L. Yang. The GLASS-JWST Early Release Science Program. I. Survey Design and Release Plans. , 935(2):110, Aug. 2022. doi: 10.3847/1538-4357/ac8158.

K. Umetsu, E. Medezinski, M. Nonino, J. Merten, A. Zitrin, A. Molino, C. Grillo, M. Carrasco, M. Donahue, A. Mahdavi, D. Coe, M. Postman, A. Koekemoer, N. Czakon, J. Sayers, T. Mroczkowski, S. Golwala, P. M. Koch, K.-Y. Lin, S. M. Molnar, P. Rosati, I. Balestra, A. Mercurio, M. Scodeggio, A. Biviano, T. Anguita, L. Infante, G. Seidel, I. Sendra, S. Jouvel, O. Host, D. Lemze, T. Broadhurst, M. Meneghetti, L. Moustakas, M. Bartelmann, N. Benítez, R. Bouwens, L. Bradley, H. Ford, Y. Jiménez-Teja, D. Kelson, O. Lahav, P. Melchior, J. Moustakas, S. Ogaz, S. Seitz, and W. Zheng. CLASH: Mass Distribution in and around MACS J1206.2-0847 from a Full Cluster Lensing Analysis. , 755 (1):56, Aug. 2012. doi: 10.1088/0004-637X/755/1/56.

K. Umetsu, A. Zitrin, D. Gruen, et al. Clash: Weak-lensing shear-and-magnification analysis of 20 galaxy clusters. *The Astrophysical Journal*, 821 (2):116, 2016. doi: 10.3847/0004-637X/821/2/116.

K. Umetsu, M. Sereno, M. Lieu, H. Miyatake, E. Medezinski, A. J. Nishizawa, P. Giles, F. Gastaldello, I. G. McCarthy, M. Kilbinger, M. Birkinshaw, S. Ettori, N. Okabe, I. N. Chiu, J. Coupon, D. Eckert, Y. Fujita, Y. Higuchi, E. Koulouridis, B. Maughan, S. Miyazaki, M. Oguri, F. Pacaud, M. Pierre, D. Rapetti, and G. P. Smith. Weak-lensing Analysis of X-Ray-selected XXL Galaxy Groups and Clusters with Subaru HSC Data. , 890(2):148, Feb. 2020. doi: 10.3847/1538-4357/ab6bca.

A. Vikhlinin, M. Markevitch, S. S. Murray, C. Jones, W. Forman, and L. Van Speybroeck. Chandra Sample of Nearby Relaxed Galaxy Clusters: Mass, Gas Fraction, and Mass–Temperature Relation. *The Astrophysical Journal*, 640:691–709, 2006. doi: 10.1086/499572.

N. Visvanathan and A. Sandage. The color - absolute magnitude relation for E and S0 galaxies. I. Calibration and tests for universality using Virgo and eight other nearby clusters. , 216:214–226, Aug. 1977. doi: 10.1086/155464.

M. Vogelsberger, J. Zavala, and A. Loeb. Subhaloes in self-interacting galactic dark matter haloes. *Monthly Notices of the Royal Astronomical Society*, 423: 3740–3752, 2012. doi: 10.1111/j.1365-2966.2012.21182.x.

W. Voges, B. Aschenbach, T. Boller, H. Bräuninger, U. Briel, W. Burkert, K. Dennerl, J. Englhauser, R. Gruber, F. Haberl, G. Hartner, G. Hasinger, M. Kürster, E. Pfeffermann, W. Pietsch, P. Predehl, C. Rosso, J. H. M. M. Schmitt, J. Trümper, and H. U. Zimmermann. The ROSAT all-sky survey bright source catalogue. , 349:389–405, Sept. 1999.

D. Walsh, R. F. Carswell, and R. J. Weymann. 0957+561 A, B: twin quasistellar objects or gravitational lens? , 279:381–384, May 1979. doi: 10.1038/279381a0.

B. Wang, J. Leja, I. Labbé, R. Bezanson, K. E. Whitaker, G. Brammer, L. J. Furtak, J. R. Weaver, S. H. Price, A. Zitrin, H. Atek, D. Coe, S. E. Cutler, P. Dayal, P. van Dokkum, R. Feldmann, D. Marchesini, M. Franx, N. Förster Schreiber, S. Fujimoto, M. Geha, K. Glazebrook, A. de Graaff, J. E. Greene, S. Juneau, S. Kassin, M. Kriek, G. Khullar, M. Maseda, L. A. Mowla, A. Muzzin, T. Nanayakkara, E. J. Nelson, P. A. Oesch, C. Pacifici, R. Pan, C. Papovich, D. J. Setton, A. E. Shapley, R. Smit, M. Stefanon, K. A. Suess, E. N. Taylor, and C. C. Williams. The UNCOVER Survey: A First-look HST+JWST Catalog of Galaxy Redshifts and Stellar Population Properties Spanning $0.2 \lesssim z \lesssim 15$. , 270(1):12, Jan. 2024. doi: 10.3847/1538-4365/ad0846.

J. Wang and S. D. M. White. Are mergers responsible for universal halo properties? , 396(2):709–717, June 2009. doi: 10.1111/j.1365-2966.2009.14755.x.

X. e. a. Wang. A hubble frontier field strong-lensing analysis of the massive galaxy cluster abell 2744 using 72 multiple images. *The Astrophysical Journal*, 811(1): 29, 2015. doi: 10.1088/0004-637X/811/1/29. URL https://doi.org/10.1088/0004-637X/811/1/29.

J. R. Weaver, S. E. Cutler, R. Pan, K. E. Whitaker, I. Labbé, S. H. Price, R. Bezanson, G. Brammer, D. Marchesini, J. Leja, B. Wang, L. J. Furtak, A. Zitrin, H. Atek, I. Chemerynska, D. Coe, P. Dayal, P. van Dokkum, R. Feldmann, N. M. Förster Schreiber, M. Franx, S. Fujimoto, Y. Fudamoto, K. Glazebrook, A. de Graaff, J. E. Greene, S. Juneau, S. Kassin, M. Kriek, G. Khullar, M. V. Maseda, L. A. Mowla, A. Muzzin, T. Nanayakkara, E. J. Nelson, P. A. Oesch, C. Pacifici, C. Papovich, D. J. Setton, A. E. Shapley, H. V. Shipley, R. Smit, M. Stefanon, E. N. Taylor, A. Weibel, and C. C. Williams. The UNCOVER Survey: A First-look HST + JWST Catalog of 60,000 Galaxies near A2744 and beyond. , 270 (1):7, Jan. 2024. doi: 10.3847/1538-4365/ad07e0.

R. H. Wechsler and J. L. Tinker. The connection between galaxies and their dark matter halos. *Annual Review of Astronomy and Astrophysics*, 56(1):435–487, 2018. doi: 10.1146/annurev-astro-081817-051756. URL https://doi.org/10.1146/annurev-astro-081817-051756.

J. S. B. Wyithe, E. L. Turner, and D. N. Spergel. Gravitational Lens Statistics for Generalized NFW Profiles: Parameter Degeneracy and Implications for Self-Interacting Cold Dark Matter. , 555(1):504–523, July 2001. doi: 10.1086/321437.

E. C. Zeeman. Catastrophe theory. *Scientific American*, 234(4):65–83, 1977.

Y.-Y. e. a. Zhang. Xmm-newton observations of the merging galaxy cluster abell 2744. *The Astrophysical Journal*, 608:732–745, 2004. doi: 10.1086/420888. URL https://doi.org/10.1086/420888.

W. Zheng, X. Shu, J. Moustakas, A. Zitrin, H. C. Ford, X. Huang, T. Broadhurst, A. Molino, J. M. Diego, L. Infante, F. E. Bauer, D. D. Kelson, and R. Smit. Young Galaxy Candidates in the Hubble Frontier Fields. I. A2744. , 795(1):93, Nov. 2014. doi: 10.1088/0004-637X/795/1/93.

A. Zitrin, T. Broadhurst, R. Barkana, Y. Rephaeli, and N. Benítez. Strong-lensing analysis of a complete sample of 12 MACS clusters at z $>$ 0.5: mass models and Einstein radii. , 410(3):1939–1956, Jan. 2011. doi: 10.1111/j.1365-2966.2010.17574.x.

A. Zitrin, T. Broadhurst, Y. Rephaeli, S. Sadeh, R. Barkana, and N. Benítez. Light-traces-mass modeling of galaxy clusters: application to clash clusters. *Monthly Notices of the Royal Astronomical Society*, 426:2944–2958, 2012. doi: 10.1111/j.1365-2966.2012.21878.x.

A. Zitrin, A. Fabris, J. Merten, et al. An improved light-traces-mass strong lensing analysis of galaxy clusters. *The Astrophysical Journal*, 762:L30, 2013. doi: 10.1088/2041-8205/762/2/L30.

A. Zitrin, A. Fabris, J. Merten, et al. Clash: The concentration–mass relation of galaxy clusters. *The Astrophysical Journal*, 801(1):44, 2015. doi: 10.1088/0004-637X/801/1/44.

A. e. a. Zitrin. Lyman-break galaxies at z 10 in the hubble frontier fields: The discovery of a candidate at z 10 in abell 2744. *The Astrophysical Journal Letters*, 793(2):L12, 2014. doi: 10.1088/2041-8205/793/2/L12. URL https://doi.org/10.1088/2041-8205/793/2/L12.

F. Zwicky. Die Rotverschiebung von extragalaktischen Nebeln. *Helvetica Physica Acta*, 6:110–127, Jan. 1933.

F. Zwicky. Nebulae as Gravitational Lenses. *Physical Review*, 51(4):290–290, Feb. 1937. doi: 10.1103/PhysRev.51.290.

Colophon

This thesis is based on a template developed by Matthew Townson and Andrew Reeves. It was typeset with LaTeX 2_ε. It was created using the *memoir* package, maintained by Lars Madsen, with the *madsen* chapter style. The font used is Latin Modern, derived from fonts designed by Donald E. Kunith.